Semiconductor Magnetoelectronics for Spintronics

and

Suspended 2DEG for Mechanoelectronics

Thesis by

Hongxing Tang

Advisor: Professor Michael L. Roukes

In Partial Fulfillment of the Requirements

for the Degree of

Doctor of Philosophy

California Institute of Technology

Pasadena, California

2002

(Defenced May 22, 2002)

Acknowledgements

Foremost, I want to thank my wife, Lin Feng, for her encouragement, devotion and endurance during my stay at Caltech. I thank my parents, my sisters and brothers, who may never understand my research at all but support and watch over me all my life.

I must express my gratitude and deep appreciation to my advisor, Professor Michael Roukes for providing his guidance and assistance throughout the course of this research, for all the opportunities he has given to me to interact with this community, and for his endless efforts and patience to my non-native style of writing and speaking. I am also very grateful to Dr. Frank Monzon for his precious training and the collaborative work at the beginning stage of my graduate work. So thanks to Jessica Arlett, Nils Asplund, Eyal Buks, Jean Carthy, Kamil Ekinci, Warron Fon, Darrell Harrington, Erik Henriksen, Jim Hone, Henry Huang, Ron Lifshitz, Mike Murphy, Dirk Orgassa, Keith Schwab, Steve Stryker, Jack Yang for their help and discussions on various topics, and for the time we have enjoyed in the subbasement of Sloan Lab. A very special note to Professor Phil Wigen for critical comments and careful reading of my drafts.

I would also like to thank the other members of my committee, Professor Mike Cross and Professor Jim Eisenstein, for reviewing my work and providing stimulating discussions.

Finally, I want to address my special thanks to our collaborators Roland Kawakami and David Awschalom on the spintronics project and Werner Wegscheider on the sus2DEG project.

Abstract

Part I of this thesis describes my experimental and theoretical efforts to understand spin injection into semiconductors. I present extensive discussions on the conditions required to achieve significant spin transfer from a ferromagnetic injector into a paramagnetic conductor. Theoretical calculations for ballistic spin-coupled transport are described. To circumvent conductivity mismatch that occurs for diffusive contacts between ferromagnetic metals and semiconductors, I designed and fabricated new spin injection devices that employ the recently discovered dilute semiconductor (Ga,Mn)As as a spin polarizer. Spin-coupled transport signals were observed in these novel devices.

In the course of this work, I discovered that bulk (Ga,Mn)As itself manifests what we have termed a "giant" planar Hall effect. This magnetoelectronic phenomenon arises from the strong, intrinsic spin-orbit interaction. This phenomenon offers new prospects for applications in magnetic sensors and storage media, extends the possibility of novel spintronic devices, and enables unprecedented, high resolution measurements of magnetic phenomena. By using the giant planar Hall effect, I have achieved a complete characterization of the magnetic properties of (Ga,Mn)As. This large effect also has enabled the first direct electrical measurements of the propagation of individual domain walls in microdevices. These experiments establish a new approach to the study of ferromagnetodynamics that does not require significant instrumentation. Individual domain walls can be monitored, trapped and manipulated in real time. By such techniques, I have been able to directly investigate the resistance arising from a single magnetic domain wall for the first time.

Part II describes my studies of the strain-dependent electrical properties of ballistic GaAs two-dimensional electron gases (2DEGs). I have developed techniques to realize freely-suspended 2DEGs with moderately high mobility. These have been incorporated into novel GaAs nanoelectromechanical systems that yield high sensitivity for NEMS motion detection. They have also led to my discovery of a new, dipolar mechanism for electromechanical actuation. Suspended quantum dots have also been successfully fabricated using my newly developed freely-suspended 2DEG fabrication methods. These demonstrate pronounced charging effects, even at elevated temperature, and offer new prospects for observing electronic interactions with confined phonons.

Table of Contents

PART I: SEMICONDUCTOR MAGNETOELECTRONICS 23

Chapter 1. Spin Injection – a Resúmé 24

1.1. Introduction to Spintronics and Spin Injection 24

1.2. Why semiconductor spintronics? 25

1.3. Spin Injection Complications 26

1.4. New Techniques for Spin Polarization Detection 26

1.5. Chapter Overviews: Spintronics 27

Chapter 2. Spin Injection from (Ga,Mn)As 29

2.1. Material Aspects of Spin Injection in Semiconductors 29

2.2. All Semiconductor (Ga,Mn)As/p-GaAs Spin Injection Devices 32

2.2.1. Motivation and Heterostructure Design 32

2.2.2. Device Fabrication 34

2.2.3. Data From All-Semiconductor Spin Injection Devices 35

2.3. Spin Injection from (Ga,Mn)As to Metals 36

Chapter 3. Giant Planar Hall Effect in Epitaxial (Ga,Mn)As Films 38

Motivation and Anomalies in Local Hall Measurements 38

3.1.1. Anomalous Two-Jump Event in Local Hall Measurement 39

3.1.2. Persistence of Hall Anomaly in an Optimized Sample 42

3.2. The Planar Hall Effect and Its Origin 43

3.2.1. Spontaneous Planar Hall Effect in (Ga, Mn)As 44

3.2.2. Field Angular Dependence of Planar Hall Effect 45

3.2.3. PHE Dependence on Crystalline Orientation 49

3.3. In-Plane Magnetic Crystalline Anisotropy of (Ga,Mn)As: Cubic Anisotropy Plus Uniaxial Anisotropy 50

3.4. Temperature Dependence of PHE and Coercivities 55

3.5. Barkhausen Jumps in Micron-size Samples 58

3.6. Summary 58

Chapter 4. Out-of-Plane Measurement – Extraordinary Hall Effect 60

4.1. Extraordinary Hall Effect 60

4.2. Out-of-Plane Transport Measurement Results 62

4.3. Modeling of Perpendicular Magnetization Reversal Process 64

4.4. Summary 72

Chapter 5. Domain Wall Measurements 73

5.1. Dynamics Measurements of Individual Domain Walls 73

5.1.1. Motivation to Study Domain Dynamics in (Ga, Mn)As 73

5.1.2. Review of Experimental Techniques of Ferromagnetodynamics 74

5.1.3. Time of Flight Measurement Using PHE Setup 79

5.1.4. Longitudinal Time of Flight Measurement 80

5.1.5. Domain Wall Dynamics 83

5.1.6. Manipulation of Single Magnetic Domain Wall 86

5.1.7. Summary 87

5.2. Resistance of Individual Domain Walls 88

5.2.1. Motivation to Study Single Domain Resistance 88

5.2.2. Single Domain Wall Resistance of Epitaxial (Ga,Mn)As Films 89

PART II: SUSPENDED TWO-DIMENSIONAL ELECTRON GAS 92

Chapter 6. Freely-Suspended Two-Dimensional Electron Gases: Realization and Applications. 93

6.1. Introduction 93

6.2. Materials 95

6.3. Electro-mechanical Background of GaAs 96

6.3.1. Beam Mechanics Summary 96

6.3.2. Piezoelectric and Piezoresistive Effect of Ga(Al)As 97

6.4. Electron-Confined Phonon Interaction 100

6.4.1. Free-Standing Wires 100

6.4.2. Suspended Quantum Dots 101

6.5. Fabrication of Self-Sensitive Suspended 2DEG Beams 101

Chapter 7. Mesoscopic Physics in Freely-Suspended 2DEGs 103

7.1. Suspended Quantum Wires 103

7.1.1. Fabrication of Suspended Hall Bars 104

7.1.2. High Field Measurement Results 105

7.1.3. Evidences of Ballistic Electron Transport in Sus2DEG Wires 107

7.2. Suspended Quantum Dots: Fabrication and Preliminary Results 113

Chapter 8. Integrated 2DEG-Based Strain Sensors for NEMS Displacement Detection 116

8.1. Characterization of Mechanical-Electrical Response by AFM Pushing 116

8.2. Dynamic Response Measurement 119

8.2.1. Experiment Setup 119

8.2.2. Observation of Mechanical Resonance 119

8.2.3. Actuation Mechanism of In-plane Gated 2DEG Beam 122

8.2.4. Temperature Dependence of Mechanical Response 123

Appendix A. Introduction to Spin Injection and Transport 125

A.1. Background 127

A.1.1 Spin Polarized Tunneling 127

A.1.2 Spin Injection in Clean Bulk Metals 128

A.1.3 Conceptual Picture of Spin Injection 131

A.1.4 Spin Injection in Impure Metal Films 134

A.2. Toward a Semiconducting "Spin Transistor" 136

A.2.1 Why a Spin Transistor? 136

A.2.2 Why Semiconductors? 136

A.2.3 Concept 137

A.2.4 Prerequisites for Realizing a Spin Transistor 138

A.2.5 Spin Lifetime in the Conduction Channel 139

A.2.6 Gate Control of the Spin Orbit Interaction (Theory) 139

A.2.7 Gate Control of the Spin Orbit Interaction (Experiment) 141

A.3. Initial Experiments on Spin Injection in Semiconductor Heterostructures 144

A.3.1 Motivation and Initial Data 144

A.3.2 Local Hall Effect 147

A.3.3 Results from Smaller, Optimized Devices 149

A.4. Spin Injection in Diffusive Systems 153

A.4.1 Basic Model for Spin Transport in Diffusive Systems 153

A.4.2 The F/N Interface 156

A.4.3 Spin Accumulation in Multiterminal Spin Valve Structures 158

A.4.4 Observation of Spin-Injection and Spin-Accumulation in an All-Metal Spin Valve 159

A.4.5 Comparison With the Johnson "Spin Transistor" 160

A.4.6 Future Prospects for Spin Accumulation and Spin Transport in All-Metal Devices 161

A.4.7 Spin Injection in a Diffusive Semiconductor 162

A.4.8 Conductivity Mismatch 163

A.4.9 Possible Solutions to Conductivity Mismatch 164

A.5. Projections and Conclusions 165

A.5.1 Retrospective: The Spin Transistor 165

A.5.2 Recent Advances in Spin Transport across Interfaces 167

A.5.3 Recent Advances in Spin Injection via Semimagnetic Semiconductors 171

A.5.4 Recent Advances in Spin Propagation in Semiconductors 172

Appendix B. Spin Transport in the Ballistic Regime 173

B.1. Multiprobe model for Ballistic Spin Polarized Transport 176

B.2. Results of Spin Resolved 4-Probe Model 180

B.3. Eight-Probe Model: Junction, Bulk, and Boundary Scattering 183

B.4. The Spin Transistor: A Closer Look 186

B.5. Other Theoretical Treatments 187

Appendix C. The QPC Spin Polarization Detector 189

C.1. Concept of a QPC detector 189

C.2. Nonlinear a.c. Detection Scheme for Enhanced Sensitivity 190

C.3. Estimate of Potential Sensitivity of the QPC Spin Polarization Detector 193

C.4. Initial QPC Spin Polarization Detection Devices 195

Appendix D. Imaging Injected Nonequilibrium Spin Polarization by MRFM 200

Appendix E. Measurement Setup 202

Reference 204

List of Figures

Fig. 2.1 Layer stack for local Hall characterization devices and all-semiconductor spin injection devices. 33

Fig. 2.2 Top and side view of our first GaAs/GaMnAs spin injection devices patterned by e-beam lithography. 34

Fig. 2.3 Preliminary magnetoresistance data from all-semiconductor spin injection devices. 35

Fig. 2.4 Micrographs showing electron beam lithography patterned (Ga,Mn)As/metal spin injection devices. Gray bars are 150 nm thick (Ga,Mn)As. Two types of geometries are patterned. (a) Regular in-line device with magnets of different sizes. (b) Contact areas for both magnets are extended to reduce contact resistances. 36

Fig. 2.5. Hysteretic phenomena from non-local measurement of a (Ga,Mn)As/Metal spin device with 2 μm injector-dectector separation. 37

Fig. 3.1 A "local Hall device" that was used to characterize a 750 nm × 10 μm (Ga,Mn)As miniature magnet. 39

Fig. 3.2 Magnetotransport measurement data on a local Hall geometry sample. Data from five different field orientations are presented. 40

Fig. 3.3 Top: sweeping pattern of magnetic field. Left: A differential plot of the Hall resistance. Horizontal axis represents H_x, vertical axis is H_y. 41

Fig. 3.4 (a) SEM micrograph showing an optimized micron-size magnet. (b) Hall measurement data on such a magnet, proving that local Hall effect is not the origin of observed magnetoresistance jumps. (c) A cross-sectional view of possible current trajectories in the device. 42

Fig. 3.5 SEM micrograph of a 6 μm Hall bar. The distance between voltage probes is 12 μm. ... 43

Fig. 3.6 Planar Hall resistance and sheet resistance of (Ga,Mn)As Hall devices at 4.2 K. An in-plane magnetic field, fixed at 20 degrees away from [110], is swept in amplitude. (a)-(c) Planar Hall resistance for Hall bars ranging in width from 1mm to 6 μm. (d) Field-dependent sheet resistance of a 100 μm-wide Hall bar. 44

Fig. 3.7 Angular dependence of the planar Hall resistance 46

Fig. 3.8 A sketch of the relative orientations of current I, magnetization M, and external field H. The Hall bar is patterned along [110] crystalline direction..... 47

Fig. 3.9 A diagram showing that planar Hall effect has its origin in the anisotropic magnetoresistance of (Ga,Mn)As. 47

Fig. 3.10 Planar Hall effect for orientational sweeps of magnetic field (fixed magnitude)..... 48

Fig. 3.11 Planar Hall resistance for Hall bars orientated 0°, 15°, 30° and 45° away from [110] crystalline axis. 49

Fig. 3.12 Polar plot of the first and second switching fields vs. orientation of external field. 50

Fig. 3.13 (a) Magnetic energy density as a function of magnetization orientation in various situations of magnetocrystalline anisotropy. (b) The equilibrium positions for a mixed cubic and uniaxial anisotropy energy surface..... 51

Fig. 3.14 An illustration of two-jump process occurring in a cubic magneto-crystalline anisotropy ferromagnet. 52

Fig. 3.15. Illustration of the procedure to yield magnetic anisotropy constant from high field orientational planar Hall measurement data (6000 Oe). The magnetization angles are first computed from experimental data by Eq. (3.5). Then phase lag between external field and magnetization are plotted as a function of magnetization angle, which is nicely fitted by a non-linear function [Eq. (3.7)] to yield anisotropy parameters..... 53

Fig. 3.16 (a) Comparison between experimental data and calculated planar Hall resistance with optimized parameters. (b) Table showing the fitting result for measurements made at in plane magnetic fields with magnitudes 4000 Oe and 6000 Oe. 54

Fig. 3.17 (a) Temperature dependence of the planar Hall resistance. (b) Plots of the planar Hall resistance jump, ΔR_H, and sheet resistance, $R_\square$, versus temperature (semi-logarithmic scale). (c) Comparison between the magnetoresistance ratio, $\Delta R_H / R_\square$, obtained from transport measurements on a 10 μm wide Hall device, and sample magnetization, M, measured by SQUID magnetometry on a macroscopic (3 mm × 3 mm) sample..... 56

Fig. 3.18 Temperature dependence of coercivities determined by planar Hall resistance..... 57

Fig. 3.19 Barkhausen jumps that are evident solely in 6 μm wide devices near the resistance transitions. 58

Fig. 4.1 Coordinate system in 3-D space for out of plane experiments. 61

Fig. 4.2 Longitudinal resistance R_{sheet} for external fields applied in three orthogonal orientations. The result for a planar Hall resistance R_{PHE} is also presented for comparison. *Inset*: enlarged view of low field magnetoresistance at low field region. 62

Fig. 4.3 Longitudinal resistance R_{sheet} and Hall resistance R_H for a 100 μm wide Hall bar subject to a perpendicular field. For comparison, the result for a planar Hall resistance R_{PHE} is also presented. 63

Fig. 4.4 An illustration of three energy minima for out-of-plane free energy. Horizontal axis is the polar angle. In this particular diagram, a large positive field is applied. 67

Fig. 4.5 Characteristic fields for films with perpendicular field: Nucleation fields: $\pm H_N$, domain annihilation fields. Magnetization precesses coherently in the linear Hall resistance region.69

Fig. 4.6 Illustration of the origin of hysteresis in out-of-plane Hall measurement. When the perpendicular magnetic field sweeps across the zero, the in-plane magnetizations are orthogonal, giving a resistance difference same as the spontaneous planar resistance jumps. 71

Fig. 5.1 Apparatus used by Sixtus and Tonks (1931). The magnetization of a nickel-iron wire reverses by the propagation of a domain boundary of the kind shown (inset)..... 76

Fig. 5.2 Left: experimental sketch for typical magneto-optical microscopy. Right: procedure to obtain the domain velocity..... 77

Fig. 5.3 (a) SEM image and schematic illustration of the sample. The sample consists of a NiFe(200Å)/Cu(100Å)/NiFe(50Å) trilayer. (b) Time variation of the resistance during the M reversal of the 400-Å NiFe layer at 77 K..... 78

Fig. 5.4 (a) Measurement setup. After a domain wall is nucleated at one side of the sample, it propagates sequentially across three Hall bars and successively generates gigantic planar Hall voltages. High input impedance differential amplifiers are used to make true potential measurements. (b) A typical planar Hall resistance (R) *vs* magnetic field (H) loop for a 100 μm wide Hall bar. 79

Fig. 5.5 (a) Planar Hall responses at three Hall crosses with in-plane field decreases from 88 Oe to 74 Oe. Inset: A magnified view demonstrates the fast dynamics that occurs at 88 Oe. 81

Fig. 5.6 (a) A comparison of resistance switching curves for T = 0.35K, 5K, and 20K. (b) Estimated domain wall profile corresponding to (a). 82

Fig. 5.7 Domain wall velocity as a function of magnetic field at 5 K, 10 K, and 20 K shown in linear and semilog formats (inset). The external field orientation is 15° away from [110]. In the normal plot, the solid lines represent fits to the high field velocities. In the semilog plot, the solid lines are linear fits to the low field region. 83

Fig. 5.8 Domain wall velocity *vs.* magnetic field orientation. Angles are measured with respect to [110]. Inset: Domain wall velocity *vs.* rescaled field (the component along [110]). Data points of different angles condense onto a single universal curve. 86

Fig. 5.9 Freezing of a single domain wall. The domain wall is driven at a slow speed and the planar Hall resistance of the central probes is monitored to reflect the passage of the domain wall. The crossing-zero of this signal triggers the removal of external magnetic field. The domain wall is found to be stationary ever since. 87

Fig. 5.10 Time-resolved magnetoresistance measured across a single domain wall at 5K. (a) PHR of two pairs of Hall probes monitoring the entrance and exit of a single domain wall. (b) Longitudinal resistances across the wall are measured simultaneously from top and bottom of the Hall bar. (c) Resistance sum rule is satisfied: difference between Hall resistances equals to the difference between longitudinal resistances $R_{xx}^{U} - R_{xx}^{D}$. (d) The variance of the average between R_{xx}^{U} and R_{xx}^{D} suitably separates major part of domain magnetoresistance and reflects excess domain wall resistance when the domain wall is completely resident between probes. (e) Temperature dependence of the overall ressitance variance. 91

Fig. 6.1 Heterostructure design and calculated band structure of suspended 2DEG. 95

Fig. 6.2 System of coordinates used in (100) oriented GaAs 99

Fig. 6.3 (a) Strain distribution in a bending beam. Dashed line is neutral plane. (b) Polarization and charge distribution on the beam. 99

Fig. 6.4. (a) Experimental data from decoupled metallic wire in Seyler *et al.* [80] The peaks corresponding to multiple inelastic phonon emissions. (b) Suspended GaAs wires in Potts *et al.* [81] 100

Fig. 6.5 Conductance spectrum through a coupled quantum dots device performed by Fujisawa et al. [82] The inelastic part may originate from phonon emission. 101

Fig. 7.1 Aerial view of the device, showing the clear undercut. This specific sample has two hall bars that are 0.7μm and 0.5μm (left one partially visible) wide and 5μm long. 105

Fig. 7.2 (a) Longitudinal magnetoresistance $R(B)$ for Hall bar with three Hall bars with 0.5μm, 0.7μm and 0.9μm lithography widths. (b) Hall effect of corresponding Hall bars. Quantum Hall effect is evident at high field. 106

Fig. 7.3 (a) At low magnetic fields the electron trajectories are forced to interact with the edges, increasing the degree of backscattering. (b) At fields $B = B_{max}$ the backscattering is maximized and μ_{eff} is reduced to its lowest value. (c) For fields such that $2r_c < W$ the backscattering is suppressed and $\mu_{eff} \rightarrow \mu_0$. 108

Fig. 7.4 Typical weak magnetic-field behavior of the Hall resistance R_H and the transfer resistance R_B at a quasi-ballistic junction: (a) Basic structure and measurement configuration; (b) Hall resistance behavior, with the classically expected linear behavior shown by the dashed line; (c) transfer resistance behavior, with the positive value expected for a macroscopic sample shown by the dashed line. 109

Fig. 7.5 Transfer resistance at one single junction and at two junctions 109

Fig. 7.6 Examples of electron trajectories giving rise to the various magnetoresistance anomalies. (a) Rebound. (b) Collimating. 110

Fig. 7.7 Magnetoresistance curves for suspended quantum wires ranging from 0.35 μm to 0.70 μm wide. Data was taken at 4.2K 111

Fig. 7.8 Fluctuating part of magnetoresistance after substracting the background. 111

Fig. 7.9 Conductance fluctuations autocorrelation function for suspended 2DEG 112

Fig. 7.10 Two classes of suspended quantum dots we have fabricated. A puddle of electrons are confined in the center islands. 113

Fig. 7.11 Columb blockade observed in suspended quantum dots at 4.2K. Upper inset: pinch curves for G2 and G4 with 0.5V gate voltage on G1. Lower inset: pinch curve for gate G1 with G2 and G4 floating. 114

Fig. 7.12. Shot noise from a single defect sitting on the suspended quantum dot. 115

Fig. 8.1 (a) Schematic view of the test setup. (b) AFM tip displacement and 2DEG beam resistance variance with repeated cycle of ~0.5 s. 117

Fig. 8.2 A pair of doubly-clamped beams containing 2DEG for AFM pushing experiments. 118

Fig. 8.3 (a) SEM image of a doubly clamped beam. The in-plane gates are formed by the 2DEG. (b) Sketch of measurement setup. A constant dc bias current (I_b) is sent through a big rf-choke (~mH) before reaching the beam. Gate drive voltage consists of both dc and rf components: $V_g = V_g^{(0)} + \upsilon_g e^{i\omega t}$. The induced signal can be expressed as $V = V^{(0)} + \upsilon\ e^{i(\omega t+\varphi)}$, where the dc voltage potential $V^{(0)} = I_b R_{dc}$ is blocked by a capacitor C and the oscillating component is amplified at both liquid helium and room temperature. 118

Fig. 8.4 (a) Voltage drop across the beam as it is driven to its lowest mechanical resonance with increasing drive amplitudes. The dc bias current is fixed at 5μA. Inset: The peak value of amplitude response as a function of driving amplitude in the linear regime. (b) Magnitude response curve at various dc bias current. Inset: The signal amplitude at resonance with sensing current increase from -26 μA to 26 μA. 120

Fig. 8.5 Cross-sectional illustration of dipoles formation on the beam (p_1) and on the driving gate (dp_2). 122

Fig. 8.6 Response curve at three different temperatures. Inset: Sketch of amplitude and frequency change vs temperature 124

Fig. A.1 Sketch illustrating the basic components of a three-terminal spin injection device. External magnetic fields are employed to controllably switch the relative orientation of the ferromagnetic electrodes (**F1**, **F2**). The ground connection (current return) for the paramagnetic conductor (**P**) is attached many spin diffusion lengths from the region of spin injection, and is therefore far from the cloud of induced magnetization (*shaded region*). The ground connection for the detected voltage need not necessarily be the same as the ground

for current return, allowing for nonlocal four-terminal measurements, as described in the text. 128

Fig. A.2 Schematic representations of the spin devices of Johnson and Silsbee employing Al foil, which was 50 μm thick and 100 μm wide [16]. (b) Representative data from all-metallic spin devices: Hanle effect experiment [16, 114, 115]. 130

Fig. A.3 Schematic diagrams of the densities of states (horizontal axis) versus energy (vertical axis) in the ferromagnets and paramagnets. In (a) the zero current bias case is shown while in (b) bias current from **F1** to **P** preferentially builds up one spin population (shaded)..... 131

Fig. A.4 (a) The geometry of Johnson's all-metal "spin transistor". (b) Data obtained from a polarize/analyze experiment with such a device {Johnson, 1993}. 135

Fig. A.5 A spin-FET proposed by Datta and Das, conceptually similar in operation to an electro-optic modulator. Two magnetic contacts serve as spin polarizer and spin analyzer. The propagation medium between them—capable of inducing a gate-controllable net rotation of spin orientation—is a two-dimensional electron gas (2DEG). 137

Fig. A.6 Shubnikov de Haas oscillations in a two-dimensional hole gas providing an especially clear demonstration of the beating characteristic of spin split bands. (After Ref. [139]). Spin-splitting in these experiments was changed by applying an electric field perpendicular to the 2-D plane $E_{\perp}$. Through simultaneous use of both front and back gate electrodes the spin splitting could be tuned while the electron density was held fixed. (a) Magnetoresistance traces, all at a density of 3.3 ×11 cm^{-2} but at different values of $E_{\perp}$. The data shown are from the low-mobility $[01\bar{1}]$ (top trace in each panel) and high-mobility $[\bar{2}33]$ (bottom trace in each panel) directions. (b) Fast Fourier transforms (FFT) of the Shubnikov de Haas oscillations, showing that the spin splitting is being tuned through a minimum. 140

Fig. A.7 Two geometries used in an InAs devices patterned by photolithography (a and b). Black areas denote contacts (NiFe on top of exposed InAs), densely spotted areas are NiFe, sparsely spotted areas are conducting mesas, and white regions show metal interconnections. Channel widths were either 3 or 6 μm and separations varied from 6 to 64 μm. In (c) and (d) data are shown for devices similar to that in (a), while in (a) shows data for a device that of (b). Black traces are for down field sweeps, grey traces are for upfield. 145

Fig. A.8 (a) Schematic side view of a device showing the magnetic fringe field whose perpendicular component, $B_{\perp}$, induces Hall voltages in the conducting underlayer. The SEM micrograph in (b) shows a NiFe magnet of width 500 nm positioned over a GaAs cross-junction. Magnetization and current flow are directed vertically, while Hall voltage is read out across the horizontal legs. 146

Fig. A.9 $\boldsymbol{H}_c$ versus w for numerous magnets with nominally the same deposition conditions and with aspect ratios of 10. All data were taken at room temperature. Vertical lines connect data points from magnets of the same width. *Inset:* A series of hysteresis loops for magnets of aspect ratio 10, but with varying widths. Traces are offset vertically..... 147

Fig. A.10 SEM micrographs of InAs quantum wire devices patterned by electron beam lithography. The channels are formed by trench etching on either side of the narrow channels (a,b). These devices have F1-F2 spacings of 1.5 μm. Magnet dimensions are 500 nm × 10 μm and 750 nm × 7.5 μm. Data from similar devices are shown in (c and d)..... 149

Fig. A.11 (a) Scanning electron microscope micrograph of an InAs spin injection device fabricated by the Groningen group. The 1μm wide 2DEG channel is horizontal, and two ferromagnetic electrodes are vertical. (b) Sketch of the two measurement configurations. The indices "SV" and "NL" refer to the classic spin-valve and the nonlocal geometry, respectively. (c) Non-local measurements for a Py/2DEG/Py device. Top two curves give the AMR traces for the two ferromagnetic electrodes, showing different coercive fields in one sweep direction. No spin signal is observed in any of the geometries. The dashed lines correspond to a sweep of the magnetic field towards positive fields..... 152

Fig. A.12 Electrochemical potentials (or densities) of spin-up and spin-down electrons with a current I flowing through an F/N interface. Both spin accumulation as well as spin coupled resistance can be observed (see text). The figure corresponds to $\lambda_N = 5\lambda_F$ 155

Fig. A.13 Sample layout in the experiment of Jedema *et al.* (a) Scanning electron microscope image of the mesoscopic spin valve junction. The two wide strips are the ferromagnetic electrodes Py1 and Py2. The vertical arms of the Cu cross (with contacts 3 and 8) lay on top of the Py strips, the horizontal arms of the Cu cross form contacts 5 and 6. Contacts 1, 2, 4, 7, and 9 are attached to Py1 and Py2 to allow four-terminal AMR measurements of the Py electrodes. (b) Schematic representation of the non-local measurement geometry. Current is

entering from contact 1 and extracted at contact 5. The voltage is measured between contacts 6 and 9..... 157

Fig. A.14 Spin valve effect at T = 4.2K (a), and room temperature (b) in the non-local geometry for a sample with 250nm Py electrode spacing. An increase in resistance is observed, when the magnetization configuration is changed from parallel to anti-parallel. The solid (dashed) lines correspond to the negative (positive) sweep direction (c), (d) illustrate the "memory effect". For clarity (c) and (d) are offset downwards. The sizes of the Py1 and Py2 electrodes are $2.0 \times 0.5\ \mu m^2$ and $14 \times 0.1\ \mu m^2$..... 160

Fig. A.15 (a) Simplified resistor model for a device consisting of a semiconductor (SC) with two ferromagnetic contacts (FM) 1 and 3. The two independent spin channels are represented by the resistors $R_{1\uparrow,\downarrow}$, $R_{SC\uparrow,\downarrow}$, and $R_{3\uparrow,\downarrow}$,. (b) and (c) show the electrochemical potentials in the three different regions for parallel (b) and antiparallel (c) magnetization of the ferromagnets. The solid lines show the potentials for spin-up and spin-down electrons, the dotted line for μ_0 (undisturbed case). For parallel magnetization (b), the slopes of the electrochemical potentials in the semiconductor are different for both spin orientations. They cross in the middle between the contacts. Because the conductivity of both spin channels is equal, this results in a (small) spin-polarization of the current in the semiconductor. In the antiparallel case (c), the slopes of the electrochemical potentials in the semiconductor are equal for both spin orientations, resulting in unpolarized current flow. (Note that the slope of μ in the metals is exaggerated). From [12]]..... 162

Fig. A.16 Dependence of α_2 and $\Delta R/R$ on β. In (a) α_2 is plotted over β for different ratios $\sigma_{fm} / \sigma_{sc}$. For a ratio of 100, α_2 is well below 0.1% for $\beta < 99\%$. In (b), again α_2 is plotted versus β with $\sigma_{fm} / \sigma_{sc} = 100$, with the corresponding values for $\Delta R/R$ on a logarithmic scale. For β between 0 and 90%, $\Delta R/R$ is smaller than 10^{-7} and thus difficult to detect in the experiment. After Ref [12]..... 164

Fig. B.1 Calculated DOS for nickel (after J. Callaway and C.S. Wang: Phys. Rev. B **63**, 1096 (1973)), and a simple Stoner model for ferromagnetic electrodes..... 173

Fig. B.2 Model for ballistic spin transport in a two-dimensional electron gas. (a) Measurement configuration: a current I is injected through the 2DEG via a ferromagnetic contact **F1** and an Ohmic contact **L**. The spin transresistance $R_s = V/I$ arises from spin-polarized carriers

traversing a distance L from the net path of the current, which induce a nonlocal voltage, V between a second, similar, pair of contacts **F2** and **R**. (b) The conductor beneath the ferromagnetic contacts (DSPR) is assumed to be a *disordered,* but *spin preserving* region. (c) The full-eight-reservoir model; complete ellipses represent spin-relaxing reservoirs, and half ellipses represent spin-resolved reservoirs. **F1** and **L** are current contacts, **F2** and **R** are voltage probes. $T_{ij}^{\alpha\beta}$ denotes the 2DEG device channel in which spin precession occurs. Other multimode leads are denoted by three arrows and ellipsis. Panels (d), (e), and (f) illustrate decomposition of the eight-reservoir model. [Panel (e) depicts the reduced four-reservoir problem.] 175

Fig. B.3 Ballistic spin transresistance in an external field normalized to $B_0 = p_F/(ew)$. (a) For a channel with $L/w = 15$ in a perpendicular field, we plot two traces representing $\omega_L/\omega_C = 1$ and 0.19, appropriate for a typical metal and for InAs, respectively. (b) and (c) Spin transresistance for three different configurations and two channel lengths $L/w = 3$ and 15. Here, $\omega_L/\omega_C = 0.19$ (InAs). 181

Fig. B.4 Spin transresistance *vs.* reduced Rashba frequency, $\hat{\omega}_R = 2m^*\alpha w/\hbar^2$, at zero applied field, for two different device channel lengths, $L/w = 3$ and 15. The Rashba field strength, characterized by $\hat{\omega}_R$, can be tuned by an external gate voltage. Shaded regions delineate the range of tunability expected for InGaAs devices [138] of three widths, 0.1, 0.3, and 0.5 μm. 182

Fig. B.5 Full eight-probe model for ballistic spin injection in two dimensions which includes ballistic junction scattering effects. (a) The measurement configuration: a current, I, is injected through the 2DEG device channel via an a ferromagnetic contact (**F1**) and ohmic contact (**L**). The spin transresistance, $R_S = V/I$, arises from spin polarized carriers a distance L from the net current path, which induce a nonlocal voltage, V, between a second, similar, pair of contacts (**F2**, **R**). *(b)* The full 8-reservoir model; *complete* ellipses represent spin-relaxing reservoirs, *half* ellipses represent separate spin-resolved reservoirs. **F1** and **L** are current contacts, **F2** and **R** are voltage probes. $T_{ij}^{\alpha\beta}$ denotes the 2DEG device channel in which spin precession occurs. 184

Fig. B.6. Spin transresistance as a function of applied magnetic field for three field configurations (indicated) and two measurement geometries. We assume a frequency ratio, $\omega_L/\omega_C = 0.19$, appropriate for InAs. 185

Fig. B.7 Spin transresistance as a function of perpendicular magnetic field in the presence of diffusive scattering. The clean limit is plotted as black curves for comparison. (a) results for the four-probe model. (b) Results for the eight-probe model that includes junction scattering. Here, the mean free path is normalized to the channel width; the specularity parameter p, is defined in the text. 186

Fig. B.8 The influence of random scattering on spin transresistance as a function of the strength of the Rashba effect. Three scattering mechanisms are considered: junction scattering, impurity scattering, diffuse boundary scattering. The upper two panels are results from the four-probe model. The lower two panels are from eight-probe model. 187

Fig. C.1. Conductance vs. gate voltage for a typical quantum point contact device. 189

Fig. C.2. Conductance vs. gate voltage for spin-resolved quantum point contact device. 190

Fig. C.3. Schematic layout of the QPC spin polarization detector. 191

Fig. C.4. Schematic depiction of the spatial decay of the chemical potential difference arising from a spin injected current. 193

Fig. C.5. Normalized second derivative response function $\left(k_B T/e\right)^2 \left[R''(V_g)/R(V_g)\right]$ at two different effective electron temperatures 4.2 K and 20 K. Horizontal axis is represented in units of subband spacing. 194

Fig. C.6. Experimental data from a trench isolated adiabatic point contact device at 4.2K. 196

Fig. C.7. Experimental data from a second trench isolated adiabatic point contact device at 4.2K. 196

Fig. C.8. (a)-(g) Quantum point contact fabrication procedure: (a) Chip cleaning. (b) Very thin layer of photoresist is spun on the wafer. (c) PMMA coating. (d) Exposure and developing of PMMA. (e) Descum. (f) Citric acid etching. (g) Mask removal. (h) A top view of of semicircular shaped trenches in GaAs. (i) A side sketch of a shallow etched QPC with in-line gates. 197

Fig. C.9. A complete QPC polarization detection device. 198

Fig. C.10. (a) Local Hall characterization of micro-magnet array. (b) I-V curve measured from the permalloy array/2DEG conctacts. In this device, the 2DEG is located about 85nm beneath the surface. 199

Fig. D.1. Geometry for imaging decay of injected spin polarization with distance from injection interface. 201

Fig. E.1. Schematic diagram of the experimental setup. All wires are coax and shielding is provided by the enclosure. 203

List of Tables

Table 5.1. Characteristic parameters determined for MnGaAs in two field regimes..... 85

Table 7.1 Carrier densities, electrical channel widths, and mobilities for a family of suspended Hall bars. 106

Table 8.1 Observed spin band splitting and Rashba coupling parameter in various InAs quantum wells. 141

Table C.1. Voltage waveform components across the QPC Spin Detector 192

Part I: Semiconductor Magnetoelectronics

Chapter 1. Spin Injection – a Resúmé

The purpose of this chapter is to provide an introductory overview of most important issues of spin injection and to summarize our earlier efforts to understand the spin-coupled transport across metal/semiconductor interfaces. I will discuss the motivation to realize spin injection into semiconductors and the fundamental obstacles that have been encountered. New techniques to detect electrically injected polarized carriers will be briefly illustrated. Extensive discussions on these topics can be found in the Appendices.

1.1. Introduction to Spintronics and Spin Injection

Limits to the scaling down of conventional electronic devices are foreseeable. In the nanometer regime, physical phenomena will ultimately impose barriers to the scale at which current devices can function reliably. These issues have motivated intensive studies on "spintronics" (which is short for "spin electronics") – referring to new classes of electronic devices in which the spin degree-of-freedom, in contrast to the electron's charge, is exploited. Magnetoresistive devices that depend on electron spin are already in commercial use. These devices are essentially stacked layers of material whose electrical resistance varies with external magnetic field ("Giant Magneto Resistance" (GMR) and Tunneling Magneto Resistance (TMR) effects[1, 2]). However, spin injection devices – and by "injection" we here denote transferal of

spin-polarized carriers into a nonmagnetic conductor – have not reached a similar, commercially viable, stage of development. Even the fundamental physics and material science of the spin injection process remains in need of significant elucidation. In **Appendix A** we present a historical review and recent developments regarding spintronic devices.

1.2. Why semiconductor spintronics?

Generally, neither GMR/TMR devices nor all-metal spin injection devices are easily capable of enabling active manipulation of spins. The high electron density of metals makes it almost impossible to achieve electrical control of electron polarization. However, in semiconductors, not only electrical carrier densities can be varied through a wide range by doping or gating, but also it is possible to tune the rotation of spin through electrical gates. In 1990, Datta and Das [3] proposed a novel "spin transistor" that is composed of a ferromagnetic injector and collector to inject and, subsequently, analyze polarized electron spins, and a semiconducting electron channel allowing modification of the propagating carriers spin state by the (tunable) spin-orbit interaction. This tunability is achieved by an external electrical gate through the so-called "Rashba effect". The basic concepts are discussed in **Appendix A2.3-A2.3**. We have extensively explored and examined the functionality of this prototype spin-FET device. Our model is based on a realistic consideration of material properties and device geometry, and clarifies the direct evidence required to confirm successful spin injection. This work is presented in **Appendix B** of this thesis.

There are four fundamental requirements for successful implementation of a spin transistor: spin *injection*, spin coherent *propagation*, induction of controlled spin *precession* and spin *detection*. A large number of experiments have been performed in recent years to implement these four basic components. For example, Kikkawa and Awschalom [4] proved that spin coherence can persist in doped semiconductors extremely long temporal (> 100 ns) and spatial scales (> 100 μm) (**Appendix A2.5**). Gate control of spin splitting has also been demonstrated in various semiconductor quantum well systems (**Appendix A2.6-A2.7**). The other requirements for spin transistor – spin injection and detection remain elusive and will be discussed sections to follow. These topics, in fact, initially motivated the research of this thesis.

1.3. Spin Injection Complications

An number of groups have recently reported the observation of very weak spin injection signals in ferromagnetic/semiconductor devices [5-7]. However clear experimental evidence from the Roukes group [8, 9] has indicated that the spin valve geometry employed in these experiments can lead to important, large-magnitude local Hall phenomena from the fringing field of the ferromagnets. For unoptimized device designs, the anisotropic magnetoresistance (AMR) phenomenon can also contribute to the spin valve signal. These spurious phenomena often mimic the signals expected from spin transport. Our view is that, to date, these experiments have, collectively, not been able to provide unambiguous demonstration of spin injection into semiconductors. The illustration of local Hall effect and its contributions in the spin injection experiments are discussed in **Appendix A3**.

The detailed nature of F/S interfaces is also of significant concern [10, 11] for attempts to realize effective spin transferal. Recent theoretical efforts have revealed that there is a fundamental obstacle for spin injection from ferromagnetic metal to diffusive semiconductors – this has been termed a "conductivity mismatch effect" [12, 13]. It was found that a direct Ohmic contact between a high conductivity ferromagnetic injector and a low conductivity non-magnetic medium will always yield a strong suppression of spin injection. This issue will be addressed repeatedly throughout this thesis. An extended theoretical analysis can be found in **Appendix C**.

1.4. New Techniques for Spin Polarization Detection

Until now, most confirmations of successful spin injection has relied on the use of spin-resolved optical detection. However, from a device point of view, it is essential to develop more general approaches that are amenable to large-scale integration. Electrical detection of spin polarization, the inverse process to that of injection, is a natural candidate. However, for spin-sensitive electrical detectors based employing Ohmic contacts, pursued by most efforts to date, similar difficulties arise as for the case of electrical injection. In **Appendix D** and **E**, we describe two alternative means that we have devised for detecting spin-polarized currents in semiconductors; these have great promise for exceptional sensitivity.

1.5. Chapter Overviews: Spintronics

In **Chapter 2** we report on our experimental attempts to realize (Ga,Mn)As-based spin injection devices. Two experimental systems have been designed and implemented. The first group of devices are essentially all-semiconductor devices, utilizing p-GaAs as the conduction channel. In the second group of devices we have employed a Au wire as the channel. These latter devices are the "complement" of the configuration used in the aforementioned (unsuccessful) metal/semiconductor devices. Here the injectors are high resistivity ferromagnetic semiconductors and the conduction channel (into which the spins are injected) is a metallic (Au) conductor. In both of these cases, it appears possible to circumvent the "conductivity mismatch problem" discussed in the previous sections. Interesting signals that may be first indications of diffusive spin-coupled transport are reported.

Chapter 3 presents our studies on the dilute magnetic semiconductor (DMS) (Ga,Mn)As and its magnetic properties. Pursuit of these studies led us to discover the *Giant Planar Hall Effect* (GPHE) in (Ga,Mn)As. In conventional (nonmagnetic) semiconductor devices, the spin of the carrier does not, in general, play an important role. Here we proved that the coexistence of magnetic and semiconducting properties greatly enhances spin-related phenomena and enables new prospects for important applications. Extremely large Hall resistance jumps are observed in microjunctions patterned from epitaxial (Ga,Mn)As layers when subjected to a swept, in-plane magnetic field. This giant "planar Hall effect" is four orders of magnitude larger than previously observed in metallic ferromagnets, and enables high angular resolution studies of the magnetic properties of (Ga,Mn)As epilayers. The unusual switching pattern recorded can be qualitatively explained as an interplay between cubic anisotropy and weak uniaxial anisotropy. From these electrical transport measurements, we are also able to deduce important magnetic parameters that are essential to test existing theories regarding the origin of ferromagnetism in DMS. The high resolution obtained by this giant planar Hall effect allow small Barkhausen jumps to be resolved in our smallest devices.

Chapter 4 describes our out-of-plane magnetoresistance measurements on (Ga,Mn)As devices. Systematic electrical transport measurements on the extraordinary Hall (EHE) have been performed. The anomalous EHE switching patterns we observe can be interpreted by modeling the domain wall energetics. This involves contributions from the intrinsic cubic magnetocrystalline anisotropy, from in-plane and out-of-plane uniaxial anisotropy, and from demagnetization effects. We have found that the magnetoresistance data (both longitudinal and

transverse) in response to an out-of-plane magnetic field reflect a competition between cubic magnetic anisotropy and an effective out-of-plane uniaxial anisotropy. The uniaxial anisotropy constant for this case is deduced from the data and compared with theoretical predictions.

In **Chapter 5** we return to the giant planar Hall effect, here employing it to isolate, manipulate, and measure the properties of individual single domain walls. The spatial profile and the propagation of individual magnetic domain walls in a 100 μm-wide lithographic wires are clearly reflected in real time voltage wave forms obtained from a multiterminal device. Domain wall (DW) velocities are determined from time-of-flight between multiple electrical probes fabricated on the sample. Measurements as a function of magnetic field strength, field orientation, and temperature allow us to estimate magnetic parameters of (Ga,Mn)As and elucidate the physical mechanisms that drive DW propagation. More importantly, the magnetoresistance induced by an individual domain wall is directly measured for the first time.

Chapter 2. Spin Injection from (Ga,Mn)As

In this chapter we present our measurement results on (Ga,Mn)As spin injection devices. The material aspect of spin injection are discussed first, providing the guideline for the design of (Ga,Mn)As spin injection devices. The fabrication and measurements of an all-semiconductor (Ga,Mn)As/p-GaAs spin transistor are summarized next. We observe interesting signals that may be representative of possible diffusive spin-coupled transport. In the final part of this chapter, we show that (Ga,Mn)As/Au devices should uniquely demonstrate the signatures of a strong spin signal. Our first generation devices have exhibited evidence of spin valve signals in polarize/analyze experiments. More complete experiments are in progress; these are based upon improved (Ga,Mn)As bi-layer wafers, where each layer provides switching at a distinct coercive field. .

2.1. Material Aspects of Spin Injection in Semiconductors

At room temperature, ferromagnetic metals with a sufficiently high Curie temperature were considered to be the best candidates for spin injection in semiconductors However, in spite of intensive experimental efforts by various groups it has been impossible to produce signals larger than 1% that can reliably be attributed to spin injection (**Appendix A.3**). The origin of this failure has recently been understood in terms of a conductivity mismatch at the diffusive contacts

between the spin-dependent low resistivity ferromagnet metal and the much higher spin-independent resistivity of the semiconductor. (See **Appendix A.4**).

One possible solution to circumvent this difficulty to allow injection of polarized electrons into a semiconductor is to make use of magnetic semiconductors, which possess both low conductivity and very high spin polarization. This approach has been carried out in the experiments of Fiederling *et al.* [14] and Ohno *et al.* [15]. They obtained a degree of polarization as high as 90% at 4.2 K using a dilute magnetic semiconductor BeMnZnSe in an external field as a spin aligner on GaAs and 1% at 6 K using ferromagnetic semiconductor (Ga,Mn)As respectively. In both cases the spin polarization vanished with increasing temperature.

From these experiments it has become clear that diffusive polarized spin injection can be obtained if there is a good match between conductivity and spin-scattering length on both sides of the injection, or when the polarization of the magnetic material is 100% as is the case in half-metallic ferromagnets.

We have shown in **Appendix A.4** that the non-local geometry in Fig. A.13 allows suppressing any "spin independent" magnetoresistance contribution. The resistance change between the parallel and anti-parallel configuration of the magnetization in the non-local configuration is given by

$$\Delta R_{NL} = R_{\square}\frac{L}{W}\frac{\alpha_F^2}{(M^2+1)(L/\lambda_N)\sinh(L/\lambda_N)} \tag{2.1}$$

with

$$M = 1+\frac{\sigma_F}{\sigma_N}\frac{\lambda_N}{\lambda_F}\left(1-\alpha_F^2\right) \tag{2.2}$$

$$\alpha_F = \frac{\sigma_\uparrow - \sigma_\downarrow}{\sigma_\uparrow + \sigma_\downarrow}. \tag{2.3}$$

The injection efficiency is largely dependent on the absolute value of ferromagnet polarization α_F. For incompletely polarized injectors, the mismatch correction factor M, determined by two ratios σ_F/σ_N and λ_F/λ_N, that play a significant role in determining whether efficient spin injection can be achieved. We shall denote those ratios by two parameters – conductivity ratio η_σ and spin diffusion length ratio η_λ – that are intrinsic to two bulk materials forming the interface. Note that if one studies Eq. (2.1) in more detail there is no direct meaning

to assign to η_λ without considering the length scale of the devices. In real devices, the channel lengths are usually on the same order of spin diffusion length in the normal conductor, and this justifies our treatment of using one single parameter η_λ to denote related length scales. Depending on the values of these two important factors, devices with four relevant ranges can be identified: metal/metal devices, metal/semiconductor devices, all-semiconductor devices, semiconductor/metal devices.

(a) Conventional metal/metal spin injection devices. This group of devices are discussed extensively in **Appendix A**. The representative experiments are the original spin injection experiments with aluminum and Gold by Johnson and Silsbee [16, 17] and recent experiments on copper by Jedema *et al.* [18]. The signal strength varies from nΩ to μΩ in 100 μm scale devices and reaches mΩ in optimized non-local submicron copper devices. Here, obviously, conductivity is nicely matched at the metal/metal interface, where the conductivity ratio is on the order of unity for poor metallic conductors and is 5 to 10 for good conductors such as gold and copper. However, a new element to the mismatch picture arises , as we can see in Eq. (2.2). This is due to a significant difference of spin diffusion lengths of two metals. In ferromagnetic metals, a typical spin diffusion length is 10 nm, whereas for all the conductor metals employed, the spin diffusion length is on the order of 1 μm. After combining the contributions from both factors, the gross mismatch factor M is from 10-100, meaning a reduction of spin injection efficiency by a factor of about 1000. This analysis is consistent with the recent results of [18].

(b) Metal/Semiconductor devices. We have significant effort in this thesis to elucidate the importance of conductivity mismatch problem in ferromagnetic metal/semiconductor junctions. In summary, the spin injection efficiency is reduced from α_F to an extremely small value of about 10^{-12} by incorporating a conductivity mismatch factor, 10^4, and a spin diffusion length mismatch factor, $\sim 10^2$. In fact, as shall be described, the spin diffusion length mismatch can be pictured as a reduction of "effective spin conductance length" of the channel down to a scale of order the Fermi wavelength, λ_F. For a typical sheet resistance of 1kΩ, a spin transresistance as tiny as 1nΩ can therefore be expected. This explains the failure of efforts worldwide to achieve metal/semiconductor spin injection devices.

(c) Semiconductor/Semiconductor devices. This materials system appears to be a natural solution to realize spin injection into semiconductors. Here the conductivity is, in general, well matched. Employing similar argument in metal / metal spin injection, the spin injection signal can be maintained at 0.1% of the sheet resistance of the nonmagnetic semiconductors, which is

typically three to four orders higher than that of the normal metal. Therefore, in an ideal situation, a spin transresistance on the order of Ohms can be expected in such devices. Two families of magnetic semiconductors have demonstrated the ability to provide highly polarized carriers in spin LED experiments. The first group are superparamagnetc semiconductors having enormous g-factors. These need an external field to maintain a finite polarization. The other group are ferromagnetic semiconductors such as (Ga,Mn)As which possess spontaneous magnetization at zero field. The latter provide unique opportunities for construction of construct integrated all-semiconductor spintronics devices.

(d) Magnetic Semiconductor/metal devices. This is not a simple reverse junction of the aforementioned metal/semiconductor device. A close examination on Eq. (2.1) and Eq. (2.2) reveals that, owing to the small value of the conductivity ratio between ferromagnetic semiconductors and normal semiconductors, the reduction factor M is close to 1, showing no mismatch problem in these devices. Even the mismatch η_λ originated from different spin diffusion length becomes unimportant because it multiples with an ultra small η_σ. Consequently the spin transresistance in a non-local geometry is the same order as the longitudinal resistance of the normal conductor itself, say, tens or hundreds of milliohms. Hence it should be easily detectable by ac lock-in techniques.

The devices discussed in (c) and (d) have never been proposed before. In the next sections of this chapter, we will explore the first-generation samples based on these ideas. We emphasize that, besides the mismatch problem, other spin-related or spin-unrelated material parameters are also important, even crucial, in the complete design of spin injection devices. These parameters are: (a) the degree of spin polarization in ferromagnet, (b) interface spin scattering, (c) paramagnet spin diffusion length, (d) the geometry factor to minimize spin dependent interface resistance, and (e) the actual measurement configuration.

2.2. All Semiconductor (Ga,Mn)As/p-GaAs Spin Injection Devices

2.2.1. Motivation and Heterostructure Design

The failure of spin injection from ferromagnetic metal to semiconductor has motivated theorists and experimentalists to study the process of spin injection more carefully. By using optical pump-probe methods, it has been confirmed that electron spin has a long lifetime in

semiconductors and can maintain its polarization while propagating far as 50 μm. However, the problem of spin transferal across an interface between ferromagnetic material and semiconductor remains a crucial issue. In addition to the fundamental problem of "conductivity mismatch" discussed in the preceding sections, the dynamics of electrons at the metal-semiconductor interface is quite complicated. The conduction bands are not, in general, matched across the interface; hence the Fermi surfaces of both sides are quite different. This gives rise to interface states originating from surface reconstructions that yield totally different crystal structure compared to the bulk. These issues have motivated us to find a material system with perfect clean, atom-matched interface to perform spin injection experiment. Fortunately, there exists one. It has been demonstrated that Mn doped GaAs is *ferromagnetic* at low temperature. At an optimum doping level it may possess a Curie temperature, T_c, as high as 110K. A spin-LED has been fabricated using (Ga,Mn)As as polarizer and demonstrated effective spin injection from (Ga,Mn)As into insulating GaAs then to a quantum well in which polarized light can be generated.

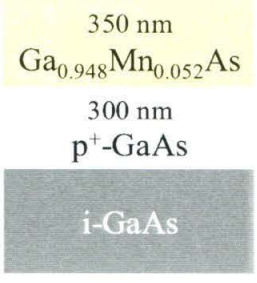

Fig. 2.1 Layer stack for local Hall characterization devices and all-semiconductor spin injection devices.

This materials system is ideal for the construction of an all semiconductor electrical spin injection device. The starting heterostructure is shown in Fig. 2.1. Since (Ga,Mn)As is heavily p-doped, to avoid forming a *pn* junction we use a Be doped GaAs as *p*-type conducting channel. Two Be doping levels have been investigated: 1×10^{19} cm^{-2} and 1×10^{18} cm^{-2}. The contacts between (Ga,Mn)As and GaAs:Be were confirmed to be ohmic for both concentrations. Compared to *n*-type semiconductors (*i.e.* those with electronic conduction), ohmic contact to *p*+GaAs:Be is easy to achieve and alloying is usually not needed. Here, however, instead of studying *electron* spin transport, we are considering *hole* spin injection in this material system. A fundamental concern for hole spin devices are their shorter lifetime compared to electrons [19, 20].

2.2.2. Device Fabrication

After cleaving and etching the sample, Ti/Pd/Au/Ti metal layers are first deposited, via electron beam lithography and lift-off techniques, to define two rectangular micro-scale bars at various separations. As in the metallic devices made previously in the Roukes group, the widths and aspect ratio of these bars are intentionally made different to yield micromagnets with slightly different coercivities after subsequent ion-mill etching (using metallic layers as self aligned mask). Meanwhile alignment marks are also put down to assist the fabrication of the remaining layers. The etch is calibrated to completely remove all the top (Ga,Mn)As epilayers and additional 50 nm – 100 nm into the *p*-type paramagnetic GaAs layers. Therefore, except for those isolated areas under metal masking layers, no continuous ferromagnetic epilayers exist on the chip, and the *p*-type conducting GaAs layers are exposed. By addtion of another electron beam lithography and lift-off step, a thick Ti layer is defined and employed as an etching mask to form - *p*-GaAs conduction channel that connects both micromagnets. The following conventional photolithography process allows the deposition of same thickness Ti masking layer for large contacts and for the leads connecting to the *p*-GaAs channel in the center. Mesa isolation is also achieved by ion-beam etching. Because of its excellent repeatability, ion-beam etching is exclusively employed in the (Ga,Mn)As device fabrication. Note that for this material, ion beam induced damage will be of less concern. The Ti masking layer is then removed by diluted HF. It is worthy of mention that the bottom thin titanium layer adhering to magnets is basically untouched since it reacts with Pd and tends to heavily dope the GaAs in that vicinity. A final composite Pd/Ti/Pd/Au layer is patterned to make contacts to both p+GaAs and micromagnets

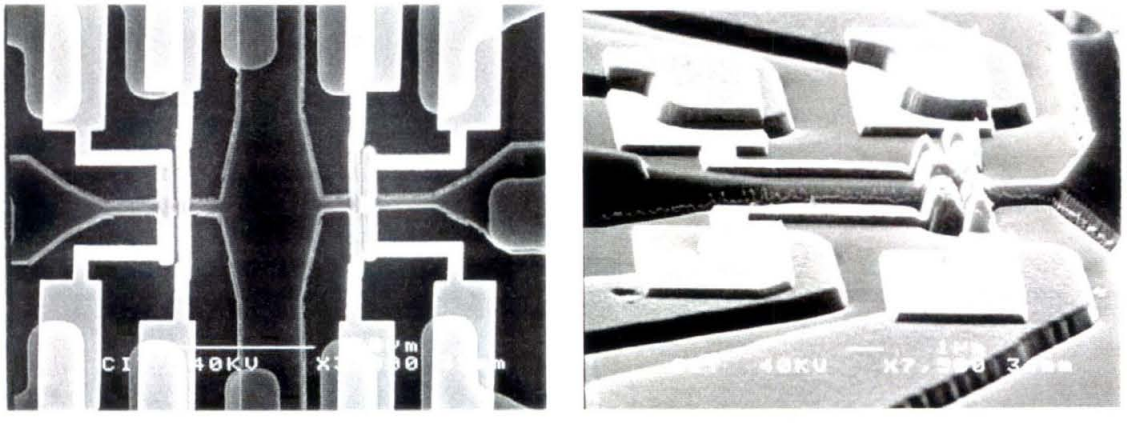

Fig. 2.2 Top and side view of our first GaAs/GaMnAs spin injection devices patterned by e-beam lithography.

(with Ti/Pd/Au on top) through combined electron beam lithography (EBL) and photolithography (PL). In summary the whole process involves three EBL and one PL steps, four thin film depositions steps, and two ion-beam etching processes.

A final polarize/analyze type device with in-line geometry is shown in Fig. 2.2, where two sets of spin injection devices with magnet separations of 0.5 μm and 0.2 μm are fabricated. The magnets widths are 0.75 μm and 0.5 μm, respectively ; these numbers have proven to yield the best hysteresis loops in permalloy magnets. We found that the resistance between ferromagnet's pads and *p*-GaAs pads are in the range of 10 kΩ to 50 kΩ, in a few cases above 100 kΩ. Most of the resistance is present at the metal/(Ga,Mn)As interface, whereas the resistance across (Ga,Mn)As/GaAs interface is very small. Further optimization of the fabrication is required to obtain consistent small contact resistances between metal and *p*+GaAs.

2.2.3. Data From All-Semiconductor Spin Injection Devices

Experimental magnetoresistance data from one of such all-semiconductor spin injection devices is presented in Fig. 2.3. Our preliminary results are inconclusive. The transitions evident

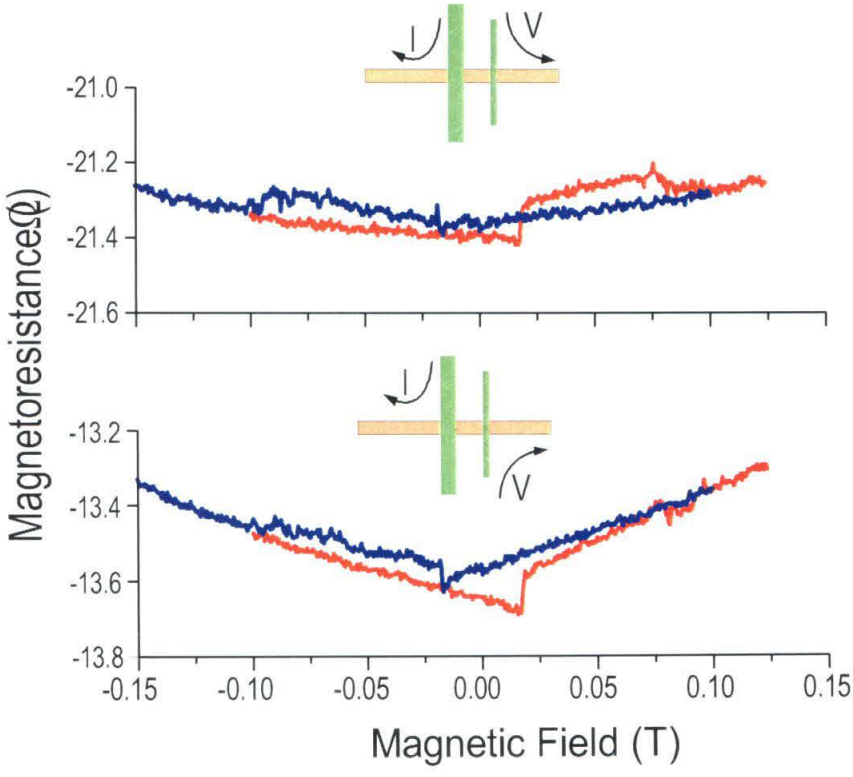

Fig. 2.3 Preliminary magnetoresistance data from all-semiconductor spin injection devices.

may reflect solely the transitions of individual magnets, given that planar Hall effect and the anisotropic magnetoresistance of the respective magnets generate two jumps under the influence of cubic magnetic anisotropy. Without independent control of the magnetization state of the injector and detector, an unambiguous conclusion as to whether or not successful spin injection is hard to make. The second-generation devices in progress employ a specially designed bi-layered (Ga,Mn)As heterostructure that is capable of being patterned into nanomagnets possessing distinct coercivities.

2.3. Spin Injection from (Ga,Mn)As to Metals

In this section, we shall explore an intriguing new class of prototype devices (proposed in Sect. 2.1) based upon the avoidance of conductivity mismatch through use of (Ga,Mn)As ferromagnets. Since we are going to use metal as paramagnetic conducting channel, the materials we used in these experiments have an insulating substrate. After a Ti mask for magnets are first patterned by electron-beam lithography, ion-beam etching is executed to define two magnets from the (Ga,Mn)As layer. Subsequenthly, a second electron beam lithography step is performed upon the exposed *i*-GaAs to define a metallic Pd/Ti/Pd/Au channel (thin film "wire") that traverses over both magnets at their respective centers. Final Pd/Ti/Pd/Au metallizations are realized in the same way as all-semiconductor spin injection devices.

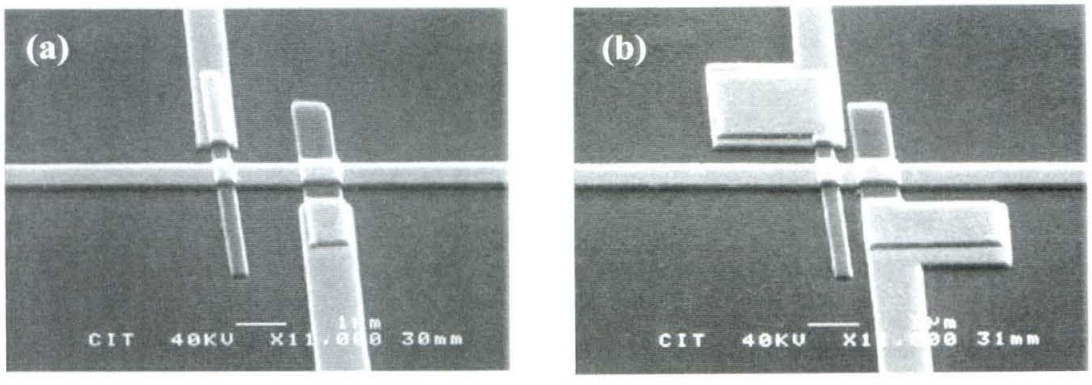

Fig. 2.4 Micrographs showing electron beam lithography patterned (Ga,Mn)As/metal spin injection devices. Gray bars are 150 nm thick (Ga,Mn)As. Two types of geometries are patterned. (a) Regular in-line device with magnets of different sizes. (b) Contact areas for both magnets are extended to reduce contact resistances.

Fig. 2.4 shows SEM images of (Ga,Mn)As/Au spin injection devices. The flat bar shaped area are micromagnets made out of (Ga,Mn)As, whereas the light area are metals. In order to reduce the contact resistance between (Ga,Mn)As and metal layer, sometimes the contact areas are enlarged as shown in Fig. 2.4b. For these specific devices, the (Ga,Mn)As magnets are 250 nm and 750 nm wide, respectively, and the gold wires shown in this figure are 1μm wide, giving a resistivity of about 0.1 Ω per square. At 10 μA sourcing current level, data from a device with 2 μm separation is plotted in Fig. 2.5. The data are very interesting and unambiguously show some form of spin-valve signal, similar to that observed in Johnson and Silsbee's original experiment. The correct negative sign of the spin signal is evident, and the signal size, which is around 0.4Ω and corresponds to resistance of four squares, is in the predicted range as we have discussed. However, instead of a transition signature with square shape, as demonstrated by Jedema et al., a triangular signal shape is detected in these experiments. This might be attributed to the occurrence of complicated magnetization transitions in our submicron scale (Ga,Mn)As ferromagnets. The new bi-layer (Ga,Mn)As devices will help to provide conclusive spin injection evidence in (Ga,Mn)As/metal devices.

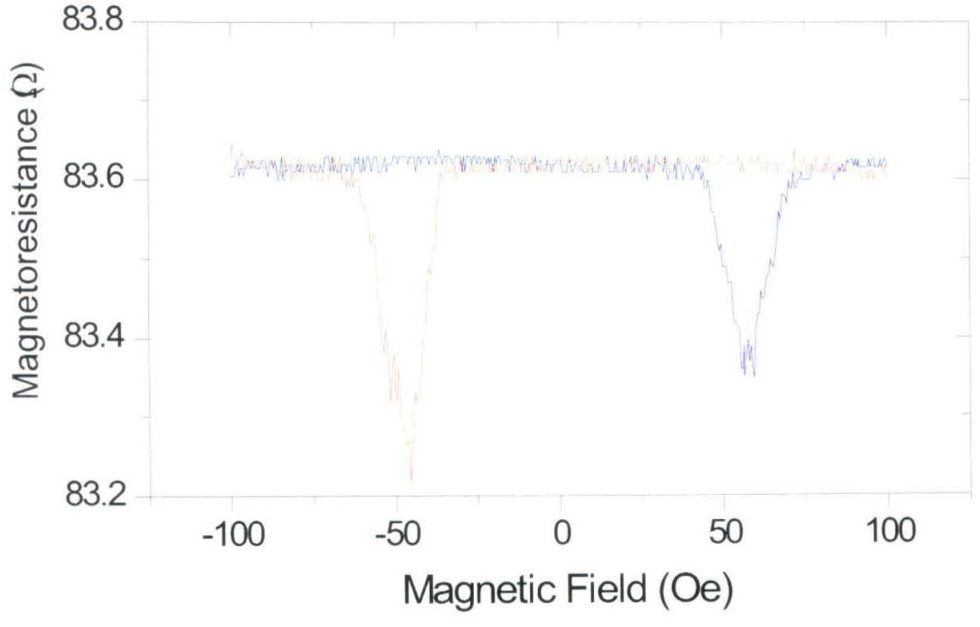

Fig. 2.5. Hysteretic phenomena from non-local measurement of a (Ga,Mn)As/Metal spin device with 2 μm injector-dectector separation.

Chapter 3. Giant Planar Hall Effect in Epitaxial (Ga,Mn)As Films

Motivation and Anomalies in Local Hall Measurements

The exciting spin-valve like signal in (Ga,Mn)As spin injection devices has led us to investigate possible interactions between (Ga,Mn)As ferromagnets and the conduction channels. From the historical review presented in **Appendix A**, this kind of investigation has proven to be crucial before any claims can be made regarding the realization of successful spin injection. Since the first successful growth of ferromagnetic (Ga,Mn)As in 1996, much effort has been focused upon investigations of this new material. At present our knowledge about it is still quite limited. Not only is the origin of ferromagnetism not well understood, but our present understanding of the basic the magnetic properties of this material is not complete. The goal in this chapter is to explore the spin transport properties of (Ga,Mn)As and gain insight on its magnetic properties through transport measurement.

3.1.1. Anomalous Two-Jump Event in Local Hall Measurement

We have described in **Appendix A3.2** how "local Hall effect" due to the fringing field of nanomagnet can be used efficiently as a very sensitive probe of magnetization. To work toward engineering a single domain nanomagnet from the (Ga,Mn)As heterostructure, as for the case with metal-semiconductor devices, the first characterization was performed through the local Hall effect. In Fig. 3.1, a 750 nm wide (Ga,Mn)As nanomagnet was patterned first by using electron beam lithography. Then a Hall cross was etched in the underlying p-GaAs by subsequent step of electron beam lithography. The Hall resistance measurements were enabled by the cross junction; these reflects the ferromagnet's magnetization. This magnetization can be switched by an external in-plane magnetic field. In our experiments, such an in-plane field is swept linearly over a range of ±1000 Oe. Prior to each sweep, an in-plane field of 6000 Oe is applied to saturate the sample magnetization, **M**. The field sample angle is first roughly adjusted by rotating the dipper.

To our surprise, along most field orientations, we observed an unexpected signal with two switching events (Fig. 3.2). This is in contrast to a single switching event in a local Hall probe measurement of single domain NiFe nanomagnet as we discussed in **Appendix A3.2**. Interestingly these signals are very similar to spin valve signals discussed in **Appendix A4.3**. The signals are extremely repeatable under many sweeping cycles and temperature cycles. Therefore, we can exclude the possibility that they originate from multiple domain behavior within the micro-magnets. However these phenomena represent a potential problem for the proposed all-

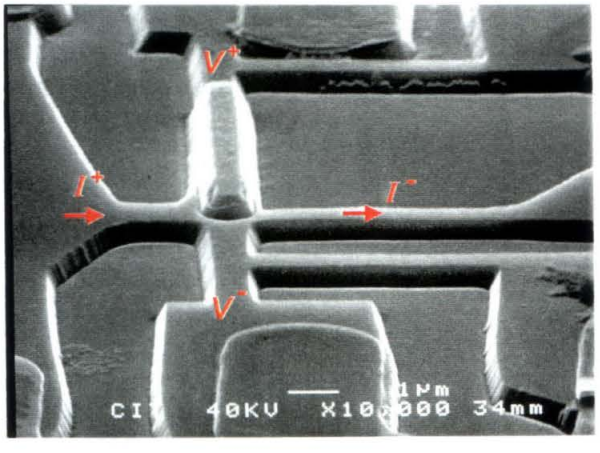

Fig. 3.1 A "local Hall device" that was used to characterize a 750 nm × 10 μm (Ga,Mn)As miniature magnet.

semiconductor spin transistor. They make it is difficult to differentiate a true spin injection signal from the switching signals originating within each individual magnet. Hence, a systematic study is required to understand the physical origin of the observed signal.

We find the magnetization of our small magnet has a rather special magnetocrystalline anisotropy. The magnitude of switching fields depends very much field sweeping orientation relative to the crystallographic axis. In most sweeping directions, two magnetoresistance jumps occur, while at certain orientations, only one jump is visible. This origin of these phenomena remained unclear we used a vector magnet system to map how the switching evolved with an in-plane field. The magnet system employed, a custom-designed apparatus with three orthogonal superconducting coils, enables us to direct magnetic field in any direction without physically disturbing the sample. The magnetic field components H_x and H_y are swept in a pattern shown in Fig. 3.3. Also shown is a differential plot of magnetoresistance. A pixel represents 2 Oe by 2 Oe. A clear signature of magnetization transition is manifested. These critical field curves are different from curves of both uniaxial anisotropy (astroid) and biaxial anisotropy (wind rose)

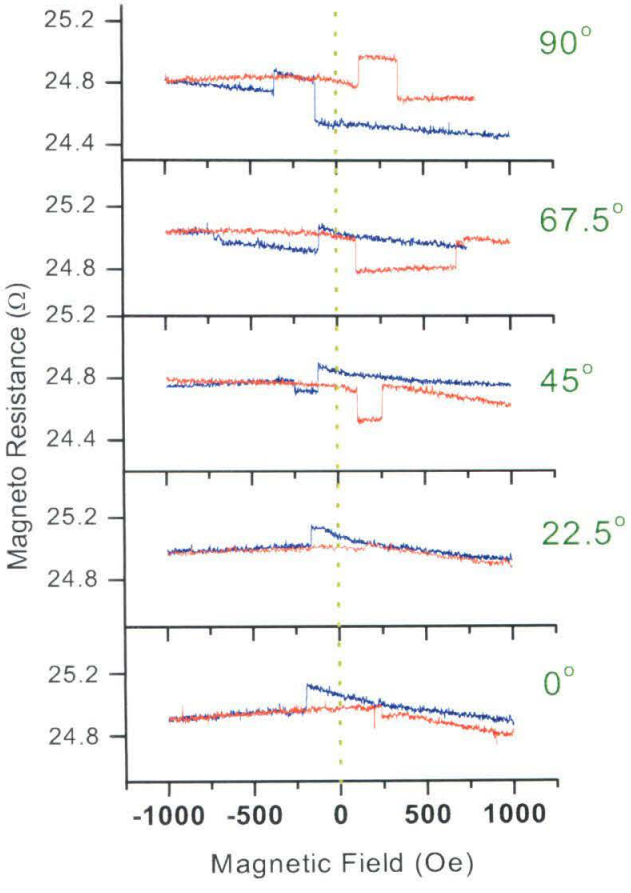

Fig. 3.2 Magnetotransport measurement data on a local Hall geometry sample. Data from five different field orientations are presented.

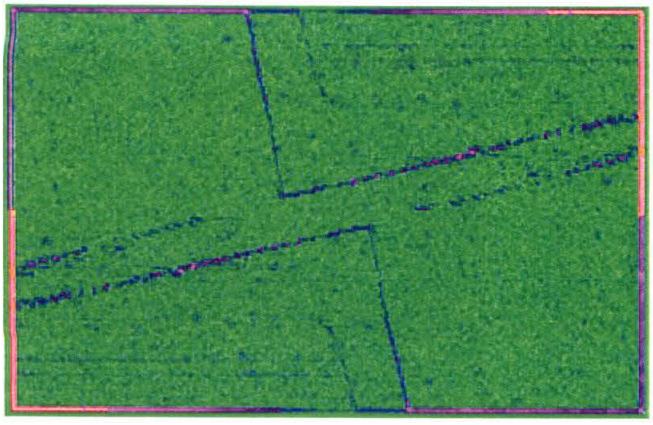

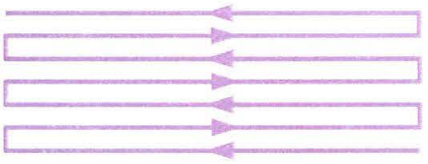

Fig. 3.3 Top: sweeping pattern of magnetic field. Left: A differential plot of the Hall resistance. Horizontal axis represents H_x. vertical axis is H_y.

predicted by classical Stoner-Wohlfarth model [21]. These observation confirm that a collective magnetization transition of a single domain magnet in the plane occurs. The in-plane magnetic anisotropy is an overall cubic anisotropy with a weaker two-fold anisotropy along one axis. As far as we know, this is the first time for a single crystalline single domain magnet to be mapped.

Dozens of nanomagnets with various widths and aspect ratios have been patterned. All samples demonstrate a switching pattern matching that in Fig. 3.3. Unlike the metallic nano-magnets we studied before, here, the magnetocrystalline anisotropy dominates the observed anisotropy. The standard method of controlling coercivities by employing shape anisotropy (such as for Permalloy) is not applicable in (Ga,Mn)As system. The expression for shape anisotropy energy is

$$E_K = \frac{\mu_0}{2} N_d M^2 , \tag{3.1}$$

where N_d is demagnetization factor. Dilute magnetic semiconductors are usually doped with a few percent of magnetic ions. Hence the magnetization M is significantly lower than that of ferromagnetic metals. This explains the small energy contribution associated with shape anisotropy.

To construct a spin-valve type transistor, work has to be done to achieve engineering of coercivities by alternative approaches.

3.1.2. Persistence of Hall Anomaly in an Optimized Sample

As a matter of fact, the signal we observed in the previous section is not a Hall signal induced by the fringing field of micromagnet. This becomes obvious after we fabricate the Hall cross at the center of the magnet. A SEM micrograph of such a sample is shown in Fig. 3.4a. This geometry has been proven to produce extremely small fringing field [8]. One would expect that Local Hall resistance in this geometry should be orders of magnitude smaller than metallic ferromagnet situation. For (Ga,Mn)As micromagnet, we estimate it would be in μΩ range considering these two factors: (a) (Ga,Mn)As has much smaller saturation magnetization value than conventional ferromagnetic metal. For the specific sample we presented, $4\pi M \sim 300$ Oe, only 3% of that of permalloy (about 10,000 Oe). (b) The hole density of p+GaAs employed is at least an order higher than the electron gas we used before, as a result the Hall coefficient, $1/pe$,

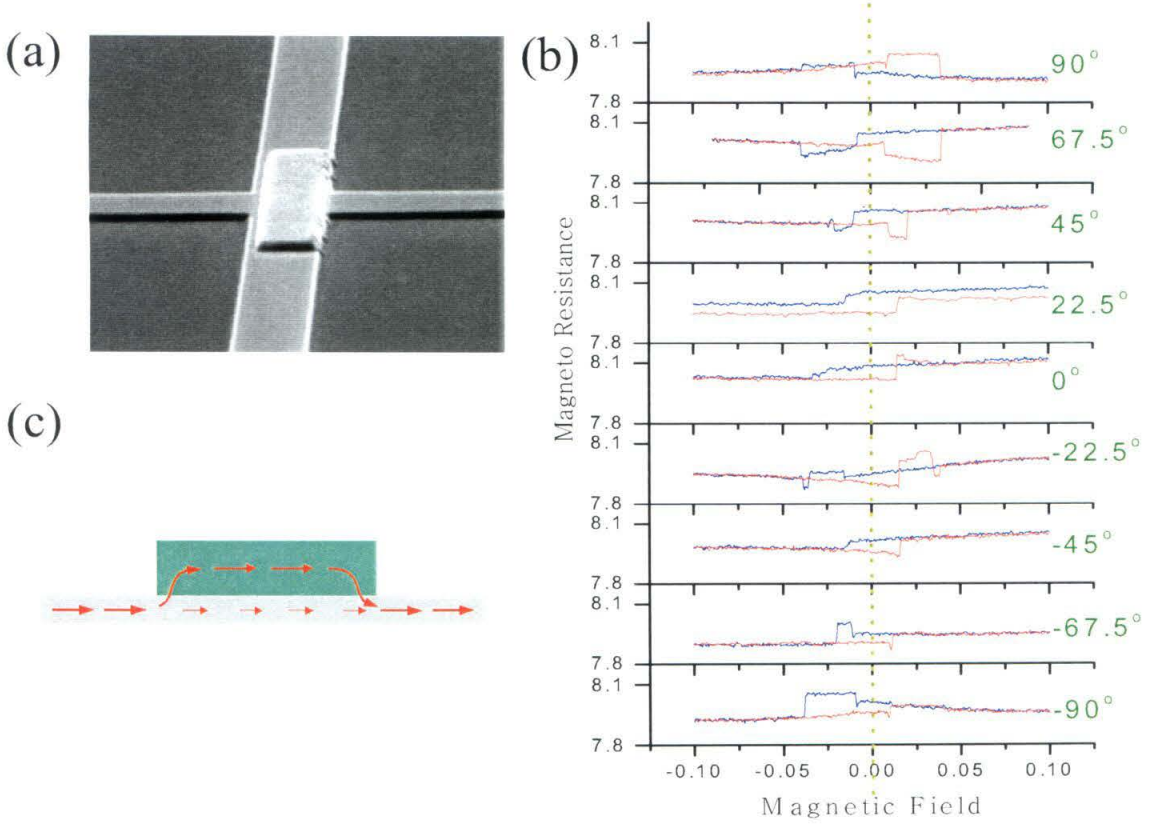

Fig. 3.4 (a) SEM micrograph showing an optimized micron-size magnet. (b) Hall measurement data on such a magnet, proving that local Hall effect is not the origin of observed magnetoresistance jumps. (c) A cross-sectional view of possible current trajectories in the device.

should be at least one order of magnitude smaller than that of n-type GaAs we used before. However, the two switching processes persist at almost every orientation with significant magnitude of resistance change (~0.2 Ohm, Fig. 3.4b), five orders of magnitude larger than that expected from local Hall effect.

One possible source of the magnetoresistance is the planar Hall effect. (Ga,Mn)As epilayers have a very high hole density (~$10^{20}cm^{-3}$). Although it was originally intended that current should flow within the samples in the p+ channels, the high conductivity of the (Ga, Mn) As epilayers induces a considerable amount of current flow through them. It is this current flow that generates a transverse planar Hall voltage in the magnet, via an anomalous "planar Hall effect" that is the focus of the next section (Fig. 3.4c).

3.2. The Planar Hall Effect and Its Origin

The unusual multiple switching observed for a single (Ga,Mn)As magnet stimulates us to systematically investigate the magnetotransport properties of thin (Ga,Mn)As films. The samples investigated were 150 nm thick $Ga_{0.948}Mn_{0.052}As$ epilayers deposited on insulating GaAs(001) substrates with buffer layersAn insulating substrate is used to avoid complications due to parallel conduction and the local Hall effect. Various thicknesses and concentrations of materials have been investigated; it is notable that *all* samples have a behavior consistent with the wafer employed to obtain the body of data presented here (UCSB wafer no. 001115A). Its Curie temperature is ~45 K and the magnetization lies in-plane due to uniaxial anisotropy arising from compressive lattice-mismatching strain and demagnetization effects.[22]

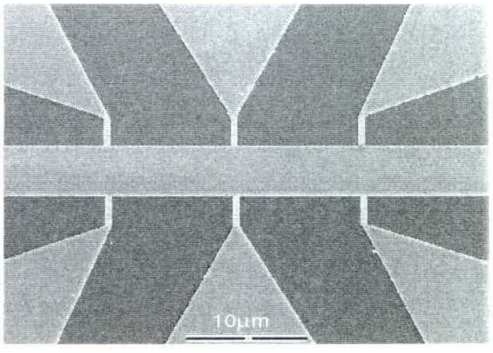

Fig. 3.5 SEM micrograph of a 6 μm Hall bar. The distance between voltage probes is 12 μm.

3.2.1. Spontaneous Planar Hall Effect in (Ga, Mn)As

Samples for magnetoresistance measurements are patterned into Hall bars with widths varying from a few to a hundred microns, with the longitudinal axis of the devices aligned along the [110] direction. This orientation is parallel to a hard, cubic axis that yields square M-H loops, as was confirmed by SQUID magnetometry in large, (mm-scale) samples prior to fabrication,. Voltage probes are carefully designed to minimize their perturbation upon current flow within the Hall bars (cf. SEM micrograph, Fig. 3.5a). After cooling these devices to liquid Helium temperature, low noise four-probe lock-in measurements are made using a 10 nA sensing current at 14 Hz, kept intentionally low to circumvent electron heating in our microdevices. In these experiments, an in-plane field is swept linearly over a range of ±1000 Oe with fixed orientation. As described previously, prior to each sweep, a large in-plane magnetic field is applied to ensure saturation of **M**. The sweep angle is stepped from 0° to 360° (with respect to the longitudinal axis of the Hall bars) at five-degree intervals.

At all angles, except for those along (110) directions, we observe two abrupt jumps in these planar Hall resistance measurements. These jumps appear at similar positions as we observed in

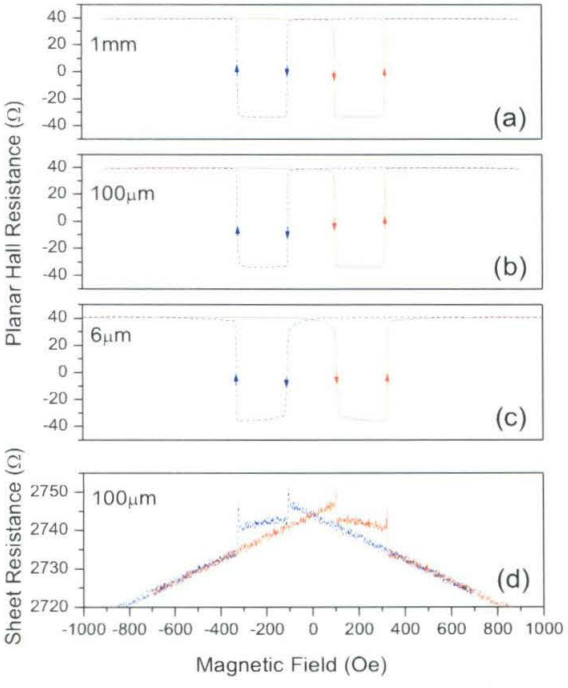

Fig. 3.6 Planar Hall resistance and sheet resistance of (Ga,Mn)As Hall devices at 4.2 K. An in-plane magnetic field, fixed at 20 degrees away from [110], is swept in amplitude. (a)-(c) Planar Hall resistance for Hall bars ranging in width from 1mm to 6 μm. (d) Field-dependent sheet resistance of a 100 μm-wide Hall bar.

the local Hall geometry but its magnitude is significantly larger. Families of data taken from Hall bars spanning from mesoscopic (6 μm) to macroscopic (1mm) dimensions are shown in Fig. 3.6(a-c). (These are obtained for orientation 20° away from [110]). For comparison, the field-dependent sheet resistance of a 100 μm Hall bar is also displayed in Fig. 3.6d.

Three distinct features are observed. a) Huge switching events at distinct magnetic fields are observed in the Hall resistance; these are accompanied by small jumps (relative to background) in the longitudinal resistance. b) Between these switching fields, the planar Hall resistance remains constant at approximately 37 Ohms. The signal polarity remains constant at very positive or negative fields, but reverses sign in the intermediate field region. c) The switching fields appear to be independent of sample size and geometry. Measurement on samples with square, van der Pauw geometry, as large as 3 mm by 3 mm, exhibit identical switching behavior as those of micron-scale devices, even though the magnitude of the Hall resistance can be suppressed in the former, presumably due to non-uniform current distribution in the sample.

3.2.2. Field Angular Dependence of Planar Hall Effect

Fig. 3.7 presents the dependence of R-H loops upon field orientation angle φ_H as it is varied from 0° to 180° in the plane. In the experiment field range, only one jump (reversal) occurs along the (110) directions. Away from these special orientations, a two-jump reversal is always observed. The first switching field H_{c1} is almost constant, while the second switching field H_{c2} decreases dramatically and approaches H_{c1} at around ±30°. The magnitude of the planar Hall resistance remains constant, although its sign reverses when the external field orientation is rotated through the (110) directions.

The jumps in the Hall resistance are understood as follows. In ferromagnetic materials, the carriers are strongly coupled to the spontaneous magnetization through spin-orbit interaction. The conductivity is dependent on the relative orientation between current and magnetization. This can be characterized by two different resistivities, $\rho_{//}$ and $\rho_{\perp}$, for current oriented parallel and perpendicular to the magnetization, respectively. If the direction of the current flow deviates from the orientation of the magnetization, the electric field tilts away from the direction of the (Fig. 3.9). To calculate the resulting electrical field, the current density is first projected along **M** and

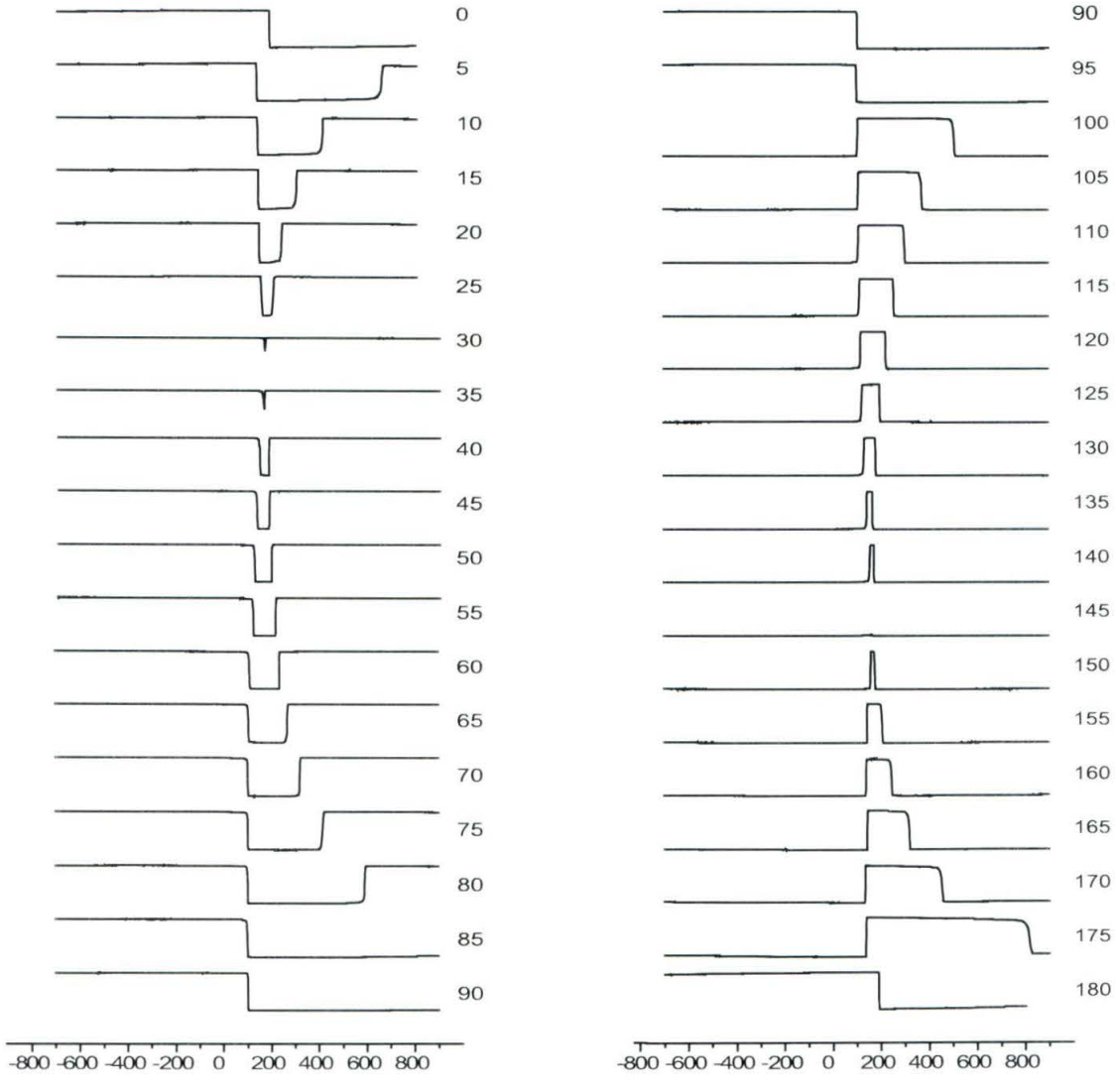

Fig. 3.7 Angular dependence of the planar Hall resistance.

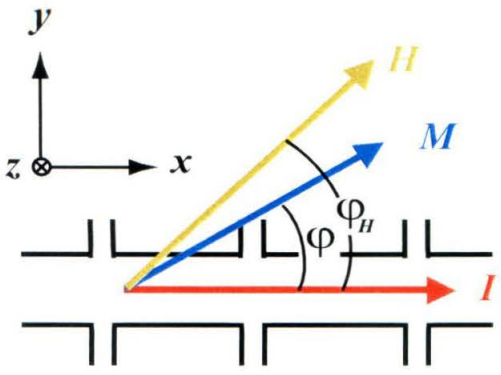

Fig. 3.8 A sketch of the relative orientations of current I, magnetization M, and external field H. The Hall bar is patterned along [110] crystalline direction.

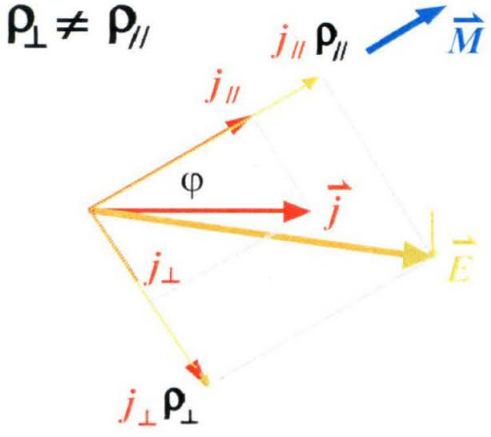

Fig. 3.9 A diagram showing that planar Hall effect has its origin in the anisotropic magnetoresistance of (Ga,Mn)As.

normal to **M**. The electrical fields along these two directions are

$$E_{//} = \rho_{//} j \cos\varphi \tag{3.2}$$

$$E_{\perp} = \rho_{\perp} j \sin\varphi , \tag{3.3}$$

where the current density j is assumed to be uniformly distributed along the Hall bar. φ is the angle between the magnetization and current density j in the Hall bar (Fig. 3.8). The electric field component parallel and orthogonal to the Hall bar direction of a single domain ferromagnetic film with in-plane magnetization can be worked out,

$$E_x = j\rho_{\perp} + j(\rho_{//} - \rho_{\perp})\cos^2\varphi , \tag{3.4}$$

$$E_y = j(\rho_{//} - \rho_{\perp})\sin\varphi\cos\varphi . \tag{3.5}$$

Here x and y are the longitudinal and transverse axes of the Hall bar, respectively. The anisotropic magnetoresistance (AMR) phenomenon is described by Eq. (3.4). The transverse resistance, *i.e.*

the planar Hall resistance, is expressed in Eq. (3.5); it exhibits extrema at $\varphi = 45^{\circ}$ and its cubic equivalents. To verify this angular dependence of the planar Hall resistance, an in-plane field of magnitude 6000 Oe is applied to saturate the magnetization, and its orientation is swept through 360 degrees (Fig. 3.10). In accordance with Eq. (3.5), the measured Hall resistance exhibits extrema for applied field orientations of ~45°, ~135°, ~225°, and ~315°. Note that the maximum of planar Hall resistance appears at 135° instead of 45°, when means $\rho_{//} - \rho_{\perp} = 73\Omega < 0$ from Eq. (3.5). This is additional unique properties of (Ga,Mn)As that is distinct from conventional ferromagnetic metals, where spin-orbit coupling makes $\rho_{//} - \rho_{\perp} > 0$. This may originate from the different roles of holes and electrons in spin-orbit interaction in ferromagnetic semiconductor (Ga,Mn)As and ferromagnetic metals.

Our observations in Fig. 3.6 demonstrate that the planar Hall resistance always begins in either a minimum or maximum resistance state, switches to the complement (maximum or minimum, respectively), then returns back to the original state. For typical behavior of the Hall resistance as shown in Fig. 3.6(a-c), this can be explained by a two-jump magnetization switching sequence: [100] ($\varphi \sim$ -45°) → [010] ($\varphi \sim$ 45°)→ [$\bar{1}$00] ($\varphi \sim$ 135°). This evolution also accounts for the accompanying longitudinal resistance jumps shown in Fig. 3.6d, but the noise level is significantly higher due to the large background in the longitudinal measurement (Eq. 1a). Between the switching transitions, the sample remains in what appears to be a *macroscopic* single domain state. In this regime the magnetization evidently rotates coherently according to Stoner-Wohlfarth model [21], hence the planar Hall effect continues to evolve to a small degree with field [23]. Scanning SQUID microscopy of (Ga,Mn)As epilayers (involving measurement of in-

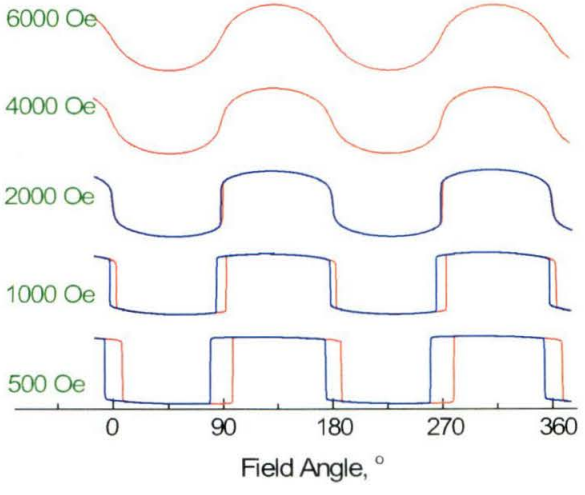

Fig. 3.10 Planar Hall effect for orientational sweeps of magnetic field (fixed magnitude).

plane magnetization) provides evidence for the existence of macroscopic single domains on length scales extending to hundreds of microns [24]. Domain states within the sample evidently exist only in the vicinity of the switching field, and the associated domain wall scattering generates the remarkable resistance spikes shown in Fig. 3.6d.

3.2.3. PHE Dependence on Crystalline Orientation

We have also investigated samples with Hall bars fabricated along many other directions besides the [110] crystalline axis reported on here. To obtain consistent results, all the Hall bars are fabricated on the same chip by one-step electron beam lithography. We find that the switching fields do *not* depend on the Hall bar orientations, even though the magnitude of planar Hall resistance jumps are systematically reduced as one moves away from the (110) direction. Representative data for Hall bars aligned along 0°, 15°, 30° and 45° from [110] crystalline direction are provided in Fig. 3.11. The field is swept at 20° degree with respect to [110] direction.

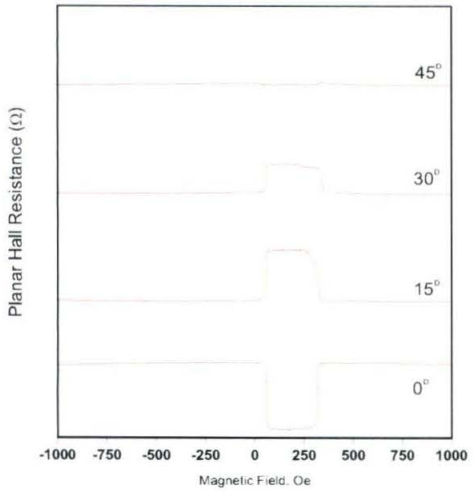

Fig. 3.11 Planar Hall resistance for Hall bars orientated 0°, 15°, 30° and 45° away from [110] crystalline axis.

In conclusion, we report the first observation of large spontaneous planar Hall effect in epitaxial (Ga,Mn)As thin films. This galvanomagnetic effect [25] appears to arise from the finite angle between the direction of current flow and the direction of the spontaneous magnetization. This effect is analogous to the Anisotropic Magnetoresistance (AMR) phenomenon that occurs within what are high-quality, single-domain magnets. In mesoscopic metallic ferromagnets this effect is usually exceedingly small in, only of order mΩ [26]. Here, the large magnitude in

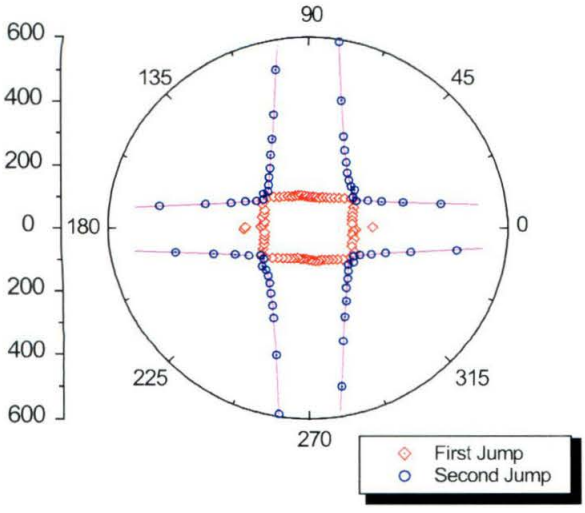

Fig. 3.12 Polar plot of the first and second switching fields vs. orientation of external field.

GaMnAs is not, at present, completely understood, but we presume it stems from the combined effect of significant spin-orbit coupling in the valence band of the zincblende crystal structure, and the large spin polarization of holes in (Ga,Mn)As. Due to the extremely high quality of these epitaxial thin films and their well-defined crystalline directions throughout the entire sample, single domain behavior occurs on a *macroscopic* scale. Due to the absence of domain walls between voltage probes, the PHE observed is always that obtained in the saturated state.

3.3. In-Plane Magnetic Crystalline Anisotropy of (Ga,Mn)As: Cubic Anisotropy Plus Uniaxial Anisotropy

Fig. 3.12 summarizes the signatures of the coercive fields manifested in our electrical transport measurements upon these (Ga,Mn)As devices. The field loci delineating the resistance transitions are shown in polar coordinates as function of applied in-plane field in polar coordinates. The H_{c1} lines form a rectangular shape, whereas the H_{c2} lines are more complicated. The latter follow the extrapolation of H_{c1} lines at low field but evolve towards the (110) axes in higher fields. Eventually, at a field around 2500 Oe, the second jump becomes smeared and its switching becomes reversible. These measurements clearly elucidate the nearly cubic four-fold magnetic anisotropy, biased by a small two-fold preference along [110], that is generic in our (Ga,Mn)As epilayers.

Unusual multiple switching, somewhat analogous to that demonstrated in this work, has also been observed in ultrathin epitaxial Fe films, through the magneto-optic Kerr effect (MOKE). A

switching pattern analogous to that of Fig. 3.12 is measured in Ag/Fe/Ag(001) system by Cowburn *et al.* [27], although with significantly less resolution in this metallic system. To explain their results a simple model is invoked, incorporating a well-defined domain wall pinning energy into a complex, anisotropic magnetocrystalline energy surface (A weak in-plane uniaxial anisotropy is superimposed along one easy axis of a strong cubic anisotropy). Our experimental data can be described by an explanation based on similar domain reversal energetics, but in our case the in-plane uniaxial easy axis is collinear with a hard axis of the cubic anisotropy. The corresponding free energy density of such a single domain magnet can be written as

$$E = K_u \sin^2 \varphi + \frac{K_1}{4} \cos^2 2\varphi - MH \cos(\varphi - \varphi_H), \tag{3.6}$$

where K_u, K_1 are in-plane uniaxial and cubic anisotropy constants, M is magnetization, H is the external field that is applied at the angle φ_H with respect to [110]. An example plot of this energy function is provided in Fig. 3.13a.

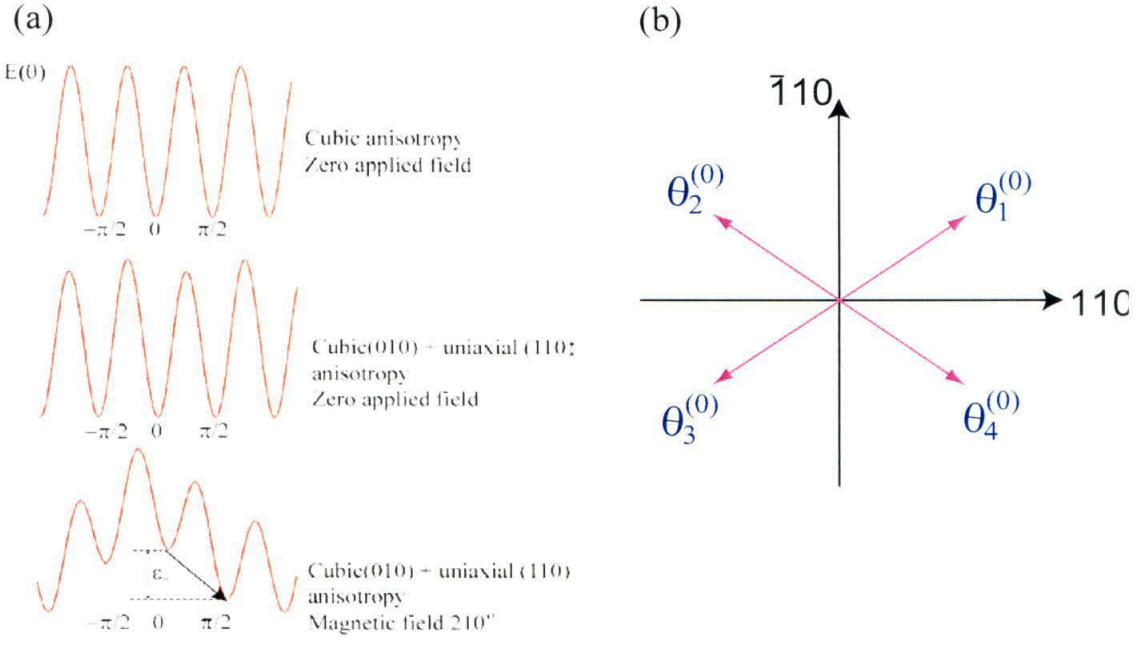

Fig. 3.13 (a) Magnetic energy density as a function of magnetization orientation in various situations of magnetocrystalline anisotropy. (b) The equilibrium positions for a mixed cubic and uniaxial anisotropy energy surface.

The equilibrium state is defined by the stable conditions,

$$\frac{\partial E}{\partial \varphi} = K_u \sin 2\varphi - K_1 \sin 4\varphi + MH \sin(\varphi - \varphi_H) = 0 \ , \ \text{with} \ \frac{\partial^2 E}{\partial \varphi^2} > 0. \tag{3.7}$$

At zero fields, four distinct magnetization states, corresponding to four local energy minima, can exist:

$$\begin{aligned} \varphi_1^{(0)} &= \frac{\pi}{4} - \delta, \ \varphi_2^{(0)} = \frac{3\pi}{4} + \delta, \\ \varphi_3^{(0)} &= -\frac{3\pi}{4} - \delta, \ \varphi_4^{(0)} = -\frac{\pi}{4} + \delta, \end{aligned} \tag{3.8}$$

where $\delta = \arcsin(K_u / K_1)$. These stable solutions are represented in Fig. 3.13b. Domains can exist over short length scales in a demagnetized thin film at zero field. Upon application of an in-plane field, these small-scale domains quickly become suppressed and the whole sample evolves into a macroscopic single domain state described by Eq. (3.8). This behavior is unique to a high quality, high anisotropy, single-crystalline epitaxial materials. When the applied field is reversed, magnetization reversal is achieved through an intermediate state, representing a local energy minimum, corresponding to the sample magnetization oriented almost orthogonal (90°) to the initial and final directions of the magnetization.(Fig. 3.14) Domain states mediate the transitions from one local energy minimum to another. For a domain wall to become liberated to propagate through the sample, the external field must be increased to the point where a characteristic pinning energy, ε, is exceeded, *i.e.*,

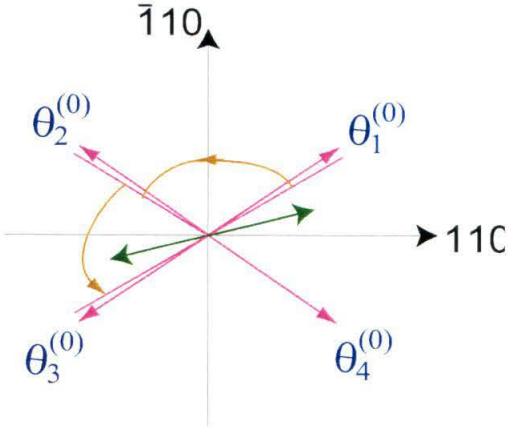

Fig. 3.14 An illustration of two-jump process occurring in a cubic magneto-crystalline anisotropy ferromagnet.

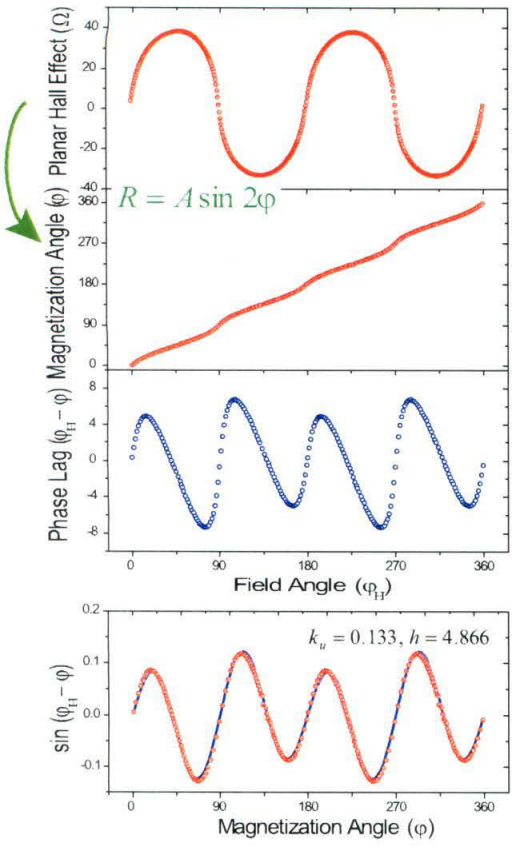

Fig. 3.15. Illustration of the procedure to yield magnetic anisotropy constant from high field orientational planar Hall measurement data (6000 Oe). The magnetization angles are first computed from experimental data by Eq. (3.5). Then phase lag between external field and magnetization are plotted as a function of magnetization angle, which is nicely fitted by a non-linear function [Eq. (3.7)] to yield anisotropy parameters.

$$\mathbf{H}_c \cdot (\mathbf{M}_2 - \mathbf{M}_1) = \varepsilon \,. \tag{3.9}$$

Here $\mathbf{M}_1$, $\mathbf{M}_2$ are the initial and final magnetization, and $\mathbf{H}_c$ is the switching field. If $\mathbf{H}_c$ is small compared to the anisotropy field, coherent rotation of $\mathbf{M}_1$ and $\mathbf{M}_2$ from the equilibrium position defined by Eq. (3.8) is negligible. For transitions from [100] to [010], a 90°-domain wall with core magnetization along [110] is required to propagate across the sample. Eq. (3.9) gives $\mathbf{H}_c \cdot \hat{x} = -\varepsilon_{110} / 2M \sin(45^\circ - \delta)$, in which ε_{110} is the corresponding domain wall pinning energy. Considering all possible orientational trajectories, we can describe the loci of transitions as follows:

$$\begin{aligned} \mathbf{H}_c \cdot \hat{x} &= \pm\varepsilon_{110} / 2M \sin(45^\circ - \delta) \\ \mathbf{H}_c \cdot \hat{y} &= \pm\varepsilon_{\bar{1}10} / 2M \sin(45^\circ + \delta). \end{aligned} \tag{3.10}$$

At low field, these describe two parallel sets of lines that are in excellent correspondence with the switching pattern observed in our experiments (Fig. 3.12). At high fields two new pieces of

physics become important. First, coherent rotation of magnetization must be considered and, second, the specific energy of a domain wall (energy/area) also becomes significantly reduced.[28] As a result, high field transitions progressively evolve towards the (110) directions.

Several additional points are worthy of mention. First, planar Hall resistance measurements enable determination of crystallographic orientation with remarkable precision; we estimate our angular error in establishing the [110] directions to be less than 0.04°. Second, apart from the singularity along these (110) directions, neither single transitions nor three-transition processes are observed. This justifies our assumption that in-plane uniaxial anisotropy does not exist along the cubic easy axes.[29]

We are able to deduce both the cubic and uniaxial anisotropy fields through PHE measurements. To achieve this, a large, constant magnetic field is applied in the plane while its orientation is rotated continuously. Fig. 3.15 shows data from such measurements for clockwise and counterclockwise sweeps of magnetic field orientation, with field magnitude fixed at 500 Oe, 1000 Oe, 2000 Oe, 4000 Oe and 6000 Oe. When $H < H_{cA}$, where $H_{cA} \sim 2500$ Oe is the dominant cubic anisotropy field, the magnetoresistance reverses whenever the magnetization is swept across the cubic hard axis, as expected. The planar Hall resistance becomes reversible for fields greater than 2500 Oe, in which case the magnetization rotates coherently with the external

(a)

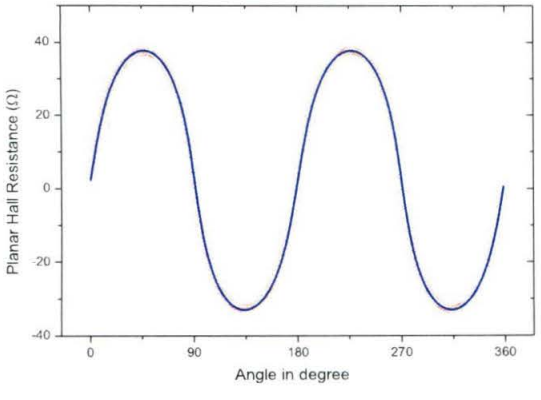

(b)

	h	H_k	k_u
H=4000G	3.414	1172	0.133
H=6000G	4.866	1233	0.133

Fig. 3.16 (a) Comparison between experimental data and calculated planar Hall resistance with optimized parameters. (b) Table showing the fitting result for measurements made at in plane magnetic fields with magnitudes 4000 Oe and 6000 Oe.

field. For a given external field angle φ_H, the macroscopic in-plane magnetization orientation, φ, can be calculated by using PHE expression in Eq. (3.5). By fitting the computed data set (φ_H, φ) to Eq. (3.7), we can unambiguously extract the anisotropy constants $H_{cA} = 2K_1 / M = 2400$ Oe, $H_{uA} = K_u / M = 160$ Oe. The fitting procedure is illustrated in Fig. 3.15. Fitting the experimental data for magnetic fields varying from 4000 to 6000 Oe gives consistent results (See Fig. 3.16).

These results can be compared with theoretical predictions for the (Ga,Mn)As system. Recently significant progress has been made in the theoretical understanding of magnetic anisotropy in III-V magnetic semiconductors [30-33]. It seems generally agreed that in addition to an intrinsic cubic anisotropy, a substantial out-of-plane uniaxial anisotropy exists for this material, with a sign that depends upon the growth conditions, *i.e.* whether tensile or compressive biaxial-strain exists at the interface. However for magnetization *in the plane*, there has been no discussion of whether an additional two-fold (uniaxial) bias to the cubic anisotropy might exist. As far as the cubic anisotropy is concerned, calculations predicted that the cubic easy axis fluctuate between [100] and [110] depending upon the hole concentration and the degree of spin-splitting. For experimentally relevant hole concentrations, these calculations predict a cubic easy axis along [110]. Our experiments do not agree with these theoretical preidictions. To date, all of our measurements indicate that the cubic easy axes are instead along the (100) axes. Further PHE studies on additional sample sets are needed to determine if the cubic anisotropy can exhibit fluctuations with the aforementioned parameters, as predicted by theory. Our experimental results do agree, however, with existing theory regarding the magnitude of the computed cubic anisotropy field, which we find to be about 2400 Oe.

3.4. Temperature Dependence of PHE and Coercivities

We have also studied the temperature dependence of PHE, which should be of significant importance in elucidating its underlying physical mechanisms. Our measurements are performed in a ^{3}He cryostat with magnetic field at fixed orientation but swept in magnitude. Fig. 3.17a shows the results of these measurements for a 10 μm Hall bar, measured under conditions of careful temperature regulation, stepped from 50 K down to 0.32 K. The magnitude of both the PHE and the coercivities increase rapidly with decreasing temperature (Fig. 3.17b). For $T < 10$K, both the PHE and sheet resistivity diverge logarithmically down to the lowest temperatures

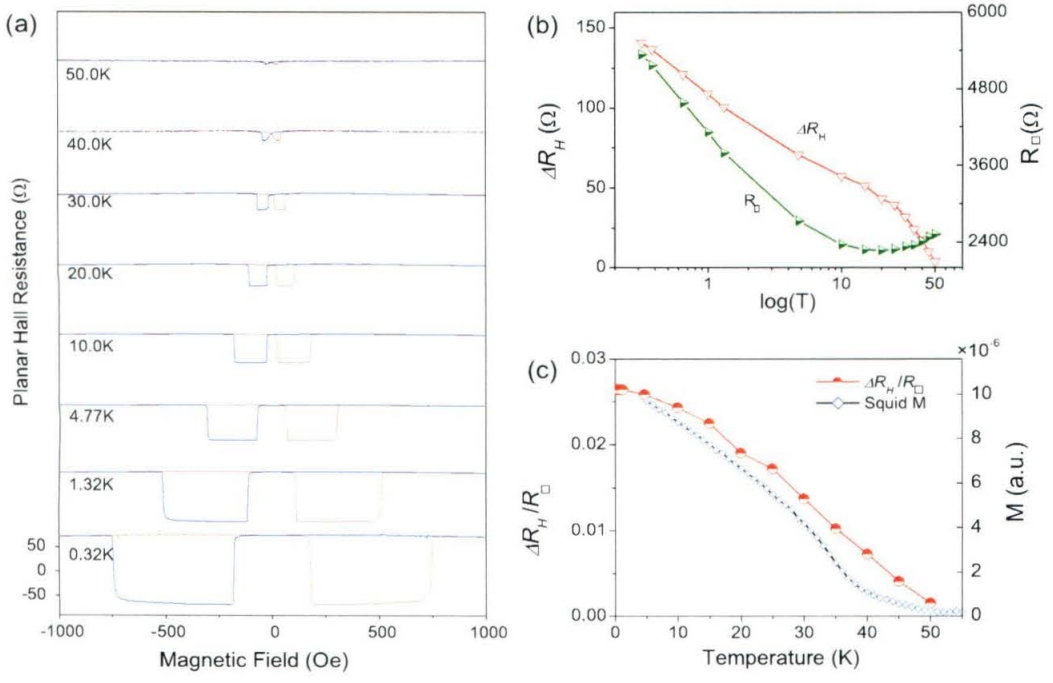

Fig. 3.17 (a) Temperature dependence of the planar Hall resistance. (b) Plots of the planar Hall resistance jump, ΔR_H, and sheet resistance, $R_\square$, versus temperature (semi-logarithmic scale). (c) Comparison between the magnetoresistance ratio, $\Delta R_H / R_\square$, obtained from transport measurements on a 10 μm wide Hall device, and sample magnetization, *M*, measured by SQUID magnetometry on a macroscopic (3 mm × 3 mm) sample.

measured, T = 0.32K, while the ratio ($\Delta R_H / R_\square$) remains nearly constant. Here, ΔR_H is the PHE resistance jump and $R_\square$ is the zero-field sheet resistance. Similar observations of an anomalous minimum in the resistivity near 20K have also been reported by Oiwa *et al.* in (Ga,Mn)As [34].

In this work we present data on samples with conductivity comparable to the Mott minimum metallic conductivity $\sigma_{\min} \approx 0.03 N_c^{1/3} e^2/\hbar \approx 25\,\mathrm{Scm}^{-1}$ ($R_\square$=2700Ω). Accordingly, the anomalous low temperature resistivity may arise from the onset of hole localization near the metal-insulator-transition. The resistivity anisotropy ratio, $\Delta R_H / R_\square$, should provide information about the hole spin polarization. It is striking that the low temperature resistivity tends toward indicating an insulating state, while the magnetic phenomena, as represented in the PHE jump amplitude continues to increase. We find that $\Delta R_H / R_\square$ decreases monotonically with

increasing temperature, and qualitatively tracks the magnetization of a 3 mm by 3 mm sample measured by SQUID magnetometry (Fig. 3.17c). However, it appears to be significant that the broad tail in the temperature dependence near T_C evident in the SQUID measurement is absent in the planar Hall data. This may reflect local variations in the Curie temperature in this alloy system – in the 10μm wide Hall devices spatial variation of T_c is greatly reduced compared to that in the macroscopic 3mm sample used for SQUID measurements.

The temperature dependence of the coercivity reflects the competition between magnetostatic energy and thermal energy on the domain wall motion. Fig. 3.18 shows a semilog plot of both coercivites (H_{c1} and H_{c2}) vs. temperature. Again, a log(T) behavior spans most of the temperature range. This is unexpected from a pure thermally assisted reversal mechanism since most thermal process follow an Arrhenius behavior. At low temperature, quantum tunneling of domains may take effect and exhibit new interesting phenomena. We haven't yet observed a low temperature saturation of the coercivity. Measurements in a dilution refrigerator are required to extend the

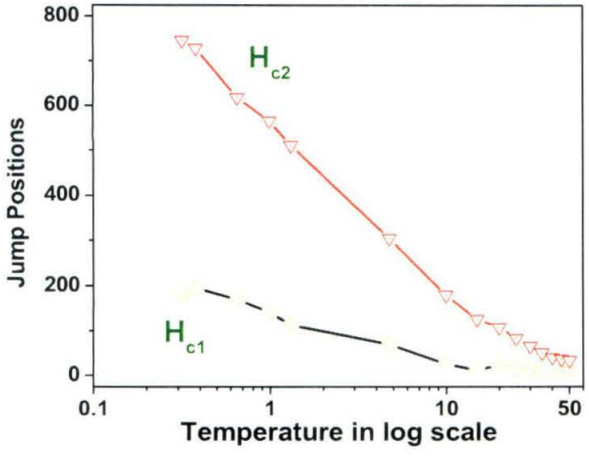

Fig. 3.18 Temperature dependence of coercivities determined by planar Hall resistance.

data to millikelvin temperature range.

3.5. Barkhausen Jumps in Micron-size Samples

When the size of the device is reduced to 6μm, we observe clear small Barkhausen jumps occurring in close proximity to the switching fields (Fig. 3.19). This appears to demonstrate that the propagation of domain walls is constrained by geometry [35, 36]. We picture this as arising from the impairment of free propagation of domain walls across the mesoscopic sample, perhaps especially impeded at Hall cross-junctions when the width of the voltage probes becomes substantial to that of the channel itself. A typical Barkhausen jumps is smally, only of order 0.2 Ω, *i.e.* equivalent to 0.25% reversal of the wire. The corresponding Barkhausen volume is estimated to be 3.4×10^{-5} μm^{-3}. This volume corresponds to a moment of only $2 \times 10^{5} \mu_B$. It is intriguing to consider the possibility of Macroscopic Quantum Tunneling (MQT) of magnetization for this number of spins. Note that our apparent measusrement resolution in this work is about two orders better than this, approaching $10^{3} \mu_B$ -.

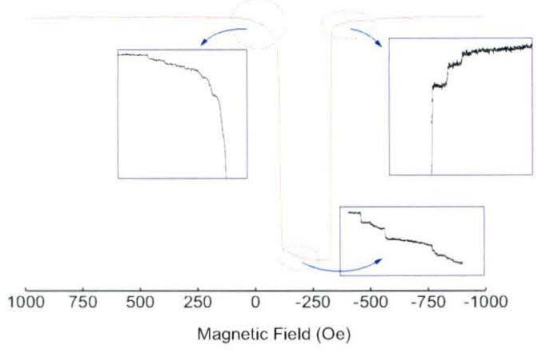

Fig. 3.19 Barkhausen jumps that are evident solely in 6 μm wide devices near the resistance transitions.

3.6. Summary

Large Hall resistance jumps are observed in microdevices patterned from epitaxial (Ga,Mn)As layers when subjected to a swept, in-plane magnetic field. This giant "planar Hall effect" is four orders of magnitude greater than previously observed in metallic ferromagnets. This enables extremely sensitive measurements of the angle-dependent magnetic properties of

(Ga,Mn)As. An interplay between cubic anisotropy and weak in-plane uniaxial anisotropy explains the unusual switching patterns for different in-plane fields. Small Barkhausen jumps become evident when the device size is reduced to ~6 μm.

We believe our Hall effect-based magnetometry approach provides an important complement to MOKE hysteresis measurements that are widely employed to study thin film magnetism. In the latter approach, significant second-order magneto-optical interactions often render MOKE hystersis loops complicated and difficult to interpret.[37] Further complications also arise in semiconducting (*i.e.*, DMS) materials since MOKE measurements are based on sample illumination; at low temperatures both carrier density and temperature can be significantly perturbed by the light beam. The direct magnetotransport technique described here enables very high-resolution measurements of magnetization in micromagnets – approaching one part in 10^5 – with only very small perturbation.

Chapter 4. Out-of-Plane Measurement – Extraordinary Hall Effect

4.1. Extraordinary Hall Effect

The intriguing planar Hall effects in (Ga,Mn)As encourage us to explore magnetotransport in the material when the magnetization is oriented out of plane. Of course the conventional Hall measurement configuration is where the field is applied perpendicular to the films.

For a single-domain magnetic material, in completely isothermal conditions, when a magnetic field **H** and current density **j** are externally applied, the electrical field induced within the sample can be expressed as [38, 39],

$$\mathbf{E} = \rho_{\perp}\mathbf{j} + (\rho_{//} - \rho_{\perp})(\mathbf{j}\cdot\hat{\mathbf{m}})\hat{\mathbf{m}} + (R_0\mathbf{H} + R_S 4\pi\mathbf{M})\times\mathbf{j}. \tag{4.1}$$

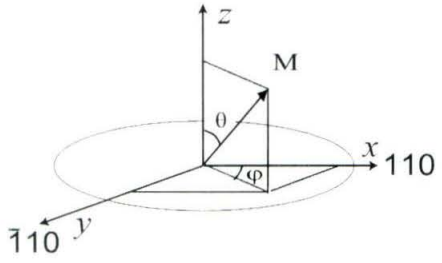

Fig. 4.1 Coordinate system in 3-D space for out of plane experiments.

Here $\hat{\mathbf{m}}$ is a unit vector directed along the magnetization, R_0 is the normal Hall resistivity and R_S is extraordinary Hall effect coefficient. In this equation, the four terms represent, respectively, the longitudinal magnetoresistance, the planar Hall effect, the normal Hall effect and extraordinary Hall effect. For ferromagnets, the extraordinary coefficient R_S in many cases is much greater than the ordinary coeffcient R_0, which is $1/pe$ in hole doped magnetic semiconductor. For example, in (Ga,Mn)As epilayers studied in this thesis, the hole density is pretty high ($\sim 10^{20}$ cm^{-3}) and the ordinary Hall resistance is estimated to be 0.2mΩ/Oe. This makes the direct influence of the external field negligible and, thus, for the sake of simplicity in the remainder of the paper we shall consider only the extraordinary contribution and refer to it as normal Hall resistance. From Eq. (4.1) the transverse and longitudinal components of the vector **E** are

$$E_x = j\rho_\perp + j(\rho_{//} - \rho_\perp)\sin^2\theta\cos^2\varphi\,, \tag{4.2}$$

$$E_y = j(\rho_{//} - \rho_\perp)\sin^2\theta\sin\varphi\cos\varphi + j(R_0 H_\perp + R_S 4\pi M_S\cos\theta)\,. \tag{4.3}$$

The expressions are made using the coordinate system shown in Fig. 4.1, where the external electric field is applied along the x direction, the polar angle θ and azimuthal φ specify the orientation of the saturated magnetic moment. If the planar Hall effect is the only term to be investigated, then the magnetic field has to be applied in the plane of the film in order to ensure that $M_\perp$ is zero. The intention in this section, however, is to measure the magnetoresistance when the field is applied at some angle to the film plane. In this case $M_\perp$ is not zero and the extraordinary Hall effect has to be taken into account.

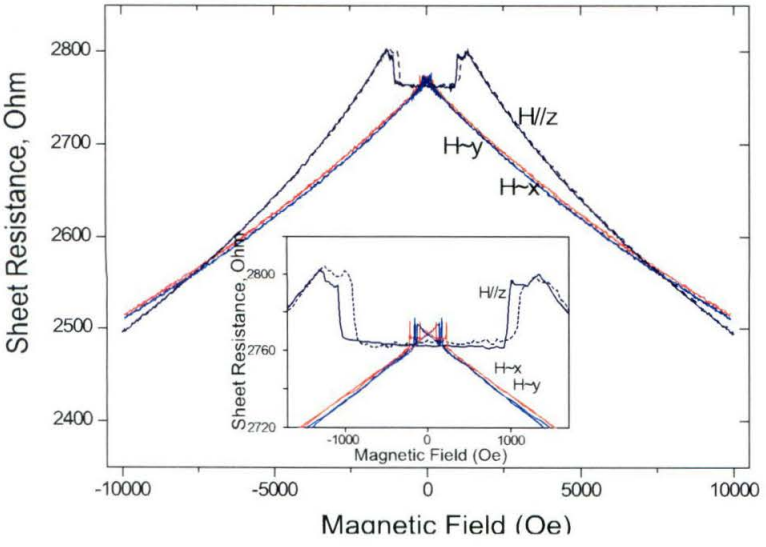

Fig. 4.2 Longitudinal resistance R_{sheet} for external fields applied in three orthogonal orientations. The result for a planar Hall resistance R_{PHE} is also presented for comparison. *Inset*: enlarged view of low field magnetoresistance at low field region.

4.2. Out-of-Plane Transport Measurement Results

Fig. 4.2 shows the longitudinal magnetoresistance R_{sheet} measured at 4.2K for magnetic field oriented along z direction and along two orthogonal in-plane angles (20° degree off x and y respectively). The field sweep range is ±10000 Oe, 10 times larger than we have performed in planar Hall resistance measurement. There is a large overall negative magnetoresistance for all field orientations. For the external field less than 6000 Oe, the normal sheet resistance is higher than both in-plane sheet resistances, in accordance with planar Hall resistance measurement result where $\rho_{//} - \rho_{\perp} < 0$. The negative magnetoresistance behavior persists beyond 1 T (the limit of our vector magnet). It is immediately clear why the jumps and spikes observed in the low field region have been overlooked by other research groups: Due to the rapidly changing large resistance background, one has to step the magnetic field small enough to resolve local small jumps in the low field region. An enlarged view of sheet resistance in the field range ±1500 Oe is reproduced in the inset of Fig. 4.2. The normal sheet resistance exhibits a pan-shape in the low field region, with jumps at about ±1300 Oe and a flat magnetoresistance region between them. The resistance change is ~ 35 Ω, about half the size of planar Hall resistance jumps (72 Ω) at this temperature.

On the other hand, in transverse (Hall) measurement, with almost zero background, the Hall signal is enormous and one could not possibly miss it. Fig. 4.3 shows the Hall resistance R_H measured as a function of perpendicular field. For comparison, the planar Hall resistance loop at 20° off [110] axis is also presented. At very large negative field, the extraordinary Hall resistance saturates corresponding to a saturated magnetization along the -z direction. This justifies our assumption that the ordinary Hall effect is *negligible*. On sweeping the field up, a broad Hall resistance jump starts at around -1500 Oe and ends at -1000 Oe. Then the planar Hall resistance varies linearly before a second jump arises at 1000 Oe. The magnetization is fully reversed at 1500 Oe and saturates again beyond this field intensity. It is apparent that the transition processes in both transverse measurement and longitudinal measurement are simultaneous and related. The total resistance change is 306 Ω, we have

$$4\pi MR_S = 153\Omega \tag{4.4}$$

From which, an extraordinary resistance coefficient $R_S = 0.6\Omega/\mathrm{Oe}$ can be deduced.

When ramping down the field, a large hysteresis occurs in the field range of ±1000 Oe. Normal Hall resistance difference between the two hysteresis curves matches the magnitude of

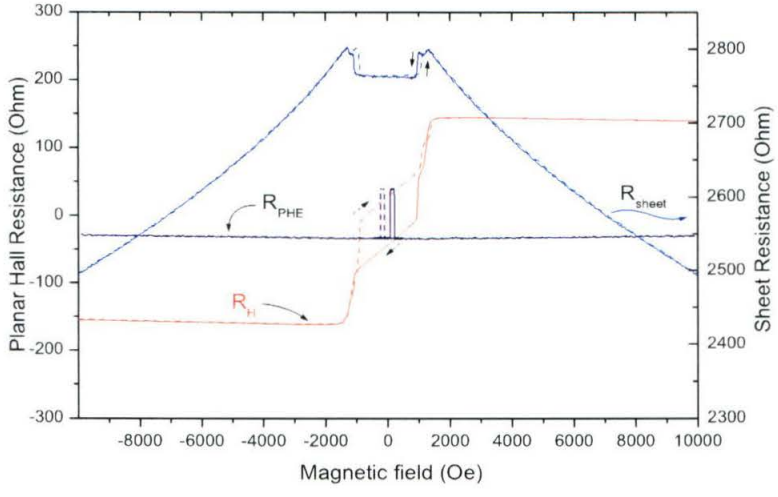

Fig. 4.3 Longitudinal resistance R_{sheet} and Hall resistance R_H for a 100 μm wide Hall bar subject to a perpendicular field. For comparison, the result for a planar Hall resistance R_{PHE} is also presented.

planar Hall resistance jumps. This matching is repeatable in all the samples we have measured. Hence we believe that this hysteresis originates from different in-plane magnetization configuration when the magnetic field is swept across zero magnetic field.

4.3. Modeling of Perpendicular Magnetization Reversal Process

In Sect. 3.3, based upon a mixture of cubic anisotropy and a weak in-plane anisotropy, we are able to explain the unusual switching behavior in the planar Hall resistance measurements. Anisotropy fields (the ratio between anisotropy energy and magnetization) are deduced from transport measurement data. As one can imagine, in a perpendicular magnetic field, in addition to the conventional in-plane and out-of-plane uniaxial anisotropy fields, the magnetic moment should be also under the influence of the other two out-of-plane cubic easy axes. Unfortunately, unlike the purely uniaxial anisotropy, the case of cubic magnetorystalline anisotropy was not fully explored before, even though it represents a lot of important materials. A full description of the magnetization reversal process needs to contain precisely all means of magnetic energy contributions. The following expression describes a complete free energy for magnetization in the 3-D space,

$$E = K_{ui}\left(\frac{\mathbf{M}_s \cdot \mathbf{u}_i}{M_s}\right)^2 + K_{uo}\left(\frac{\mathbf{M} \cdot n}{M_s}\right)^2 + K_1\left(\alpha_1^2\alpha_2^2 + \alpha_2^2\alpha_3^2 + \alpha_3^2\alpha_1^2\right) + 2\pi\left(\mathbf{M} \cdot \mathbf{n}\right)^2 - \mathbf{M} \cdot \mathbf{H}, \quad (4.5)$$

where the direction cosines $(\alpha_1, \alpha_2, \alpha_3) = (M_x / M, M_y / M, M_z / M)$. K_{ui} and K_{uo} are in-plane and out-of-plane uniaxial anisotropy constants, respectively, and K_1 is cubic anisotropy constant, the higher-order magnetocrystalline energy contributions are ignored. The fourth term is magnetostatic energy, *i.e.*, demagnetization field induced shape anisotropy. The last term represents Zeeman energy. As we have demonstrated before, the in-plane uniaxial anisotropy is very weak; hence, in the analysis of out-of-plane magnetization reversal, for simplicity we will abandon this term. The out-of-plane uniaxial anisotropy, originated from the compressive strain that exists at the (Ga,Mn)As/GaAs interface, favors the alignment of magnetization in the plane and accordingly has a positive value. Theoretical calculation predicted a value of the uniaxial anisotropy field of about 4000 Oe. [32] Combining it with the shape anisotropy, an effective out-of-plane uniaxial anisotropy energy can be defined as

$$E_u = 2\pi\left(1+\frac{2K_{uo}}{4\pi M_s^2}\right)(\mathbf{M}\cdot\mathbf{n})^2 = 2\pi\eta(\mathbf{M}\cdot\mathbf{n})^2, \tag{4.6}$$

where $\eta = 1+\dfrac{H_{uo}}{4\pi M_s}$ is a number on the order of 10 (In our sample $4\pi M$ = 265 Oe). By using the coordinate system depicted in Fig. 4.1, for a field H applied perpendicular to the film, the magnetic free energy density is written as

$$E(\theta,\varphi) = \frac{1}{4}K_1\left(\sin^4\theta\cos^2 2\varphi + \sin^2 2\theta\right) + 2\pi\eta M^2\cos^2\theta - MH\cos\theta\,. \tag{4.7}$$

Since the field is applied along the z direction, no additional angular variable is needed to describe its orientation. The stable equilibrium conditions can be expressed in polar coordinates as

$$\frac{\partial E}{\partial\theta} = 0, \tag{4.8}$$

$$\frac{\partial E}{\partial\varphi} = 0, \tag{4.9}$$

$$\frac{\partial^2 E}{\partial\theta^2}\frac{\partial^2 E}{\partial\varphi^2} - \left(\frac{\partial^2 E}{\partial\varphi^2}\right)^2 > 0, \tag{4.10}$$

$$\frac{\partial^2 E}{\partial\varphi^2} > 0\,. \tag{4.11}$$

These equations put a restriction to the angle φ of the equilibrium position,

$$\cos 2\varphi = 0\,, \tag{4.12}$$

which is the same as the in-plane situations. Depending on the magnetization history, the magnetization remains in the directions of minimum energy with φ = 45°, 135°, 215° or 305°. The weak in-plane uniaxial anisotropy may cause the actual φ orientations to deviate by a very small angle from those angles. An effective one-dimensional energy density can be found by substituting the value determined by Eq (4.12) into Eq. (4.7),

$$E_{eff}(\theta) = \frac{1}{4} K_1 \sin^2 2\theta + 2\pi\eta M^2 \cos^2\theta - MH\cos\theta . \tag{4.13}$$

This free energy density expression is analogous to the in-plane energy density [Eq. (3.6)], but with opposite signs for both the cubic term and the uniaxial term. It is worthy to mention that here the out-of-plane uniaxial anisotropy is much stronger than the in-plane uniaxial anisotropy. As we will show later, the competition between this uniaxial anisotropy and cubic anisotropy provides a unique magnetization reversal process and is able to account for all the anomalous normal magnetoresistance behavior. At zero external field, the stable solutions for θ are multiple of 90°. Since θ is in the range of [0°, 180°], instead of four equilibrium orientations, now only three exist at zero field: 0°, 90° and 180°. For nonzero external field, they may move away from these values and can be solved directly from Eqs. (4.8) - (4.11) or from the analysis of the effective energy density described by Eq. (4.13),

$$M\sin\theta\left\{H - \left[(H_{cA} + 4\pi\eta M)\cos\theta - 2H_{cA}\cos^3\theta\right]\right\} = 0 \tag{4.14}$$

$$H_{cA}\cos 4\theta - 4\pi\eta M\cos 2\theta + H\cos\theta > 0 \tag{4.15}$$

Here, $H_{cA} = 2|K_1|/M$ is the cubic anisotropy field whose value has been obtained through planar Hall resistance measurement. Eq. (4.14) gives

$$\sin\theta = 0 \Rightarrow \theta_1 = 0°, \theta_3 = 180° \tag{4.16}$$

$$\theta_2 = 90° - \delta_0, \text{ with } (H_{cA} + 4\pi\eta M)\sin\delta_0 = H + 2H_{cA}\sin^3\delta_0 \tag{4.17}$$

The first two solutions are north/south poles in polar coordinates, representing a saturated out of plane magnetization. The third solution is a close to plane solution ($\theta \sim 90°$). To which direction the magnetization points is determined by the criteria Eq. (4.15) and the magnetic history. Fig. 4.4 exemplifies the situation when a large positive magnetic field is applied. In such a case, magnetization is saturated in the positive z direction and θ coordinate stays at zero.

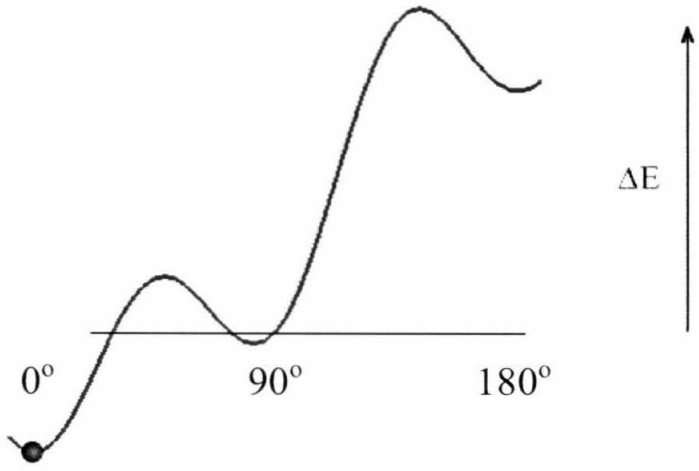

Fig. 4.4 An illustration of three energy minima for out-of-plane free energy. Horizontal axis is the polar angle. In this particular diagram, a large positive field is applied.

We base upon the analysis of the magnetic anisotropy energy in Eq. (4.13) to understand the abnormal magnetization reversal shown in Fig. 4.3. In a high positive field, the magnetization saturates at $\theta = \theta_1$, which is the only stable solution. On reducing the magnetic field, a new stable magnetization orientation $\theta = \theta_2$ starts to develop. In the presence of thermal excitation and interaction of local defects, magnetic domains can be launched in this new polarization. This nucleation field, hereafter it is referred to as H_N and is defined by

$$\frac{\partial^2 E(\theta, H_N)}{\partial \theta^2} = 0 \text{ and } \frac{\partial E(\theta, H_N)}{\partial \theta} = 0 . \tag{4.18}$$

Simple calculus yields,

$$H_{C1} = H_N = \frac{\sqrt{6} H_{cA}}{9} \left(1 + \frac{4\pi\eta M}{H_{cA}} \right)^{3/2} . \tag{4.19}$$

This critical field has its direct origin from cubic anisotropy energy surface of (Ga,Mn)As. There is no correspondence in a conventional magnetic material with uniaxial anisotropy, evident from the fact that H_{C1} approaches infinity when H_{cA} goes to zero.

The domains of the second phase grow continuously on further reducing the field. Note that for perpendicularly magnetized films, the energetics is different from the in-plane case, where single domain behavior appears on a macroscopic scale and magnetization switching is achieved through domain wall nucleation, depinning and subsequent sweeping through the sample. In the

latter case, distinct domain wall pining energy has to be overcome in the switching process. For perpendicular magnetization, the initial and final magnetization states are not so well defined, it is hard to describe the domain wall pinning energy by a definite value. Imaging of magnetic domain structures in (Ga,Mn)As has been achieved by scanning Hall microscopy and scanning SQUID microscopy at low temperature.[24] The film with perpendicular anisotropy has a maze domain structure more similar to that of conventional ferromagnetic materials, whereas the film with in-plane magnetization has unconventional domain structures that show no evidence of domain wall in a fairly large area (about 300 μm by 300 μm). Therefore, it is reasonable to assumed that on decreasing the external field, once the free energy at θ_2 matches that of θ_1, i.e., $\varepsilon = 0$ in equation (3.9), domain wall nucleation processes terminate and all domains fall into this new, more favorable stable configuration. Coherent domain wall rotation starts to dominate magnetization reorientation. This critical field, H_{C2}, can be obtained by solving the equation

$$E(\theta = 0, H = H_{C2}) = E(\theta = \theta_2, H = H_{C2}). \tag{4.20}$$

For $H_{cA} = 0$, *i.e.*, only uniaxial anisotropy terms are present, this equation gives $H_{C2} = 4\pi\eta M$, in agreement with the coercivity predicted by the Stoner-Wohlfarth model for uniaxial crystalline anisotropic materials. For nonzero H_{cA} values, the root is not straightforward. An analytical solution does exist but it is very complicated. By expanding to the second order of $\cos\theta$, a nice approximation can be derived:

$$H_{C2} = 2\pi\eta M\left[1 + \frac{1}{2(1 + H_{cA}/4\pi\eta M)}\right]. \tag{4.21}$$

This is the beginning field of the linear normal Hall resistance in Fig. 4.3. After all the magnetic moments settled down in the intermediate equilibrium state, the magnetization starts to evolve coherently with external field according the Eq. (4.17). At this point, it is more convenient to express **M** in terms of its out-of-plane component,

$$H = (H_{cA}/M + 4\pi\eta)M_\perp + 2H_{cA}M_\perp^3/M^3. \tag{4.22}$$

Since $M_\perp \sim 0$, the third-order term can be ignored. Consequently the perpendicular component of magnetization is a linear function of external field,

$$M_\perp = H/(H_{cA}/M + 4\pi\eta). \tag{4.23}$$

In the limit of $H_{cA} = 0$, the conventional uniaxial magnetic behavior is restored. For magnetic moments close to in-plane orientations, effectively, the cubic anisotropy field combines with uniaxial anisotropy fields and behaves like an ordinary uniaxial magnet in regards to the z-component of the magnetization. This linear evolution of magnetization comes to an end at external field $H_{C3} = - H_{C2}$, where its energy matches the magnetic energy at $\theta = \theta_3$. Following that, nucleation process to create domains θ_3 dominates. This nucleation process persists until the intermediate state $\theta = \theta_2$ vanishes at a large negative threshold field $H_{C4} = - H_{C1}$. Domain walls disappear beyond this field and the magnetization reversal is accomplished.

Both longitudinal magnetoresistance and normal Hall resistance shown in Fig. 4.2 and Fig. 4.3 can be explained by incorporating the analysis of the magnetization process described above. In a down-swept field, the overall transition sequence of θ coordinate is summarized as, $\theta = 0^\circ$ $\rightarrow$ nucleation, $\rightarrow \theta = \theta_2 \sim 90^\circ$, coherent rotation, $\rightarrow$ nucleation $\rightarrow$ $\theta = 180^\circ$. For longitudinal resistance, $\sin^2\theta$ in Eq. (4.2) changes from 0 to a value close to 1 then back to 0. From Eq. (4.2), the size of the two jumps is $|\rho_{\parallel} - \rho_{\perp}|/2 \sim 36\Omega$, consistent with the value observed. For the $\theta = \theta_2$ region, θ deviates from 90° degree by a small number, therefore the sheet resistance exhibits an almost constant value that matches the sheet resistance with in-plane magnetization (Fig. 4.2 inset). The two jumps in the normal Hall resistance and normal sheet resistance reflect the magnetization transitions from 0° to 90° and from 90° to 180°. When the field is ramped down, the nucleation starts at around 1460 Oe (H_N) and ends at about 990 Oe (H_{C2}). Employing simulated $H_{cA} = 2400$ Oe in section 3.3, we estimate $4\pi\eta M = 1635 \pm 65$ Oe. A more accurate

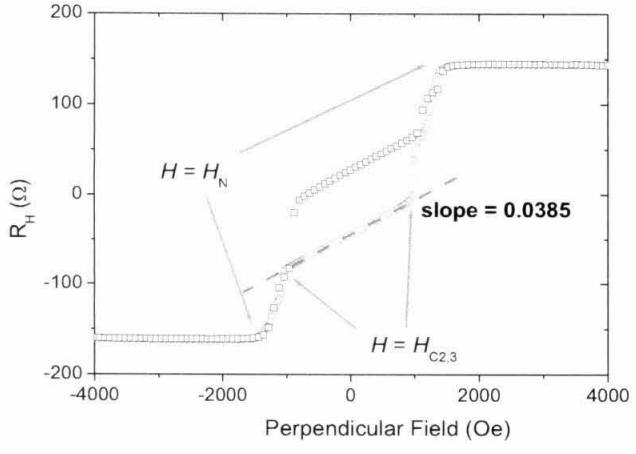

Fig. 4.5 Characteristic fields for films with perpendicular field: Nucleation fields: $\pm H_N$, domain annihilation fields. Magnetization precesses coherently in the linear Hall resistance region.

value can be deduced by fitting to the linear part of the Hall resistance. To first order in $M_\perp$, the Hall resistance in Eq. (4.3) gives,

$$R_H = R_S 4\pi M_\perp . \tag{4.24}$$

By applying Eq. (4.23) and Eq. (4.24), we have,

$$R_H = \frac{R_S 4\pi M}{H_{cA} + 4\pi\eta M} H = \frac{303\,\Omega/2}{H_{cA} + 4\pi\eta M} H . \tag{4.25}$$

A typical fitting is presented in Fig. 4.5, indicating $H_{cA} + 4\pi\eta M = 3972$ Oe. And the effective uniaxial anisotropy field is

$$4\pi\eta M = 1572 \text{ Oe}. \tag{4.26}$$

Using $4\pi M = 265$ Oe measured by SQUID magnetometer, the value of η is found to be 5.93, giving a perpendicular uniaxial anisotropy field 1307 Oe.

In conclusion, through planar Hall resistance and normal Hall resistance measurement, we have deduced all the magnetic anisotropy fields with high precision: Cubic anisotropy field ~ 2400 Oe, in-plane uniaxial anisotropy field ~133 Oe (along [110]), out-of-plane uniaxial anisotropy field (planar cone) ~1307 Oe. To our knowledge, this kind of techniques has never been established before. The deduced out-of-plane uniaxial anisotropy field is less than the theoretical prediction made by Dietl *et al.*[32] Systematic study of magnetic anisotropy on (Ga,Mn)As epilayers with varying thickness and Mn concentration will enable further examination of existing theories regarding the origin of the magnetic anisotropy and ferromagnetism mechanism. Meanwhile, we have measured the spontaneous magnetoresistance anisotropy constant $\rho_\perp - \rho_\parallel \sim -72\Omega$, and the extraordinary Hall resistance coefficient $4\pi M R_S = 153\Omega$. Both of them have their origin in the spin-orbit interaction; it is not clear how these numbers are related.

Our next task is to understand the hysteresis behavior in the low field region of the normal Hall resistance data. The fact that the resistance difference is exactly the size of the planar Hall resistance jumps convinces us that the magnetization must follow a trajectory depicted in Fig. 4.6. As illustrated, the magnetization falls into different stable trajectories with orthogonal φ values.

When the perpendicular field is swept across zero, the in-plane angles are normal to each other for the up-sweep cycle and the down-sweep cycle, producing a resistance difference the same as that for the spontaneous planar Hall resistance jumps.

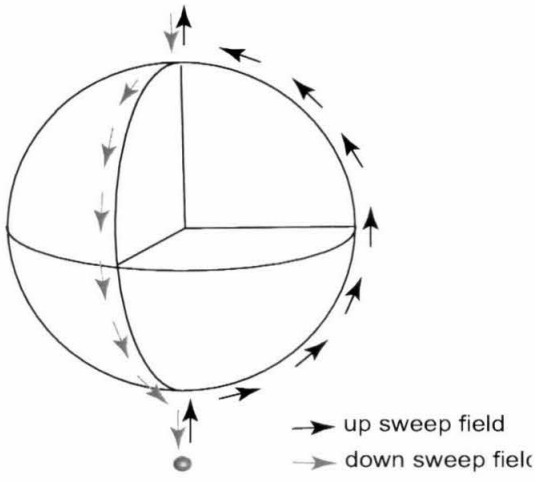

Fig. 4.6 Illustration of the origin of hysteresis in out-of-plane Hall measurement. When the perpendicular magnetic field sweeps across the zero, the in-plane magnetizations are orthogonal, giving a resistance difference same as the spontaneous planar resistance jumps.

We attribute the hysteresis to uncontrolled misalignment of the vertical magnetic field with the film normal. If the external field is applied exactly along the film normal, the magnetization trajectory will be random. But in all our experiments, once set up, reproducible hysteresis patterns are observed on all samples. Suppose the external field is slightly tilted away from the firm normal by coordinates (θ_0, φ_0), the equation (4.5) is rewritten as

$$\begin{aligned} E(\theta,\varphi) = & \frac{1}{4}K_1 \sin^4\theta\cos^2 2\varphi - MH\sin\theta\sin\theta_0\cos(\varphi-\varphi_0) \\ & + \frac{1}{4}K_1\sin^2 2\theta + 2\pi\eta M^2\cos^2\theta - MH\cos\theta\cos\theta_0. \end{aligned} \tag{4.27}$$

The terms containing angle φ look very similar to the in-plane magnetic anisotropy energy with cubic energy replaced by $K_1 \sin^4\theta$ and the effective magnetic field replaced by $H\sin\theta\sin\theta_0$. The φ coordinate evolution depends on the ratio between these coefficients, whose values vary significantly on approaching the poles. It is not surprising that, for the external field not perfectly aligned along the field normal, the magnetization φ coordinate will switch alternatively along possible configurations in successive field cycle.

4.4. Summary

The normal Hall resistances also demonstrate usual behavior that we find is characteristic of competing interplay between cubic magnetocrystalline anisotropy and an effective uniaxial anisotropy that combines interface induced out-of-plane uniaxial anisotropy energy and demagnetization energy. By the simulation of the measured normal Hall resistance, our model successfully interprets all the relevant data and provides the out-of-plane uniaxial anisotropy constant for the first time.

Chapter 5. Domain Wall Measurements

In this chapter, we describe some of the first applications of the unique magnetotransport properties of epitaxial (Ga, Mn)As. The most striking are our detailed studies of single magnetic domain walls in (Ga,Mn)As. Magnetic domain walls are a boundary between different magnetic domains. In general, they are very small (<10 nm across), hence very difficult to measure. We have been able to carry out the first electrical measurements on individual domain wall dynamics. We shall describe these experiments in the section below. This studies culimante with the manipulation of an individual domain wall. The unique, and first direct measurement of the resistance across a single domain wall enables by our approach are discussed and compared with the rich and conflicting background of existing theoretical predictions.

5.1. Dynamics Measurements of Individual Domain Walls

5.1.1. Motivation to Study Domain Dynamics in (Ga, Mn)As

In the previous chapters, we have demonstrated intriguing macro- and micromagnetic properties involving single domains in (Ga,Mn)As films. Phenomenological models explain the observed data with a high degree of accuracy. To understand the underlying physics in detail, a systematic investigation of the dynamical properties of domain wall (DW) is essential. Such

understanding is crucial for engineering a spin transistor or a memory unit, since these require precise control of magnetization reversal. After decades of concerted study on metallic ferromagnetic thin films, it is generally agreed that in high-quality thin samples magnetization reversal occurs by nucleation followed by domain wall propagation. Experimentally, time-resolved imaging of magnetic domains based upon the magneto-optical Kerr effect (MOKE) is extensively used to study domain wall motion [40, 41]. This usually involves a significant amount of image processing and data analysis. Recently, the propagation of magnetic DWs in a 400Å permalloy magnetic wire was investigated by employing the giant magnetoresistance (GMR) effect [35]. The observed GMR jumps in these experiments are of order 1Ω. This method enables a new approach for probing magnetic domain walls at ultra-low temperature with extremely small levels of excitation. This opens new experimental possibilities such as observing macroscopic quantum tunneling of magnetization. Direct exchange interaction with additional ferromagnetic layers and the stray field of these layers might limit its application.

In the study of single DW dynamics, there have been a number of efforts to reduce the dimensions of magnets to achieve a magnetically uniform media, free of size or shape distribution. Due to the extremely high quality of GaMnAs epitaxial thin films, most especially that their magnetocrystalline anisotropies are well defined throughout the entire sample, single domain behavior occurs on a *macroscopic* scale in these films. This enables fundamental studies in magnetism and new exciting properties to be manifested in fairly large devices. (0.1-1mm).

In microjunctions patterned from epitaxial GaMnAs layers, we have observed and characterized enormous planar Hall resistance jumps on the order of 100 Ω at liquid helium temperature. This "planar Hall effect" is four orders of magnitude larger than previously observed in mesoscopic metallic ferromagnets, two orders of magnitude larger than the GMR signal size in [35]. Here we use this enormous planar Hall effect to allow detection of local magnetization switching with extremely high sensitivity—sensitivity that rivals that of SQUID-based techniques [42].

5.1.2. Review of Experimental Techniques of Ferromagnetodynamics

Ferromagnetodynamics studies the magnetization change in both space and time. In this section, we shall briefly first review early experimental techniques employed ever since the beginning of last century and then outline the state-of-the-art development on the subject from the experimentalists' point of view.

Experimentally, the subject really began just after 1930, when the idea of ferromagnetic domains was very new and very little was known about the way in which the magnetization could change with time. The title of a long paper appeared in 1906 by Lyle and Baldwin [43] – "Experimental on the propagation of longitudinal waves of magnetic flux along iron wires and rods" – tells us a great deal about the early attitude towards ferromagnetism. In those days, ferromagnets were considered to be homogeneous media. Lyle and Baldwin made experiments in which they excited the center of a long iron wire by means of a coil wound around it. They then explored what was happening along the length of the wire with a search coil and came to the conclusion stated in their article's title.

The concept of magnetic domains was first introduced by Pierre Weiss [44] in his famous paper on the molecular field theory of ferromagnetism, but it was not taken up by experimentalists until Barkhausen showed that the magnetization could change in a very discontinuous way (Barkhausen effect). The first "Bitter pattern" observation of magnetic domains was published by Francis Bitter in 1931.

Landau and Lifshitz ([45], 1935) introduced the idea that the magnetization could change by a movement of the boundary between domains, and that domain magnetized in the direction of the applied field would expand at the expense of the domains magnetized against the applied field. However, it was experiments performed by Sixtus and Tonks [46, 47] that were leading those theorists and made it a popular theory that was cited by generations of scientists.

(a) The Experiments of Sixtus and Tonks. The apparatus of classical experiments by Sixtus and Tonks is shown in Fig. 5.1. It was centered around a nickel-iron alloy wire that was in tension. The magnetization was first saturated by applying a large bias field using the bias field coil. Then the bias field was reduced to zero and reversed to a field just below the coercive field of the wire. Magnetic reversal of the wire was achieved in a controlled way by passing a pulse current through the nucleation field coil to initiate a seed domain in this region of the wire. The nucleated reversed domain was then driven by the bias field, and the propagation of one end of the expanding domain along the wire could be observed by means of the voltage pulses induced in the two pick-up coils shown in Fig. 5.1. By measuring the time difference between the two pulses, for various spacings and positions of the two coils, it was possible to work out the velocity of propagation of the domain boundary.

Sixtus and Tonks discovered that the velocity along the wire was linear to the applied field. They suggested that the eddy current loss induced by moving magnetic boundary would give rise

to a viscous damping term, linear in velocity. In order to compare their experimental results with theory, Sixtus and Tonks also supposed that the boundary was cone-like, as shown in the inset in Fig. 5.1. The cone occupies a length many times its diameter. O'Handley used this technique to study domain wall kinetics in ferromagnetic glass $Fe_{96}P_{12}C_7Cr_{4.5}B_{0.5}$ and found that the length of the cone was almost constant, independent of velocity and position, at 25mm, more than 200 times the diameter of the wire.

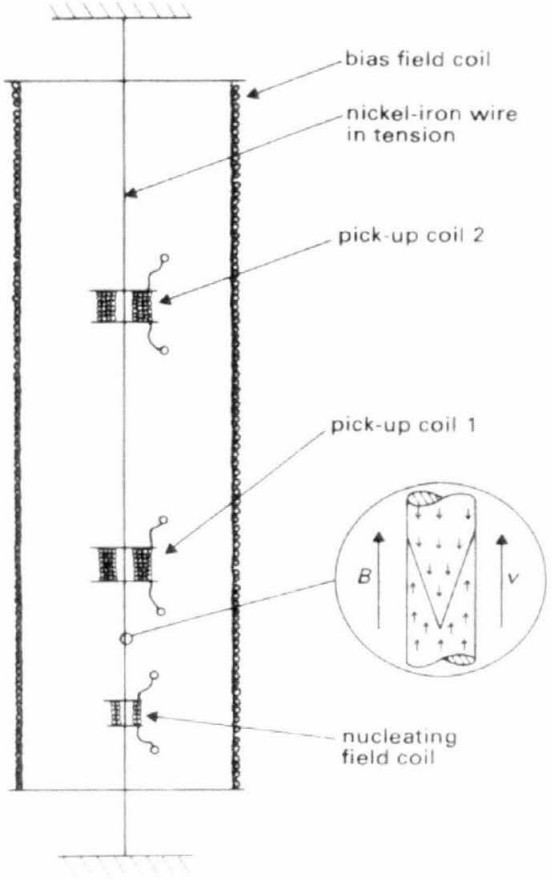

Fig. 5.1 Apparatus used by Sixtus and Tonks (1931). The magnetization of a nickel-iron wire reverses by the propagation of a domain boundary of the kind shown (inset).

(b) The Use of Optical Techniques. The induction methods we described above were clearly open to some ambiguity and there was urgent need for a more direct technique for emerging attempts to make high-speed memories and storage media ever since 1956. The first high-speed photographs of ferromagnetodynamics were taken at Caltech by Conger and Moore (1963) of the magnetic reversal process in a 0.1 μm thick film. A thin layer of ZnS with color contrast Kerr effect was deposited on the surface of the magnetic film. In 1969-1970, also at Caltech, Humphrey group pushed high-speed ferromagnetodynamics to a time resolution of 10 ns, which laid the foundation for subsequent intensive studies on magnetic bubbles.

In today's magneto-optical microscopy, spatial resolution down to 150 nm can be obtained with ultrahigh time resolution. An example of the experimental sample environment is given in Fig. 5.2. The magnetic domain structure is visualized by means of a magneto-optic microscope equipped with a CCD camera. The images are subsequently digitized and improved by image processing. In the DW velocity measurements, a short negative magnetic pulse field is applied in the little coil to initiate a few nucleation centers in a remanent saturated magnetization state. Immediately after recording the nucleated domains, a longer drive field is applied for a duration t and a second image is recorded. From the comparison between these two images, the average DW velocity is deduced.

(c) Magnetoresistance Method. Electrical and transport measurements are promising methods for investigating fast magnetization reversal dynamics. Very recently, fast domain wall

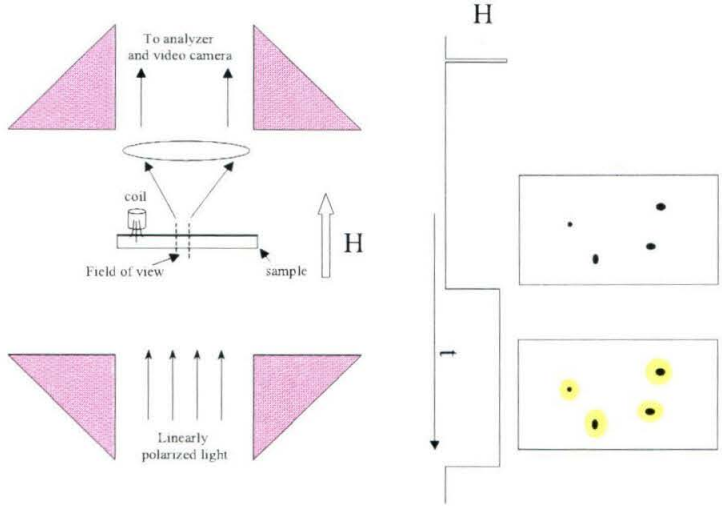

Fig. 5.2 Left: experimental sketch for typical magneto-optical microscopy. Right: procedure to obtain the domain velocity.

motion in a submicrometer magnetic wire has been detected by use of the giant magnetoresistance effect. The experiment is based on a non-coupled-type GMR multilayers composing NiFe(200Å) /Cu(100Å)/NiFe(50Å). The GMR change is directly proportional to **M** in one of the ferromagnetic layers. After sitting the external field close to the coercive field of the top FM layer, the resistance change is monitored as shown in Fig. 5.3b. The velocity is calculated as a ratio between the wire length and reversal time.

This experimental method is complementary to the prevailing magneto-optic microscopy in that it can be applied to extreme situation such as ultralow temperature or ultrasmall volume where the sensitivity of MOKE is limited or undesirable. However, we would like to point out that the information the GMR two terminal wires offered is ambiguous: The total magnetization change measured does not unequivocally reflect a domain wall expansion. The effect of the other FM layer on the magnetization of focus layer is unpredictable. Above all the resistance change is less than 1% on top of a significant two terminal resistance background.

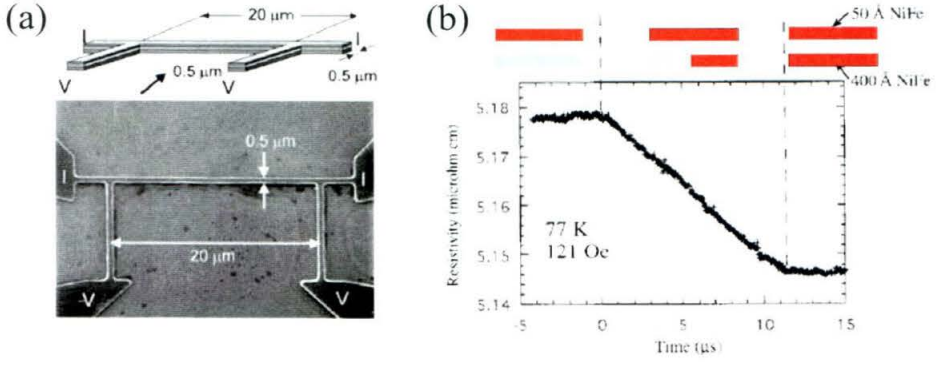

Fig. 5.3 (a) SEM image and schematic illustration of the sample. The sample consists of a NiFe(200Å)/Cu(100Å)/NiFe(50Å) trilayer. (b) Time variation of the resistance during the M reversal of the 400-Å NiFe layer at 77 K.

5.1.3. Time of Flight Measurement Using PHE Setup

The giant PHE in (Ga,Mn)As enables us to study the domain wall motion in our lithographic wires. Samples for these experiments are the same group of samples used in the planar Hall resistance measurements (and normal Hall measurements). A sketch of our measurement setup and a SEM image of a typical sample are presented in Fig. 5.4b. Three pairs of voltage probes with 100 μm separation were patterned. To avoid introducing geometrical pinning of domain walls [36], the size of the voltage probes are minimized with respect to the fixed Hall bar width of 100 μm. In all measurements, a constant dc current (10 μA) supplied by a floating battery supply is driven through the Hall bar. Induced Hall voltages are picked up by triaxial cables and led to three electrically isolated room temperature differential amplifiers (1 MHz Amplifer). A

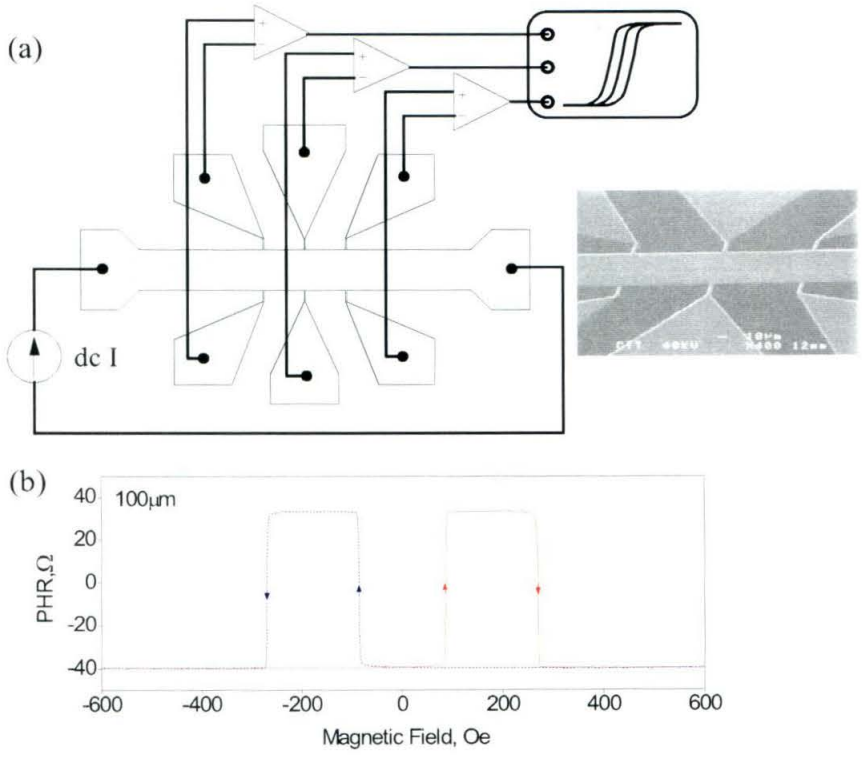

Fig. 5.4 (a) Measurement setup. After a domain wall is nucleated at one side of the sample, it propagates sequentially across three Hall bars and successively generates gigantic planar Hall voltages. High input impedance differential amplifiers are used to make true potential measurements. (b) A typical planar Hall resistance (R) *vs* magnetic field (H) loop for a 100 μm wide Hall bar.

multichannel Agilent digital oscilloscope is used to acquire time records of the generated voltage waveforms. Dc signal coupling is used both at the input of the amplifiers and at the input of the oscilloscope. The temperature of the samples is regulated from 0.3 K to 45 K. The same set of magnets is used to generate a magnetic field that is rotatable in any direction of 3-D space.

(Ga,Mn)As films are magnetized in plane due to a combination of compressive lattice-mismatch-induced strain and demagnetization effects. A representative $R - H$ full loop with a field ramping rate at 10 Oe/s along 15° is shown in Fig. 5.4b (obtained at 5K). The first jump corresponds to a magnetization transition from $[0\bar{1}0]$ to [100]. The second jump completes the reversal by switching from [100] to [010]. In (Ga,Mn)As, except for those directions exactly on the overall easy axes, the magnetization transitions evolve via the formation of a 90°-domain wall. In this chapter, we concentrate on the time-domain study of the first jump, which occurs with a high degree of sharpness, at a low switching field, and involves initial and final states that are very close to zero field equilibria. To our knowledge, domain wall dynamics associated with a 90° magnetization switching have never been investigated before.

Prior to each sweep, a strong negative in-plane field is supplied to saturate the magnetization in a selected direction. Then a positive constant field is established in close proximity to the first coercive field to launch the nucleation of domain wall and to drive the DW propagation across the sample. Domain walls are always injected from the wide current contact pad into the wire [48]. With this protocol, completely reproducible signals are detected, regardless of the magnetic history of the sample.

5.1.4. Longitudinal Time of Flight Measurement

Fig. 5.5 shows a series of time dependence of planar Hall measurements at 5 K with driving constant fields varying from 74 Oe to 88 Oe. The measured voltages are normalized to the sense current to yield an effective "resistance" response. The successive, sequential in the voltage-time records in the oscilloscope's three channels correspond to a single domain wall passing through the individual Hall probes. At a given field, the three rises have identical magnitude and rise time. It is found that domain wall propagation between adjacent pairs of voltage probes evolves equal time intervals as expected, given their constant spacing of 100 μm. Normalization of all the switching curves in the abscissa axis by the half switching time yields a universal curve irrespective of the magnetic field strength and Hall probe position. Furthermore, during the switching process, the resistance varies almost linearly with time, which is evident both at fast

domain wall motion limit (88 Oe) and slow domain wall motion limit (74 Oe). All this behavior appears consistent with the picture that the domain wall propagates across the Hall bar while retaining a constant shape. Therefore, a well-defined domain wall velocity can be computed by measuring the time-of-flight between Hall probes.

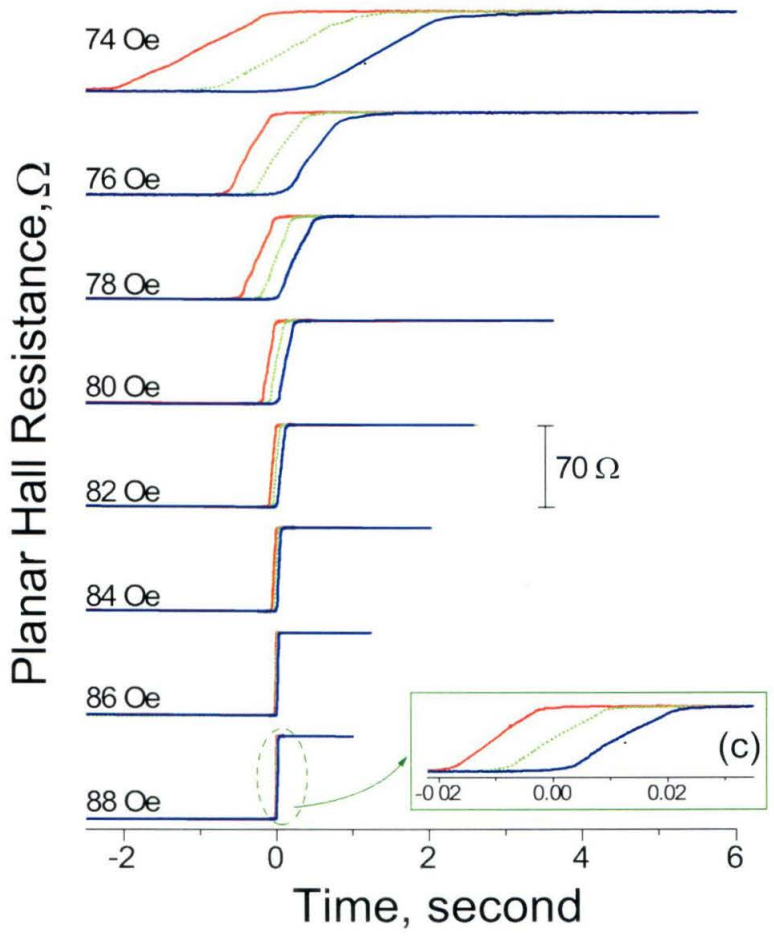

Fig. 5.5 (a) Planar Hall responses at three Hall crosses with in-plane field decreases from 88 Oe to 74 Oe. Inset: A magnified view demonstrates the fast dynamics that occurs at 88 Oe.

In the classical experiment by Sixtus and Tonks, two search coils (0.65 cm) were used to pick up the magnetic pulse generated by DW transport in a bulk NiFe wire (65.5 cm long). Here an integrated DW dynamics measurement has been realized in a single chip. By measuring time of passage of single DW through a set of probes, the DW orientation with respect to Hall bar can be estimated. During the switching process, the resistance varies almost linearly with time, which is evident both at fast domain wall motion limit (88 Oe) and slow domain wall motion limit (74 Oe).

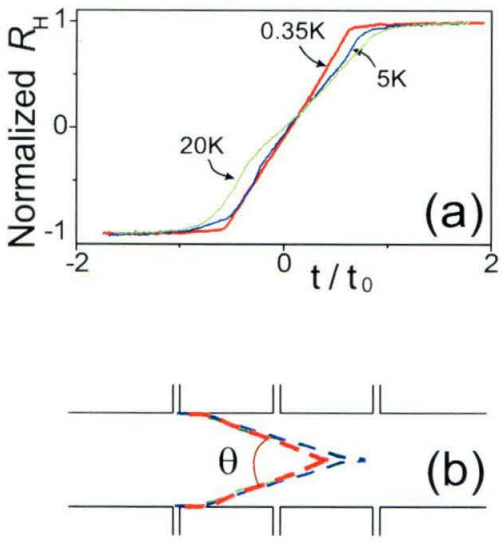

Fig. 5.6 (a) A comparison of resistance switching curves for T = 0.35K, 5K, and 20K. (b) Estimated domain wall profile corresponding to (a).

At the temperature range above helium temperatures, extended tails do exist at the beginning and the closing stages of the reversal. On further increasing temperature, domain wall becomes frustrated and kink structure start to develop. However, those tails are not present at the lowest measured temperature (0.35K) and the switching curves become extremely linear, as exemplified in Fig. 5.6a (The horizontal axis value is normalized to time-of-flight between adjacent probes, whereas the vertical resistance is normalized to unity). Based on the calibration from the measured time-of-flight of single DW through a set of probes, the DW profile in the Hall bar can be estimated. For $T = 0.35$ K, the ratio of passage time and propagation time between neighboring Hall crosses is typically 1.4 ± 0.2. Assuming the domain walls take a V shape,[46] this gives a DW angle of $20° \pm 2°$ with respect to Hall bar direction ([110] crystalline direction), hence the cone angle is $40° \pm 4°$. (Fig. 5.6b) At elevated temperature ($4\,\mathrm{K} < T < 25\,\mathrm{K}$), except for possible existence of prolonged tails, the overall domain wall shape does not change a lot. The Fig. 5.6b illustrates the instantaneous configuration of such a domain wall in the Hall bar. For comparison, domain wall shape at elevated temperature ($T > 4$K) is also drawn.

We note that GMR method employed in [35] essentially measures a two-terminal resistance change of a magnetic wire. These results reflect the volume expansion of spin-reversed region. The domain wall ("wave-front") profile we exhibit here is not accessible by such a technique.

Here, by employing separate local probes, not only is a large background subtracted, but the evolution of DW can be monitored in real time. The extraordinary Hall effect was used to study domain wall dynamics in micron-scale cross-junctions patterned from Co films [36]. The resistance change in this case is in the range from 0.01Ω to 0.1Ω, and AC lock-in measurements are required to improve sensitivity. This restricts experimentation solely to very slow dynamics, on the orders of seconds.

5.1.5. Domain Wall Dynamics

At temperature below 25 K, we observe steady domain wall propagation through the sample. Fig. 5.7 presents the measured dependence of DW velocity on applied field strength, for temperature at 5 K, 10 K, and 20 K, respectively, representing a span of four decades of domain wall velocity. The upper speed limit originates from the finite time required for the magnet coil to establish a high field, *i.e.*, the finite ramp rate of the magnet. A pulsed magnetic field would

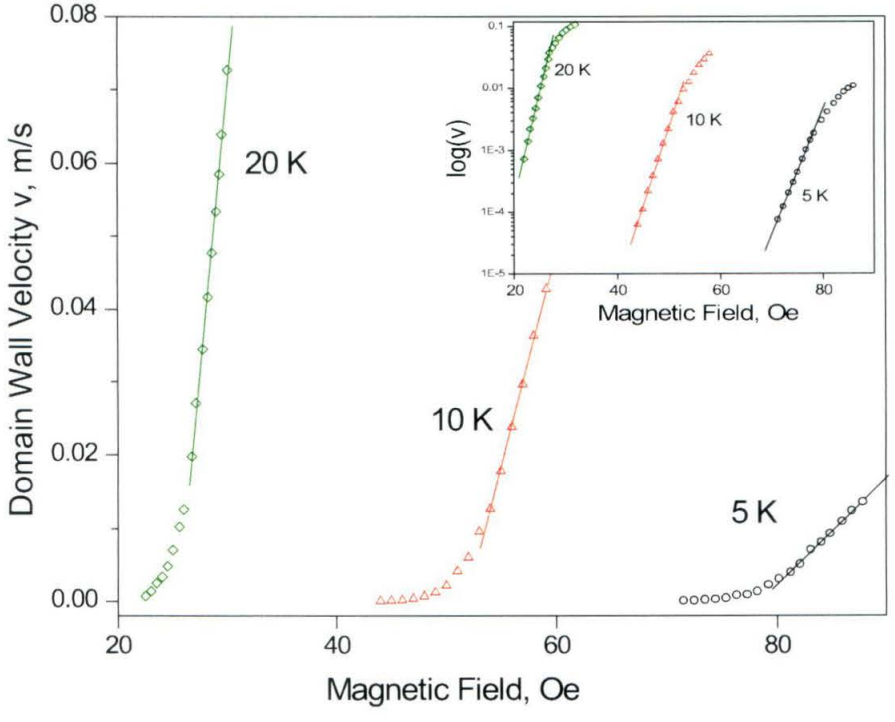

Fig. 5.7 Domain wall velocity as a function of magnetic field at 5 K, 10 K, and 20 K shown in linear and semilog formats (inset). The external field orientation is 15° away from [110]. In the normal plot, the solid lines represent fits to the high field velocities. In the semilog plot, the solid lines are linear fits to the low field region.

enable us to access much faster domain dynamics. The ultimate limits of our dynamic electrical measurement are imposed by the parasitic electrical coupling, bandwidth of amplifier, and the time resolution of oscilloscope. The lowest measurable domain wall speed is unlimited if one waits long enough for the triggering signal, which arrives after large waiting times for nucleation and subsequent expansion of large domains.

The overall v-H curves are highly nonlinear. Depending on the magnitude of the magnetic field, the $v(H)$ variation can be divided into two regimes. For driving field H larger than a threshold H_0, (which is related to the coercive field H_c), the influence of disorder-induced pining can be ignored. In this case, as expected, a linear $v \sim H$ relation is obtained that is characteristic of viscous flow of domain walls. The wall velocity can be expressed as

$$v = \mu(H - H_0) \tag{5.1}$$

with μ is the domain wall mobility. This mobility varies strongly with temperature, increasing from 1.4 mm/s·Oe at 5 K to about 14 mm/s·Oe at 20 K. The linear regime also expands when temperature is raised. Our results are summarized in Table. I.

The temperature dependence of the DW mobility is of importance because it can give information about the source of spin damping in the magnetic system. Two types of processes govern the mobility of domain walls in ferromagnets: (i) Interactions of DWs with local obstacles present in the specimen, e.g., with dislocations or small particles of a second phase. Often these obstacles are referred to as pinning centers. (ii) Nonlocal dissipative processes, e.g., eddy current damping. The eddy current damping has a limiting mobility $\mu = g\rho/(\mu_0 M_s d)$.[49] Here ρ is the resistivity, M_s is magnetization, g is a geometrical factor and d is the film thickness. The high resistivity of (Ga,Mn)As yields an extremely small value for this kind of damping. When the temperature is relatively high and the damping is purely of magnetic origin, the relation $\mu \propto T^{-2}$ (four-magnon interaction, see, e.g., Ref.[50]) holds in single crystals of high quality. However, our experimental result does not follow this prediction.

Table 5.1. Characteristic parameters determined for MnGaAs in two field regimes.

Temperature (K)	Mobility (mm/s·Oe)	α (Oe^{-1})	V_N (μm^3)
5	1.39	0.185	6.0×10^{-6}
10	6.11	0.260	18.6×10^{-6}
20	14.2	0.342	52.2×10^{-6}

On reducing the magnetic field well below H_0, domain wall velocity in our system decays dramatically. Similar behavior has been reported in Co films [41], where a domain-wall glass state was assumed to sustain a low field domain creep rate $v \propto \exp[-(U_p / kT)(H_0 / H)^{1/4}]$. Here U_p is the collective pinning energy and is relevant for describing vortex dynamics in scalable random media [51]. Here, we find that our data are better fitted by a direct thermally activated depinning formula [52],

$$v = v_0 \exp[(\mathbf{H} \cdot \Delta\mathbf{M} V_N - E_p)/k_B T] = v_0 \exp[\alpha(H \cos\varphi_H - H_0)], \qquad (5.2)$$

where E_p is the activation energy for DW propagation, V_N is the activation volume. $\Delta\mathbf{M} = \mathbf{M}_2 - \mathbf{M}_1$ with $\mathbf{M}_1$ is the initial magnetization (close to $[0\bar{1}0]$) and $\mathbf{M}_2$ the magnetization after switching (close to [100]). φ_H is the magnetic field orientation and $\alpha = M_S V_B / k_B T$, with M_S representing the saturated magnetization of (Ga,Mn)As. From the low-field slopes of our semi-logarithmic curves (Fig. 5.7, inset) we can estimate the activation volumes for different temperatures (Table I). A typical value of activation volume is $10^{-5}\mu m^3$, which is equivalent to a film area of about 150 nm^2. The domain wall thickness is about 10 nm. Considering the high quality of the epitaxial sample and the stability of time resolved signal, such a size of pinning site could only exist continuously on the wire edge, where both the exchange interaction and magnetic anisotropy are drastically reduced from that of a continuous film.

By investigating the v - H curves along various sweep angles, we have further confirmed the validity of Eq. (5.1). Fig. 4 is the measured dependence of DW velocity on applied field swept along 5°, 15°, 22°, and 30° orientations. After scaling the magnetic field by $\cos\varphi_H$, all curves fall onto one universal curve. This suggests that only the field component along [110] direction is

effective in driving the domain wall. At temperature higher than 25 K, domain wall nucleation dominates the magnetization reversal process. In this case, our time of flight method cannot consistently provide direct information on the domain wall velocity.

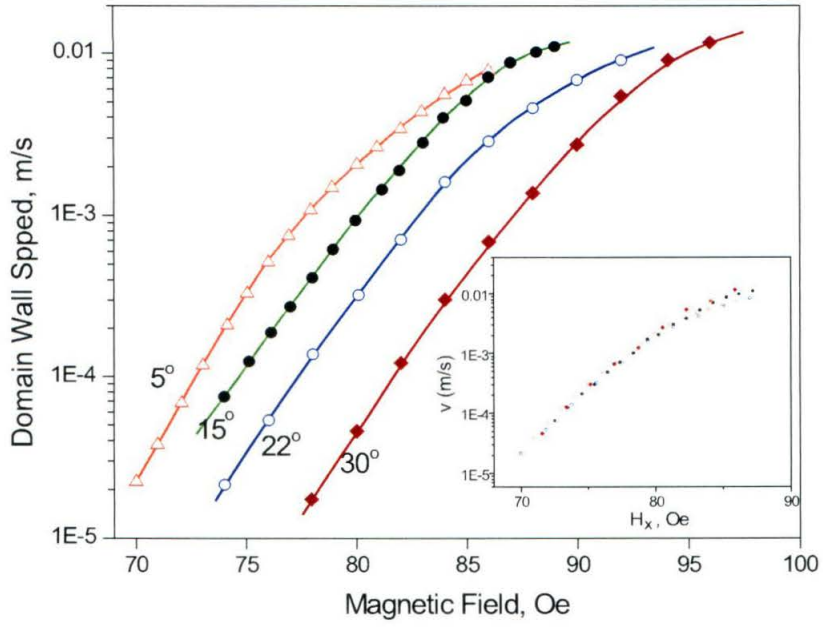

Fig. 5.8 Domain wall velocity *vs.* magnetic field orientation. Angles are measured with respect to [110]. Inset: Domain wall velocity *vs.* rescaled field (the component along [110]). Data points of different angles condense onto a single universal curve.

5.1.6. Manipulation of Single Magnetic Domain Wall

In the previous sections, we have shown that the domain wall motion rate is controllable – in a range of four orders of magnitude by supplying external magnetic fields of different strengths. This offers an excellent opportunity to manipulate a domain wall in real time. After the nucleation of a domain wall, we drive it very slowly across the Hall bar and watch the planar Hall voltage from the center pair of Hall probes. By removing the external field as soon as this voltage hits zero, we can freeze this specific domain wall between these two probes. The domain wall remains

stationary ever since. An example of such an operation is illustrated in Fig. 5.9. We did not found domain wall overshooting in the planar Hall measurement, indicating a quick magnetization damping on the time scale shorter than the field removal time. We kept recording the planar Hall signals from the three pair of probes, as shown in the figure, for next three days. No change was detected in either channel. This domain wall remained inactive as long as the temperature is regulated lower than 25K. The motion can be resumed by applying a suitable magnetic field and leads the reversal of the entire sample.

Our ability to trap a single magnetic domain wall enables us to study some other properties associated with a stationary domain wall, such as domain wall resonance and macroscopic quantum tunneling of domain walls. Relevant experiments are in progress.

5.1.7. Summary

In conclusion, we have performed the first measurements of single domain wall propagation through patterned (Ga,Mn)As conductors possessing in-plane magnetization. The dependence of DW velocity on applied field is characteristic of thermally assisted domain wall motion. By employing the enormous planar Hall effect that we have shown is intrinsic to the dilute ferromagnetic semiconductor (Ga,Mn)As, the profile and propagation of 90° single magnetic domain walls in a 100μm wide wire are clearly recorded in real time voltage wave form. Domain

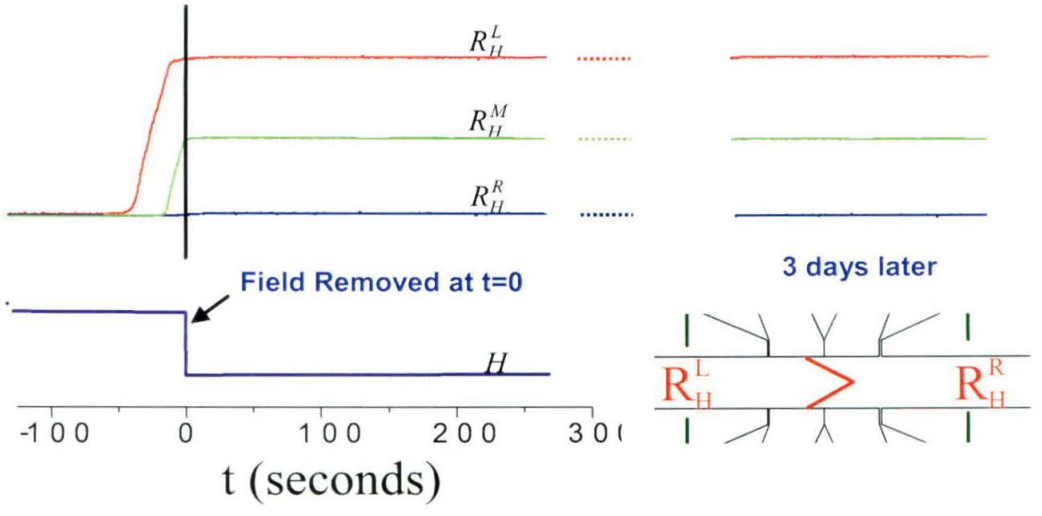

Fig. 5.9 Freezing of a single domain wall. The domain wall is driven at a slow speed and the planar Hall resistance of the central probes is monitored to reflect the passage of the domain wall. The crossing-zero of this signal triggers the removal of external magnetic field. The domain wall is found to be stationary ever since.

wall (DW) velocities are determined from time-of-flight between multiple electrical probes fabricated on the sample. Measurements as a function of magnetic field strength, field orientation, and temperature allow us to estimate magnetic parameters of (Ga,Mn)As and elucidate the physical mechanism driving DW propagation motion. For fields well below the coercivity threshold, a thermally assisted magnetization switching theory can be applied to interpret all the data. Our results exhibit a new, simple and precise method to investigate thin film domain dynamics. Our technique can be applied to temperature down in the millikelvin range, where thermal fluctuations cannot overcome anisotropy barrier and macroscopic quantum tunneling (MQT) of domains should set in.

5.2. Resistance of Individual Domain Walls

5.2.1. Motivation to Study Single Domain Resistance

Even though small and difficult to measure, domain wall resistance has become popular due to the challenge it poses on both experimental and theoretical investigations on the spin coupled electron transport across the domain wall. Considering that the wall width is much greater than the Fermi wavelength, early theoretical studies [53-55] described *adiabatic* electron transfer across the wall and predicted that that the domain walls have negligible effect on the resistance of 3d ferromagnets. A possible disturb of the current distribution due to Hall effect of adjacent domain magnetizations was also pointed out. In earlier experimental approaches, domain wall resistances are inferred indirectly by measuring the excess resistance when large ensemble of domain walls are nucleated in the samples. [56-58] Recent progress in domain imaging and nanofabrication allows resistance measurement of pre-imaged nanoscale wires with significant reduced number of domain walls.[59-62] Experimental results are quite conflicting. Both positive and negative domain wall resistance have been reported. Theoretical justifications of either positive and/or negative domain wall resistance also exist.[63-65] The major difficulty associated with these experiments involves non-intrinsic contribution to the magnetoresistance either in an uncontrolled remnant domain pattern or in geometrical constrained domain walls (where both the domain wall and current density configurations can be largely modified). Unambiguous qualification of individual domain wall is highly demanded. In this work, we successfully drive and isolate a single domain wall in (Ga,Mn)As single crystal epilayers. The resistance across the wall is measured locally. Since only one single domain wall is involved in an everywhere uniform crystalline structure, the magnetoresistance (MR) of domains and DWR are properly separated.

5.2.2. Single Domain Wall Resistance of Epitaxial (Ga,Mn)As Films

Our ability to identify a single domain wall's presence between voltage probes allows us to make direct electrical resistivity characterization of individual single domain walls. This is achieved quasistatically. The driving field is adjusted to let the domain wall propagate across the sample at very slow speed (typically 100 s from probe to probe). A constant dc sensing current is driven between contact 1 and 5. Longitudinal resistances of top side and bottom side of the Hall bar ($R_{xx}^{U} = R_{15,24}$, $R_{H}^{D} = R_{15,86}$) are measured simultaneously. Meanwhile the Hall resistances of left and right probes ($R_{H}^{L} = R_{15,28}$, $R_{H}^{R} = R_{15,46}$) are also recorded to monitor the entrance and exit of the DW. The analog outputs from the differential amplifers are digitized by the same multi-channel oscilloscope. (Balance circuits are required for longitudinal resistance measurement to suppress digitization noise).

Experimental results at 5K are discussed first. Fig. 5.10b shows the longitudinal resistance change in the event a single domain wall is trapped in the conduction channel (reflected by PHR changes in Fig. 5.10a). In R_{xx}^{U} trace, a resistance enhancement as large as 30 Ohms is recorded, corresponding to about 0.6% of the total resistance. However, we should not literally regard it as intrinsic domain wall contribution to the resistance. Evidently, the resistance measured from the bottom side exhibits decreased resistivity. Because the presence of domain wall between probes, planar Hall resistance mixes into the measured longitudinal resistance and contributes most of the excess resistance with a sign dependent on the wall propagation direction. In fact, a potential sum rule holds: the difference between R_{xx}^{U} and R_{xx}^{D} equals that between PHE resistances R_{H}^{R} and R_{xx}^{L}. This is illustrated in Fig. 5.10c. To accurately describe the domain wall resistance, local current distribution has to be numerically simulated and its modification of resistance should be subtracted from the measured MR. This scheme is not practical since the exact shape of domain wall is unknown. Instead, we take the average of the measured longitudinal resistances, $\delta R_{xx} = R_{xx}^{U} + R_{xx}^{D}$, as if a single big contacts capable of electrical potential averaging were used on each side of the sample. The result is displayed in Fig. 5.10d. In the regions that DW enters or leaves the probes, the non-uniform current distribution still has significant effect, on the order of 0.2% of the resistance background. The non-uniform current distribution can be decomposed into a uniform current and a d.c. eddy current loop localized on the domain wall. When the whole piece of DW is enclosed between probes, δR_{xx} would reflect resistivity contribution from a

single DW. The linear part in the center of Fig. 5.10d indicates a linear resistance change domain wall propagates in the channel. Except for a small negative offset, this is consistent with an interpolation of asymptotic resistance values of initial and final states. This offset, corresponding to 0.44Ω, is within our resistance measurement sensitivity, which is about 1 part in 10,000 or 0.5 Ω. Similar conclusion can also be made at lower temperatures, for example at 0.35K shown in Fig. 5.10e, where the contribution of eddy current is largely suppressed. In contrast, for temperature higher than 10K, frustrated domain wall enhances eddy current and it is very hard to isolate the linear resistance part. We conclude that, when properly separated from MR of domains, single domain walls in (Ga,Mn)As epilayer do not supposedly yield high resistivity. If present, the value should be less than 0.01% of the bulk resistance of (Ga,Mn)As. Our results suggest that local spin modulation does not cause additional correction to electrical resistance. The proposal of utilizing single domain wall separated region as spin-diode requires revision. [66].

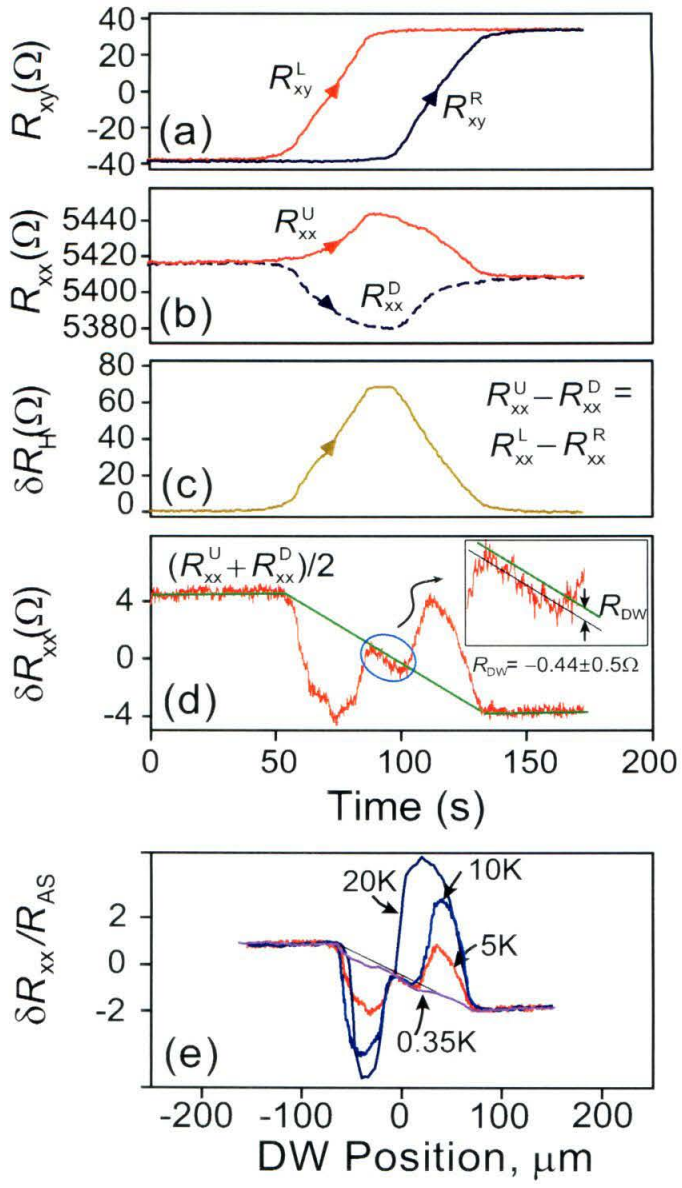

Fig. 5.10 Time-resolved magnetoresistance measured across a single domain wall at 5K. (a) PHR of two pairs of Hall probes monitoring the entrance and exit of a single domain wall. (b) Longitudinal resistances across the wall are measured simultaneously from top and bottom of the Hall bar. (c) Resistance sum rule is satisfied: difference between Hall resistances equals to the difference between longitudinal resistances $R^U_{xx}-R^D_{xx}$. (d) The variance of the average between R^U_{xx} and R^D_{xx} suitably separates major part of domain magnetoresistance and reflects excess domain wall resistance when the domain wall is completely resident between probes. (e) Temperature dependence of the overall ressitance variance.

Part II: Suspended Two-Dimensional Electron Gas

Chapter 6. Freely-Suspended Two-Dimensional Electron Gases: Realization and Applications.

6.1. Introduction

Recent developments in Nanoelectromechanical systems (NEMS) allow chip-based fabrication of motional devices that are scaled down from the realm of microelectromechanical systems (MEMS). The high resonant frequencies of NEMS in vacuum offer unique advantages, e.g. they open new possibilities to attain efficient electromechanical filters and resonators. On the other hand, suspended, thermally isolated devices also offer prospects for very sensitive bolometers and represent model systems for high sensitivity calorimetry [67].

Compared to MEMS, motion transduction in NEMS presents a significant engineering challenge. Traditional methods in MEMS, such as electrostatic transduction and optical interferometry, cannot be scaled down to provide the necessary sensitivity. This gives rise to the need for novel, fully-integratible sensors and actuators for NEMS. Below, we describe our work with micromachined GaAs heterostructures. These are able to provide an enhanced piezoresistive signal [68-70] meanwhile providing a direct FET-like readout that employs gate electrodes.

In our approach, a two-dimensional electron gas, known for its high mobility at low temperature, is incorporated in the freely-suspended nanostructures. In-plane isolated gates are fabricated to provide actuation. These imply potential benefits comparing with conventional approaches with metallic or silicon materials systems: 1) Both actuation and transduction can be

achieved on the chip by electrical methods, suitable for the requirement of integration of mechanical systems. 2) GaAs/AlGaAs high mobility devices can operate at high speeds (>250 GHz) that are far above the highest attainable resonant frequencies in NEMS (~3GHz). 3) Due to their high mobility, GaAs/AlGaAs HEMTs are known for producing the lowest noise, which is essential for an imbedded system that has a lot of parasitic factors affecting the observed signal.

In addition to offer new scheme of detecting motion in NEMS, this system establishes a novel mesoscopic system where both electrons and phonons are confined, and their interactions provide new physical phenomena, such as resonant phonon emissions and adsorptions in free standing quantum dot or coupled dots.

In the remaining sections of this introductory chapter, we first discuss the design of heterostructure for the purpose of construction of suspended high mobility 2DEG. The mechanical characteristics and responses of suspended beams and mechanical-electrical properties of GaAs are described next. Section 3 of this chapter presents our motivations to study electron-phonon coupling in suspended wires and quantum dots. This chapter ends with a summary of the processing techniques of suspended 2DEGs.

Chapter 7 demonstrates our successful realization of suspended quantum wires and suspended quantum dots. The mesoscopic transport phenomena in ballistic Hall bars are explored and employed to characterize the 2DEG electrical properties such as electron densities, mobilities and depletion depths. The observation of Columb blockade and single electron charge effect in suspended quantum dots are reported in the final part of this chapter.

Chapter 8 describes the implementation of suspended 2DEG beam as self-sensing displacement detector. The chapter begins with the description of the static mechanical-electrical response of doubly clamped 2DEG beams by AFM manipulation methods. The chapter next discusses the measurement of mechanical resonance from doubly clamped beams. The resonant frequencies are around 10 MHz and correspond to an out-of-plane fundamental vibration mode. The beams are driven electrically by rf voltage applied on the in-plane side gates. The drive mechanism is attributed to a novel dipole-dipole interaction. The deflection readout is achieved by measuring the electrical potential drop across the 2DEG with constant d.c. sensing current. Combined piezoelectric and piezoresistive mechanisms can be employed to interpret the observed mechanical-electrical resonance signal.

6.2. Materials

The wafer material was a specially designed MBE-grown 2DEG heterostructure. The structural layer stack comprises seven individual layers having a total thickness of 115 nm (Fig. 6.1). The top and bottom are formed by thin GaAs cap layers preventing oxidation of the AlGaAs:Si donor layers that follow beneath. The central 10 nm thick GaAs layer forms a quantum well sustaining a high mobility 2DEG located 37 nm below the top surface and surrounded by two AlGaAs spacer layers. Below the structural layer stack is a 400 nm $Al_{0.8}Ga_{0.2}As$ sacrificial layer. Note that the stack structure was intentionally made asymmetric to avoid neutralizing the piezoelectric effect of GaAs.

The calculated band structure is also shown in Fig. 6.1. Different from the ordinary 2DEG heterostructure configurations, here an additional GaAs layer at the bottom is included to avoid carrier depletion from the lower surface once exposed to the vacuum. The calculation indicates that the donor regions are particularly susceptible to illumination, and that parallel conduction might be possible. However, in our measurements no obvious contribution from such channels is evident even after continuous illumination.

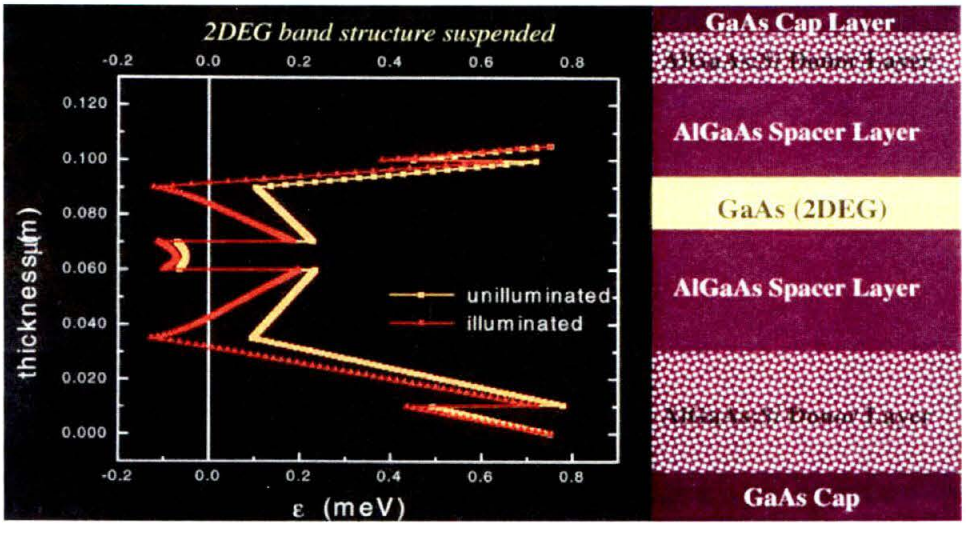

Fig. 6.1 Heterostructure design and calculated band structure of suspended 2DEG.

6.3. Electro-mechanical Background of GaAs

6.3.1. Beam Mechanics Summary

We first present a review of the characteristics of doubly clamped beams to allow a comprehensive of understanding and for the purpose of optimization in GaAs NEMS devices. For a beam with thickness t, width w, and length L, its deflection function $u(x,t)$ obeys the following differential equation, [71]

$$-EI\frac{\partial^4 u(x,t)}{\partial x^4}+\sigma A\frac{\partial^2 u(x,t)}{\partial x^2}=\rho A\frac{\partial^2 u(x,t)}{\partial t^2}, \tag{6.1}$$

where E is Young's modulus of the cantilever material and I is the moment of inertial of the beam cross section. $A=wt$ is the cross-sectional area, σ is internal stress and ρ mass density. Solving this equation using conditions of fixed boundaries gives an expression for the resonance frequency of the beam. The lowest mode will vibrate at a frequency,

$$f_0=1.03\frac{a}{L^2}\sqrt{\frac{E}{\rho}(1+\frac{12L^2\sigma}{4\pi^2Ea^2})} \tag{6.2}$$

For GaAs the mass density is $\rho=5315\ \mathrm{kg/m^3}$ and for beams with length along the [110] direction $E=1.2\times10^{11}\ \mathrm{N/m^2}$ [72]. Thus in the absence of internal stress for GaAs beams with rectangular cross sections f_0 can be written as

$$f_0=4890\frac{t}{L^2}\ \mathrm{Hz} \tag{6.3}$$

with t and L in meters. This frequency is independent of the cantilever width due to the linear dependence on width of both the spring constant and mass.

In order to sense the deflection of the beam, we would like to know the strain produced by a given force, generally a uniform force. A static deflection produced by a uniform force results in a uniaxial strain field in the beam,

$$\varepsilon(x,z)=z\frac{\partial^2 u(x,z)}{\partial x^2}=z\frac{F_0}{12EI}(6x^2-6Lx+L^2), \tag{6.4}$$

where x is the distance from the beam base and z is the distance from the center of the beam in the plane of the bending. The maximum strain occurs at the center of both ends of the beam, with

$$\varepsilon_{\max} = \frac{F_0 L}{2Ewt^2} = \frac{16t}{L^2} u(L/2) \tag{6.5}$$

is the maximum strain produced by a force F_0 corresponding to a deflection of the center of the beam of $u(L/2)$. Dynamic response of the beam at frequency f is given by its complex force-to-deflection transfer function,

$$h(f) = \frac{f_0^2 / k}{(f_0^2 - f^2) + i(ff_0 / Q)}, \tag{6.6}$$

where f_0 is the resonant frequency and Q is the quality factor of the beam.

6.3.2. Piezoelectric and Piezoresistive Effect of Ga(Al)As

Mechanisms that are responsible for an electronic response to strain in GaAs are the deformation potential and the piezoelectric effect. The former usually gives a resistance change to a strained material, whereas the latter may cause an electrical potential change in addition to resistance change.

The deformation potential is the change in semiconductor band energy in response to a compressed or expanded unit crystal cell. For the conduction band in GaAs this change dE_c is given by [73],

$$dE_c = a(\varepsilon_{xx} + \varepsilon_{yy} + \varepsilon_{zz}). \tag{6.7}$$

Here a is the hydrostatic deformation potential with a value between –7 to –9 eV. This will yield a resistance change in a uniformly material. For 2DEG, the conduction band of the strained region is shifted and electrons will flow into or out this region to balance the chemical potential, effectively producing an electrical potential gradient that might gates the electrons and cause additional resistance change.

Piezoelectric effect is found in crystals lacking a center of inversion symmetry in which a strain or deformation can induce an electronic polarization. GaAs is considered as one of the weaker piezoelectric materials, having piezoelectric constants of similar magnitude to that of

quartz and about 100 times smaller than that found in good piezoelectrics like the ceramic PZT. Nevertheless, comparing to Si based semiconductors that have inversion symmetry, GaAs is a better choice.

The anisotropic nature of crystals complicates the description of piezoelectric properties in the sense that a stress in one direction, whether shear or uniaxial, may cause the polarization in any given direction. Thus, a piezoelectric tensor is required to relate each polarization component to the stress tensor. Phenomenologically, this can be described by

$$P_i = \sum_{k=1}^{3} \varepsilon_{ik} E_k + \sum_{\mu=1}^{6} d_{i\mu} \sigma_\mu \,, \tag{6.8}$$

where P_i is the component of polarization in the $i = (x, y, z)$ direction, ε_{ik} are dielectric constants of the crystal. σ_{jk} represents the components of the stress tensor and $d_{i\mu}$ represents the components of the piezoelectric tensor for GaAs. Two types of piezoelectric effect can be distinguished: (a) The longitudinal effect is expressed by d_{ii}. The charge is generated at the same surfaces on which the stress is applied. (b) For the transverse effect, d_{ij} with $j = 1..3$ and $i \neq j$ are the piezoelectric constants for a charge produced on the surfaces normal to e_i caused by a stress parallel to e_j. If the crystal has the surface A_i and A_j normal to e_i and e_j, respectively, the charge Q_i caused by a force F_j is expressed as $Q_i = \frac{A_i}{A_j} d_{ij} F_j$. Note that the sensitivity of the force can be enhanced by the geometry A_i / A_j. (c) The piezoelectric shear effect is denoted by the piezoelectric constant d_{ij} with j = 3, 4, 5, 6. For (100) oriented $Al_xGa_{1-x}As$, the nonzero piezoelectric constants are $d_{14} = d_{25} = d_{36} = (-2.69 - 1.13x) \times 10^{-12}$ C/N .[74] Since in this orientations only shear effect appears, other orientations of the crystal have to be used for the longitudinal and transverse effect. The piezoelectric matrix $d_{i\mu}$ for (100) orientated material with a rotation around the e_1 axis is, [75]

$$d_{(100)} = d_{14} \begin{pmatrix} 0 & \delta_1 & -\delta_1 & \delta_2 & 0 & 0 \\ 0 & 0 & 0 & 0 & \delta_2 & 2\delta_1 \\ 0 & 0 & 0 & 0 & -2\delta_1 & \delta_2 \end{pmatrix} \tag{6.9}$$

with $\delta_1 = \cos\varphi\sin\varphi$, $\delta_2 = \cos^2\varphi - \sin^2\varphi$. The maximum sensitivity of the transverse effect is achieved with $\varphi = 45^\circ$. The advantage of this configuration is that a stress applied in the e_1 axis is not affected by a possible shear due to a nonideal mounting. Additionally this is easy to

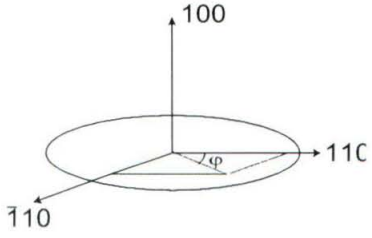

Fig. 6.2 System of coordinates used in (100) oriented GaAs.

reproduce, since its faces are parallel to the natural cleavage planes of GaAs which are the {110} planes. GaAs integrated circuits are usually realized on (100) oriented substrates.

To quantitatively predict the magnitude of the electronic response in a two-dimensional electron gas due to the piezoelectric effect in a deflected beam, we need to know the stress distribution and then derive the bound charge. For beams with symmetric cross section, there exist a neutral line running in the center of the beam where there is zero strain. The volume below (above) this line is compressed (expanded), giving opposite polarization coupled through d_{12} term, as shown in Fig. 6.3. The induced bound charge distribution given by $\rho_b = \hat{n}\cdot\vec{\mathbf{P}}$ at interface and $\rho_b = -\nabla\cdot\vec{\mathbf{P}}$ in the bulk. For a beam consisting of more than one material, such as the heterostructure we used, bound charge induced at every interface. All these charges act on the 2DEG as an effective gate and deplete or increase the 2DEG carrier density.

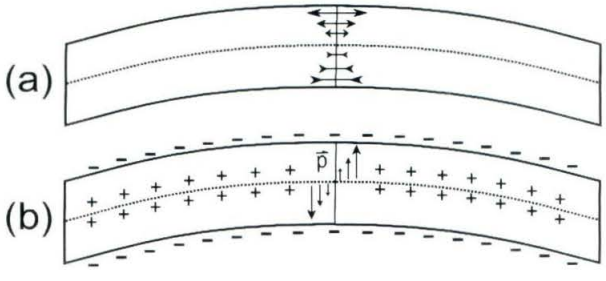

Fig. 6.3 (a) Strain distribution in a bending beam. Dashed line is neutral plane. (b) Polarization and charge distribution on the beam.

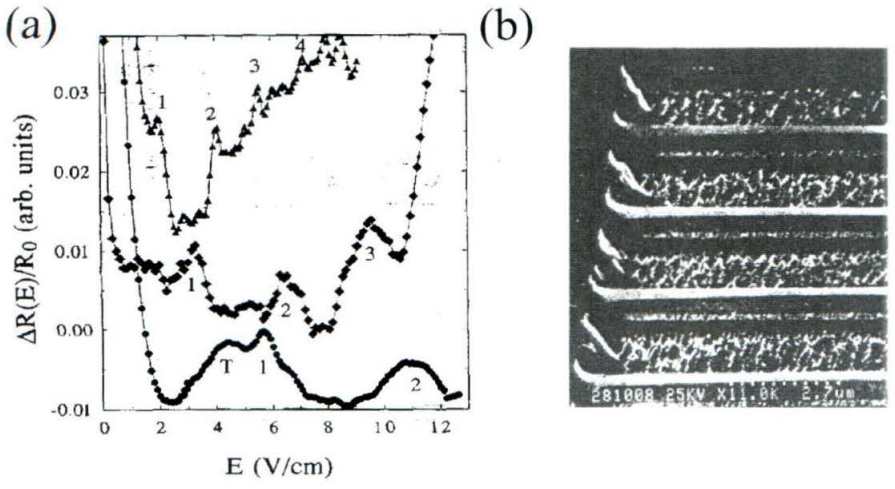

Fig. 6.4. (a) Experimental data from decoupled metallic wire in Seyler *et al.* [80] The peaks corresponding to multiple inelastic phonon emissions. (b) Suspended GaAs wires in Potts *et al.* [81]

6.4. Electron-Confined Phonon Interaction

6.4.1. Free-Standing Wires

In ensemble of nanoscale metallic particles, confined phonons have been shown to drastically influence the electronic band structure.[76] In free-standing patterned nanostructures, the disconnection from the bulk substrate offers the possibility to study the influence of well-defined ballistic phonons without thermal excitation from the environment. This was first proposed by Kelly [77] and later examined in nanoscale free-standing metallic wires by Lee *et al.* [78] and Smith *et al.*[79]. At 20mK, the dominant phonon wavelength λ_{ph} is of the order of 5 μm and exceeds the nanostructure's dimensions. Since only certain phonon modes are allowed to transport in the nanowire, resonant emission and absorption of phonons should be expected.

As a matter of fact, acoustic waveguide modes coupling with electrons were observed a decade ago by Seyler and Wybourne[80]. An array of metallic lines with width varying from 30nm to 90nm were deposited on silicon substrate. The dynamic resistance of the films was measured as a function of source drain potential drop. They discovered resonance structure on the order of $10^{-4}R_0$.(Fig. 6.4a).

MBE grown single crystalline semiconductors seem to be more appealing to observe single phonon mode. Potts *et al.* [81] successfully fabricated an array of free standing doped GaAs wires. (Fig. 6.4b). The cross section is triangular with 0.4μm width. The conduction channel had an overall diameter of 0.12μm. They did not find the resonance.

6.4.2. Suspended Quantum Dots

In a recent experiment, Fujisawa *et al.*[82] employed tunable two-level system provided by a coupled quantum dot device to investigate their interaction with the bosonic environment, presumably dominant by phonons. Besides elastic resonance tunneling between dots, they also observed extended inelastic spectrum and attributed it to a phonon assisted tunneling process. The conclusion is not convincing because the coupled quantum dots are fabricated from embedded normal 2DEG system. There is no direct evidence to assume the phonon energy is constrained in a certain range. By using suspended quantum dots, we are able to obtain discrete phonon energy band and will provide unambiguous demonstration of phonon emission spectrum if realized.

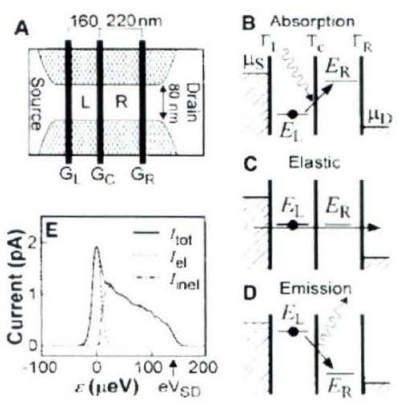

Fig. 6.5 Conductance spectrum through a coupled quantum dots device performed by Fujisawa et al. [82] The inelastic part may originate from phonon emission.

6.5. Fabrication of Self-Sensitive Suspended 2DEG Beams

Samples were cleaved from a 2-inch wafer along {110} preference crystal planes. To obtain high yield, careful cleaning of sample surface is very important. The samples were first cleaned following a standard procedue of 15 minutes boiling consecutively in hot trichloroethylene(TCE), hot acetone, hot methanol. These steps remove most of the organic contaminations. Then the sample were dipped into IPA:H2O mixture to remove metal particles, rinsed in IPA and blown

dry. A 5-10 minutes ozone stripping was usually followed to completely vaporize some tough organic residues on the sample. But meanwhile an unwanted oxide layer formed on the sample and had to be removed by dipping into diluted HCl (1:10) for 10 seconds. The latter has been proved essential to obtain a reliable etching rate in the following.

Ohmic contact to the sub-surface 2DEG are formed by annealing thermally evaporated Au(800 Å)Ni(200 Å)Ge(430 Å) metallic contacts at 450°C. The contacts were deposited by a combination of standard photolithography and liftoff technique. After confirming the formation of ohmic contacts using probe station both at room temperature and liquid N_2 temperature, thick layer of PMMA is spun on the chip, followed by a single electron-beam lithography step to expose trenches in PMMA that isolate the beam from its side gates. PMMA was then employed as a direct mask against a low voltage ECR electron cyclotron reactor (ECR) etch performed to further etch the trenches to the sacrificial layer. To minimize the damage to the 2DEG from dry etching, significant efforts have been expended to optimize the etching process. After experimenting with numerous plasma mixtures, a Cl_2/He plasma was chosen because of its excellent etching characteristics such as smooth surface morphology and vertical sidewall. A stable etching speed at 35Å/s is obtained under conditions of less than 150V self-bias (20W constant RF power), Cl_2 and He flow rate ratio 1:9, 3 mTorr pressure, and 300W microwave power.

To avoid structure collapsing caused by large undercut area, shallow etching is desirable for mesa isolation. This was achieved by another PMMA masked ECR etching procedure. The electron beam lithography pattern was aligned to the former layer by the alignment mask etched in the former fabrication step. 30 nm to 60 nm etching from the surface is enough to fully electrically isolate the beam and its in-plane gates.

After stripping off the PMMA, final structure relief is achieved by removing the sacrificial layer beneath the beams with diluted HF (1:10). To prevent mechanical structure from sticking to the underlying substrate, critical point drying is usually followed to dry the sample.

Chapter 7. Mesoscopic Physics in Freely-Suspended 2DEGs

7.1. Suspended Quantum Wires

As mentioned earlier, HEMT (high electron mobility transistor) heterostructures are highly vulnerable to damage created during the fabrication process. All high mobility, two-dimensional gas systems investigated so far are well buffered from the substrate, from the bottom side, by careful designed MBE growth layers. By contrast, from the top surface the electron gas is buried under just a few thin layers. In our case, after structural relief, another free surface at the bottom of the heterostructure layers becomes exposed to vacuum. This inevitably introduces additional scatterers to the electron gas, which is generally only 60 nm away. One of the nanofabrication goals is to achieve nearly vertical walls; to achieve this, plasma etching must be performed instead of wet etching. The damage from dry etching processes can be disastrous for HEMT structures. As a matter of fact, before the optimization of our fabrication process, all the patterned electron gas channels become non-conducting after suspension. Unambiguous characterization methods are required in order to characterize the 2-dimensional electron gases after patterning.

The suspended 2DEG itself represents a coupled electron-phonon system in which both the electrons and the phonons are subject to reduced dimensionality. Hence these structures enable

entering a new regime of mesoscopic physics. In this chapter, we will describe our measurements on suspended Hall bars and compare the results with an more convenetional, unsuspended two-dimensional electron gas systems. A high mobility electron gas exhibiting ballistic transport behavior on the device scale has been demonstrated. Universal conductance fluctuations in suspended wires will be discussed in the last section.

7.1.1. Fabrication of Suspended Hall Bars

The heterostructure, with wafer id. 03-25-97.1 was grown by our collaborator, Wegscheider group, in Germany. The layer structure and band diagram have been discussed in **Chap. 6.** The initial mobility and density are 4.0×10^5 cm^2/Vs, 2.64×10^5 cm^2/Vs, respectively. After illumination, we measured a density of 1.26×10^{12} cm^{-2} and mobility of 5.1×10^5 cm^2/Vs. The estimated second subband filling of quantum well is $n = 2 \times 10^{12}$cm^{-2} (courtesy to JPE). Therefore, even after illumination, the Fermi level remains in the lowest subband.

The processing begins by AuNiGe Ohmic contact deposition followed by annealing in a forming gas at 430°C. Good contact to the subsurface 2DEG is confirmed both at room temperature and liquid Nitrogen temperature (on cold copper block) by probe station. Then CrAuTi layers are evaporated to form bond pads coving Ohmic contacts and leading to the center of the chip. Ti is used as a protection layer for dry etching. All subsequent electron beam lithography steps are aligned to these layers since they generally have better contrast under SEM than Ohmic contacts. 100 nm thick Ti layer with Hall bar shape is patterned afterward by electron beam lithography and lift-off. Two kinds of dry etching techniques are performed in these experiments: chlorine assisted ion beam etching and Cl_2/He electron cyclotron reactor etching. Both methods yield a vertical sidewall but the latter is proved later to have minimum damage to the electron gas. A final 10-15 seconds diluted HF etch releases the three-dimensional structure and removes Ti masking layer. The suspended structure obviously prohibits us blowing the sample dry. To gain a high yield, a CO_2 critical point drying is preferred.

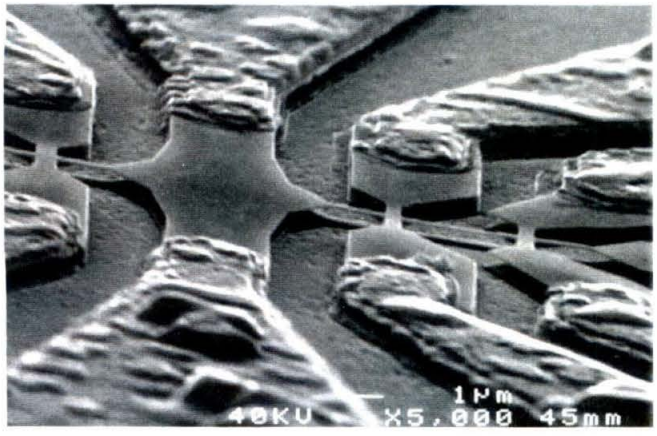

Fig. 7.1 Aerial view of the device, showing the clear undercut. This specific sample has two hall bars that are 0.7μm and 0.5μm (left one partially visible) wide and 5μm long.

The Hall bars we investigated have widths varying systematically between 0.5 and 1 μm. A typical freely standing 2DEG device is shown in Fig. 7.1. A clear undercut is seen beneath the Hall bar. In contrast to the usual Hall bar having a wide 2DEG region and small voltage probes, the Hall bars in our design have almost similar fairly small width in current and voltage leads (less than 1 μm). To fully undercut larger size membranes, the leads that supporting the structure are undercut as well, causing the whole structure to collapse. Since more than ten squares of 2DEG are measured, the influence of non-ideal Hall bars is considerably reduced.

7.1.2. High Field Measurement Results

Without illumination, the samples show inconsistent conductivity at low temperature and the carrier density is exceptionally low, possibly due to depletion. The Hall bars are in general not electrically symmetric. After brief illumination with a light-emitting diode, we can maintain a stable electron concentration on the sample in months' period. Fig. 7.2a displays longitudinal magnetoresistance of a family suspended Hall bars with lithography width 0.5μm, 0.7μm and 0.9 μm respectively. Clear Shubnikov-de Hass (SdH) oscillations are observed in high field region. In the low field region, a broad peak centered around zero field appears due to localization effect. For the 0.5 μm wide sample, an additional dip structure shows up for field below 2000 Gauss; this have its origin in boundary scattering of the quantum wire. The electron density is obtained through the standard relation, $\Delta(1/B) = 2e/hn_s$, n_s = 6.8, 6.5, and 6.6 × 10^{11} cm^{-2} correspondingly. Quantum Hall effect is also evident in Fig. 7.2b, where a linear fitting in the low field regime can also directly yield electron density given that $R_H = H/n_s e$, where H is the external field. The value of n_s is 6.7 × 10^{11} cm^{-2} for 0.5μm wide Hall bar and 7.2 × 10^{11} cm^{-2} for 0.7 μm and 0.9 μm Hall bars, all consistent with the longitudinal measurement result.

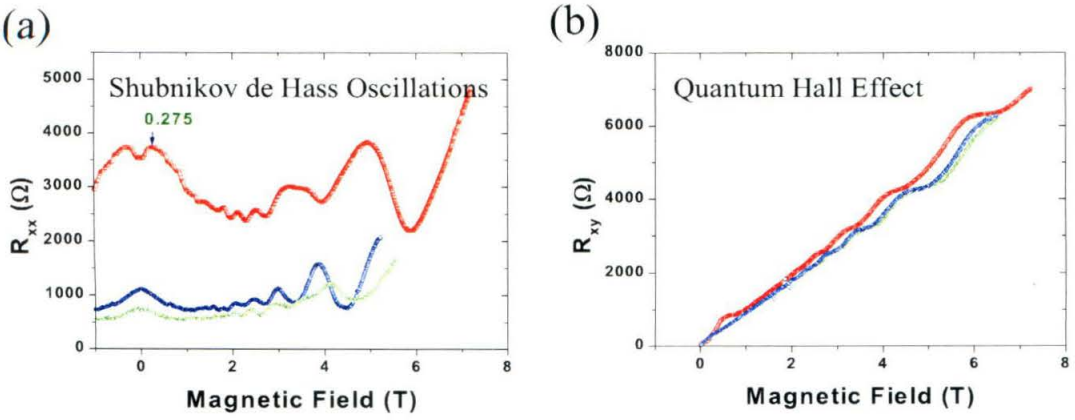

Fig. 7.2 (a) Longitudinal magnetoresistance $R(B)$ for Hall bar with three Hall bars with 0.5μm, 0.7μm and 0.9μm lithography widths. (b) Hall effect of corresponding Hall bars. Quantum Hall effect is evident at high field.

However, mobilities of the suspended Hall bars are difficult to obtain considering the fact that the actual electrical width of the channel is unknown and may be affected by etch conditions. Fortunately, the electrical width can be inferred from the boundary scattering peak, shown in the longitudinal resistance trace as a hump representing the fact that the scattering of electrons from the channel sidewalls usually has a non-specular, or diffusive, component. [83] This results in a magnetoresistive peak centered at a characteristic field $B_{\max} = 0.55\hbar k_F / eW$, where k_F is Fermi wavevector whose value can be calculated from the electron density and W is the electrical width of the channel. (We shall discuss this in more detail in Sect. 7.1.3) This expression shows that $B_{\max}$ is larger for narrower channels. Having extracted the correct value for W, we can then obtain mobility from $R_{xx} = (n_s e\mu)^{-1} L/W$ where we use the minimum value for $R_{xx}(H)$ where the boundary scattering phenomena have died off but Shubnikov de Haas phenomena have not yet commenced. Values for a representative sampling of chips are summarized in Table 7.1. The

Table 7.1 Carrier densities, electrical channel widths, and mobilities for a family of suspended Hall bars.

Litho width μm	Electrical width μm	n_s(SdH) 10^{11}cm^{-2}	n_s(Hall) 10^{11}cm^{-2}	μ (cm^2/Vs)	l μm
0.50	0.20	6.8	6.7	110,000	1.5
0.70	-	6.5	7.2	169,000	2.2
0.90	-	6.6	7.2	137,000	1.8

channel depletion for 0.5 μm wire is estimated to be 300 nm.

7.1.3. Evidences of Ballistic Electron Transport in Sus2DEG Wires

The electron mean free paths deduced from our measured electron densities and mobilities vary from 1.5μm to 2.2μm, exceeding the Hall bar width and but less than the Hall bar length. This falls into quasi-ballistic electron transport region, where the electrical properties of a semiconductor sample can show large deviations from the classically expected properties. This section concentrates on the magnetoresistance effects demonstrated in our fabricated high-mobility 2DEG system, involving four kinds of phenomena: diffusive boundary scattering, last Hall plateau, negative transfer resistance, and universal conductance fluctuation.

7.1.3.1. Diffusive Boundary Scattering

In a quasi-ballistic submicron wire, the majority of electrons will be scattered by the boundaries before they suffer an elastic collision within the wire. If the boundary scattering is specular, the longitudinal momentum of the electron is conserved. The conductance of a wire of length L and width W can then be expressed as $G = ne\mu W / L$ where μ is the mobility measured in a wide sample and is the sheet density. If some fraction of the boundary scattering is diffusive, however, the extra scattering will lead to a smaller effective mobility, μ_{eff} and a corresponding reduction in the conductance. The effect of diffusive boundary scattering on the weak localization (quantum interference) corrections was considered in [84].

By applying a perpendicular magnetic field, the contribution that boundary scattering makes to the total resistivity of a narrow wire can be varied. At low fields, the resistivity is initially increased but can be reduced to the bulk value by a sufficiently large magnetic field. The reasons for this behavior are illustrated in Fig. 7.3. At zero and very small magnetic fields (Fig. 7.3a), the electrons with a large component of momentum parallel to the wire interact infrequently with the edges and can contribute significantly to the conductivity. However, as the field is increased, these electrons are forced to collide with the edges (Fig. 7.3b) and the extra diffuse scattering will increase the resistivity. The low-field positive magnetoresistance saturates and a maximum in the resistance occurs at a magnetic field, $B_{\max}$, such that $W/L_c = 0.55$ where $L_c = \hbar k_F / eB_{\max}$ is the cyclotron radius at this field. This value for the ratio W/L_c is derived from a calculation based on classical electron trajectories[85] but a fully quantum mechanical calculation gives a very similar

result [86]. At still higher fields the cyclotron diameter will be smaller than the wire width and the electrons will be confined to the edges (Fig. 7.3b). At this stage diffuse backscattering is suppressed over distances of order l_0 and we recover the bulk resistivity ρ_0.

The magnetoresistance of a 0.5μm wide suspended quantum wire is shown in Fig. 7.2a. Above about 1T, the data is practically identical to that from a wide sample of the same material. Below 1T, the increased resistance indicates the localization effect. The peak around 0.28 T is also clearly observed. We already showed in Sect. 7.1.2 that the electrical width of the wire could be deduced from this peak position.

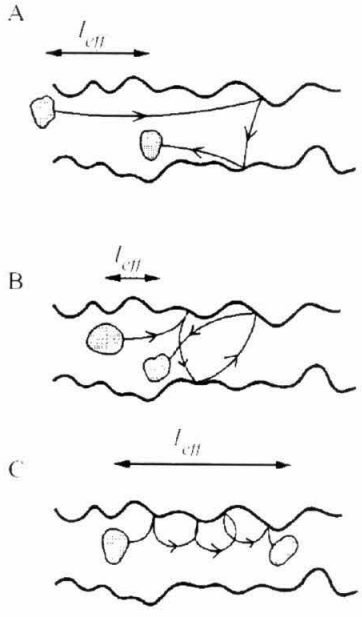

Fig. 7.3 (a) At low magnetic fields the electron trajectories are forced to interact with the edges, increasing the degree of backscattering. (b) At fields $B = B_{max}$ the backscattering is maximized and μ_{eff} is reduced to its lowest value. (c) For fields such that $2r_c < W$ the backscattering is suppressed and $\mu_{eff} \rightarrow \mu_0$.

7.1.3.2. Last Hall Plateau and Negative Transfer Resistance

These two phenomena are related classical behavior of electron transport in microjunctions. Fig. 7.4 shows the typical weak magnetic field behavior of the Hall resistance and the transfer resistance. The Hall resistance is quenched below its classical expected value for magnetic fields $|B| < B_{max}$, and then rises to a plateau. These phenomena occur well before the onset of the quantum Hall plateaux and some cases the quenching is so strong that the Hall resistance is negative around zero magnetic field. [73, 87, 88]. We observed similar behavior in our suspended structure as shown in Fig. 7.2b.

The transfer resistance in a cross-shaped junction is negative for zero magnetic field under quasiballistic conditions. Application of a magnetic field perpendicular to the plane in which the current flows makes the transfer resistance increase, and positive peaks are typically observed at $B = \pm B_{max}$. For comparison, we present our result of typical transfer resistance measurement in

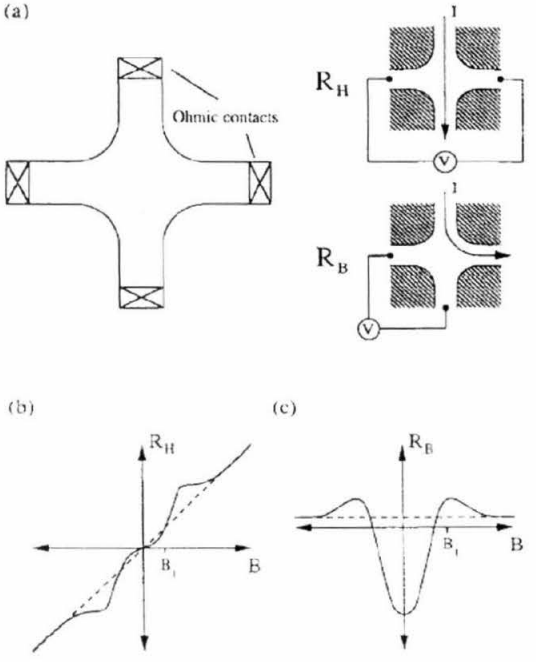

Fig. 7.4 Typical weak magnetic-field behavior of the Hall resistance R_H and the transfer resistance R_B at a quasi-ballistic junction: (a) Basic structure and measurement configuration; (b) Hall resistance behavior, with the classically expected linear behavior shown by the dashed line; (c) transfer resistance behavior, with the positive value expected for a macroscopic sample shown by the dashed line.

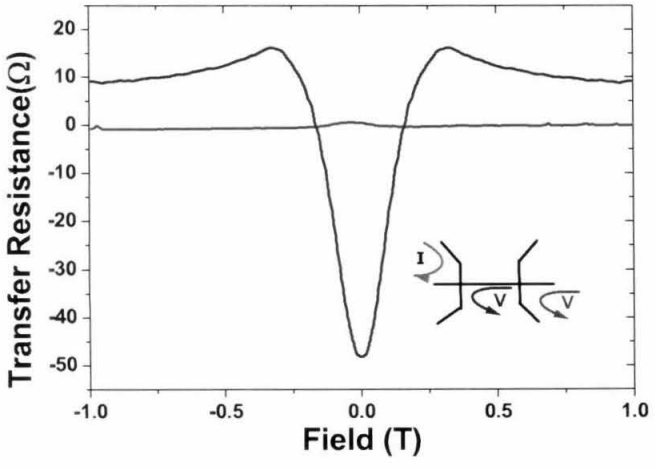

Fig. 7.5 Transfer resistance at one single junction and at two junctions.

Fig. 7.5.

The theoretical effort to explain these phenomena involves a semiclassical billiard-ball model[89] as we employed in **Appendix B**. Ballistic electron can be regarded as hard balls bouncing back and forth between the wire boundaries. When an electron is injected into the Hall junction, the magnetic field tried to guide it to the exit at one of the voltage probe. But on most occasions, before it reaches that exit, it is bounced back into the opposite probe. The "rebound" trajectories depicted in Fig. 7.6a contribute a lot in balancing normal Hall voltage and form the "last Hall plateau". Similarly, in weak magnetic field, flaring at the end of the wire focuses the classical electron trajectories thereby enhancing the probability of forward transmission. In contrary to diffusive transport, the voltage is accumulated at the opposite probe and gives a negative transfer resistance.

Note that in Fig. 7.5 we also performed an "offset" transfer resistance measurement, in which case the current is flown in one junction while the voltage accumulation is measured on a remote junction. If the mean free path is longer than the junction-center distance, we should also expect a negative magnetoresistance. However, we observe a normal, diffuse-like positive peak at zero field in this case. The size of this cross junction is 0.9 μm and the distance between these two junctions is 4μm. We confirm from transfer resistance measurement that the electron mean free path is indeed between 0.9μm and 4μm.

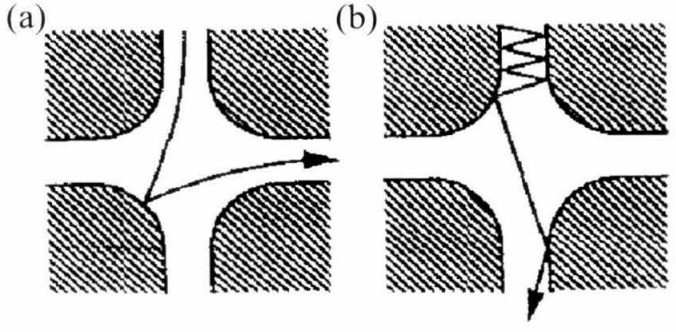

Fig. 7.6 Examples of electron trajectories giving rise to the various magnetoresistance anomalies. (a) Rebound. (b) Collimating.

7.1.3.3. Universal Conductance Fluctuation

By ramping the magnetic field in smaller steps, we observed striking aperiodic resistance fluctuations in the low field region just before SdH oscillations start to develop. Fig. 7.7 shows magnetoresistance curves for a family of suspended quantum wires from 0.35 μm wide to 0.70 μm wide. Resistance fluctuations have been observed in narrow wires fabricated in metal films[90, 91], GaAs/AlGaAs heterostructures[92, 93], and Si MOSFET[84, 94]. The fluctuations are a consequence of variations in the interference pattern of the various electron paths when the magnetic field is changed. In a two-probe configuration at $T = 0$ K, the amplitude of the fluctuations in the conductance G ($= 1/R$) of a diffuse system is of the order e^2/h. These conductance fluctuations are called universal conductance fluctuations because their size is

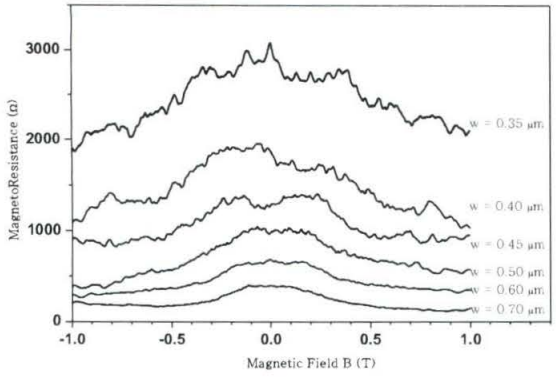

Fig. 7.7 Magnetoresistance curves for suspended quantum wires ranging from 0.35 μm to 0.70 μm wide. Data was taken at 4.2K.

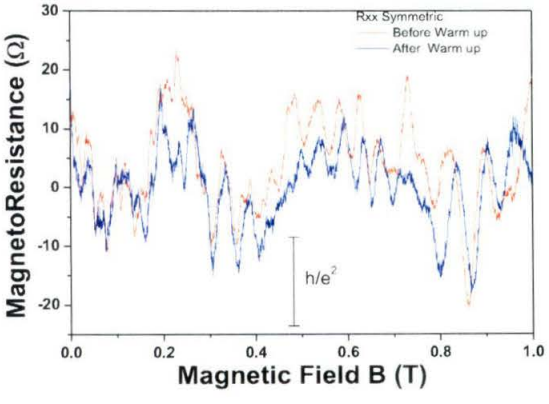

Fig. 7.8 Fluctuating part of magnetoresistance after substracting the background.

independent of the material and geometrical properties.[95] At higher temperatures, the fluctuations are a function of the phase coherence length $l_\phi = \sqrt{D\tau_\phi}$, the thermal diffusion length $l_T = \sqrt{\hbar D / k_B T}$ and the sample size L:[96]

$$\frac{\delta R}{R^2} = N_v \alpha \sqrt{6} \frac{e^2}{h} \left(\frac{l_\phi}{L} \right)^{3/2} \left[1 + \frac{9}{2\pi} \left(\frac{l_\phi}{l_T} \right)^2 \right]^{-1/2} \tag{7.1}$$

This explains the reduction of fluctuations as the wire width is increased. The fluctuation part of the magnetoresistance curves $\Delta R(B)$ is obtained by subtracting the background resistance from the measured data. Results for $\Delta R(B)$ of 0.35 μm wide wire are shown in Fig. 7.8. A repeated measurement after one thermal cycle is also plotted and a different resistance pattern is displayed. The fluctuations are on the order of h/e^2, which means that the phase coherence length l is on the order of the channel electrical width 0.15μm.

The magnitude of the fluctuations decays in wider suspended wires, indicating that electrical width of the conducting wire exceeds the phase coherence length and the fluctuations tend to be averaged out.

To analyze the experimental data, it is useful to calculate the magnetic field shifted autocorrelation function of the resistance fluctuations $F(\Delta B)$:

$$F(\Delta B) = \langle \Delta R(B) \times \Delta R(B + \Delta B) \rangle, \tag{7.2}$$

where $\langle\ \rangle$ means an average over the magnetic field range. The autocorrelation function corresponding to the data shown in Fig. 7.8 is plotted in Fig. 7.9. A kink structure is visible at 500

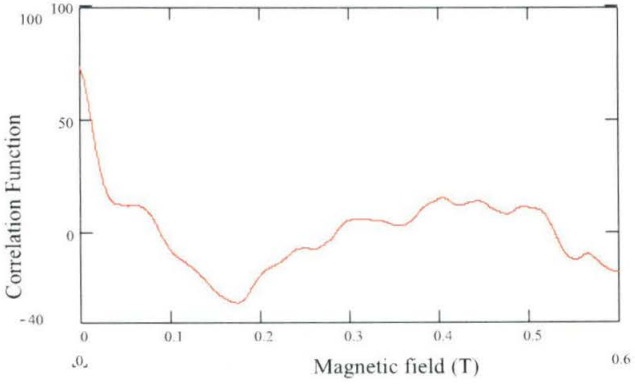

Fig. 7.9 Conductance fluctuations autocorrelation function for suspended 2DEG.

Gauss. For UCF, the correlation function should monotonically decay with field. One possible origin may come from the discrete acoustic phonon mode for suspended beams.

7.2. Suspended Quantum Dots: Fabrication and Preliminary Results

We have successfully fabricated suspended quantum dots and obtained preliminary results from these dots. Two kinds of dot geometry are employed as shown in Fig. 7.10. For suspended structure, in-plane gates are preferred over top split gates, not only because the fabrication of metallic top split gates involves many more tricky steps, but also minimal mechanical perturbation is achieved by isolated in-plane gates. In geometry I, four isolated 2DEG area serve as in-plane gates and can be tuned independently. G1 works with G2 and G4 to pinch down the conducting channels leading from the dot to the source and drain. The plunger gate G3 is capacitively coupled to the dots and enables direct tuning of the electrical states in the dot. The geometry II, having only two gates, offers a simpler device design. G1 is used to pinch and isolate the quantum dot. G2 is the plunger gate. The yield of devices with Geometry II is higher but Geometry I devices are capable of providing a better control of the tunneling rate of quantum dot to the source and drain.

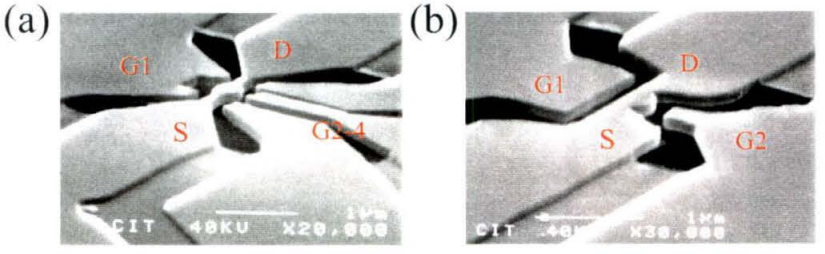

Fig. 7.10 Two classes of suspended quantum dots we have fabricated. A puddle of electrons are confined in the center islands.

The fabrication of suspended quantum dots is similar to the recipe we used for resonators with in-plane gates. To avoid the collapse of the gates (they are actually cantilevers), the deep ECR etching to the sacrificial layer is executed first. Then a well-calibrated shallow wet etching or ECR etching process is followed to remove the top 60nm of GaAs/AlGaAs. After the structure release, only the area around the quantum dot (5μm × 5μm) is undercut.

For the devices we show in Fig. 7.10, the dots have a lithography size of about 300nm × 400nm. The design has account for the larger depletion depth in suspended structure than ordinary 2DEG structure. After deducting the depletion region, the dots have a diameter of about 100nm and contain about 120 electrons. As a matter of fact, channels that lead to the dot are already depleted after suspension. In order to form an isolated island by tunnel barriers of comparable size, we applied positive voltages to pinch gates to open the channel to obtain the same conductivity in both contacts. Typical pinch curves for gates G1, G2 and G3 are shown in the insets of Fig. 7.11. Then the conductivity through the island is measured as a function of the gate voltage applied to plunger gate. (for example G3 in geometry I devices). Fig. 7.11 shows the measured conductivity as a function of the plunger gate voltage at 4.2K. Even at this elevated temperature, Columb blockade oscillations are still evident. The period of the oscillation in gate voltage is about 400 mV, which is exceptionally large comparing to ordinary split-gated quantum dots.(typically 2 mV) This can be rationalized by the improved 3-D confinement for the suspended quantum dot and the much smaller dot-gate capacitance of the in-plane gates. The air gap between gates and dot has a dielectric constant as low as 1 and could reduce the dot-gate

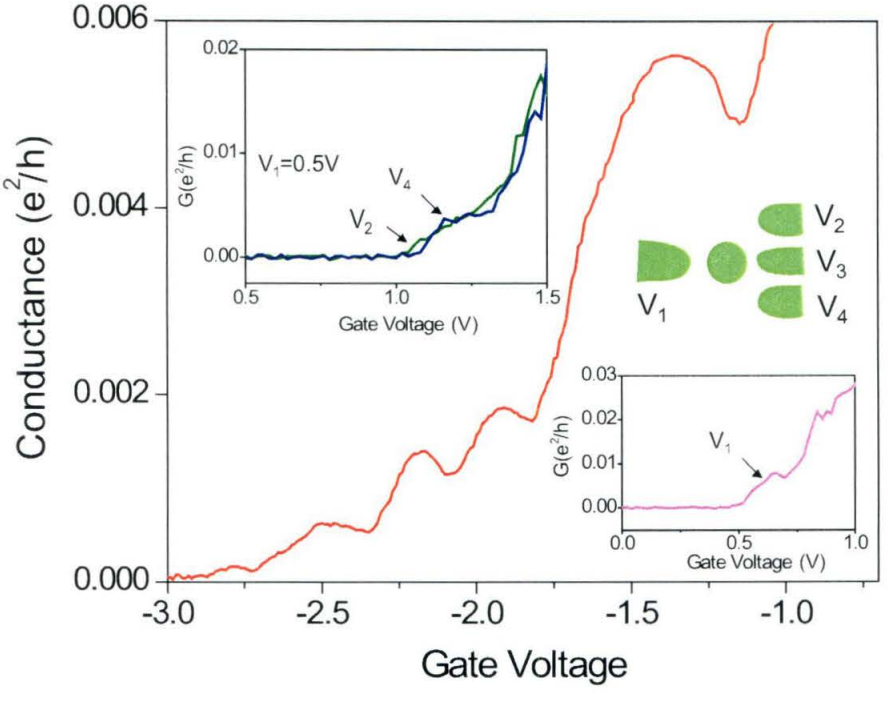

Fig. 7.11 Columb blockade observed in suspended quantum dots at 4.2K. Upper inset: pinch curves for G2 and G4 with 0.5V gate voltage on G1. Lower inset: pinch curve for gate G1 with G2 and G4 floating.

capacitance by a factor of 13 for GaAs.

This unique property of suspended quantum dot is actually very valuable in our proposed experiment to study phonon spectrum in coupled quantum dots. The energy resolution will be improved by a factor of 200 due to elongated horizontal axis.

The high sensitivity of the isolated dot also enables us to study the behavior of a single defect sitting on the dot. Fig. 7.12 shows the conductance of a quantum dot reflecting a discharging event of a defect.

Experiments are in progress to perform the measurement at dilution refrigerator temperature by employing improved materials.

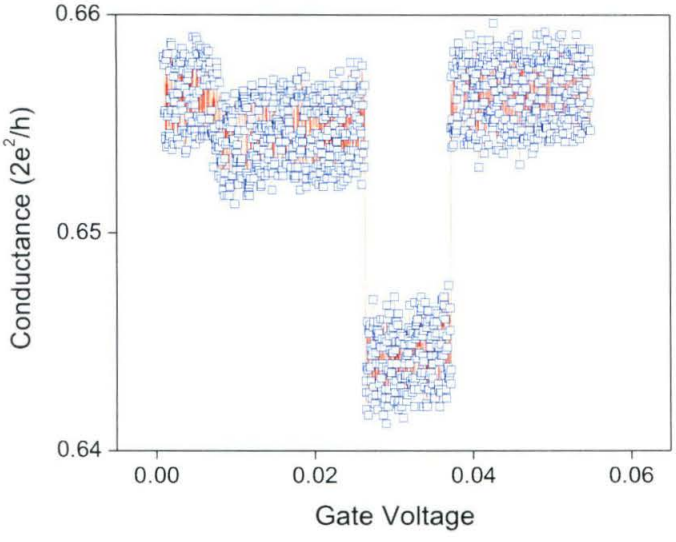

Fig. 7.12. Shot noise from a single defect sitting on the suspended quantum dot.

Chapter 8. Integrated 2DEG-Based Strain Sensors for NEMS Displacement Detection

8.1. Characterization of Mechanical-Electrical Response by AFM Pushing

In the previous chapter, we have fully characterized 2DEGs within freely-suspended Hall bars and have shown that considerably high electrical mobility can be maintained. Before the benefits of suspended 2DEGs can be fully exploited in NEMS, their mechanical behavior must also be properly quantified. Below we describe use very stiff AFM tips to bend doubly-clamped beams fabricated from 2DEG heterostructures described previously, while we simultaneously record the resistance of the beam. The coupled mechanical-electrical response can be characterized by the resistance change induced by the static deflection.

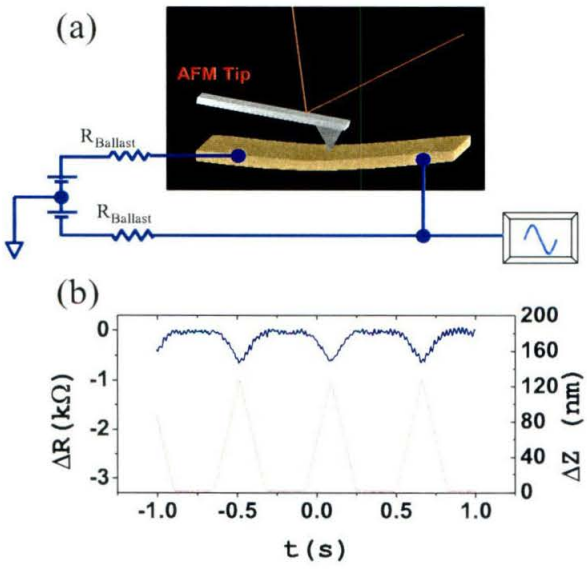

Fig. 8.1 (a) Schematic view of the test setup. (b) AFM tip displacement and 2DEG beam resistance variance with repeated cycle of ~0.5 s.

The experimental setup is shown in Fig. 8.1a. Two battery sets are used to supply a constant voltage across the series combination of two 10 MΩ ballast resistors and the device. This provides a constant dc bias current across the sample. The resistance variance due to the applied strain is reflected by a voltage waveform in the oscilloscope. After the beam was imaged by tapping-mode AFM, the AFM tip was positioned above the center of the beam and the AFM was switched to the force mode. The AFM tip was programmed to push and bend the sample downward in the linear response region. Then the tip was retracted at the same speed as it was pushed. The pushing-retracing cycle was repeated in a pattern represented by the lower trace in Fig. 8.1b. The AFM tips used in these experiments are Si tips having spring constant larger than 40 N/m, significantly larger than the calculated spring constant of the beam (~0.25 N/m). Therefore, the deflection of the tip can be ignored and we can use the displacement of the piezotube to represent the travel distance of tip. The piezotube voltage was used as the triggering source for sampling and averaging.

The samples probed in this experiment are doubly clamped beams having dimensions 10 μm × 0.5 μm × 0.1 μm. The fabrication is similar to the suspended Hall bar as we discussed before. A picture of a sample containing a pair of doubly clamped beams is shown in Fig. 8.2.

Fig. 8.1b shows the trip displacement and sample resistance evolution during repeated measurement cycle. The maximum tip travel distance is 120 nm (lower trace). The resistance of the sample decreases whenever the beam is bent down and recovered as the beam is released. The magnitude of the resistance change is about 600 Ohms. Therefore the mechanical-electrical response of the 2DEG beam is deduced to be about 5×10^{9} Ω/m or 5 Ω/nm. It is notable that the mechanical deformation and electrical resistance response are both reversible after many cycles. The drifting of the signal mainly comes from the lateral uncontrolled motion of the AFM tip.

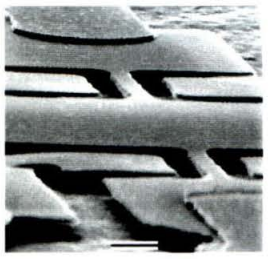

Fig. 8.2 A pair of doubly-clamped beams containing 2DEG for AFM pushing experiments.

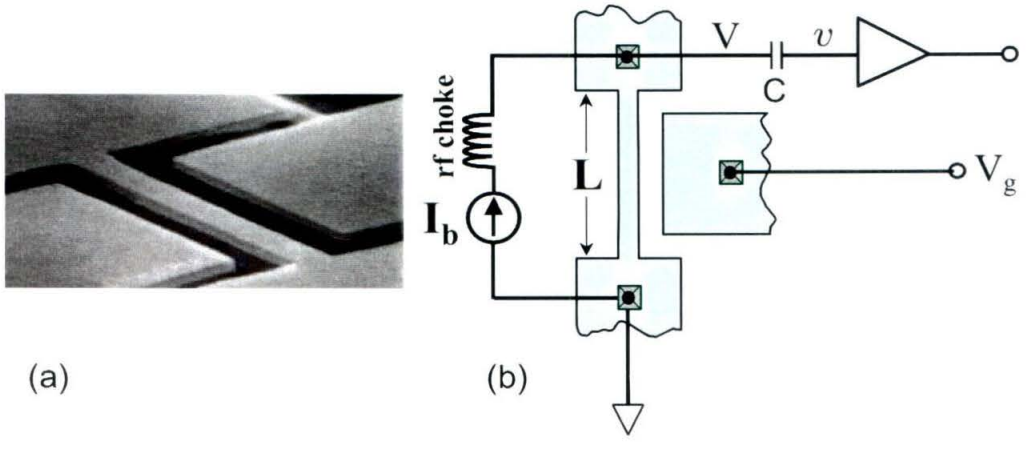

Fig. 8.3 (a) SEM image of a doubly clamped beam. The in-plane gates are formed by the 2DEG. (b) Sketch of measurement setup. A constant dc bias current (I_b) is sent through a big rf-choke (~mH) before reaching the beam. Gate drive voltage consists of both dc and rf components: $V_g = V_g^{(0)} + \upsilon_g e^{i\omega t}$. The induced signal can be expressed as $V = V^{(0)} + \upsilon\, e^{i(\omega t+\varphi)}$, where the dc voltage potential $V^{(0)} = I_b R_{dc}$ is blocked by a capacitor C and the oscillating component is amplified at both liquid helium and room temperature.

8.2. Dynamic Response Measurement

8.2.1. Experiment Setup

A typical device is shown in Fig. 8.3. The beams are 0.5μm wide and 6μm long, having a calculated spring constant of 0.25 N/m. When cooled to liquid helium temperature, their two-terminal resistance is about 100 kΩ. After illumination, this drops to about 5 kΩ. The electrical width of the beam is about 0.3 μm with $R_{\square}$ = 170 Ω.

In nanoelectromechanical (NEMS) system, both the induction and the detection of motion pose important challenges. In our devices, the actuation is relatively trivial and very effective. The rf-drive is supplied directly to one of the side gates, which is large area of 2DEG connected to the output of network analyzer through alloyed Ohmic contact. Since the gate-beam separation can be as narrow as 100 nanometers, a small driving amplitude proves sufficient. In this paper, all the trenches have a constant width of 0.5μm. The devices are first measured at 4.2 K in vacuum. A constant dc sensing current ranging from 0 to 26μA is supplied to the vibrating beam through a 10mH rf-choke, whose value is chosen big enough to avoid loss of the small signal that is induced. The oscillatory signal is picked up by a low temperature amplifier placed in close proximity to the device, whose output is led out of the cryostat through a coaxial cable. Before connecting the signal to the input of network analyzer, a room temperature amplifier may be used to improve signal to noise ratio. The combined amplifiers have a voltage gain of about 200 in the frequency range of these experiments.

8.2.2. Observation of Mechanical Resonance

We observed very strong vibration signal around the first mechanical resonance. The magnitude response curves at various driving amplitudes are shown in Fig. 8.4a. Calculations confirm this resonance corresponds to the first out-of-plane vibrational mode. When the drive amplitude is increased above 45mV, the response curve becomes nonlinear and assumes an asymmetric Lorentzian shape. In the linear response region, the amplitude at resonance is proportional to the ac gate voltage amplitude.

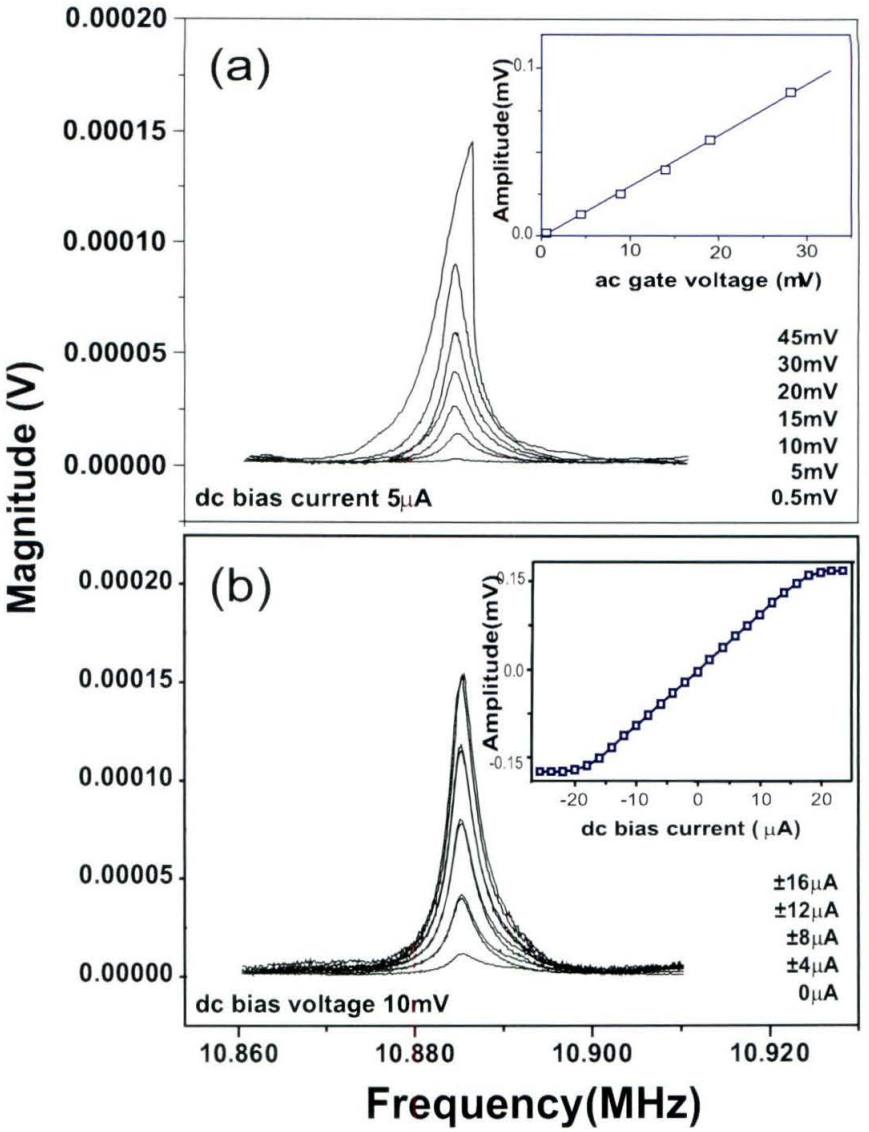

Fig. 8.4 (a) Voltage drop across the beam as it is driven to its lowest mechanical resonance with increasing drive amplitudes. The dc bias current is fixed at 5μA. Inset: The peak value of amplitude response as a function of driving amplitude in the linear regime. (b) Magnitude response curve at various dc bias current. Inset: The signal amplitude at resonance with sensing current increase from -26 μA to 26 μA.

To clarify the origin of the observed signal, we fixed the drive at 10 mV and then varied the dc bias current from -26μA to 0 then to 26 μA. The response amplitude *vs* drive amplitude at resonance is presented in Fig. 2b. Two features are evident from this data. First, at the highest currents close to 20 μA, the signal becomes saturated for two reasons: (a) Joule-heating of the

small beam, and (b), saturation of the drift velocity at such high applied electrical field (~15kV/m). Second, at intermediate current, the signal strength at resonance is proportional to the dc bias current, as indicated in the inset of Fig. 8.4b. In addition, when we reverse the current direction, we also find that the induced signal changes its sign (180 degree phase change). Therefore we conclude that the dominant contribution to the observed signal is a change of resistance due to beam vibration. This appears to originate from both piezoresistive effect of bulk GaAs and transverse piezoelectric charge gating of 2DEG. Note that a small signal is observed even for zero current bias. From the slope of the linear part in the inset of Fig. 8.4b, a nominal drive of 10mV induces a resistance change of about 10Ω in the device.

We now estimate the sensitivity of this technique. By looking at the critical amplitude at the onset of nonlinearity, we can determine the amplitude of vibration of the resonating beam. This critical displacement amplitude depends only on the geometry of the beam, and is approximately given as [97]

$$x_c \sim \frac{2h}{\sqrt{0.5Q(1-\nu^2)}}, \tag{8.1}$$

where h is the thickness of the beam in the vibration direction, and ν is the Poisson's ratio for GaAs. Plugging in measured values of $Q = 2600$ and $\nu = 0.31$, we obtain x_c = 6 nm, which is attained at a drive level of about 45mV. The minimum resolvable signal is achieved at 0.1 mV drive and about 5 μA sensing current. Hence, at the highest possible current of 20 μA, we can detect a resonance at $x_c/450/4$ = 0.03Å, or 3 × 10^{-3}Å/√Hz, which is consistent with our estimate based on Johnson noise from beam resistance at 4.2K. The corresponding force sensitivity is 75fN/√Hz, comparable with previous schemes to detect small NEMS resonators by optical inteiferometry [98] and the magnetomotive method [99]. The required force to drive the beam to non-linearity threshold is 1.5nN. The displacement resolution can be improved by using 2DEG heterostructures with even higher mobility, or by operating at ~100 mK with a state-of-the-art low temperature preamplifier.

8.2.3. Actuation Mechanism of In-plane Gated 2DEG Beam

Note that in Fig. 8.4 all the driving force we applied corresponds to an applied a.c. gate voltage. We did not find any significant change of resonant frequency or magnitude with dc bias on the gate. This is indicative of a coupling mechanism different from electrostatic force between the gates and the beam. Electrostatic force is proportional to the product of dc and ac components of gate potential so that the response should directly scale with the dc gate voltage [100]. This assumes a direct Coulomb interaction between coupling plates. In our in-plane gate configuration, the net charge on the beam is $C(V_g^{(0)} + v_g e^{i\omega t})$. The capacitance between coplanar 2DEG areas has an estimated value of 18 aF/μm,[101] which is very small compared to parallel plates. With a nominal 1V dc gate voltage, there are only a few hundred induced electron charges on the beam. The upper bound of the electric field applied on the gate is d is the beam-gate separation (Fig. 8.5). Thus the total electrostatic force applied on the beam with angular frequency ω is $f = CV_g^{(0)} v_g e^{i\omega t} / d$. Only a projection of this force drives the beam along the out-of-plane (y) direction. A reasonable estimate of the effective y-component of this force is

$$f_y = CV_g^{(0)} v_g e^{i\omega t} y_0 / d^2, \tag{8.2}$$

where y_0 is a static offset due to, *e.g.*, uncontrolled asymmetry of suspended beam. A 10nm misalignment of the beam with respect to gate should be observable in our devices (but is not seen). Therefore, we take this number as the upper limit of in the estimation of y_0. At a nominal 1V dc gate voltage, 45mV ac gate voltage, the force originating from the electrostatic drive mechanism is calculated to be $f_y \approx 0.2$pN. This is four orders of magnitude smaller than the force required to drive the beam into non-linear response.

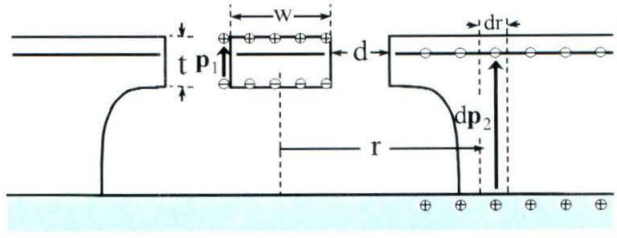

Fig. 8.5 Cross-sectional illustration of dipoles formation on the beam (p_1) and on the driving gate (dp_2).

Given the absence of electrostatic a.c. forces, we propose that a new driving mechanism, a short-range dipole-dipole interaction, is dominant in our nanoelectromechanical system. This dipole-dipole interaction potential can be expressed as

$$U = \int \frac{1}{4\pi\varepsilon_0} \frac{p_2 dp_1}{r^3}, \tag{8.3}$$

which can be understood as rf-coupling between two dipole moments dp_1 and p_2. Here dp_1 is the dipole momentum of a slice of the gate, $dp_1 = \varepsilon_r \varepsilon_0 L V_{ac} e^{i\omega t} dr$ and p_2 is the fixed dipole moment due to piezoelectric effect of strained (GaAs/AlGaAs beam. y is the beam displacement, $p_2 = 3Ed_A wt^2 \Delta y / L$ and L, w and t are beam length, width and thickness (Fig. 8.5). ε_r is dielectric constant of GaAs. Here $E \sim 85$Gpa is Young's Modulus and $d_A \sim 3.8$ pC/N is the appropriate piezoelectric constant of AlGaAs.[75] The resulting force along y direction is

$$f_y = \frac{\partial U}{\partial y} = \frac{3\varepsilon_r}{4\pi}(Ed_{13})\left(\frac{wt^2}{d^2}\right) V_{ac} e^{i\omega t} \tag{8.4}$$

This force is *independent* of the dc gate voltage, consistent with our observation. At 45mV a.c. gate voltage drive, f_y is estimated to be 1.2nN from this mechanism, four orders of magnitude higher than the direct Coulomb interaction. This is consistent with the force we observe at the onset of non-linearity. Because of its short-range characteristics, this dipole-dipole interaction is unique to NEMS and is insignificant in microelectromechanical systems (MEMS).

8.2.4. Temperature Dependence of Mechanical Response

We have also studied the temperature dependence of our strain sensitive devices. Measurements were performed at three different temperatures in vacuum. The results are shown in Fig. 8.6. The drive and sensing current are kept at the same level. The devices perform exceptionally well at liquid helium and nitrogen temperatures, but at room temperature, the response is diminished. The decay of signal strength at resonance with respect to temperature can be explained by the significant reduction of 2DEG mobility at higher temperature. At elevated temperature the increased two-terminal beam resistance acts as a large voltage divider, and only a small fraction of induced signal voltage drops across the input of rf-amplifier

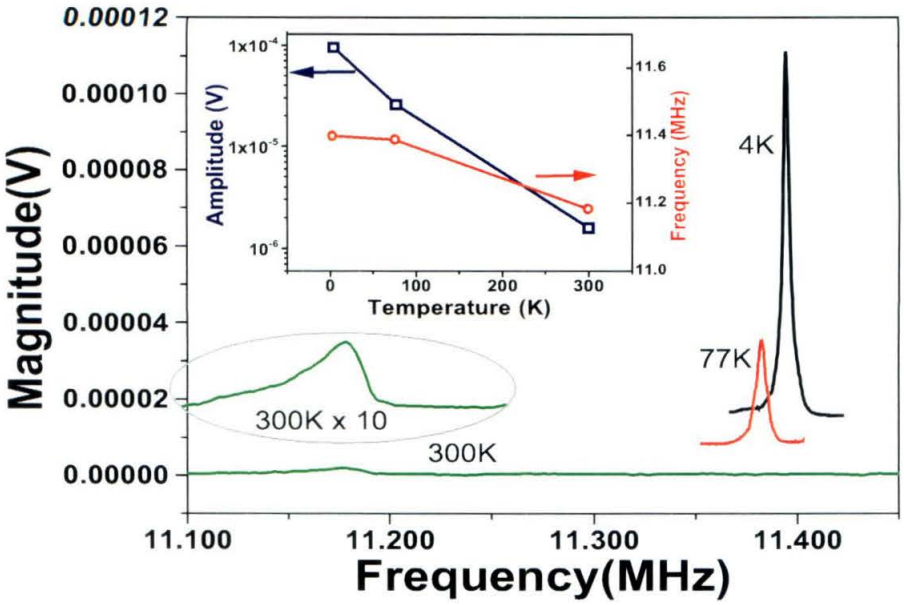

Fig. 8.6 Response curve at three different temperatures. Inset: Sketch of amplitude and frequency change vs temperature.

Appendix A. Introduction to Spin Injection and Transport

This appendix serves as a self-contained introduction to the subject of electrical spin injection in submicron scale devices. The main body of the text is taken from a chapter I authored for the book edited by D. D. Awschalom, D. Loss and N. Samarth, "Semiconductor Spintronics and Quantum Computation", May 2002, Springer Verlag, New York. For completeness, with acknowledgement to the co-authors F. J. Jedema, A. T. Filip and B. J. van Wees, I also included their contributions to this book chapter.

Experiments to explore the transfer of a spin-polarized electric current within small devices have been ongoing for nearly 30 years. But attaining the same level of exquisite control over the transport of *spin* in micro- or nanoscale devices, as currently exists for the flow of charge in conventional electronic devices, remains elusive. Much has been learned since the time of the first demonstrations of spin polarized tunneling by Tedrow and Meservey. During this period we have witnessed the transformation of spin-based electronic devices from laboratory experiments to the realm of commercially available products. This has been driven especially, just in this past decade, by the robust phenomena of giant magnetoresistance (GMR) [1]. Even more recently, magnetic tunnel junction devices, involving transport of spin-polarized electrons across interfaces, have proceeded to commercial development [2]. Meanwhile, spin injection devices—and by "injection" we here denote transferal of spin-polarized carriers into an otherwise *nonmagnetic conductor* (or semiconductor)—have not reached a similar, commercially viable, state of maturation. In fact, it is fair to say that, at present, even the fundamental physics and materials science of the spin injection process remains in need of significant elucidation.

Yet the problem of spin injection continues to capture the focus of many researchers including ourselves. Ongoing interest in spin electronics—especially in semiconductors of late—is, in part, motivated by the expectation that, in the near term, this field may lead to the large scale integration of semiconductor micro- and nano- devices capable of performing very high speed logic and memory operations, such as performed via conventional charge based electronics, but at a fraction of the power. In the long term, surveying the spectrum of other possible solid-state embodiments, many researchers anticipate that the spin degree of freedom may provide the most robust foundation upon which practical realizations of qubits and quantum computers may ultimately be constructed. All of these prospects clearly require us to understand how to transfer electron spins across interfaces, and how to preserve their polarization during this traversal.

In this chapter, we shall review some of the most important developments in the field of spin injection that have emerged since the earliest experiments. We strive herein more to develop a coherent overall perspective, rather than for absolute completeness of coverage. Below we shall attempt to summarize the evolution of thinking about spin injection by describing, in part, the succession of research that has ensued.

A.1. Background

A.1.1 Spin Polarized Tunneling

In 1971 Tedrow and Meservey (TM) first studied spin polarized tunneling using superconductor/insulator/ferromagnet devices based upon Aluminum/Aluminum Oxide junctions [102-104]. Their experiments took advantage of the fact that application of a magnetic field splits the superconductor quasiparticle density of states into spin up and spin down bands. This splitting, equal to the Zeeman energy of electronic spins in the magnetic field, allows the superconductor to be used as a spin analyzer. Varying the voltage between the ferromagnet and superconductor produces a tunneling current that is sensitive to the detailed combined density of states in both the ferromagnet and the superconductor. The ferromagnet's density of states can then be obtained by deconvolving the tunneling conductance. Polarization values obtained for some of the elemental ferromagnets by TM were 44% for Fe, 34% for Co, and 11% for Ni. These are in direct proportion to the saturation magnetization of the bulk materials: 1.714×10^3, 1.422×10^3, and 0.484×10^3 emu/cm^3 respectively [49].

This correspondence may be intuitively sensible, but is not particularly straightforward to understand quantitatively. Even the ostensibly simpler question as to whether it is majority or minority spins that comprise the larger percentage of the tunneling current is complicated. The sign of the polarization observed by TM in their tunneling experiments was, in fact, the opposite expected for majority spins. Attempts at resolving this apparent discrepancy took several years. Investigation into the precise nature of the injected electrons continues today, but first discussions were first provided by Stearns [105], later by Sloncezwski [106], and, subsequently, several other groups [107-111]. Collectively the picture that has emerged from this work is that the tunneling conductance can vary dramatically from band to band, and the contribution from one particular minority channel band at the Fermi energy may be predominant in the overall majority spin conductance. A detailed analysis of the electronic band structure of materials at the interface is therefore required to understand the complex behavior observed in experiments.

In 1975, Julliere extended this class of tunneling experiments to a system with two ferromagnets (Fe/Ge/Co); these were carried out at 4.2K where the Ge became semi-insulating [112]. In this work the magnetization of Fe and Co could be varied independently, which resulted in a variation of the tunneling conductance for the parallel and antiparallel magnetization configurations. Based upon TM's previous analysis, Julliere expressed this magnetoconductance

(the difference in conductance values for the parallel and antiparallel magnetization configurations) as $\Delta G/G = 2P_1P_2/(1+P_1P_2)$, where P_1 and P_2 represent the conduction electron spin polarizations in the Fe and Co. The maximum measured value was 14%, somewhat below the anticipated value based on the 26% polarization previously deduced by the measurements of TM. Importantly, Julliere pointed out that both coupling between the ferromagnets (resulting in less-than-saturated magnetization), and spin-flip scattering in the Ge or at the interfaces, could reduce the overall effect. This first demonstration of spin-filtering, without the use of a superconducting analyzer film, opened up concrete experimental prospects for spin injection at higher temperatures.

A.1.2 Spin Injection in Clean Bulk Metals

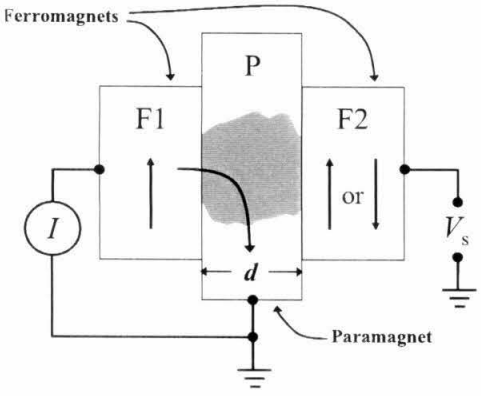

Fig. A.1 Sketch illustrating the basic components of a three-terminal spin injection device. External magnetic fields are employed to controllably switch the relative orientation of the ferromagnetic electrodes (**F1**, **F2**). The ground connection (current return) for the paramagnetic conductor (**P**) is attached many spin diffusion lengths from the region of spin injection, and is therefore far from the cloud of induced magnetization (*shaded region*). The ground connection for the detected voltage need not necessarily be the same as the ground for current return, allowing for nonlocal four-terminal measurements, as described in the text.

In 1976, A. G. Aronov predicted that electron spin resonance (ESR) signals could change in the presence of a spin-polarized current injected directly from a ferromagnet into a normal metal [113]. The injected spins, he proposed, would also induce a polarization of the nuclei as the spins scattered. His proposal implies that one should be able to quantify the injected spin density through a local measurement of the spin polarization of either the conducting electrons or the nuclei.

Direct evidence of spin-polarized transport within an "Ohmic", non-tunneling configuration was first provided in 1985 by Johnson and Silsbee (JS). They carried out experiments where a non-ferromagnetic, paramagnetic metal (**P**) was placed between two metallic ferromagnets [16]. Fig. A.1 provides a conceptual illustration of the experimental configuration for this class of experiments. A current sourced through a ferromagnet, **F1**, acquires a spin polarization due to the remnant magnetization of the ferromagnetic material. Injection of this current into a nonmagnetic metal, **P**, induces a net spin polarization within it (represented as a shaded cloud of magnetization in Fig. A.1); this decays spatially with a characteristic length scale λ_{sf}. If the separation, d, between the two ferromagnets **F1** and **F2**, is less than this spin diffusion length, one would expect that the second ferromagnet, **F2** should "interact" in some characteristic way with this nonequilibrium spin polarization. As described below, for conditions of open-circuited output terminals this interaction results in an induced voltage, V_s, as shown in Fig. A.1. The initial ideas and experiments involved *diffusive* electron transport; this is valid in the limit where both d and λ_{sf} greatly exceed the mean free path for momentum scattering.

For such experiments it is crucial to confirm that the induced voltage, V_s, is truly representative of spin accumulation within the paramagnet, rather than simply being the result of spurious, uncontrolled potential drops within the device. In the spin injection work to date, there are two principal ways in which this has been pursued. The first, and most unambiguous of these techniques was employed by JS in their 1985 experiments; it is based on what is called the Hanle effect. (Below, we shall describe the second technique, which we term "polarize/analyze" experiments.) The Hanle effect experiments involve application of an external magnetic field to induce precession of the injected spins as they traverse from injector to collector across the device. Changing the magnitude of this field changes the rate of precession and, hence, the total precession angle accrued by each carrier during its traversal of the device. (Special care must be taken to insure the magnetization of both the ferromagnetic injector and collector remain unaffected by the applied field which is usually applied perpendicular to the plane of the sample). The total spin current from injector to collector obviously involves the entire ensemble of diffusing carriers, hence there can be a rather wide variation in the path lengths that are traversed. This leads to a wide variation in transit times, and in the total precession accrued by the individual spins during their traversal. When the external field is sufficient to result in an *average* total precession during transit of order π, the net effect sums incoherently over the ensemble, and the spin-induced signal at the collector V_s becomes suppressed. These arguments directly lead to a field scale for the decay of the Hanle effect in a diffusive system [114].

Fig. A.2a provides a schematic of the actual device geometry employed by JS. In their first experiments **P** comprised a ~50 μm thick aluminum foil; atop this a thin permalloy (a NiFe alloy) film was lithographically patterned to form both the ferromagnetic injector and detector electrodes. The device dimensions were quite large by contemporary scales, but this was compensated by the high purity of the single crystal Al foil employed, which in some devices was reported to yield an electron mean free path of 17 μm. The spin diffusion lengths, λ_{sf} (discussed below), were therefore also correspondingly large, reportedly approaching 500 μm. In these experiments the separation between injector (**F1**) and detector (**F2**) was varied between 50 μm and 300 μm.

Representative Hanle effect data obtained at liquid helium temperatures from these devices are shown in Fig. A.2b. The signal levels observed in these first experiments were exceedingly low—at best of order tens of picovolts, even for current drive levels up to ~30 mA. The data

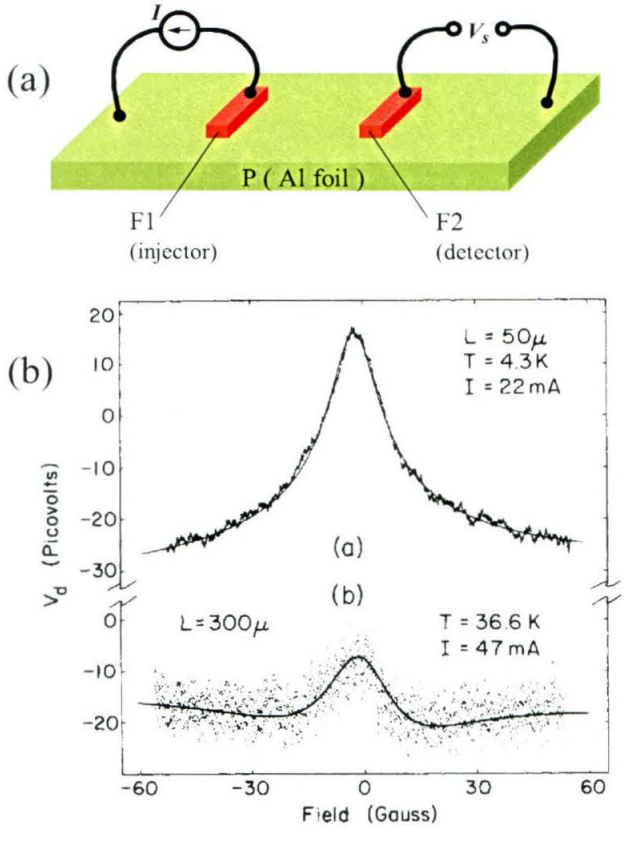

Fig. A.2 Schematic representations of the spin devices of Johnson and Silsbee employing Al foil, which was 50 μm thick and 100 μm wide [16]. (b) Representative data from all-metallic spin devices: Hanle effect experiment [16, 114, 115].

were obtained by sourcing current through **F1** and into the Al bar, then extracting it from the near end, *i.e.*, away from **F2**. A SQUID picovoltmeter was used to measure the induced voltage V_s at **F2** with respect to opposite end of the Al foil. From this a spin transresistance, $R_s = V_s / I_s$, could be deduced. This nonlocal, four-terminal measurement configuration (sometimes termed a "potentiometric" measurement) is conceptually equivalent to that pictured in the three-terminal device of Fig. A.1. Here it allows further decoupling of the "spin component" of transport, arising from diffusion of spin-polarized electrons in the Al from one ferromagnet to the other, without obfuscation from potentially large background voltage offsets potential drops associated with the regular unpolarized components of transport. However, the measurements can still be plagued by small background offsets due to asymmetries in electric field gradients (arising from device asymmetries) and from Hall voltages in the paramagnetic conductor. The latter can be especially vexatious in semiconductors; we shall discuss them in more detail below.

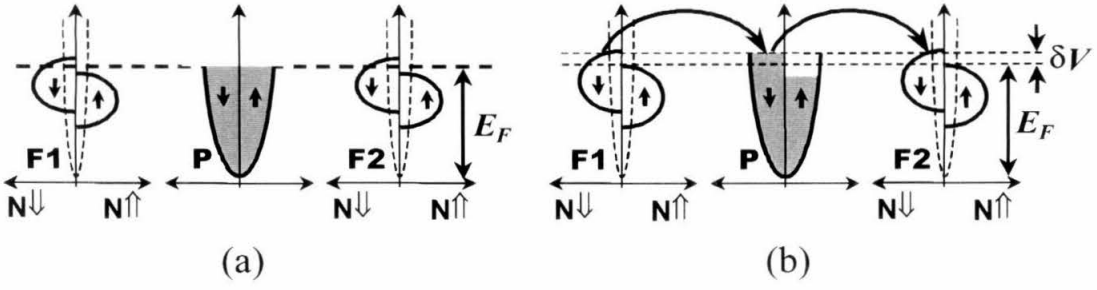

Fig. A.3 Schematic diagrams of the densities of states (horizontal axis) versus energy (vertical axis) in the ferromagnets and paramagnets. In (a) the zero current bias case is shown while in (b) bias current from **F1** to **P** preferentially builds up one spin population (shaded)

Particularly noteworthy is that despite the clear evidence that the Hanle effect provides for spin injection—to date, the data of Fig. A.2b are still, to our knowledge, the only such traces that can be found in the entire literature of spin injection.

A.1.3 Conceptual Picture of Spin Injection

A conceptual understanding of the basic origin of spin-induced signal is provided in Fig. A.3 for the all-metallic case, based upon the qualitative picture developed by JS in their early work [114, 115]. A series of density of states diagrams representing the device components are shown, each with spin down on the left of the vertical axis and spin up on the right. This represents the

case in which the magnetization of the ferromagnets is parallel. At zero current bias, as shown in Fig. A.3a, the Fermi levels in the injector (**F1**), paramagnet (**P**), and detector (**F2**) all line up and the system is in equilibrium. When a current is sourced into **F1**, as shown in Fig. A.3b, spin polarized electrons are injected from **F1** into **P**; as a result its down-spin population increases, while its up-spin population decreases as the initially unpolarized carriers depart from the current return lead. The steady-state balance between spin injection and spin relaxation in **P** directly determines the amount by which the electrochemical potentials of its two spin subbands are offset. The open-circuit boundary condition on **F2**, which corresponds to an ideal voltage measurement, implies that (in steady-state) there is no net current flow into **F2**. For this to hold, the down-spin electrochemical potential of **F2** must rise to match that of the down-spins in **P**. In this very simple picture it is assumed that the device is formed from ideal (Stoner) ferromagnets, **F1** and **F2**, possessing 100% spin polarization at the Fermi energy, and that **P** is a simple free-electron paramagnetic metal.

Based on this simple picture of spin injection it is possible to arrive at a crude estimate of the spin-induced voltage [114, 115]. Magnetic moments are injected into **P** at the rate J_m per unit area, this magnetization current density injected into the paramagnet can be written as,

$$J_m = \eta \frac{\mu_B J_e}{e}, \tag{A.1}$$

where J_e is the electric current density; μ_B is the Bohr magneton; e is the electron charge, and η is a phenomenological parameter that subsumes all "nonidealities" associated with the injection process, such as partial polarization at the Fermi energy, differences in Fermi velocities, and partial or inefficient spin transfer across the interface. We shall discuss it further below.

In steady state, these injected spins are relaxed at the rate $1/\tau_{sf}$, where τ_{sf} represents a simple relaxation time approximation for the spin flip scattering rate (*i.e.*, some form of k-space average over the Fermi surface electrons). Therefore the resulting nonequilibrium magnetization, M, in **P** is

$$M = \frac{J_m \tau_{sf}}{d} = \frac{\eta_1 \mu_B J_e \tau_{sf}}{ed}, \tag{A.2}$$

where d is the separation between **F1** and **F2** and η_1 is the "non-ideality parameter" for injection across the **F1**-**P** interface. Again, we stress that this result applies to the diffusive case which

holds for $d \gg \ell = v_F \tau$, where v_F and τ are the Fermi velocity and momentum lifetime in **P**, respectively. We also assume that the separation d is smaller than (or at least comparable to) the spin diffusion length $\lambda_{sf} = \sqrt{v_F^2 \tau \tau_{sf} / 3}$, so the effect is not diminished by spin relaxation. The spin-induced voltage detected at **F2** is proportional to the rise in chemical potential in **F2** associated with the injected spins in **P.** Since M/μ_B is the number of nonequilibrium spins:

$$\eta_2 \frac{M}{\mu_E} = N(E_F) e V_s , \tag{A.3}$$

where $N(E_F)$ is the density of states at the Fermi level. This is valid assuming linear response, *i.e.*, that V_s is sufficiently small so that $N(E)$ has a roughly constant value $\sim N(E_F)$ over the energy range of the injected electrons. Assuming **P** is a simple, free electron metal, $N(E_F) = 3n/2E_F$, where n is the volume density of electrons, we arrive at

$$R_s = \frac{2\eta_1 \eta_2}{3e^2} \frac{E_F \tau_{sf}}{nAd} . \tag{A.4}$$

Apparently the success of the simple description above hinges upon the phenomenological parameters, η_1 and η_2. (In the simplest picture used here, one assumes that the interfacial properties are uniform and identical over the entire contact area A, hence $\eta \equiv \eta_1 = \eta_2$. Buried within these "fudge factors" are the real physics of spin injection from the ferromagnet into the paramagnet (and vice versa).

With knowledge of all parameters on the right side of expression Eq. (A.4), values for R_s can be extracted. However, it is clear that there is significant ambiguity regarding the values for τ_{sf} that should be applicable to such experiments, and almost complete lack of *a priori* knowledge about the appropriate values for the spin injection efficiencies η_1 and η_2. If we assume τ_{sf} is equal to T_2 ~10ns, as measured in CESR experiments on Aluminum at 4K [116], and furthermore assume the ideal situation holds where $\eta_1 = \eta_2 = 1$, the maximum expected spin transresistance should be of order $R_s \sim 1\mu\Omega$. The value found in the JS experiments is significantly smaller, $R_s \sim$ 2nΩ. Alternatively, one can turn the problem around by assuming the interfaces behave identically, and deduce values for $\eta_1 = \eta_2 \equiv \eta$. from the measured values of R_s and values of τ_{sf} (assumed equal to T_2) obtained from the literature. For these early Al spin injection devices, the

values for η deduced for range from 0.043 to 0.075. Given that Tedrow and Meservey observed Fermi surface spin polarization for metallic ferromagnets in the range of tens of percent, it initially appears that an additional order-of-magnitude suppression of the spin injection occurred. Presumably this may have arisen from uncontrolled interfacial effects. But the results of this qualitative and rather incomplete picture should not be interpreted too literally. Soon after the publication of the JS experiments, van Son [117] *et al.* provided a more detailed model of transport across the metal-metal interface that provides deeper insight to the problem. After careful matching of the chemical potential for different spin bands, they found that the spin splitting could be significantly suppressed due to the high conductivity of metals. This shall be described in further detail in Sect. A.4 of this chapter.

A.1.4 Spin Injection in Impure Metal Films

In 1993 Johnson announced the realization of a spin (injection) transistor based upon thin metallic films [17]. From the results obtained, prospects for non-volatile transistor-like memory elements and spin injection logic elements were raised [118-120]. The devices formed a sandwich structure, as depicted in Fig. A.4a, in which the two thin metal film ferromagnets, **F1** and **F2**, were positioned on opposite sides of a 1.6μm-thick disordered, polycrystalline, Au film (labeled **P**). A second normal metal contact, **N**, (which sensed the average local, spin-averaged electrochemical potential in **P**) was positioned near the detector ferromagnet **F2** to provide a local "ground" reference for the spin-dependent voltage that was detected.

Evidence for spin injection in these devices was based solely through the second of the two aforementioned techniques, namely polarize/analyze experiments. These are somewhat easier to carry out, compared to spin precession experiments; the measurements involve application of a magnetic field in the plane of the sample, along the easy axis of the ferromagnets. This is swept to cause their relative magnetizations to switch. A voltage jump at the detection terminals, *i.e.*, in V_s, is expected when the injector and detector magnetizations change from parallel to antiparallel. In other words, these devices yield a two-state output depending on the relative orientation of the magnetization in the two ferromagnetic contacts.

Representative data from these experiments are shown in Fig. A.4b. The pronounced dips in voltage correspond to antiparallel orientation of the magnetization in the ferromagnetic contacts. An injected current of several mA resulted in a spin-induced voltage at the output of order several μV—*immensely* larger than in the first experiments. The possible explanation advanced at the time was that the much smaller size of the paramagnet yielded a profound increase in the efficiency of spin accumulation. The magnitude was much greater than should be expected, however, even for 100% polarization of the injected electrons. This profound signal enhancement occurred despite the known, and dramatic reduction in λ_{sf}, (deduced to be ~1.5μm), suffered as a direct result of the much lower quality of the impure, polycrystalline Au films employed for **P**. The data could only be explained by values of η exceeding unity. This is obviously unphysical and reflects an incomplete understanding of the nature of the data obtained. Furthermore the device geometry of [17] suffers from the fact that the current flows not only perpendicular, but also parallel, to the **F** layers. This means that any magnetoresistance in the layers (in particular AMR) may contribute to, or even completely dominate the measured signal.

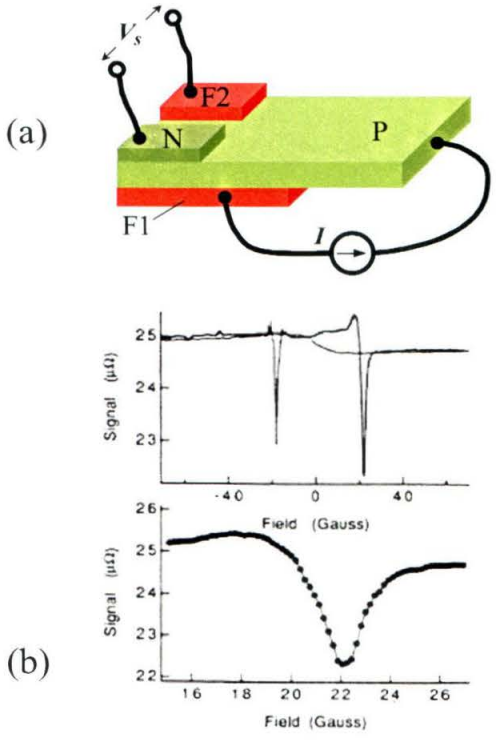

Fig. A.4 (a) The geometry of Johnson's all-metal "spin transistor". (b) Data obtained from a polarize/analyze experiment with such a device {Johnson, 1993}.

Eight years elapsed before further confirmation of spin injection phenomena in all-metal systems was obtained. These latter experiments, in conjunction with significant theoretical

development that occurred in the intervening period, have significantly enhanced our understanding of the complexities of spin injection. These more recent experimental and theoretical developments in diffusive spin injection are described in Sect. A.4.

A.2. Toward a Semiconducting "Spin Transistor"

A.2.1 Why a Spin Transistor?

Johnson motivated his work on the all-metal spin transistor by proposing that such devices would offer new routes for realizing nonvolatile memory and spin-based logic elements [118-120]. However, since that time, as mentioned, spin injection has continued to be a topic of fundamental research while the much more robust phenomena of GMR and magnetic tunneling have already evolved into commercial products. Although the push to develop spin-injection based *memory elements* has evaporated in the intervening period, interest in low power logic may remain [121]. In fact, recent concepts for novel, all-semiconductor spintronic devices have emerged, and these are generating new enthusiasm for "spin transistor" research [122-124]. More specifically, motivation for realizing robust electrical spin injection now arises from recent developments in "spin transfer" [125] and "spin imprinting" [126]. The former refers the use of spin-polarized currents to achieve magnetic actuation (*e.g.*, domain reversal in nanomagnets), and the latter refers to prospects for electrical control of the polarization of localized nuclear or electronic moments. Both phenomena may ultimately play important roles in future spintronic systems and in the longer-term quest for realizing solid-state quantum logic.

A.2.2 Why Semiconductors?

Semiconducting materials offer the possibility of new device functionalities not realizable in metallic systems. Equilibrium carrier densities can be varied through a wide range by doping. Furthermore, because the typical carrier densities in semiconductors are low compared to metals, electronic properties are easily tunable by gate potentials. There is, of course, a vast body of knowledge concerning semiconductor materials and processing; these are amongst the most pure materials available commercially. All these attributes converge to allow definition of microelectronic devices with power gain, enabling the fan-out necessary to create massively integrated systems. Additionally, recent advances have allowed optimization of interfaces, at the level of atomic-scale control, between different epitaxial materials. In fact, many of these

processes have already been scaled up to commercial production lines. These factors, in concert with recent advances in materials science of high-quality magnetic semiconductors now make semiconductor materials perhaps the first, and natural choice for future spintronic applications, especially those involving large scale integration of spintronic devices.

A.2.3 Concept

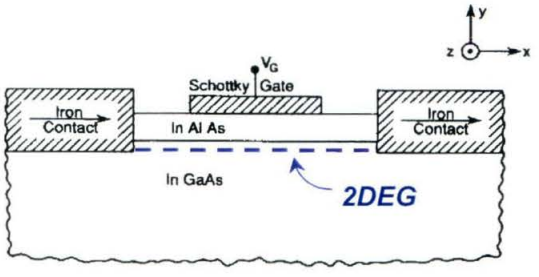

Fig. A.5 A spin-FET proposed by Datta and Das, conceptually similar in operation to an electro-optic modulator. Two magnetic contacts serve as spin polarizer and spin analyzer. The propagation medium between them—capable of inducing a gate-controllable net rotation of spin orientation—is a two-dimensional electron gas (2DEG).

In 1990, special attention was drawn to the possibilities of spin injection in semiconducting systems by the proposal of Datta and Das for a "spin transistor". Their idea was based upon the manipulation of the spin state of carrier via controlled spin precession [3]. This device is at first glance much like a conventional FET; it has a current source, a current drain, and a channel in between with a tunable conductance. However, the spin transistor was based upon contacts envisaged as spin selective, *i.e.*, capable of injecting and accepting only one spin component of the carrier distribution. Of course, polarize/analyze experiments are configured precisely in this manner. However, the similarity with previous spin injection experiments carried out with diffusively propagating carriers ends here.

The Datta/Das proposal was couched in terms of spin-coherent *transmission* through a hypothetical transistor. Their idea was drawn from direct analogy to an electro-optic modulator (EOM), a device that provides electrically tunable optical transmittance. An EOM operates by first polarizing the incident light, then rotating the resulting beam's polarization by propagating it through an optical medium with birefringence that can be tuned electrically. Finally, modulation of the beam's intensity is realized when this transmitted beam is "analyzed" by a second polarizer just before exiting the device. In the spin transistor, by analogy, the proposed method of

achieving controlled rotation of the transmitted "beam's" *spin* orientation was through gate-tunable spin-orbit coupling for the electrons within the device channel. This will be described in more detail below.

Initially it might seem that the same conditions required for observation of the Hanle effect in a diffusive system—namely, that the spin diffusion length greatly exceeds the device dimensions—should be sufficient for the operation of spin transistor. This is not the case; the requirements for operation of the spin transistor are far subtler. The substantial additional complexity arises from the fact that the magnetic field that induces spin precession is here not simply an externally applied uniform magnetic field as in the Hanle case. Instead, as described below, for the spin transistor it is an effective "Rashba field" that is relevant. Its dependence upon carrier momentum introduces new ways in which spin coherence can be scrambled as the carriers propagate from the injector to collector within a spin transistor.

For a completely ballistic device, these issues become somewhat simplified as is described in **Appendix B** of this thesis. But even in this limit if the injected electron distribution is characterized by finite occupancy of *multiple* momentum states (subbands), significant complexity persists. Hence the simplest case, considered by Datta and Das, is that of a ballistic device involving occupancy of a *single* transverse subband (**Appendix B**). At this juncture even for *unpolarized* electrons it remains quite difficult to realize ballistic, single-subband transport within devices having any appreciable length. Since the original demonstration of single-subband transport in a quantum point contact [127, 128], such transport over longer "device scale" dimensions has been demonstrated solely, to our knowledge, in quantum wires fabricated by cleaved-edge overgrowth [129] and in nanotubes [130].

A.2.4 Prerequisites for Realizing a Spin Transistor

There are four fundamental requirements for successful implementation of a spin transistor: *injection* of a spin polarized current, spin coherent *propagation,* induction of controlled spin *precession,* and spin-selective *collection.* Below we shall first briefly review the status quo of our knowledge regarding spin coherent propagation and the gate control of spin precession. The state of the art of electrical spin injection and spin-selective collection will emerge in subsequent sections of this chapter.

A.2.5 Spin Lifetime in the Conduction Channel

In the past four years, it has been proven experimentally that spin coherence can persist in doped semiconductors on very long temporal (>100 ns at low temperatures) and spatial scales (> 100 μm) [4, 131-134]. All of these experiments were carried out using optical techniques, involving time resolved pump-probe method. This involves excitation of spin-polarized electron-hole pairs by short pulses of circularly polarized light from an ultrafast laser. This excitation results in carriers far from equilibrium. In general the spin polarized holes are found to relax quickly, but the spin polarized electrons persist for long times. At present, the extent to which the spin dynamics of these hot electrons differ from those of spin-polarized electrons at Fermi surface is unclear. Since spin scattering is closely related to momentum scattering, one might expect the spin relaxation rate at the Fermi surface to be *even slower* than that observed for hot carriers. But, to date, difficulties in manipulating near-equilibrium electrons, have precluded measurement of spin lifetime at the Fermi surface. But the picture that emerges is extremely promising for electrical spin injection devices.

A.2.6 Gate Control of the Spin Orbit Interaction (Theory)

Most III-V semiconductors have zincblende lattice structure, which is asymmetric with respect to inversion. The intrinsic crystal fields lead to a conduction band spin splitting proportional to k^3, even at zero magnetic field. Spin-orbit coupling can also be induced by an *interfacial electric field* within a heterostructure. Carriers confined to moving in an asymmetric quantum well will experience an effective magnetic field, called the Rashba field that may induce spin precession [135]. The rate of this Rashba-field-induced precession should be tunable through an external gate voltage, which can serve to alter the pre-existing, "built-in" confinement potential. The Rashba Hamiltonian is usually written as

$$H_R = \alpha \left[\boldsymbol{\sigma} \times \mathbf{k} \right] \cdot \hat{z} , \tag{A.5}$$

where the spin-orbit interaction parameter α is linearly dependent on $\langle E_z \rangle$ through the energy gap and the effective mass, a represents the Pauli spin matrices, and σ is the direction of the electric field. The total Hamiltonian, assuming that the Rashba effect dominates all other spin-coupled factors, is, where $H_k = \hbar^2 k^2 / 2m^*$ is the kinetic energy part of the Hamiltonian. The eigenstates for up and down spins are then [135],

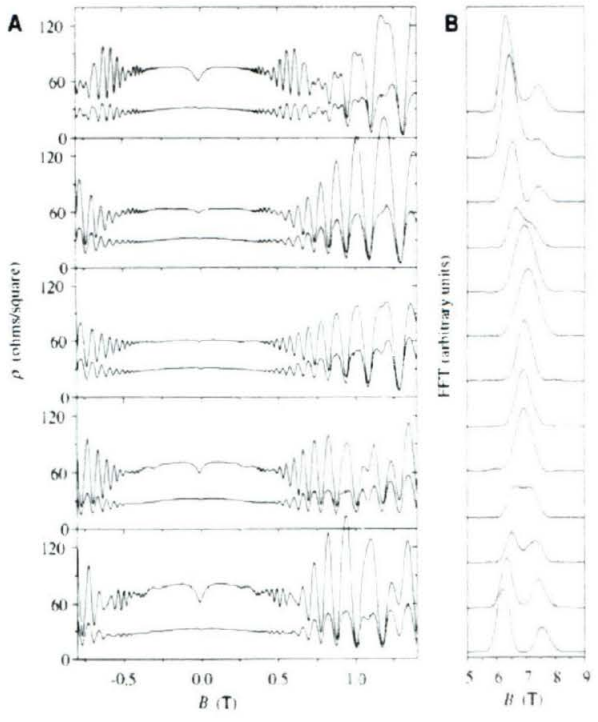

Fig. A.6 Shubnikov de Haas oscillations in a two-dimensional hole gas providing an especially clear demonstration of the beating characteristic of spin split bands. (After Ref. [139]). Spin-splitting in these experiments was changed by applying an electric field perpendicular to the 2-D plane $E_{\perp}$. Through simultaneous use of both front and back gate electrodes the spin splitting could be tuned while the electron density was held fixed. (a) Magnetoresistance traces, all at a density of 3.3 ×11 cm^{-2} but at different values of $E_{\perp}$. The data shown are from the low-mobility $[01\bar{1}]$ (top trace in each panel) and high-mobility $[\bar{2}33]$ (bottom trace in each panel) directions. (b) Fast Fourier transforms (FFT) of the Shubnikov de Haas oscillations, showing that the spin splitting is being tuned through a minimum.

$$E^{\pm}(k) = \frac{\hbar^2 k^2}{2m^*} \pm \alpha |k| . \tag{A.6}$$

So that the spin splitting energy, Δ_R, at zero magnetic field at the Fermi energy is $\Delta_R = 2\alpha k_F$. In traversing a distance L in the quantum well, an electron will precess an amount $\Delta\theta = \omega_L L / v_F$, where $\omega_L = \Delta_R m^* L / \hbar^2 k_F$. The angle through which an electron precesses in traversing a distance L is thus [3],

$$\Delta\theta = 2m^{*}\alpha L/\hbar^{2}. \qquad (A.7)$$

Values for α given by Nitta *et al.* [136, 137] and Heida *et al.* [138] range between 0.5 and 1 × 10^{-11} eVm, corresponding to an energy splitting Δ_R = 1.5 to 6meV. From the expression above, the tunability of spin-orbit coupling is derived through tuning the value of the parameter a by an external gate. We now examine the evidence for such tunability.

A.2.7 Gate Control of the Spin Orbit Interaction (Experiment)

Gate control of spin splitting in quantum wells has been demonstrated in various two dimensional electron gas systems. There have been considerable theoretical studies on the spin-splitting of the conduction band in zincblende compounds [139-143]. Experimental estimates have been presented, mostly through extrapolations to zero field of magnetotransport data and (with reduced accuracy) through electron-spin resonance experiments. Other experimental measurements of this splitting have been obtained from spin relaxation [144], spin precession [145], weak-localization magnetotransport measurements [146], and zero-field Raman scattering experiments [147].

Table 8.1 Observed spin band splitting and Rashba coupling parameter in various InAs quantum wells.

Quantum Well type	Δ_R (meV)	α ($\times 10^{-11}$eVm)	Tunability	Reference
GaSb/InAs/GaSb	3.7	0.9	-	Luo [148]0}
AlSb/InAs/AlSb	3.3-4.5	0.6	No	Heida [138]8}
AlSb/InAs/AlSb	0	0	-	Brosig [149]1}
AlSb/InAs/AlSb	0	0	-	Sasa [150]2}
AlGaSb/InAs/AlSb	5.6-13	1.2-2.8	-	Sasa [150]2}
InGaAs/InAs/InGaAs	5.1-6.8	0.6-1.1	Yes	Nitta [151]1}
InGaAs/InAs/InGaAs	9-15	2-4	Yes	Grundler [152]2}
SiO_2/InAs(p-type)	5.5-23	1-3	Yes	Matruyama [153]3}

(a) **AlGaAs/GaAs systems.** There has been extensive study of both two-dimensional electron gases (2DEG) and two-dimensional hole gases (2DHG) in GaAs heterostructures. Using electron-spin-resonance techniques, the spin splitting at zero magnetic field for an $Al_xGa_{1-x}As$/GaAs 2DEG was found by extrapolation to be about 30 μeV [154]. This result, however, was

later argued to be an artifact of extrapolation from the small magnetic field range over which the experiments were performed, namely in the regime where the Fermi energy located between spin-split Landau levels [155]. Through Raman scattering a spin splitting energy of 0.74 meV was measured at zero magnetic field for an 18nm-thick quantum well. By detecting the beating pattern in the Shubnikov-de Haas oscillations, Ramvall [156] *et al* measured an increase in the spin splitting from 0.46 to 0.61 meV with fixed electron concentration. Given their control of the density, this increase was attributed to gate-controlled increase in the value of α. These measured zero-field spin splittings are quite small compared to those reported for 2DEG's in narrow-gap systems (usually 1.5 to 3.5 meV). The dominant mechanism inducing such zero-field splitting is generally considered to originate from interfacial potential. Nevertheless, in most cases direct modulation of α through an external gate does not seem to be unequivocally demonstrated. Magneto-transport measurements of 2DHG's in both triangular and square quantum wells of GaAs/AlGaAs were made by Störmer [157] and Eisenstein *et al* [158]. Their results reveal a lifting of the spin degeneracy in triangular quantum wells, but the spin degeneracy remains in structures with symmetric wells. Recently, very convincing evidence has been provided for wide tunability of α in both classes of quantum wells, via the application of both substrate and surface gate biases [159], [139].

(b) **InGaAs system.** This is the system originally motivated the idea of the spin transistor, and it enables achievement of both high mobility and high zero-field spin-splitting. Extremely clear MR oscillations were first reported by Das *et al.* [160], and the 1.5-2.4 meV spin splittings deduced from them were attributed to the Rashba mechanism. Nitta *et al.* subsequently measured the spin-orbit interaction in InGaAs in an inverted InGaAs/InAlAs quantum well [136]. In this case the spin-orbit coupling was tunable from 0.6 to 1×10^{-11} eVm by a gate potential. The corresponding changes in the spin-splitting energy were from 6 to 4.5 meV. Later, in experiments performed on a quantum well with higher In concentration, anisotropic spin-orbit coupling was found [161] with values as high as 7.8×10^{-11} eVm in certain crystallographic directions. On the other hand, Engels *et al.* [162] also found that significant tuning of α is possible in a modulation doped InP/InGaAs/InP quantum well, by biasing with a top gate.

(c) **InAs quantum well.** Because of its small effective mass and narrow bandgap, this system has received much attention for its potential application as a medium for realizing the spin transistor. Spin splitting is generally predicted to increase in smaller band gap materials [142]. These materials also have the additional advantage that ohmic contacts can be easily be formed

between them and ferromagnetic metals since there is no Schottky barrier at the interface. Conflicting results have been presented in InAs 2DEGs over the past decade. Zero-field spin splittings as large as 3.7 meV were first observed by Luo *et al.* [148] in InAs/GaSh quantum wells, via magnetotransport measurements. The Rashba mechanism was purported to be dominant over intrinsic, crystal field effects and a spin-orbit coupling constant $\alpha_s = 0.9 \times 10^{-11}$ eVm was deduced for a 7.5nm well. In the InAs/AlSb system, tunability was not initially demonstrated [138], [149, 150], although many attempts were made to realize spin injection devices in this system. Even the spin splitting itself remains controversial in this materials system. Heida *et al.* [138] first reported a spin splitting of 3.3-4.5 meV at zero magnetic field. The value of α derived from their measurements did not change significantly with electron density. Subsequent experiments indicated that the expected beat pattern in the magnetoresistance is completely absent in square quantum wells made from this materials system [149, 150]. These difficulties subsequently induced more careful heterostructure designs involving asymmetric quantum wells. These efforts have now proven to be quite successful. One method that was developed is to replace AlSb on one side of the quantum well by AlGaSb [150], which gives a fairly large band splitting (13 meV) and (values as high as 3×10^{-11} eVm). The other trend is to asymmetrically insert an InAs quantum well into an inverted InGaAs/InAlAs heterostructure (InGaAs system). Nitta *et al.* reported that the spin splitting parameter, (for such an InAs inserted InGaAs/InAlAs quantum well) is of order of 10^{-11} eVm, and was directly controllable by an applied gate voltage [151]. Very recently, Grundler revealed a very pronounced band splitting on a similar structure tuned by a positive back-gate voltage [152]. An astonishingly high value for the resulting Rashba parameter, α, was reported, and it was tunable over a factor of about 2 using an additional front gate without perturbing the well. On the other hand, comparably large tuning of α has been achieved in a 2DES confined in inversion layers of metal-oxide-semiconductor field-effect transistors on *p*-type bulk InAs [153]. A potential of triangular shape with a rather steep and high barrier is formed at the InAs/SiO_2 interface.

In summary, zero field spin splitting has now been observed in all of the above systems. It is generally agreed that in heterostructures such as 2DEGs, 2DHGs, and quantum wells, this is dominated by inversion asymmetry arising not from the crystal lattice, but from the artificially grown interfacial structure. It is clear that the Rashba coupling constant α can be tuned to a very large extent in a carefully designed selected quantum well.

The status quo regarding the remaining two prerequisites for realizing the spin transistor—spin injection and spin-selective collection—will emerge through discussions in subsequent

sections of this chapter, which review recent work. We shall provide an overall summary of the state-of-the-art in Sect.A.3.

A.3. Initial Experiments on Spin Injection in Semiconductor Heterostructures

A.3.1 Motivation and Initial Data

We begin this section by applying the model of JS to estimate the performance of a spin device in which the paramagnetic metal is replaced by an InAs quantum well. The result we obtain is of historical significance because the profound increase in the spin transresistance that was indicated provided part of the original incentive to attempt experiments in high mobility two-dimensional electron gases. However this simple estimate is expressly carried out for a diffusive system; similar ideas for *ballistic* spin polarized electron transport in high mobility electron gases are explored in **Appendix B**.

For a two-dimensional system such as an InAs quantum well, the Fermi energy is

$$E_F = \frac{\hbar^2 k_F^2}{2m^*} = \frac{\pi\hbar^2 n_s}{m^*}, \tag{A.8}$$

with m^* the electron effective mass in InAs (~1/40 of the free electron mass [163]), k_F the magnitude of the Fermi wavevector, and n_s the sheet density of electrons. Plugging this into Eq. (A.4) and substituting w (the width of the injection region) in this two-dimensional case for A (the injection area, which was relevant in 3D), we arrive at:

$$R_s = \frac{2\eta_1\eta_2}{3e^2}\frac{\pi\hbar^2\tau_{sf}}{m^* wd}. \tag{A.9}$$

The appropriate value of τ_{sf} that should be used to characterize the decay of non-equilibrium magnetization decay in InAs devices is not obvious at the outset. As a first approximation, we take the value τ_{sf} = 1.75 ps, obtained from weak antilocalization experiments [164]. This is likely to be a significant underestimate of the spin lifetime, since weak antilocalization experiments probe the electron's phase-breaking time, a much more sensitive quantity. For suppression of the spin accumulation, the entire distribution must be relaxed. On the other hand, Boggess *et al.*[165]

determined a spin relaxation time around 19 ps by subpicosecond pump-probe measurements in bulk InAs, even at room temperature. But such experiments involve hot carriers, and relaxation at the Fermi surface might be quite different.

Also unknown are the appropriate values of the spin transfer efficiencies, η_1 and η_2. To be conservative, in the absence of detailed knowledge of interfacial spin transfer in these devices, we use a value of 0.05 for the parameters η_1 and η_2. This is in the middle of the range found in the original JS experiments. Of course the ferromagnetic metal/InAs interface is completely different than the metal/metal interfaces of the JS experiment, but these initial guesses provided a point of departure for subsequent, more enlightened estimates. For a device with $w = d = 1\ \mu$m, Eq. (A.9) gives us $R_s \sim 200\ \text{m}\Omega$, about five *orders of magnitude* larger than in the all-metallic Au devices (the "Johnson spin transistor"), and *eight orders* larger than in the original JS experiments on Al foils. More importantly, a signal of this strength should be easily detectable, precluding the need for sensitive SQUID voltmeters. Moreover, if realized, this would offer substantial device potential.

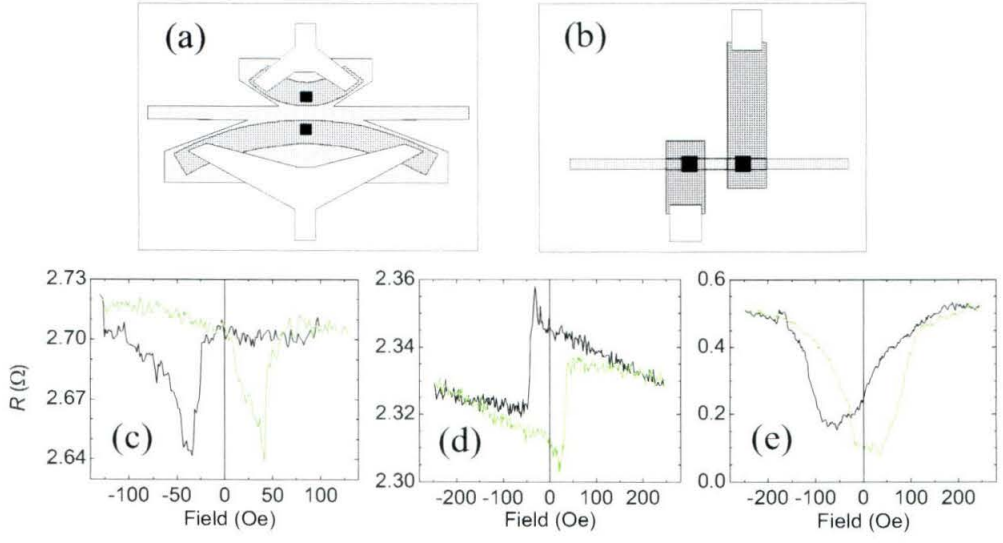

Fig. A.7 Two geometries used in an InAs devices patterned by photolithography (a and b). Black areas denote contacts (NiFe on top of exposed InAs), densely spotted areas are NiFe, sparsely spotted areas are conducting mesas, and white regions show metal interconnections. Channel widths were either 3 or 6 μm and separations varied from 6 to 64 μm. In (c) and (d) data are shown for devices similar to that in (a), while in (a) shows data for a device that of (b). Black traces are for down field sweeps, grey traces are for upfield.

There are two significant problems with the estimate above: (1) Transport is presumed diffusive, whereas 2DEG gas channels are known to be ballistic, or quasi-ballistic, over typical microdevice dimensions. Hence different spin-scattering mechanisms are operative [166]. (2) The physics of spin transfer across the interface is lumped into the phenomenal constant η, which subsumes important concerns such as the nature of interfacial magnetism, interfacial spin relaxation, and band matching and electron transmission through the interface, which may actually be spin dependent [10, 167, 168]. These are, in general, not likely to be constant factors but instead may exhibit sensitive dependence upon the non-equilibrium spin population itself. In recent, relevant experiments with optically excited (hot) electrons, the detailed and complex physics of the spin transport across interfaces is beginning to emerge. Similar work near the Fermi surface is clearly necessary and important to understand spin dynamics in electrical devices.

Despite these uncertainties, the surprising magnitude of the estimate for R_{spin} motivated several groups to pursue spin injection into InAs 2DEGs [6, 9, 169, 170]. Experimental results obtained by the Caltech group are reviewed first.

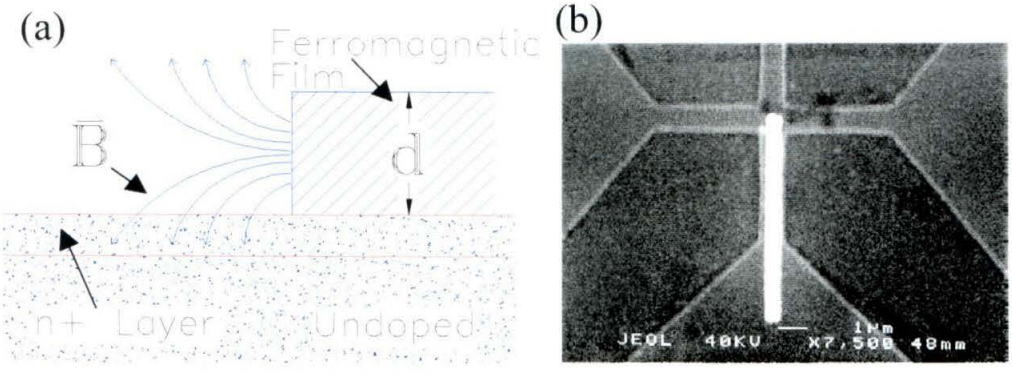

Fig. A.8 (a) Schematic side view of a device showing the magnetic fringe field whose perpendicular component, $B_{\perp}$, induces Hall voltages in the conducting underlayer. The SEM micrograph in (b) shows a NiFe magnet of width 500 nm positioned over a GaAs cross-junction. Magnetization and current flow are directed vertically, while Hall voltage is read out across the horizontal legs.

Monzon *et al.* carried out an extensive set of experiments using several different device geometries patterned by photolithography (PL) and, in later work, by electron beam lithography (EBL). Two representative PL geometries are shown in Fig. A.7. Measurements were obtained by sending a low-frequency a.c. drive current through **F1** and detecting the voltage at **F2** by a lock-in amplifier while slowly sweeping an applied, in-plane, magnetic field. In the diffusive regime

these polarize/analyze experiments should produce the characteristic signature of spin transport, namely a dip in detector voltage when **F1** and **F2** are anti-aligned. This group explored a very large number of devices at both small and large separations—and many showed such signals, suggestive of spin-coupled transport. However, as exemplified in Fig. A.7d, other forms of hysteretic behavior was also observed. After much effort this group arrived at the conclusion that, despite their similarity with the expected polarize/analyze signals, the data obtained, such as represented by the traces of Fig. A.7(c and e), are unlikely to be the result of spin injection and accumulation in the 2DEG. The origin of the signals that were seen could ultimately be traced to what is termed the "local Hall effect".

A.3.2 Local Hall Effect

Two-dimensional electron gases (2DEGs) have extremely large Hall resistances compared to metals. This is a consequence of their vastly smaller carrier densities, which makes them extremely sensitive to magnetic fields. And strong magnetic fringe fields near the edges of ferromagnets are, of course, the rule rather than the exception when working at micro- or nanometer scale dimensions. The Caltech group performed extensive experiments to understand the role that fringe magnetic fields might play in their devices [8, 171]. Fringe field close to the edge of NiFe ferromagnets can be of order 1T, and it is reasonable to assume that such a field, though it dies off quickly away from the ferromagnet, can induce sizable "local Hall" voltages in

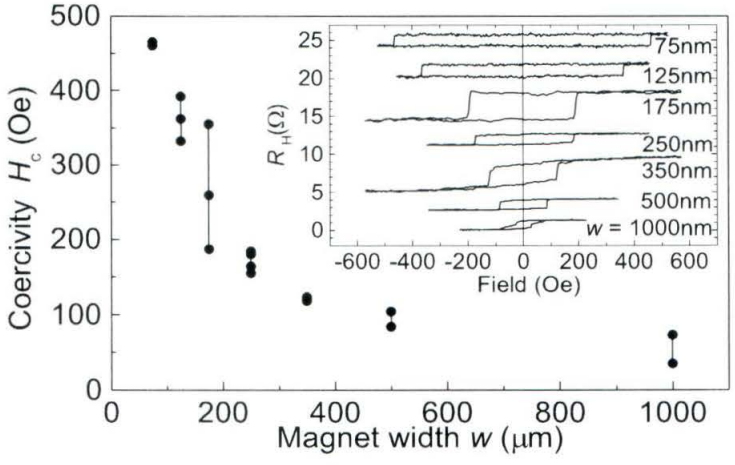

Fig. A.9 $\boldsymbol{H_c}$ versus w for numerous magnets with nominally the same deposition conditions and with aspect ratios of 10. All data were taken at room temperature. Vertical lines connect data points from magnets of the same width. *Inset:* A series of hysteresis loops for magnets of aspect ratio 10, but with varying widths. Traces are offset vertically.

the low density InAs. Special devices were developed which allowed separate evaluation of these local fields, in the absence of any spin injection phenomena. Fig. A.8 shows the device configuration utilized to characterize this local Hall effect. A small patterned ferromagnet film, **F**, is deposited atop of a semiconducting cross-junction so that one edge of **F** is positioned directly over the center of the cross. A small ac bias current is applied to the cross-junction while an external, in plane magnetic field is varied. Fringe fields from the edge of **F** induce an ac Hall voltage that is directly proportional to the magnitude and direction of the particle's magnetization. This Hall voltage is then detected with a lock-in amplifier.

Fig. A.9 shows data NiFe magnets deposited by electron beam evaporation onto Hall cross junctions patterned from 75nm thick n+ GaAs ($n \approx 10^{18}$ cm^{-3}). These data not only confirm the important role of these local Hall fields, but also demonstrate the utility of small, low electron density Hall devices for characterizing nanomagnets. Fig. A.9 displays results for a family of magnets of different widths, all with aspect ratio (length/width) ~10.

The shape of the hysteresis loops, and the coercivity of the magnets, H_c, both vary greatly with aspect ratio and width. As seen, for the narrowest magnets the hysteresis loops become very square, indicative of quasi-single domain behavior. This work demonstrated that the switching characteristics for micro- and nanofabricated NiFe magnets were quite reproducible, indicating that the previous polarize/analyze experiments were not compromised by uncontrolled magnet variation.

These results confirmed the suspicion that much of what initially appeared to be polarize/analyze effects in spin injection was, instead, most likely the result of uncontrolled local Hall fields. The sizable Hall coefficients of semiconductors place a very high threshold for believability in such experiments; the experimenter must conclusively prove that local Hall fields play no role in their experiments. It no longer seems likely that that there is a substantial body of work following these initial efforts that lacks sufficient safeguards against the local Hall effect. One must conclude that these latter efforts fail to surmount this threshold. The Caltech group subsequently used these results to design refined configurations to suppress such phenomena in nanoscale semiconductor spin devices; this is described in the next section.

A.3.3 Results from Smaller, Optimized Devices

Fig. A.10 shows SEM micrographs of two devices fabricated by electron beam lithography. These devices differed in several significant ways from the previous optically patterned devices investigated by the Caltech group. First, the magnets were completely planar. In the earlier devices the magnetic films were patterned over the edge of a mesa and the resulting height variations, albeit small, are likely to have given rise to local domain structure in the magnetic films. Second, the magnets were sufficiently narrow to be in the regime where square hysteresis loops, indicative of nearly single domain behavior were found in the local Hall measurements. The ends of these nanomagnets, from which the fringe fields of these nanomagnets emanate, were situated far from the InAs conduction channels to minimize local Hall phenomena. Finally, each chip had a set of diagnostic devices including local Hall measurements on separate nanomagnets co-fabricated with those on the spin devices, and magnetotransport devices (without nanomagnets) allowing complete characterization of the InAs quantum wires beneath. The former

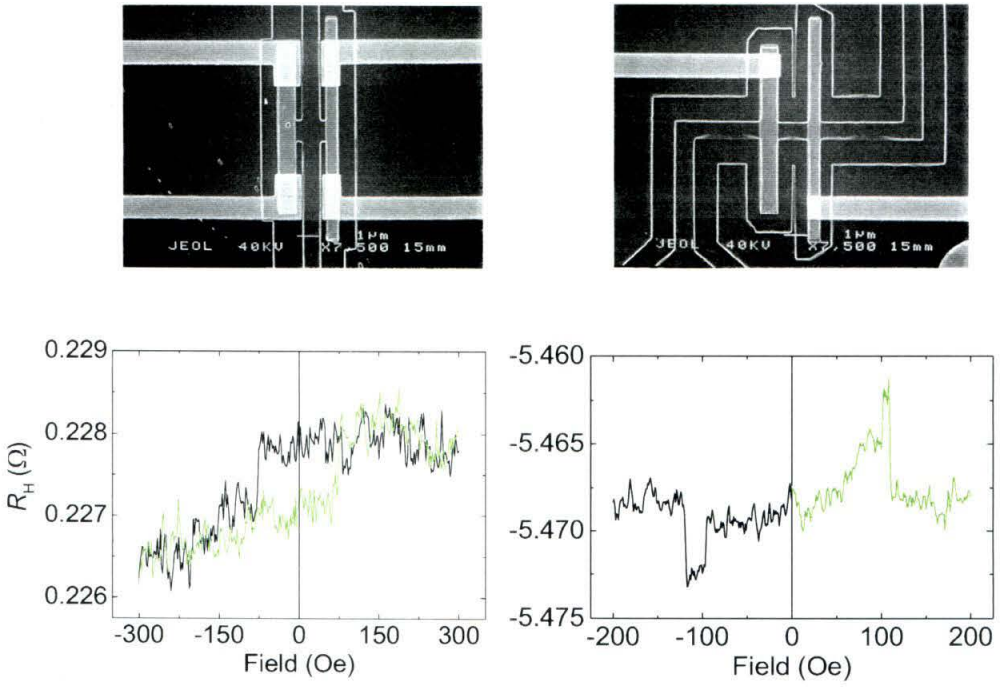

Fig. A.10 SEM micrographs of InAs quantum wire devices patterned by electron beam lithography. The channels are formed by trench etching on either side of the narrow channels (a,b). These devices have F1-F2 spacings of 1.5 μm. Magnet dimensions are 500 nm × 10 μm and 750 nm × 7.5 μm. Data from similar devices are shown in (c and d).

indicated that magnets switched sharply (within a few Oe) and at well separated coercivities attained by patterning the magnets with different aspect ratios. The latter indicated that the carrier mobility decreased in the patterned channels decreased somewhat due to the fabrication processes, but the elastic mean free path always remained above 2μm. Many dozens of spin devices patterned by electron beam lithography as exemplified by Fig. A.10, were studied [9].

In contrast to the previous generations of optically patterned devices, hysteretic phenomena in this refined family of devices were extremely scarce, occurring on only a few devices. Fig. A.10c shows data from a device similar to that of Fig. A.10a, with 750 nm **F1-F2** separation. The hysteresis loop has ~1mΩ full-scale deflection assumed to be the result of local Hall fields. Noteworthy is the fact that the scale of these local Hall signals is hundreds of times smaller in these devices compared to those observed in previous, unoptimized device configurations. This underscores the importance of controlling the role of local Hall fields in such work. Here, both moving the edges of the ferromagnets far from the conduction channel of the device and implementing quasi-single domain magnets profoundly reduced the role of magnetic fringe fields in nanoscale device operation. It was concluded that convincing spin transresistance signals were completely absent in these very large families of optimized devices. The observed magnitude of the residual, strongly suppressed local Hall signals (~1mΩ, Fig. A.10c) were taken as an *upper* bound on the spin transresistance of these devices. This upper bound can, in turn, be used to establish an upper bound on the spin transfer efficiency operative at the interfaces. The previous, simplistic estimates indicated that a spin-coupled resistance of 175 mΩ should arise for a spin transfer efficiency across the ferromagnet/InAs interface of $\eta = 0.05$. As mentioned, however, in most of the devices measured by the Caltech group a signal of only a *few* mΩ would have been readily detected. Within this simple model, obtaining such small spin transresistance values would require $\eta \leq 0.005$, meaning that the spin polarization of the current injected into the InAs must be significantly less than 1%.

As a final, cautionary note, we describe data displayed in Fig. A.10d from one particular device studied by the Caltech group. This structure was similar to the one shown in Fig. A.10b with a 1.5μm injector-to-collector separation. For this geometry one does not expect to see a hysteresis loop even if the LHE is significant. The trace, obtained from just this one device out of the very large family, looks tantalizingly like the type of spin injection data expected from a polarize/analyze experiment. But these data were inconsistent with expectations; instead of exhibiting two features with the same polarity, both a peak and a dip were observed. Furthermore,

the widths of these features were not consistent with the measured coercive transitions in co-fabricated nanomagnets. The conclusion one must draw here is that the polarize/analyze experiment, while an excellent method of quickly determining whether magnetoelectronic phenomena are at work in a device, cannot alone provide conclusive proof of spin injection. The more rigorous demonstration provided by the Hanle effect is more convincing. Hanle effect experiments performed on the particular device of Fig. A.10d failed to show the expected behavior. However even Hanle effect experiments are not a panacea. As shall be described in **Appendix B**, in the ballistic or quasi-ballistic regime it may prove difficult to separate the spin injection phenomena from magnetoresistive backgrounds arising from ballistic junction scattering phenomena. But without the clear demonstration of Hanle phenomena, any claim of spin-coupled transport must be treated with skepticism, because local Hall fields from micro- or nanomagnetic contacts are clearly unavoidable (and can play a role even in all-metal devices).

A second significant body of work on spin injection from ferromagnetic metals into small InAs 2DEG devices originated from the University of Groningen [170]. An electron micrograph and schematic layout for a representative device is shown in Fig. A.11a and (b). Both non-local measurements, and standard spin-valve type measurement were made on these devices.

Fabrication involved patterning a two-dimensional electron gas (2DEG), existing within a 15 nm thick InAs layer, into 1μm wide mesa structure. Before mesa etching and metal deposition, the whole cap layer was removed by selective wet etching. After this process, the channel mobility decreased to 1.5 $m^2/V{\cdot}s$. Ferromagnetic contacts were then made across the 2DEG mesa, after removing the oxide by Kaufmann sputtering.

Various ferromagnetic metallic contacts (Py, Co, Ni) were investigated. These metallic ferromagnets were configured to incorporated multiple terminals on each, enabling on-chip characterization of their magnetic properties. In contrast to the characterization by Caltech group carried out on co-fabricated nanomagnets via the local Hall effect measurements, characterization here of the actual magnets used in the spin devices was possible by four-terminal anomalous magnetoresistance (AMR) measurements. Different magnet widths were chosen to obtain different coercive fields for the injector and collector.

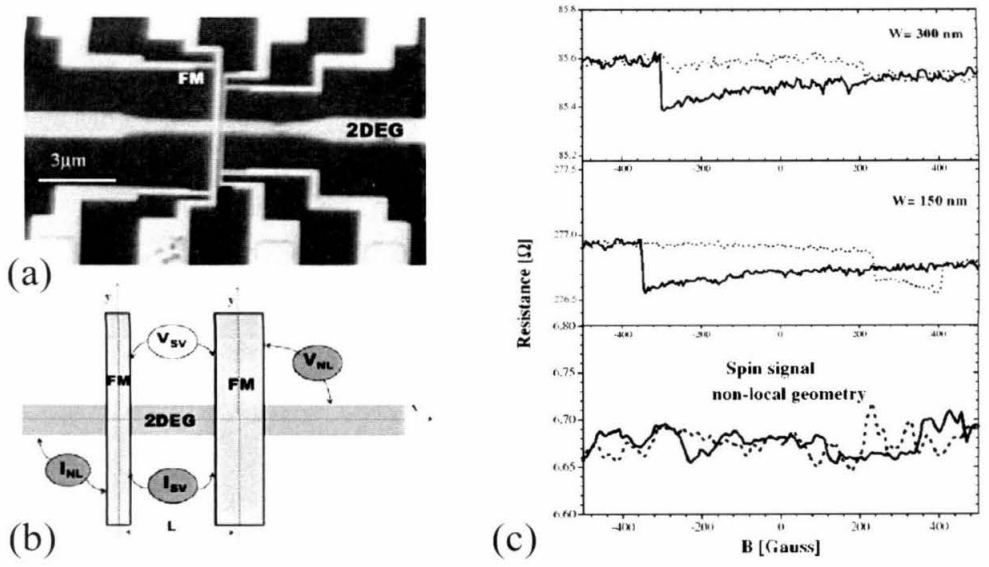

Fig. A.11 (a) Scanning electron microscope micrograph of an InAs spin injection device fabricated by the Groningen group. The 1μm wide 2DEG channel is horizontal, and two ferromagnetic electrodes are vertical. (b) Sketch of the two measurement configurations. The indices "SV" and "NL" refer to the classic spin-valve and the nonlocal geometry, respectively. (c) Non-local measurements for a Py/2DEG/Py device. Top two curves give the AMR traces for the two ferromagnetic electrodes, showing different coercive fields in one sweep direction. No spin signal is observed in any of the geometries. The dashed lines correspond to a sweep of the magnetic field towards positive fields.

Fig. A.11c shows the results obtained at 4.2 K. By measuring the magnetoresistance of the ferromagnetic electrodes, as shown in the top two traces, it can be established that the two electrodes have different coercive fields. However, the non-local voltage measurements displayed in the bottom trace of Fig. A.11c show that no spin signal was detected when the two ferromagnets switch from a parallel to an antiparallel configuration. More than 20 devices with different ferromagnetic materials were carefully characterized. None showed signals that could be attributed to spin injection, confirming the results of the Caltech group.

A number of groups have recently reported the observation of very weak spin injection signals among these are: Hu *et al.* [5], Gardelis *et al.* [6], Hammar *et al.*[7]. However, our view is that, to date, concerted effort failed to produce a *conclusive* demonstration of electrical spin injection phenomena in ohmic all-electrical ferromagnetic/semiconductor (2DEG) devices. Principal obstacles present in such structures appear to be the strong "local Hall effect", as

described above, but perhaps more importantly, the effects of "conductivity mismatch", as described in the following section, which are most severe for *Ohmic* contacts between ferromagnetic metals and non-magnetic semiconductors. In this context, it is noteworthy that the all of the initial efforts centered upon *Ohmic* contacts to the electron gas. This was motivated by the desire to realize low impedance devices which, it was presumed, would be most amenable to large scale integration for memory or logic applications. In the intervening period, however, engineering for memory devices employing (by comparison) relatively high impedance magnetic tunnel junctions has been developed. So the presumed constraint to create Ohmic devices has been lifted. As we shall describe, this "evolved" perspective opens important new horizons for efficient spin injection into semiconductors.

A.4. Spin Injection in Diffusive Systems

This section deals with the basic physics of spin injection, accumulation and detection in media where the transport is diffusive, which means that the electron mean free path l is shorter than the dimensions of the system. For metallic systems this is usually the case. For semiconductors both diffusive and ballistic (*e.g.*, in two-dimensional electron gases) transport regimes are encountered. A description of spin injection in the ballistic case is discussed in **Appendix B**. Here we discuss the linear transport regime, where the measured voltages are linear functions of the applied currents. This should be contrasted with the non-linear transport regime, which is relevant for various semiconductor diode structures. For further reading, particularly concerning the role of spin accumulation for the giant magnetoresistance (GMR) effect in multilayer structures we refer to reviews [172, 173].

A.4.1 Basic Model for Spin Transport in Diffusive Systems.

We first give a review of the basic model for the spin transport (which we will call the "standard" model). The description of electrical transport in a ferromagnet in terms of a two-current (spin-up and spin-down) model dates back to Fert and Campbell [174]. Van Son *et al.* [117] extended the model to describe transport through ferromagnet-normal metal interfaces. A firm theoretical underpinning, based on a Boltzmann transport description, has been given by Valet and Fert [175]. They applied the model to describe the effects of spin accumulation and spin dependent scattering on the giant magnetoresistance effect (GMR) in magnetic multilayers. This model allows for a detailed quantitative analysis of the experimental results. An alternative

model, based on thermodynamic considerations, has been put forward and applied by Johnson [176]. In principle both models describe the same physics, and should therefore be equivalent. However the Johnson model has a drawback in that it does not allow a direct calculation of the spin polarization of the current (η in Ref. [176]), whereas in the standard model all measurable quantities can be directly related to the parameters of the system.

In the standard model transport in the ferromagnet is described by spin dependent conductivities:

$$\begin{aligned} \sigma_\uparrow &= N_\uparrow e^2 D_\uparrow, \text{ with } D_\uparrow = 1/3 \; v_{F\uparrow} l_\uparrow \\ \sigma_\downarrow &= N_\downarrow e^2 D_\downarrow, \text{ with } D_\downarrow = 1/3 \; v_{F\downarrow} l_\downarrow \end{aligned} \tag{A.10}$$

Here $N_{\uparrow,\downarrow}$ denotes the spin-dependent density of states *(DOS)* at the Fermi energy, and $D_{\uparrow,\downarrow}$ the spin dependent diffusion constants, expressed in spin-dependent Fermi velocities $v_{F\uparrow,\downarrow}$ and electron mean free paths $l_{\uparrow,\downarrow}$. Note therefore that the spin dependence of the conductivities is determined by *both* density of states and diffusion constants. This should be contrasted with magnetic $F/I/F$ or $F/I/N$ tunnel junctions, where the spin polarization of the tunneling electrons is determined by the *DOS* only. According to the Eqns. (A.10), in a bulk ferromagnet the current is spin-polarized, with a polarization is given by

$$\alpha_F = (\sigma_\uparrow - \sigma_\downarrow)/(\sigma_\uparrow + \sigma_\downarrow). \tag{A.11}$$

The next step is the introduction of spin flip processes, which can be described by a spin relaxation time $\tau_{\uparrow\downarrow}$, the average time to flip an up-spin to a down-spin, and $\tau_{\downarrow\uparrow}$ for the reverse process. Note that the detailed balance principle imposes that $N_\uparrow/\tau_{\uparrow\downarrow} = N_\downarrow/\tau_{\downarrow\uparrow}$, so that in equilibrium no net spin scattering takes place. This implies that in a ferromagnet $\tau_{\uparrow\downarrow}$ and $\tau_{\downarrow\uparrow}$ are generally not the same. Usually these spin-flip times are larger than the momentum scattering time $\tau = l/v_F$. The transport can then be described in terms of parallel diffusion of the two spin species, where spin-flip processes couples the carrier densities in the two spin reservoirs. It should be noted, however, that in certain ferromagnets (*e.g.*, various permalloy alloys [177]), the spin flip times can become comparable to the momentum scattering time. In this case, an (additional) spin-mixing resistance arises [172], which will not be discussed further here.

The effect of spin-flip scattering can be described by the following equation (assuming diffusion in one dimension only):

$$D\frac{\partial^2(\mu_\uparrow - \mu_\downarrow)}{\partial x^2} = \frac{(\mu_\uparrow - \mu_\downarrow)}{\tau_{sf}}, \tag{A.12}$$

Here $D = D_\uparrow D_\downarrow (N_\uparrow + N_\downarrow)/(N_\uparrow D_\uparrow + N_\downarrow D_\downarrow)$ is the spin-averaged diffusion constant, and the spin-relaxation time τ_{sf} is given by: $1/\tau_{sf} = 1/\tau_{\uparrow\downarrow} + 1/\tau_{\downarrow\uparrow}$. The general solution of Eqns. (A.10) and (A.12) for a uniform one-dimensional ferromagnet or nonmagnetic wire is now given by

$$\begin{aligned}\mu_\uparrow &= a + bx + c/\sigma_\uparrow \exp(-x/\lambda_{sf}) + d/\sigma_\uparrow \exp(x/\lambda_{sf}) \\ \mu_\downarrow &= a + bx - c/\sigma_\downarrow \exp(-x/\lambda_{sf}) - d/\sigma_\downarrow \exp(x/\lambda_{sf})\end{aligned} \tag{A.13}$$

Here, as before, the spin diffusion length is $\lambda_{sf} = \sqrt{D\tau_{sf}}$ where $D = v_F^2\tau/3$ is the elastic diffusion constant. The coefficients *a*, *b*, *c*, and *d* are determined by the boundary conditions imposed at the junctions where the conducting channel is coupled to other conducting channels, etc. In the absence of spin flip scattering at the interface, the boundary conditions are: 1) continuity of $\mu_\uparrow, \mu_\downarrow$ at the interface, and 2) conservation of spin-up and spin down currents $j_\uparrow, j_\downarrow$ across the interface.

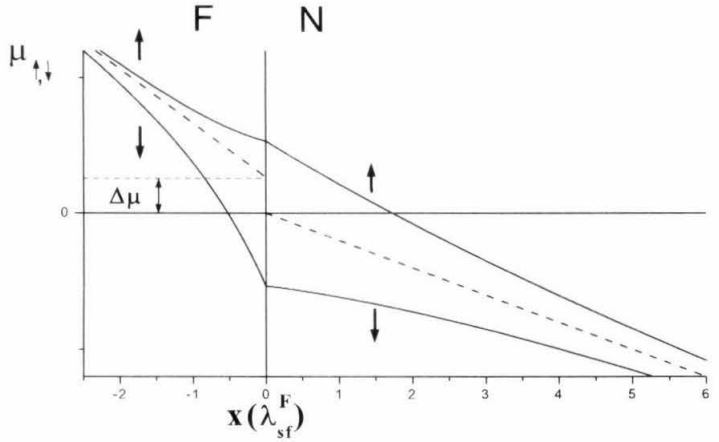

Fig. A.12 Electrochemical potentials (or densities) of spin-up and spin-down electrons with a current *I* flowing through an F/N interface. Both spin accumulation as well as spin coupled resistance can be observed (see text). The figure corresponds to $\lambda_N = 5\lambda_F$.

It should be noted that physics of spin injection and detection with F/N tunnel junctions is quite different from that of clean, Ohmic F/N contacts. The most important difference is that for tunnel contacts the spin polarization of the current is determined by the composition and properties of the first few atomic layers of the ferromagnet next to the tunnel barrier. A non-magnetic ("magnetically dead") region of only a few atoms thick can completely suppress any polarization in the transmitted current. By contrast, as will be shown in the next section, for clean contacts the spin polarization is determined by a region of thickness λ_F away from the interface. Since usually $\lambda_F > l$, this can be considered as a "bulk" property of the ferromagnet. As long as spin-flip processes can be ignored, a non-magnetic interface will have no effect on the spin polarization.

A.4.2 The F/N Interface

Van Son *et al.* [117] applied Eqns. (A.11)a – (A.13)b to describe the spin accumulation and spin-coupled resistance at a (clean) F/N interface. Fig. A.12 shows how the spin-polarized current in the (bulk) ferromagnet is converted into a non-polarized current in the paramagnetic region (a non-magnetic metal or semiconductor) away from the interface. As can be seen, two phenomena occur. First a "spin-coupled" interface resistance arises given by

$$R_j = \frac{\Delta\mu}{eI} = \frac{\alpha_F^2(\sigma_N^{-1}\lambda_N)(\sigma_F^{-1}\lambda_F)}{(\sigma_F^{-1}\lambda_F)+(1-\alpha_F^2)(\sigma_N^{-1}\lambda_N)} \tag{A.14}$$

The second phenomenon is that at the interface the electrochemical potentials $\mu_\uparrow, \mu_\downarrow$ of spin-up and spin-down electrons diverge. This implies that spin accumulation occurs, which has the maximum value at the interface:

$$\mu_\downarrow - \mu_\uparrow = \frac{2\Delta\mu}{\alpha_F} \tag{A.15}$$

with $\Delta\mu$ given by Eq. (A.14). In addition the expression for the spin polarization of the current at the interface is

$$P = \frac{I_\uparrow - I_\downarrow}{I_\uparrow + I_\downarrow} = \frac{\alpha_F\sigma_N\lambda_F}{\sigma_N\lambda_F + (1-\alpha_F^2)\sigma_F\lambda_N} \tag{A.16}$$

For conventional ferromagnets α_F is expected to be in the range $0.1 < \alpha_F < 0.7$. Thus, the expressions above show that the magnitude of spin-coupled resistance, spin accumulation and polarization of the current is essentially limited by $\sigma_N^{-1}\lambda_N$ or $\sigma_F^{-1}\lambda_F$, whichever is largest. Since the condition $\lambda_F << \lambda_N$ holds in almost all cases for metallic systems, this implies that the spin-flip length in the ferromagnet is the limiting factor. This problem becomes progressively worse, when (high conductivity) metallic ferromagnets are used to inject spin-polarized electrons into (low conductivity) semiconductors. We will discuss this "conductivity mismatch" problem in Sect. A.4.8.

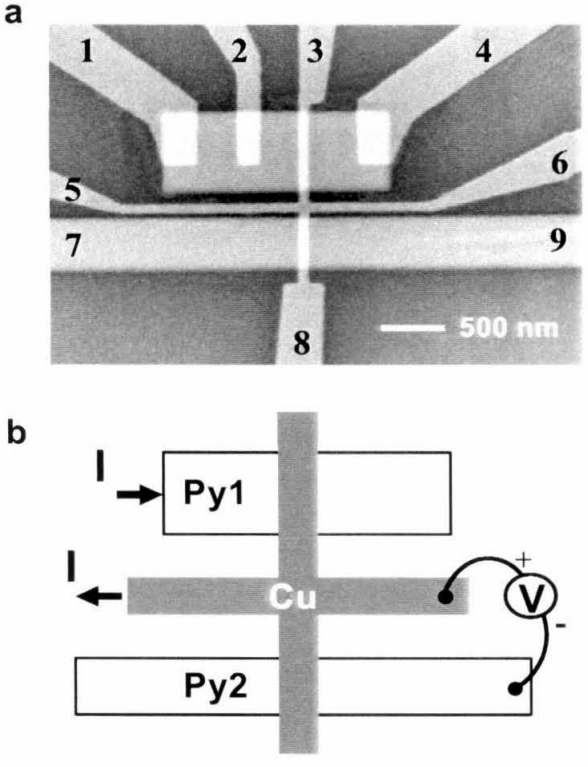

Fig. A.13 Sample layout in the experiment of Jedema *et al.* (a) Scanning electron microscope image of the mesoscopic spin valve junction. The two wide strips are the ferromagnetic electrodes Py1 and Py2. The vertical arms of the Cu cross (with contacts 3 and 8) lay on top of the Py strips, the horizontal arms of the Cu cross form contacts 5 and 6. Contacts 1, 2, 4, 7, and 9 are attached to Py1 and Py2 to allow four-terminal AMR measurements of the Py electrodes. (b) Schematic representation of the non-local measurement geometry. Current is entering from contact 1 and extracted at contact 5. The voltage is measured between contacts 6 and 9.

A.4.3 Spin Accumulation in Multiterminal Spin Valve Structures.

The fundamental way to study spin accumulation effects is to use spin-valves. These can be F/F, F/N/F, or the corresponding multilayer (...F/N/F/N/...) structures. Spin accumulation effects play an important role in these systems (for reviews see [172, 173]). However, the effects of spin accumulation are often difficult to separate from the magnetoresistance of the ferromagnets – effects such as anisotropic magnetoresistance (AMR), spin dependent interface scattering, (anomalous) Hall effects, etc. A solution is provided by using a multiterminal geometry, in which separate current and voltage contacts are and can be configured for non-local measurement. This technique was employed by JS, in their spin injection on single crystal Al at low temperatures (Fig. A.2). However, due to the relatively large size of their samples and the extremely low resistances (in the $n\Omega$ range) that resulted, SQUID based measurements were required to measure the small signals. A second experimental system employing nonlocal measurements was the Johnson spin transistor (Sect. A.1.4). This technique was also employed in the experiments of Jedema *et al.* [18], who fabricated and studied mesoscopic spin valve structures for the study of spin accumulation in metal systems. The device geometry is depicted in Fig. A.13. Two 50 nm thick ferromagnetic permalloy (Py) strips, with composition of $Ni_{0.8}Fe_{0.2}$, are deposited on a substrate. Their aspect ratio (length/width) is chosen in order to obtain different coercive fields. In a second evaporation step, a Cu cross is deposited. Care is taken that the interface between the Py and the Cu is kept clean, by using Kaufman ion source to ion mill any oxide or contamination before deposition.

Referring to Fig. A.13, in the "potentiometric" [176], or (equivalently) "nonlocal" [18] geometry, current is sent from 1 to **S** and the voltage is measured between 6 and 9. The voltage drop in the injector ferromagnet is not measured, whereas there is no net (charge) current, and therefore no voltage drop, within the ferromagnetic electrode that measures the voltage. Therefore all magnetoresistance effects emanating from the ferromagnets themselves are eliminated from these measurements.

By matching solutions Eqs. (A.13) at the F/N interfaces and the center of the Cu cross, one obtains the following expression for the measured resistance in parallel $R_{\uparrow\uparrow}$, and in anti-parallel configuration [170]:

$$R_{\uparrow\uparrow,\downarrow\uparrow} = \pm\frac{\Delta R}{2} = \pm \frac{1}{2} \frac{\alpha_F^2 \lambda_N \exp(-L/2\lambda_N)}{\sigma_N A(M+1)\left[M\sinh(L/2\lambda_N)+\cosh(L/2\lambda_N)\right]} \quad \text{(A.17)}$$

Here A is the cross sectional area of the Cu wires, and $M = (1-\alpha_F^2)\lambda_N\sigma_F / \lambda_F\sigma_N$. In the experiments one expects $\lambda_N >> \lambda_F$. Then Eqn. (A.17) has two limits: For $L << \lambda_N$ the spin signal scales as $\Delta R \propto 1/L$, whereas for for $L >> \lambda_N$ the signal is attenuated exponentially: $\Delta R \propto \exp(-L/\lambda_N)$. Also, depending on the ratio of spin flip lengths and conductivities in the ferromagnet and nonmagnetic regions, the signal can be attenuated, even in the absence of spin-flip scattering. We will discuss this "conductivity mismatch" in Sect. 0. For comparison, in the "conventional" spin valve measurement current is send from electrode 1 to 7 and the voltage is measured between 4 and 9. For this case the following expression is obtained:

$$R_{\uparrow\uparrow,\uparrow\downarrow} = R_{series} \pm \Delta R \quad \text{(A.18)}$$

with ΔR given by. Eqn. (A.18). The magnitude of the spin signal is twice that in the other geometry. However, as pointed out already, this geometry suffers from the fact that a resistance R_{series} of the ferromagnet is measured. The AMR contribution is given by $\Delta R / R = C\cos^2\varphi$, where φ is the angle between the magnetization direction and the current direction, and C is of the order of 3 %. This shows that in the case of imperfect switching, when the magnetization does not switch through 180° at the coercive field, a problem arises, this has been indeed observed by authors of Ref. [170].

A.4.4 Observation of Spin-Injection and Spin-Accumulation in an All-Metal Spin Valve

Jedema *et al.* [18] succeeded in using the principles described above to demonstrate spin injection and detection in an all-metal spin valve structure. Representative data from their measurements are shown in Fig. A.14. When the applied magnetic field is swept from negative to positive, an increase in the resistance is obtained when the ferromagnetic strip with the smallest coercive field switches, and an anti-parallel magnetization is obtained. When the coercive field of the second strip is exceeded, a drop in the resistance is observed, corresponding to parallel orientation of the magnetization of the injector and collector. The hysteresis behavior observed in Fig. A.14c,d corresponds to the situation where the direction of the magnetic field sweep is

reversed, while the second strip has not switched yet. As can be seen in the data, the spin valve signal increases when the temperature is reduced to 4.2 K.

Equation (A.17) shows that there are three unknowns in the experiment: α_F, λ_F, and λ_N. In order to determine the values of these, a series of measurements was performed with increasing electrode spacing L, ranging from 250 nm to 2 μm. By fitting the measured ΔR to (A.13), the spin flip length could be extracted. At room temperature it was deduced that $\lambda_N \approx 350$ nm, and $\lambda_N \approx 1000$ nm at 4.2 K. It was also concluded that the fitting procedure was not sensitive enough to obtain α_F and λ_F separately, however the product $\alpha_F \lambda_F$ was deduced to be ~1 nm. Using an estimated value λ_F = 5 nm obtained from the literature [175] yields $\alpha_F \sim 0.22$.

A.4.5 Comparison With the Johnson "Spin Transistor"

The signals of Jedema *et al.* [18], when scaled to the cross sections utilized in the impure Au film devices of Ref. [17] (the "Johnson spin transistor"), are about 10^4 times *smaller* than

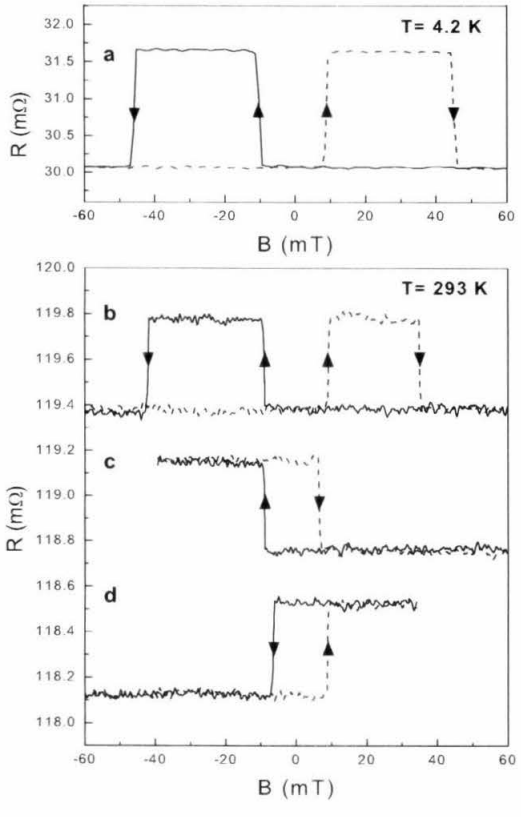

Fig. A.14 Spin valve effect at T = 4.2K (a), and room temperature (b) in the non-local geometry for a sample with 250nm Py electrode spacing. An increase in resistance is observed, when the magnetization configuration is changed from parallel to anti-parallel. The solid (dashed) lines correspond to the negative (positive) sweep direction (c), (d) illustrate the "memory effect". For clarity (c) and (d) are offset downwards. The sizes of the Py1 and Py2 electrodes are 2.0×0.5 μm^2 and 14×0.1 μm^2

obtained in that previous work. However in that earlier work it was necessary to invoke a spin-polarization greatly exceeding 100% to explain the results in terms of spin accumulation [167], [178]. In contrast the recent results of Ref [18] correspond to a spin polarization of about 1-2%. (Note that the amplitude of the spin signal scales with the square of the spin polarization). Given the unexplained discrepancies of the earlier work, and the more consistent values obtained in the recent work, it is our opinion that the results of [108, 109] are associated with spin injection and spin accumulation.

In this light, it should be noted that for the sandwich structure used in [17], the current not only flows perpendicular to the F/N/F layers, but also parallel to them. Therefore the magnetoresistance of these layers (in particular the AMR) can contribute to the measured signal, if the magnetic switching of the layers is not perfect. One expects this to be the case if a multidomain structure is formed before or during the switching. The data of [17] indeed show that the switching of the layers is not abrupt. Jedema *et al.* [18] noted in their "conventional" spin valve measurements that a contribution of the AMR to the signal could also be observed. In particularly unfavorable cases, this could fully overwhelm spin accumulation signals.

A.4.6 Future Prospects for Spin Accumulation and Spin Transport in All-Metal Devices

The average time for spin relaxation found in the recent metal-based spin injection work at Groningen is about 10^3 times the momentum relaxation time. Similar ratios have also been found from conduction electron spin resonance (CESR) experiments, which allow the determination of the spin flip time T_2 from the width of the observed resonance [179]. The spin-orbit interaction was found to be the dominant mechanism for spin flip in non-magnetic materials. It can be induced by phonon scattering, or by scattering from static imperfections, such as impurities, dislocations, and surface scattering. This implies that the spin-diffusion length $\lambda_{sf} = \sqrt{D\tau_{sf}}$ scales in direct proportion to the electron mean free path. We believe that by reducing the scattering (in particular surface scattering which is the limiting factor for thin films), it should be possible to extend the spin-flip length to several micrometers. This will make it possible to study the effects of spin accumulation in more complicated devices, such as the "spin-flip" transistor proposed by Brataas *et al.* [180]

The second issue is that the observed spin signals in all-metal lateral spin valve devices are small, in the mΩ range. This is due to their high conductivity, but also, as pointed out above, it is

due to the fact that the polarization obtained so far in lithographically defined structures is only about 1-2%. As will be discussed in the next section, however, by using tunnel junctions as injectors and detectors it should be possible to increase the polarization to about 10% or more, and this should make it possible to increase the signals to about 1Ω.

A.4.7 Spin Injection in a Diffusive Semiconductor

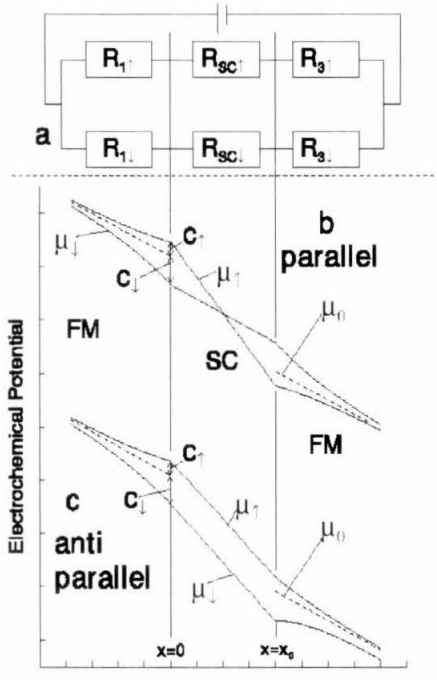

Fig. A.15 (a) Simplified resistor model for a device consisting of a semiconductor (SC) with two ferromagnetic contacts (FM) 1 and 3. The two independent spin channels are represented by the resistors $R_{1\uparrow,\downarrow}$, $R_{SC\uparrow,\downarrow}$, and $R_{3\uparrow,\downarrow}$. (b) and (c) show the electrochemical potentials in the three different regions for parallel (b) and antiparallel (c) magnetization of the ferromagnets. The solid lines show the potentials for spin-up and spin-down electrons, the dotted line for μ_0 (undisturbed case). For parallel magnetization (b), the slopes of the electrochemical potentials in the semiconductor are different for both spin orientations. They cross in the middle between the contacts. Because the conductivity of both spin channels is equal, this results in a (small) spin-polarization of the current in the semiconductor. In the antiparallel case (c), the slopes of the electrochemical potentials in the semiconductor are equal for both spin orientations, resulting in unpolarized current flow. (Note that the slope of μ in the metals is exaggerated). From [12]].

The discussion above shows that, since the time of the anomalous results of [17], significant additional understanding of spin injection and accumulation in thin film metallic systems has been attained. These recent experiments can be fully understood within the framework of the standard model, and the parameters extracted are in acceptable agreement with those obtained from CESR experiments and the analysis of magnetotransport in multilayers. This raises once again the question whether spin injection in semiconductors can also be achieved in similar fashion, *i.e.*, by using direct, Ohmic injection from ferromagnetic electrodes. In the next section the diffusive model is applied to this situation.

A.4.8 Conductivity Mismatch

If we apply the standard model to deduce the expected (nonlocal) signal for the device geometry pictured in Fig. A.15a, we find that

$$R_{\uparrow\uparrow,\downarrow\uparrow} = \pm\frac{\Delta R}{2} = \pm\frac{\alpha_F^2 \lambda_N}{\sigma_N A\left[(M^2+1)\sinh(L/\lambda_N)+2M\cosh(L/\lambda_N)\right]}$$

(A.19)

with $M = (1-\alpha_F^2)\lambda_N\sigma_F / \lambda_F\sigma_N$. The crucial point to be noted here that, unlike the case for metal/metal contacts, for metal/semiconductor (2DEG) contacts the ratio of conductivities is about 10^3, and therefore one finds $M \approx 10^3$. As seen from Eq. (A.19), this leads to a very large attenuation of the spin signal, even when $L \ll \lambda_N$, and no spin flip scattering takes place within the 2DEG. Although it cannot be excluded that there may be additional reasons for the suppression of the spin signal in metal/semiconductor devices (such as random spin precession induced by the spin-orbit interaction in InAs channel, or non-ideal interfacial transfer), it follows that the "conductivity mismatch" has very major consequences for this system. The conductivity mismatch problem has been described in detail by Schmidt *et al.* [12]

The fundamental reason for suppression due to conductivity mismatch is that the ratio of spin-up and spin-down currents is determined by the total resistance encountered in a region of the length $\lambda_F + \lambda_N$. In the above case the spin-independent resistance of the semiconductor dominates, leading to an equalization of both currents.

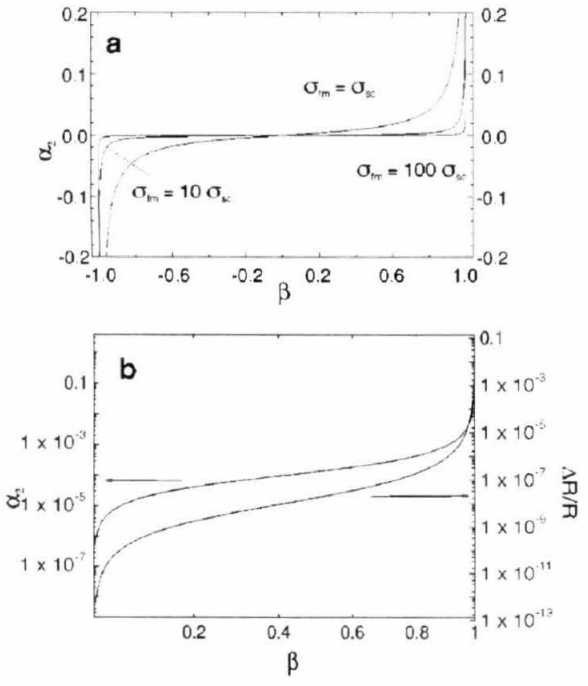

Fig. A.16 Dependence of α_2 and $\Delta R/R$ on β. In (a) α_2 is plotted over β for different ratios $\sigma_{fm} / \sigma_{sc}$. For a ratio of 100, α_2 is well below 0.1% for $\beta < 99\%$. In (b), again α_2 is plotted versus β with $\sigma_{fm} / \sigma_{sc} = 100$, with the corresponding values for $\Delta R/R$ on a logarithmic scale. For β between 0 and 90%, $\Delta R/R$ is smaller than 10^{-7} and thus difficult to detect in the experiment. After Ref [12]

Fig. A.16 shows the calculated results from [12]. It is clear that, except for α_F very close to one, the attenuation of the spin signal due to conductivity mismatch is substantial. In our opinion a direct ohmic contact between a high conductivity ferromagnetic injector/detector and a low conductivity non-magnetic medium will always yield a strong suppression of spin injection phenomena.

A.4.9 Possible Solutions to Conductivity Mismatch

Two solutions offer themselves: The first is to use injectors which have α_F close to 1, *e.g.*, using magnetic semiconductors. For the case where non-fully spin polarized ferromagnets are used, a possible solution to the problem is the use of tunnel barriers, so that the spin-dependent resistance of the tunnel barrier becomes comparable to the spin-independent resistance of the normal metal [170, 181]. It should be noted however that the mechanism for spin selectivity changes, and this will impose more stringent conditions on the fabrication technology. Recent work on tunnel injection will be discussed further in **Chap. B.2**.

A.5. Projections and Conclusions

A.5.1 Retrospective: The Spin Transistor

The concept of a spin transistor is founded upon the assumption that spin polarized electrons can survive traversal over an entire device structure. This involves three distinct and important pieces of physics. First, the transfer of spins across the *injection* interface, *i.e.*, between a magnetic and a non-magnetic material, must be possible without wholesale loss of polarization. We have seen that conductivity mismatch can seriously impair this process for Ohmic contacts between metals and semiconductors. Second, once the "source" interface is traversed, spin polarization must be largely preserved while the spin current undergoes *propagation* through the device. This means that there must be minimal spin relaxation within the paramagnetic channel, *i.e.*, the initially unpolarized electron gas in which the electron propagates from "source" to "drain". Third, the final prerequisite is implementation of a spin analyzer at the far end of the device, which is capable of *collection—i.e.*, resolving the chemical potential imbalance between spin bands arising from spin injection. It is clear that understanding the detailed physics of these three elements of device operation—injection, propagation, and collection—and using this information to engineer materials and device geometries for next-generation structures, will be the focus of much spin electronics research in the next decade.

Realizing the spin transistor is one of the longest standing hopes of spin-based electronics [182]. Although the initial motivation for work on this has diminished somewhat, advances on many fronts of spin electronics (briefly outlined in Sect. A.2.1) have heightened interest in achieving robust and controllable spin-polarized currents in small devices. Despite the widespread interest generated by the proposal of Datta and Das, and the past decade of effort that ensued, the "spin transistor" has not yet been achieved. It is thus fair to say that it remains a singular challenge for the community of researchers interested in these issues. In fact, since the initial demonstration in 1985 of spin injection in metal-based devices, the recent work of Jedema *et al.* [18] represents the only unambiguous work confirming that all-electrical spin injection devices are possible. To be fair, most effort has been placed on semi-conducting systems with *Ohmic contacts*—apparently owing to the prevailing assumptions that they offer both the greatest device potential and the highest likelihood for adoption by the mainstream microelectronics

community. We shall examine these assumptions below. Thus far, however, most putative claims of all-electrical, spin injection devices in semiconducting materials have been engulfed in a shroud of controversy. The disappointingly small signals observed have failed to convince the greater magnetoelectronics community that robust spin injection effects have yet been attained. Nonetheless, if we take the most positive of interpretations, data from these experiments allow an upper bound to be placed on the magnitude of the current polarization induced—and this appears extremely small, of order 1% at best [5, 8, 169, 170, 183-185]. As mentioned, what is most troublesome about signals at this level is that conventional magnetoresistance measurements are plagued with a host of comparable, obfuscating, non-spin-injection related magnetoelectronic phenomena, such as AMR and the local Hall effect (Sect. A.3.2 and A.4.5, respectively). Accordingly, obtaining the correct interpretation of the signals obtained in such devices is very problematic.

But the situation is actually not as grave as this discourse might initially lead one to believe. Recently, very significant advances within three separate areas of spin electronics have emerged, and these provide growing optimism that spin injection transistors will soon be realized. We list these advances here, and then separately review each of them in more detail below. First, robust electrical spin transfer across interfaces has been demonstrated in spin polarized light emitting diodes (LEDs). The emission of circularly polarized light from these devices provides rather compelling evidence that electrical injection of hot, spin polarized carriers can indeed be achieved. What is interesting about these structures is that they involve electrical spin injection across *epitaxial* interfaces. Such interfaces are far more ideal than those employed in efforts with all-electrical, Ohmic spin injection devices to date. Second, there is also a growing body of work confirming the first reports of successful spin injection, carried out almost a decade ago, across a tunnel barrier. These two sources of evidence soundly demonstrate that spin polarization, in amounts varying from very small to substantial, can be preserved in injected currents if they traverse an *optimal* contact interface. Third, long lifetimes for spin-polarized carriers have been observed in optically excited systems [131, 186]. This demonstrates that carriers can propagate within a semiconducting electron gas without significant loss of spin polarization. Collectively, this recent work—and the body of spin injection research that has preceded it—serves to demonstrate that new materials, ideal interfaces, and optimal device geometry are crucial for realizing new classes of magnetoelectronic devices.

A.5.2 Recent Advances in Spin Transport across Interfaces

(a) Optical Methods. Optical methods have recently provided compelling evidence that, with optimal conditions, spins can be *effectively* transferred through epitaxial semiconductor heterointerfaces. This has been most clearly demonstrated by Malajovich *et al.* [187] in experiments where optically generated, spin polarized carriers were allowed to diffuse across an epitaxial interface between ZuSe and GaAs. Loss of polarization was surprisingly minimal. This group subsequently demonstrated that spin-transfer efficiency could be increased by five to forty times, when electric fields are used to 'drag' spins across a semiconductor interface [188]. They applied laser pulses, tuned to create a long-lived 'reservoir' of spin-polarized carriers in the sourcing epilayer and then, in two separate experiments, showed that both externally applied and "built-in" internal electric fields could be highly effective at transferring spins from this reservoir, across an epitaxial interface, to another semiconductor. In the latter case, "built-in" fields were created during growth, through controlled doping of semiconductor layers, to employ the natural potential arising at *p/n* junction.

(b) Ohmic Contacts. As originally envisaged, the spin-FET involved ferromagnetic source/drain electrodes and a semiconducting electron gas "channel" that were electrically connected by *Ohmic* contacts. With Ohmic contacts, the two-terminal (drain/source) device impedance is kept quite low, and this circumvents problems arising in high impedance devices such as limited fan-out (due to source loading), slow dynamical response, and large power dissipation at steady bias. These were the principal reasons that motivated efforts on the spin transistor over the past decade that were focused upon Ohmic structures.

Efficient spin injection is possible, even for diffusive transport in a "half metallic" ferromagnet where the conduction electrons are nearly 100% spin-polarized. There are a number of materials that have this nearly complete polarization [189, 190]; however, these have not yet been applied to semiconducting spintronics, presumably due to the significant difficulties associated with integrating them into advanced growth and fabrication processes for high-quality semiconductors.

Recently Hammar *et al.* [7] reported a novel, indirect means of detecting spin injection across a single interface between a metallic ferromagnet and a heavily doped InAs 2DEG. The observations, reported to persist even above liquid nitrogen temperature, were interpreted as the consequence of a spin dependent resistance that the authors believe is intrinsic to such an interface. As in other spin injection experiments involving Ohmic contacts between metallic

ferromagnets and semiconductors, however, only a very minute change in device resistance could be correlated with changes in ferromagnet orientation. Given the host of other phenomena of comparable magnitude known to be operative at ferromagnetic/semiconductor interfaces, compounded with the unknown quality of the interfaces studied, these results have not met with widespread acceptance to date. Alternative explanations, including ones based upon the local Hall effect, have been advanced [191-193]. The underlying physical mechanism proposed for this effect involves a non-equilibrium spin polarization induced by current flow in a spin-orbit-split conduction band [194]. Recently theoretical models for a spin-dependent interfacial resistance involving spin-orbit coupling have been formulated in both the ballistic [195, 196] and diffusive [197] regimes. However, very fundamental questions have been raised regarding correctness of such interpretations [198]. To date, the feasibility and effectiveness of this current-induced spin polarization for spin injection appears to be unsettled.

Convincing evidence of spin injection has been realized in efforts involving polarized light emission induced by spin polarized carriers injected across a *p/n* junction. Among such experiments, the spin-LED recently reported by Ohno *et al.* [15] employs spin injection from a *p*-type ferromagnetic semiconductor (GaMnAs) into an intrinsic GaAs region. The spin polarized current subsequently flows through the intrinsic region into an *n*-doped InGaAs quantum well. Hence one may consider this device as first involving spin injection across an Ohmic, unipolar junction, and then involving injection across a subsequent barrier.

Finally, we note that recent experiments with nanoscale point contacts formed between ferromagnetic and non-ferromagnetic metals have demonstrated that ballistic injection of highly (> 40%) spin-polarized currents into the non-ferromagnet is possible [199, 200].

(c) Tunnel Contacts. We have mentioned the underlying reasons why Ohmic contacts have been pursued most vigorously to date. Given the significant difficulties mentioned above, however, it now seems worthwhile to explore the possibility of electrical spin injection by alternate methods—*i.e.*, by tunnel or Schottky contacts despite the fact that the resulting two-terminal device impedances may be larger. Especially noteworthy in this context is the recent adoption of magnetic tunnel junction structures for memory applications by the commercial sector. This demonstrates that large two-terminal impedances need not preclude utility for commercial electronics. A tunnel contact has the additional advantage that it can provide a diffusion barrier between ferromagnetic metals and semiconductor materials. This is important given the extensive past work (described below) demonstrating the ease with which these systems can interdiffuse, even at relatively low growth or processing temperatures.

Of course the most ideal barrier is vacuum itself. A decade ago, Alvarado and Renaud [19] showed that spins can be injected into a semiconductor by vacuum tunneling. They demonstrated this using a scanning tunneling microscope outfitted with a ferromagnetic tip. Recently, La Bella and coworkers have extended this work to image the orientation-dependent spin injection probability and the spin lifetime for spin polarized carriers injected into a pristine surface of GaAs [201].

Recent theoretical work by Rashba [181], Smith [202], Heersche *et al.* [203] and Flatte *et al.*, has explored the effectiveness of spin injection via tunneling contacts. Collectively, what is emerging from these investigations is that, for the case of small transmission, the spin-dependent density of states for the two electrodes determines transport across a tunnel barrier. In this limit of regime of linear response the electrodes remain in equilibrium and their respective spin-dependent conductivities play a minimal role in determining transport across the interface. Hence, either a FM (ferromagnet metal)-semiconductor Schottky diode or a FM-insulator-semiconductor tunnel diode may be effective for injecting spins into a semiconductor system.

(d) Schottky Contacts. There has been growing interest in the study of epitaxial ferromagnetic metal/semiconductor heterostructures. Such efforts have a long history; more than twenty years ago, Prinz showed that single crystal Fe films could been stabilized on GaAs through molecular beam epitaxy [204]. The lattice constant of GaAs (a_0 = 5.654 Å) is almost exactly twice that of Fe (a_0 = 2.866Å). Much recent effort has continued the focus upon GaAs materials; among systems explored are Fe/GaAs [205-208], Py(permalloy)/GaAs [209], and Fe-Co/GaAs [210]. It was realized very early in the course of these studies that, under non-optimal growth conditions, a magnetically dead layer can exist at the interface between these materials. This has been shown to arise from intermixing, yielding a magnetically depleted phase [206] or half-magnetized [208] phases such as $FegGa_{2-x}As_x$. However, it has also been found that, under optimal conditions, growth of only a few monolayers is sufficient for the ferromagnetic film to recover the full magnetic properties of the bulk [211]. Additional work has been carried out on the Fe/InAs [212-214] system. The crystal structure of InAs is very similar to that of GaAs, but the lattice mismatch of Fe and InAs (a_0 = 6.058Å) is 5.4%, poorer than that of Fe/GaAs. It has proven possible to grow single crystal bce Fe on InAs (100) surface, however Ohmic rather than Schottky contacts are achieved [213]. In all these grown materials, clear *in situ* MOKE (magneto-optic Kerr effect) hysteresis loops have been demonstrated after only 5-8 monolayers of Fe is deposited.

For spin injection devices, Schottky barriers represent another alternative to Ohmic contacts. The differences between the spin-split conduction bands of the ferromagnetic metal and the spin-degenerate conduction band of a semiconductor yield a spin-dependent interfacial transmissivity. The picture is conceptually clear for ballistic electrons; for a high quality epitaxial interface, it is generally assumed that the transverse momentum of incident electrons is conserved after transport through the barrier. In this case a straightforward description emerges for the spin-dependent ballistic transmission and reflection probabilities of the interface [215, 216]. Such simple pictures are almost certainly *not* expected to hold for ordinary interfaces, however ballistic electron emission microscopy (BEEM) studies demonstrate that, for "generic" surfaces, diffuse scattering is predominant [217].

Spin injection across a Schottky barrier between a ferromagnetic metal and a semiconductor appears to be very promising. Zhu *et al.* [218] have recently reported a room temperature spin-injection efficiency of 2% with a Fe-GaAs Schottky contact. In their experiments the injected spin polarization was detected by polarization-resolved electroluminescence. This has been confirmed by recent experiments of Hanbicki *et al.* [219], who studied spin injection from an epitaxial Fe layer grown on AlGaAs/GaAs quantum well LED structures. Also using polarization-resolved electroluminescence, they deduced a 30% spin injection efficiency for such structures at 4.5K, which shrank by a factor of about three (to ~9%) at room temperature.

An interesting variant on spin injection involves the use of spin-polarized "hot" electrons with energies much greater than E_F [220, 221]. Filipe *et al.* [11] demonstrated a novel spin filter effect involving spin injection across a Schottky barrier. Quasi-monoenergetic, spin-polarized electrons are tunneled across a vacuum gap into a thin ferromagnetic metal layer deposited upon an *n*-doped GaAs substrate. Spin-dependent transmission probabilities are deduced by measuring the current transmitted through this Schottky barrier. Before the deposition of ferromagnet, the n+- GaAs surface was oxidized by an ozone system to form a 2-nm-thick oxide layer. This oxide layer proves to be very efficient in preserving spin polarization. A spin filter efficiency up to about 25% has been achieved.

In recent experiments [222], hot electrons have been tunnel injected from a STM tip across a barrier into a ferromagnetic layer, in a technique termed BEMM (ballistic electron magnetic microscopy). Since the majority-spin and minority-spin electrons have much different inelastic mean free paths, passage of hot electrons through, for example, a 3 nm Co layer has proven sufficient to result in a ballistic electron current with > 90% spin polarization [218]. This highly polarized hot-electron current can then be employed to interrogate, for example, underlying

metal-semiconductor interfaces. In this situation the spin-dependent transmission probability of the barrier can be probed. If spin-flip scattering at the interface is minimal, then the ballistic electron current entering the semiconductor will be highly polarized (> 90%). Furthermore, the energy of the injected electrons, relative to the bottom of the conduction band in the semiconductor, is tunable via the bias voltage across the tunnel barrier. However, the disadvantage of hot electron injection is that the overall efficiency (yield) is low.

A.5.3 Recent Advances in Spin Injection via Semimagnetic Semiconductors

Oestreich *et al.* have explored use of a semimagnetic Mn-based diluted magnetic semiconductor as the spin-injecting contact. In the presence of a large applied magnetic field, electron spins in this large-g material will be strongly polarized [223]. They used time- and polarization-resolved photoluminescence to demonstrate that optically excited carriers became spin aligned in a $Cd_{1-x}Mn_xSe$ layer, and that spin-polarized electrons were transferred into an adjacent CdTe layer with little loss in spin polarization.

Fiederling *et al.* [14] have demonstrated efficient electrical injection of spin-polarized carriers from the epitaxially grown semimagnetic semiconductor, ZnMnSe, into a GaAs semiconductor heterostructure. A light-emitting diode structure (spin-LED) was constructed which enabled direct proof, by spin polarized emission measurements, that the current was spin polarized. As in other spin LED structures, the diode is always biased at more than 1 volt to achieve appreciable emission. This voltage scale is greater than the band gaps of the quantum wells employed. The device incorporated an intrinsic spacer layer (GaAs), in which the electrons have a very high energy relative to the Fermi level. Recent efforts in this area have been reported by Jonker *et al.* [224]

Given the ability to grow ZnMnSe epitaxially upon GaAs, semimagnetic contacts appear to be a very interesting alternative for spin injection devices, at least in initial research efforts [13]. There are several notable drawbacks that must be considered, however. Large magnetic field operation precludes the commercial viability of this approach. Perhaps most important is the fact that the applied (large) magnetic field obviously determines the direction of polarization. For fundamental experiments there is no clear way to perform polarize/analyze or spin precession (Hanle effect) experiments—such as can be done with *ferromagnets* given their spontaneous, remnant polarization, which enables both configurations with antiparallel magnetic contacts, and the application of magnetic fields non-collinear with respect to the injected polarization.

A.5.4 Recent Advances in Spin Propagation in Semiconductors

In the past four years, it has been proven experimentally that spin coherence can persist in doped semiconductors on very long temporal scale, exceeding > 100 ns at low temperatures. Local optically excited, spin polarized "puddles" of carriers have been transported laterally through semiconducting materials for distances over 100 μm by applied electric fields, while maintaining spin coherence [4, 131-134]. As mentioned, the spin polarized holes are found to relax quickly, but the spin polarized electrons persist for long times. At present, the extent to which the spin dynamics of these hot electrons differ from those of spin-polarized electrons at Fermi surface is unclear. Since spin scattering is closely related to momentum scattering, one might expect the spin relaxation rate at the Fermi surface to be *even slower* than that observed for hot carriers. But, to date, difficulties in manipulating near-equilibrium electrons, have precluded measurement of spin lifetime at the Fermi surface. But the picture that emerges is extremely promising for electrical spin injection devices.

Appendix B. Spin Transport in the Ballistic Regime

Pursuit of spin injection phenomena in two-dimensional electron gas systems has been motivated by the expectation spin transport phenomena should become greatly enhanced in these materials (see Sect. A.3.1 in this chapter). This is especially true for devices with submicron dimensions, where mean free paths for momentum scattering can easily exceed device dimensions. Furthermore, sufficiently narrow conductors of such materials become quantum wires in which current is carried by only a small number of transverse subbands [225]. If a quantum wire is short enough, intersubband scattering becomes inconsequential and quantization of electrical conductance is manifested [127, 128]. Most previous modeling of electrical spin injection and spin transport phenomena has been predicated on the assumption that electron transport is *diffusive*. In this section, we describe simple modeling allowing exploration of spin injection and precession phenomena when transport is *ballistic*. Although the approach taken is straightforward in concept, it provides a very important intuitive understanding about the unique aspects of ballistic spin transport, and underscores significant gaps in our current understanding of the problem's details. These models also provide important benchmarks for observational expectations in ballistic systems. The previous discussion makes it clear that this is in a realm where the signatures of spin transport phenomena may be ambiguous or even obfuscated by other phenomena. As mentioned (Sect. A.3.2), semiconducting systems can be profoundly sensitive to

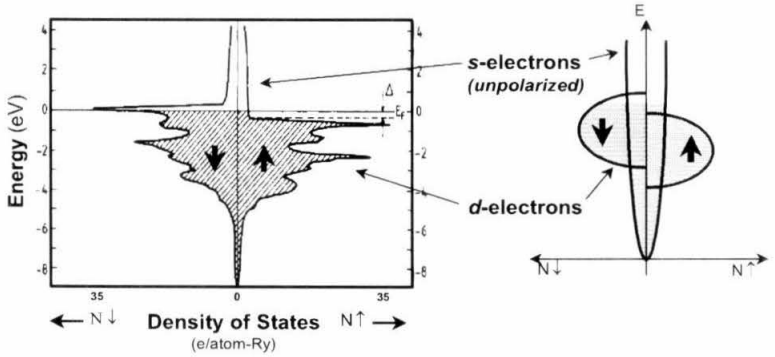

Fig. B.1 Calculated DOS for nickel (after J. Callaway and C.S. Wang: Phys. Rev. B **63**, 1096 (1973)), and a simple Stoner model for ferromagnetic electrodes.

extraneous magnetic fields given their large Hall coefficients. The models described here culminate in predictions for observable precessional phenomena, analogous to the Hanle effect in the diffusive regime, which should constitute definitive experimental demonstrations of spin injection, transport, and detection in all-electrical semiconductor devices. To date these remain to be realized.

Ballistic transport in nanoelectronic devices is usually described within the Büttiker-Landauer model. Current flow is pictured as reservoir-to-reservoir transport—in contrast to the case for diffusive systems; here we do not usually define *local* electrochemical potential, which would give rise to a continuous voltage drop within the conducting channel. Instead, current flow is viewed as a *ballistic,* or, in certain situations, *phase-coherent,* flux of carriers that propagates without scattering through the conducting channel. Equilibrium occurs solely at the reservoirs formed by Ohmic contacts at the ends of the channels. Conductance is then described as the ratio of the electron flux (proportional to the *current)* to the steady state electrochemical potentials of these reservoirs.

For spin electronics, one needs to transform these ideas to the cases where transport is spin polarized. One is immediately faced with a complication: what is the underlying physics of spin-selective contacts? Büttiker's multi-terminal formalism is based on the ansatz that the reservoirs are *perfectly absorbing.* Specifically, he assumed that every electron impinging from the channel upon a "collecting" contact is admitted, and thereby contributes to the development of that reservoir's electrochemical potential in steady state. For the rather low density electron gases which form quantum -wires, -point contacts and -dot structures, this is physically justifiable. The density of states of the metallic contacts is immense compared to that of the channels themselves. It is therefore almost a certainty that a state can always be found within the reservoir that is well-matched, both in energy and momentum, to the discrete "modes" of the electron gas channels.

It is not so clear, however, what the correct picture should be for *spin selective* contacts. Is it possible that spin-polarized reservoirs can be created that will reflect impinging carriers in the "wrong" spin state? For the ferromagnetic metal/semiconductor contacts, this seems highly unlikely. Except for the so-called "half metallic" ferromagnets, there is appreciable density of states in both (polarized) *d*-like and (unpolarized) *s*-like bands at the Fermi surface in metallic ferromagnets (Fig. B.1). Any carrier of the wrong spin type that impinges upon a polarized d-band state is quite likely to find a match within the s-band. This brief discussion, rather than striving to be definitive, is meant to serve as an introduction to important issues regarding spin-polarized contacts in the ballistic regime.

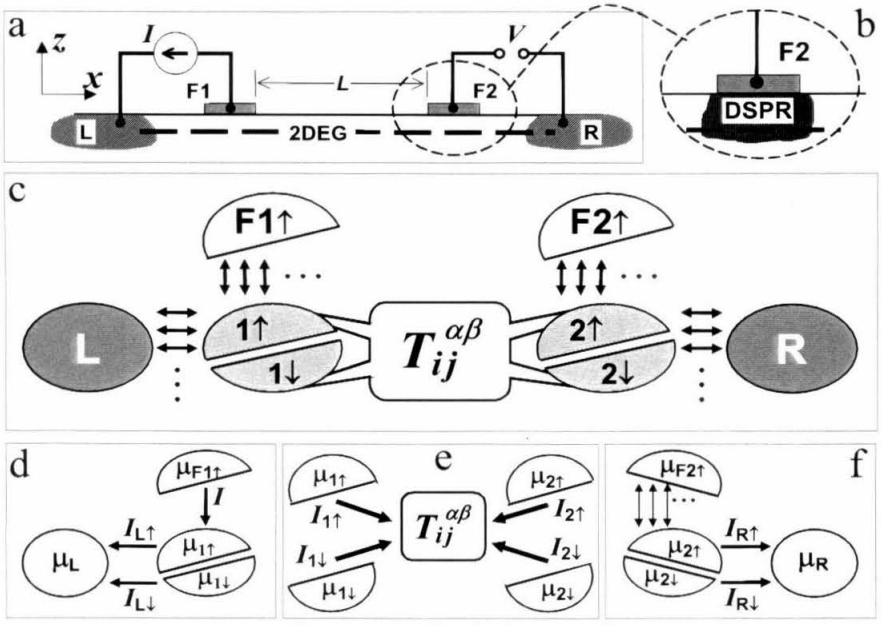

Fig. B.2 Model for ballistic spin transport in a two-dimensional electron gas. (a) Measurement configuration: a current I is injected through the 2DEG via a ferromagnetic contact **F1** and an Ohmic contact **L**. The spin transresistance $R_s = V/I$ arises from spin-polarized carriers traversing a distance L from the net path of the current, which induce a nonlocal voltage, V between a second, similar, pair of contacts **F2** and **R**. (b) The conductor beneath the ferromagnetic contacts (DSPR) is assumed to be a *disordered,* but *spin preserving* region. (c) The full-eight-reservoir model; complete ellipses represent spin-relaxing reservoirs, and half ellipses represent spin-resolved reservoirs. **F1** and **L** are current contacts, **F2** and **R** are voltage probes. $T_{ij}^{\alpha\beta}$ denotes the 2DEG device channel in which spin precession occurs. Other multimode leads are denoted by three arrows and ellipsis. Panels (d), (e), and (f) illustrate decomposition of the eight-reservoir model. [Panel (e) depicts the reduced four-reservoir problem.].

The semiconducting spin injection transistor envisaged by Datta and Das [3] was predicated upon single-subband, ballistic transport from source to drain. In this first formulation of the problem, the specific details of how spin polarized current might be injected into the channel were sidestepped—their focus was upon controllable, spin-selective *transport* within the channel itself. Below we shall explore spin transport and precession in ballistic regime in more detail, investigating the role that effects such as multisubband transport and scattering will play in real devices. We can also make some general statements about spin transmission at contacts. Concrete microscopic models for the contacts, however, are only possible for the case of specific, well-

controlled experimental realizations of the interfacial transport involved. Recent advances in epitaxy are now permitting growth of heterostructures with nearly ideal interfaces between ferromagnetic and non-magnetic semiconductors. This research is greatly accelerating our rate of understanding of interfacial spin transmission—and it should also begin to clarify what is physically possible regarding the realization of spin selective contacts.

A three- or four-terminal spin transistor device (cf. Fig. A.1 and Fig. A.2) is most clearly characterized by spin transresistance R_s, defined in Fig. B.2a, which provides the most direct demonstration of spin transport. In the *diffusive* regime for the geometry shown, if the current contact **F1** is replaced with one that is unpolarized no voltage will appear between the analyzer contact **F2** and a suitably defined ground reference **R**. In this case these voltage contacts, being well outside the net current path, remain at the same equipotential. However, if the current from **F1** is spin polarized, the injected magnetization can lead to steady state *spin accumulation* that persists over the entire length of the channel when $\lambda_{sf} \geq L$. This spin accumulation induces disequilibrium between the electrochemical potentials at the collecting contacts on the far end of the device, **F2** and **R**, and thereby yields a finite value of R_s. As before $\lambda_{sf} = \sqrt{\ell_0 \ell_s / 2}$ is the spin diffusion length, $\ell_s = v_F \tau_s$ and $\ell_0 = v_F \tau_0$ are the spin and momentum mean free paths, τ_s and τ_0 are the effective spin and momentum relaxation times.

B.1. Multiprobe model for Ballistic Spin Polarized Transport

To describe spin transport in the *ballistic* regime Büttiker's picture for mesoscopic transport within a multiprobe conductor is employed[226]. Here it is augmented with a simple, experimentally motivated model that describes the essential physics of spin-selective contacts [227]. The procedure involves four principal steps: (a) a simple description of spin-resolved contacts is developed, based upon careful consideration of the ferromagnetic/semiconductor contacts in real devices. (b) An eight-reservoir model is constructed, in the spirit of Büttiker's formalism, to describe the spin injection experiment. (c) Careful consideration of the boundary conditions yields constraints upon the spin-resolved currents and chemical potentials. This process leads to an expression for R_S in terms of reservoir-to-reservoir, *spin-resolved* transmission probabilities, $T_{ij}^{\alpha\beta}$, of the 2DEG that forms the device conduction channel. Here the indices *i, j* specify the reservoirs themselves, and α, β their constituent spin bands. Finally, (d) the

requisite $T_{ij}^{\alpha\beta}$ are calculated semiclassically, using a modified Monte Carlo numerical technique. This is carried out by following the electrons' ballistic trajectories *and* the phase of their spin wavefunctions as they pass through the device, while the phase of their spatial wavefunctions is ignored. To account for the properties of real devices, it is also necessary to include both junction scattering and scattering at the surfaces and in the interior of the channel. For unpolarized ballistic systems, this semiclassical approach has provided a theoretical description remarkably consistent with experimental data at $T \sim 4$K, the regime where the electron phase coherence length is smaller than typical dimensions of nanoscale devices [228]. We expect that the semiclassical model is capable of providing equally valuable insights for spin polarized systems.

Fig. B.2b depicts a simple model for spin-selective contacts based on experimental considerations. It comprises two elements: **F2**, a fully spin-polarized reservoir which is in perfect contact with what we shall term, a disordered (*i.e.*, momentum-randomizing) but spin-preserving region (hereafter denoted as DSPR). The DSPR consists of separate spin-up and spin-down bands that internally equilibrate, in the sense of momentum relaxation, while preserving the overall spin imbalance. The separate spin-resolved reservoirs comprising the DSPR ($1\uparrow$, $1\downarrow$, $2\uparrow$, $2\downarrow$) model low mobility regions always present beneath unalloyed ferromagnetic metal contacts, *e.g.*, in typical InAs devices (Sect. A.3 of this chapter). Disorder within these special regions yields significant momentum randomization and, hence, a short ℓ_0. However, in contrast to the usual picture describing unpolarized reservoirs [226], we assume these special contacts are small compared to λ_{sf}, thus any spin disequilibrium within them is preserved. This, in fact, is consistent completely general and with the more restrictive constraint, $\delta_{sf} \geq L$, which is fundamental to *any spin injection experiment.* If significant spin relaxation occurs anywhere in a "spin transistor", including in the vicinity of the ferromagnetic contacts, spin-selective transport will be suppressed. For sake of clarity, we consider the most ideal situation, initially assuming that **F1** and **F2** are fully polarized at the Fermi surface (half-metals). This approximation serves to illustrate the most important aspects of the underlying physics. Of course, many complexities in real devices may diminish spin transport effects, such as partial spin polarization and additional unpolarized bands at E_F in **F1** and **F2,** variations in band structure near the interfaces, magnetic disorder and spin scattering at the *F/S* interface, momentum and spin scattering in the 2DEG, and thermal smearing. Here our aim is to clarify at the outset what may be expected in ballistic systems under the most favorable of conditions.

Measurement of R_S involves four terminals (Fig. B.2a), two that are spin-selective (**F1**, **F2**), and two that are conventional, *i.e.*, momentum- and spin-relaxing (**L**, **R**). Here we assume the spatial extent of these contacts is sufficient to allow both spin and momentum relaxation; they are "conventional" reservoirs as described by Büttiker [226]. As depicted in Fig. B.2(d, e, f), the full problem separates into three sub-components. Fig. B.2d represents the spin-up and spin-down currents ($I_{L\uparrow}$, $I_{L\downarrow}$) that flow between **F1**, $1\uparrow$, $1\downarrow$, and **L**. A Sharvin resistance [229], $R_{sh} = (h/2e^2)(k_F w)/\pi = (h/2e^2)N_{ch}$, arises between $1\uparrow$, $1\downarrow$ and the multichannel conductors connecting them to **L**. Under conditions of current flow this yield the spin-resolved electrochemical potential differences $\mu_{1\uparrow} - \mu_L = 2eR_{sh}I_{L\uparrow}$ and $\mu_{1\downarrow} - \mu_L = 2eR_{sh}I_{L\downarrow}$. Here, the factors of 2 arise because transport is spin resolved; k_F, w, and N_{ch} are the Fermi wave vector, channel width, and number of occupied modes within the 2DEG device channel, respectively. Similarly, at the rightmost side of Fig. B.2f, current flow between the reservoirs $2\uparrow$, $2\downarrow$ and **R** establishes the electrochemical potential differences $\mu_{2\uparrow} - \mu_R = 2eR_{sh}I_{R\uparrow}$ and $\mu_{2\downarrow} - \mu_R = 2eR_{sh}I_{R\downarrow}$. Also, $\mu_{F2\uparrow} = \mu_{2\uparrow}$ since no current flows between these reservoirs. Note that all I's here represent net currents (forward minus reverse contributions). In our model, the following sum rules hold: $I = I_{L\uparrow} + I_{1\uparrow}$, $I = I_{L\uparrow} + I_{L\downarrow}$, $0 = I_{R\uparrow} + I_{R\downarrow}$, and $I_{1\uparrow} + I_{1\downarrow} = I_{2\uparrow} + I_{2\downarrow} = 0$. As the reservoirs in Fig. B.2f are voltage contacts, net current is conserved separately for each spin band, $I_{R\uparrow} + I_{2\uparrow} = I_{R\downarrow} + I_{2\downarrow} = 0$. These expressions can be manipulated

$$\begin{pmatrix} \mu_{1\uparrow} \\ \mu_{1\downarrow} \\ \mu_{2\uparrow} \\ \mu_{2\downarrow} \end{pmatrix} = \begin{pmatrix} \mu_L + 2eR_{sh}(I - I_{1\uparrow}) \\ \mu_L + 2eR_{sh}I_{1\uparrow} \\ \mu_R - 2eR_{sh}I_{2\uparrow} \\ \mu_R + 2eR_{sh}I_{2\uparrow} \end{pmatrix}. \tag{B.1}$$

Given these relations, calculation of R_S reduces to a four-terminal problem that solely involves the four spin-resolved reservoirs: $1\uparrow$, $1\downarrow$, $2\uparrow$, and $2\downarrow$ and the 2DEG device channel that connects them [Fig. B.2e]. Modifying Büttiker's formula to account for the spin-resolved transport, the four-terminal linear response at zero temperature becomes

$$I_{i,\alpha} = \frac{e}{h}\left[(N_{ch} - R_{ii}^{\alpha\alpha})\mu_{i,\alpha} - T_{ij}^{\alpha\beta}\,\mu_{j,\beta}\right] \equiv \frac{e}{h}\,U_{ij}^{\alpha\beta}\,\mu_{j,\beta}, \tag{B.2}$$

Transport within the ballistic multimode 2DEG conductor, is hence fully represented by the transmission coefficients $T_{ij}^{\alpha\beta}$, and the reflection coefficients $R_{ii}^{\alpha\alpha}$. These describe carriers incident from the lead i with spin polarization α, that are transmitted into lead j with final spin state β; and carriers incident from i, α that are reflected back into the same lead and spin channel. The coefficients U_{ij} in Eq (B.1) satisfy the sum rule $\sum_j U_{ij} = \sum_i U_{ij} = 0$ ensuring the current sum rules, and that all currents vanish when the μ_i are equal.

Simplification of Eqs. (B.1) and (B.2) yields

$$\begin{pmatrix} I_{1\uparrow} \\ I_{1\downarrow} \\ I_{2\uparrow} \\ I_{2\downarrow} \end{pmatrix} = \boldsymbol{S} \begin{pmatrix} \tilde{\mu}_L + I \\ \tilde{\mu}_L \\ \tilde{\mu}_R \\ \tilde{\mu}_R \end{pmatrix}, \tag{B.3}$$

where $\tilde{\mu}_L = \mu_L / 2R_{sh}e$ and $\boldsymbol{S} \equiv (\boldsymbol{I} + \boldsymbol{U})^{-1}\boldsymbol{U}$. The elements of $\boldsymbol{S}$ satisfy the same sum rules that constrain $\boldsymbol{U}$ (for identical reasons). These steps lead to an explicit expression for the R_S. For parallel alignment of polarizer and analyzer **(F1,F2),** which we denote by the superscript ($\uparrow\uparrow$). these steps yields

$$R_S^{(\uparrow\uparrow)} = -2\frac{S_{31}S_{42} - S_{32}S_{41}}{S_{31} + S_{32} + S_{41} + S_{42}} R_{sh}. \tag{B.4}$$

For antiparallel alignment, only the sign changes: $R_S^{(\uparrow\downarrow)} = -R_S^{(\uparrow\uparrow)}$.

We obtain the requisite elements of $\boldsymbol{S}$ numerically, extending the semiclassical billiard model [228] to allow tracking of an electron's spin wavefunction along ballistic trajectories between the spin-resolved reservoirs ($1\uparrow$,$1\downarrow$,$2\uparrow$,$2\downarrow$) at either end of the 2DEG device channel. We consider electrons confined within a hard-wall channel, of length L and width w, at zero temperature. $T_{ij}^{\alpha\beta}$ are calculated by injecting and following a large number of electron trajectories (typically $>10^4$), made up of straight line or circular arc segments that specularly reflect from the walls until they are collected into one of the reservoirs. We implicitly assume that, compared to the Fermi energy, the spin splitting is small (and, hence, that the $T_{ij}^{\alpha\beta}$ are essentially energy-independent on this scale). This is valid for the narrow gap, low density semiconductor systems that are the focus of our study. For a uniform external field, B_{ext}, we decompose the spin wavefunctions into linear

combinations of spin eigenstates. If, say, B_{ext} is applied along z (normal to the 2DEG plane, Fig. B.2), then the z-polarized states (hereafter denoted as $|+\rangle$, $|-\rangle$)) form the basis, and we then represent $\pm x$ and $\pm y$ polarized state as $|\pm x\rangle = (\ |+\rangle \pm |-\rangle\ )/\sqrt{2}$ and $|\pm y\rangle = (\ |+\rangle \pm i\ |-\rangle\ )/\sqrt{2}$, respectively. For this field orientation, the phase of an electron's spin wavefunction evolves as it traverses the 2DEG device channel. For example, if at time zero an electron subject to $B_{ext} \| \hat{z}$ is characterized by $|\sigma\rangle = C_+ |+\rangle + C_- |-\rangle$, then at a later time t, $|\sigma, t\rangle = C_+ \exp(-i\omega_L t/2)|+\rangle + C_- \exp(i\omega_L t/2)|-\rangle$. Here $\omega_L = g^* eB/2m$ is the Larmor frequency for that particular path segment, g the effective electron g-factor, and m the free electron mass. (The case involving a Rashba field, described below, is more complex.) Total precession is then accumulated for each complete trajectory as part of our Monte Carl procedure.

B.2. Results of Spin Resolved 4-Probe Model

In Fig. B.3a we display $R_S^{(\uparrow\uparrow)}$ as a function of perpendicular magnetic field strength. The prominent and striking new feature is that R_s is *oscillatory*, a ballistic phenomenon not found in the diffusive regime. In Fig. B.3b and Fig. B.3c, we display $R_S^{(\uparrow\uparrow)}$ calculated for three orientations of the external field—two that are in-plane and the perpendicular case, displayed again for comparison. In all three cases the **F1, F2** magnetizations are parallel and $\hat{y}$-oriented.

When the external field is along $\hat{y}$, the injected carriers remain in spin eigenstates and do not precess. In this situation $R_S^{(\uparrow\uparrow)}$ is a positive constant. However, with an $\hat{x}$-oriented field precession is maximal, and R_s oscillates. Since orbital effects are absent for an in-plane field, the oscillations in this case arise purely from spin precession and the oscillation *period*, ΔB, is determined by the condition $2n\pi = \omega_L t_{TR}$, *i.e.*, $\Delta B = h/(g^* \mu_B t_{TR})$. Here $t_{TR} = S/v_F$ is a typical transit time from 1 → 2, and μ_B is the electronic Bohr magneton. ΔB is thus inversely proportional to S, a typical path length averaged over the injection distribution function. The *decay* of R_S occurs on a field scale where $\omega_L \delta t_{TR} \sim \pi$; *i.e.*, for $B = \hbar\pi/(g^* \mu_B \delta t_{TR})$, beyond which precession among the different contributing trajectories tends to get out of step. Here $\delta t_{TR} = \sqrt{t_{TR}^2 - \langle t_{TR} \rangle^2}$ is the variance in path lengths traversed while propagating from 1→2.

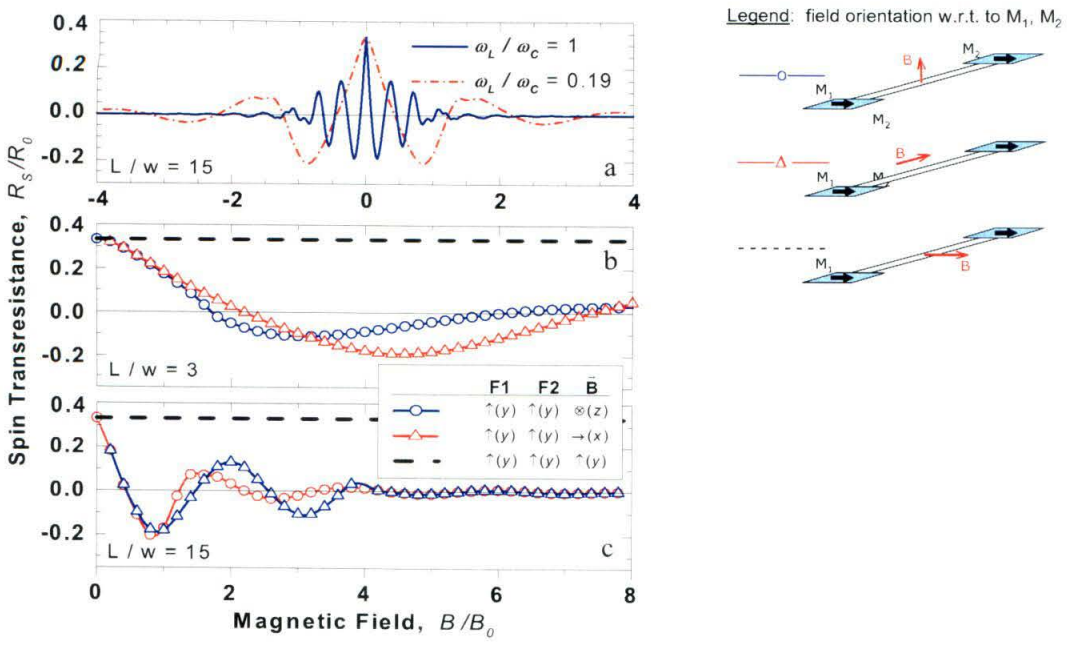

Fig. B.3 Ballistic spin transresistance in an external field normalized to $B_0 = p_F/(ew)$. (a) For a channel with $L/w = 15$ in a perpendicular field, we plot two traces representing $\omega_L/\omega_C = 1$ and 0.19, appropriate for a typical metal and for InAs, respectively. (b) and (c) Spin transresistance for three different configurations and two channel lengths $L/w = 3$ and 15. Here, $\omega_L/\omega_C = 0.19$ (InAs).

The perpendicular field ($B_{ext} \parallel \hat{z}$) is special—it induces both spin and *orbital* effects. (The characteristic field scale for the latter is $B_0 = p_F/ew$, at which the cyclotron diameter $d_c = 2v_F/\omega_C$ equals the channel width, w.) The frequency ratio $\omega_L/\omega_c = (g^*/2)(m^*/m)$ describes the relative importance of orbital and spin transport phenomena. Here, p_F is the Fermi momentum, $\omega_c = eB/m^*$ the cyclotron frequency, and m^* the effective mass. For InAs (m*~0.025, g*~15) this ratio is ~0.19, for InGaAs ~0.1, whereas it is roughly 1.0 for most metals. In the latter case spin and orbital effects will have similar periodicity so disentangling them is difficult. As mentioned, electrons confined within an InAs heterostructure are subject to an internal Rashba field that is present even for zero applied magnetic field. This can be modeled by a term $H_R = \alpha[\vec{\sigma} \times \vec{k}] \cdot \hat{z}$. Comparing H_R to the Zeeman term we write the effective Rashba field as

$$\vec{\mathbf{B}}_R = \frac{2\alpha_{SO}}{g^* \mu_B} \frac{\vec{k} \times \hat{z}}{} . \qquad \text{(B.5)}$$

Using data from Heida *et al.* [138], we estimate the typical strength of this internal field to be about 5T for an InAs 2DEG. The spin precession induced by $\vec{\mathbf{B}}_R$ dramatically alters the $T_{ij}^{\alpha\beta}$. For each straight- ($B_{ext} = 0$) or arc- ($B_{ext} \neq 0$) segment of the electron's trajectory (traversed between reflections from the boundaries) its spin precession can be calculated analytically and incorporated into the Monte Carlo procedure.

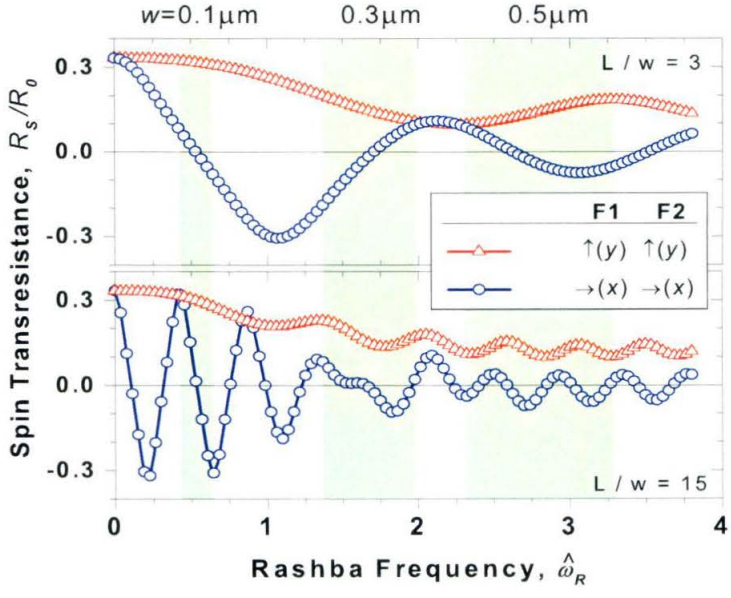

Fig. B.4 Spin transresistance *vs.* reduced Rashba frequency, $\hat{\omega}_R = 2m^* \alpha w / \hbar^2$, at zero applied field, for two different device channel lengths, L/w = 3 and 15. The Rashba field strength, characterized by $\hat{\omega}_R$, can be tuned by an external gate voltage. Shaded regions delineate the range of tunability expected for InGaAs devices [138] of three widths, 0.1, 0.3, and 0.5 μm.

Fig. B.4 displays how Rashba-induced spin precession is manifested in R_S for zero external field. We represent the effective Rashba field strength by the dimensionless frequency $\hat{\omega}_R = \frac{2\alpha}{\hbar^2} \frac{m^* w}{}$; at $\hat{\omega}_R = 1$ an electron precesses one radian after traversing a distance w. As

shown, the oscillations initially decay quickly but exceedingly slowly thereafter. No spin precession occurs for $\hat{\omega}_R = 0$, hence $t = 1$ yielding $R_S^{(\uparrow\uparrow)} = R_S^{(\rightarrow\rightarrow)} = R_{sh}/3$. For finite $\hat{\omega}_R$, R_S displays strong dependence upon the orientation of the magnetizations, $\bar{\mathbf{M}}$, (of **F1,F2;** assumed parallel) in relation to device channel's principal axis ($\hat{x}$). For $\bar{\mathbf{M}} \parallel \hat{x}$ (parallel to the channel), precessional effects are maximal. With increasing Rashba field, the variance in contributing path lengths causes the oscillations in R_S to decay, as was described previously for the case of finite external field. Here, however, contributions from short paths (direct propagation between the DSPR's involving few or no boundary reflections) continue to add coherently for large $\hat{\omega}_R$, resulting in very slow decay. For $\bar{\mathbf{M}} \parallel \hat{y}$, most of the injected carriers experience a Rashba field nearly aligned with their spin. At intermediate Rashba field these yield small oscillations that center about a *finite* value of R_S. The other carriers make a contribution to R_S at small $\hat{\omega}_R$, but this becomes incoherent and thus quickly decays for large $\hat{\omega}_R$.

B.3. Eight-Probe Model: Junction, Bulk, and Boundary Scattering

In general, transport under the ferromagnetic contact will not be completely diffusive. In this situation one must consider the effects of junction scattering in this region [225]. Fig. B.5 represents the simplest idealized case that captures the essential physics of junction scattering in a ballistic spin transport device. The polarized contacts are now modeled as a DSPR offset from the main channel by a ballistic "t"-junction. To analyze this situation, one must be explicitly consider 8 reserviors; *i.e.*, two spin reservoirs for each of the four physical contacts. The junction scattering matrix couples *all* of these ballistic channels. The requisite analysis is conceptually depicted by Fig. B.5b. For simplicity of the analysis, the external field is assumed to be applied only within the ballistic channel itself. In this configuration, the boundary constraints on currents and potentials can be succinctly represented as: $\mu_{F2\uparrow} = \mu_{2\uparrow}$, $\mu_{L\uparrow} = \mu_{L\downarrow}$, $\mu_{R\uparrow} = \mu_{R\downarrow}$, $I_{1\uparrow} = I$, $I_{1\downarrow} = 0$, $-I = I_{L\uparrow} + I_{L\downarrow}$, $0 = I_{R\uparrow} + I_{R\downarrow}$, and $I_{2\uparrow} = I_{2\downarrow} = 0$. As a result of the increased number of trajectories able to carry the current in this model, oscillations in the spin transresistance damp

more quickly than for the previous four-probe model. Fig. B.6 illustrates that only one oscillation peak is observable for this case.

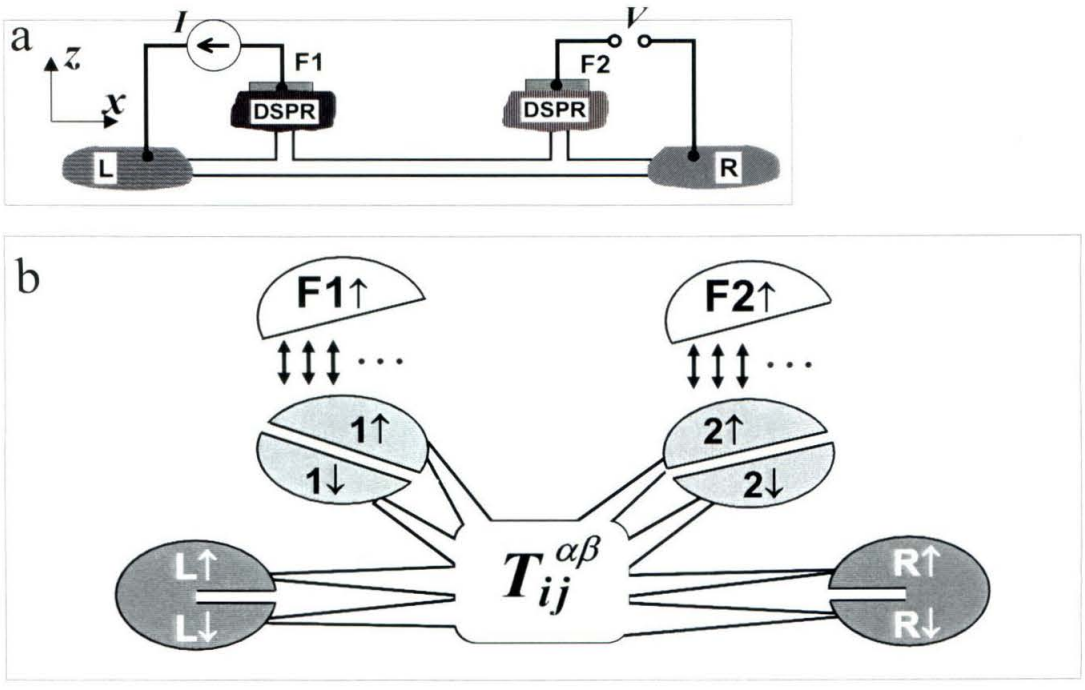

Fig. B.5 Full eight-probe model for ballistic spin injection in two dimensions which includes ballistic junction scattering effects. (a) The measurement configuration: a current, I, is injected through the 2DEG device channel via an a ferromagnetic contact (**F1**) and ohmic contact (**L**). The spin transresistance, $R_S = V/I$, arises from spin polarized carriers a distance L from the net current path, which induce a nonlocal voltage, V, between a second, similar, pair of contacts (**F2**, **R**). *(b)* The full 8-reservoir model; *complete* ellipses represent spin-relaxing reservoirs, *half* ellipses represent separate spin-resolved reservoirs. **F1** and **L** are current contacts, **F2** and **R** are voltage probes. $T_{ij}^{\alpha\beta}$ denotes the 2DEG device channel in which spin precession occurs.

In real devices, we must consider the role played by scattering. Spin flip scattering will serve to equalize the spin populations and uniformly suppress the spin transresistance. The effects of momentum scattering processes on R_S will also be important, but are more subtle. There are two kinds of random scatterings that must be considered: boundary scattering and bulk elastic scattering. In the simplest relaxation time treatment, they can be characterized by a mean free path l_e, and by a boundary specularity parameter p, respectively. For the latter, $p = 1$ implies completely specular reflection, while $p = 0$ represents completely diffuse scattering. Operationally, bulk scattering is modeled by imposing a probability $P(l) = \exp(-l/l_0)$ on all

ballistic trajectories, which is essentially the approach of Chambers[230]. It represents a given carrier's likelihood of survival (*i.e.*, remaining in a specific momentum state) on a given trajectory after traversing a distance *l*. Similarly, as we follow an electron's successive reflections at the channel boundaries (modeled as hard walls), the probability of a momentum-randomizing diffuse boundary collision is $1 - p$ per interaction. The evolution of spin transresistance in the presence of two types of diffusive scattering is depicted in Fig. B.7. As expected, the scattered trajectories act to suppress the "coherence" of spin transport in the junction. The oscillation peaks are notably suppressed when the mean free paths is about an order of magnitude larger than the channel width, or when the boundary specularity is less than about 90%. (The effects of these phenomena are coupled). In the completely diffuse limit, negative transresistance disappears and we get a monotonically-decreasing Hanle effect, such as observed in the first spin injection experiments (Fig. A.2), emerges [176].

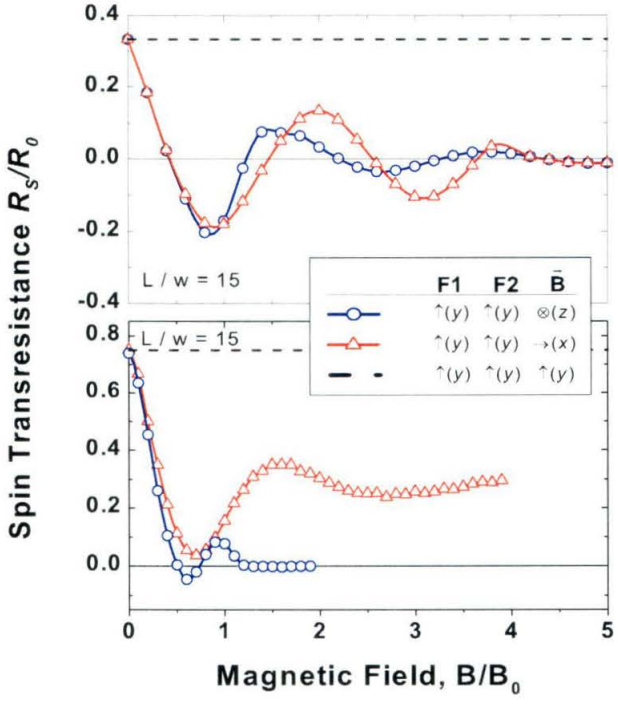

Fig. B.6. Spin transresistance as a function of applied magnetic field for three field configurations (indicated) and two measurement geometries. We assume a frequency ratio, $\omega_L/\omega_C = 0.19$, appropriate for InAs.

The dependence of the spin transresistance upon the spin-orbit coupling strength for finite bulk and boundary scattering is shown in Fig. B.8. We find that both tend to wash out spin related phenomena, *i.e.*, both the asymptotic effects and the high field oscillations.

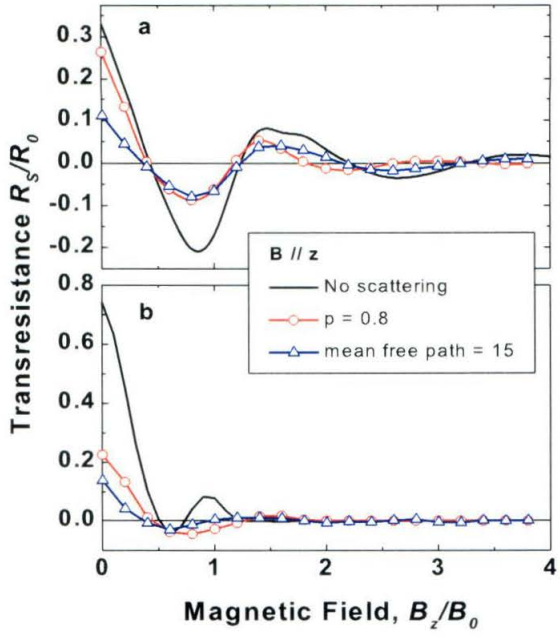

Fig. B.7 Spin transresistance as a function of perpendicular magnetic field in the presence of diffusive scattering. The clean limit is plotted as black curves for comparison. (a) results for the four-probe model. (b) Results for the eight-probe model that includes junction scattering. Here, the mean free path is normalized to the channel width; the specularity parameter p, is defined in the text.

B.4. The Spin Transistor: A Closer Look

The spin transistor was originally envisaged as allowing external control of the spin precession rate, via a gate potential acting in concert with the intrinsic confinement potential. In Fig. B.4 we show how a typical range of tunability, here assumed to be of order 30% (Sect.A.2.6), translates into direct modulation of R_S, for three device widths. Our calculations

clearly illustrate that the "conventional" spin transistor configuration, $\vec{\mathbf{M}} \parallel \hat{y}$, (which is most easily fabricated) is, in fact, *not* optimal—*even for a very short channel* ($L \sim \ell_s$). We find that tunability is maximized for $\vec{\mathbf{M}} \parallel \hat{x}$.

As originally conceived, the spin transistor was pictured as a one-dimensional device, with only a single transverse subband populated. Realizable devices in the near term will more likely employ two-dimensional or, perhaps, quasi-one-dimensional channels. Their increased phase space for scattering can lead to quick suppression of R_S, especially in the presence of moderate levels of diffuse boundary or bulk scattering within the channel. These results confirm that an extremely narrow channel is a basic requirement for a spin transistor.

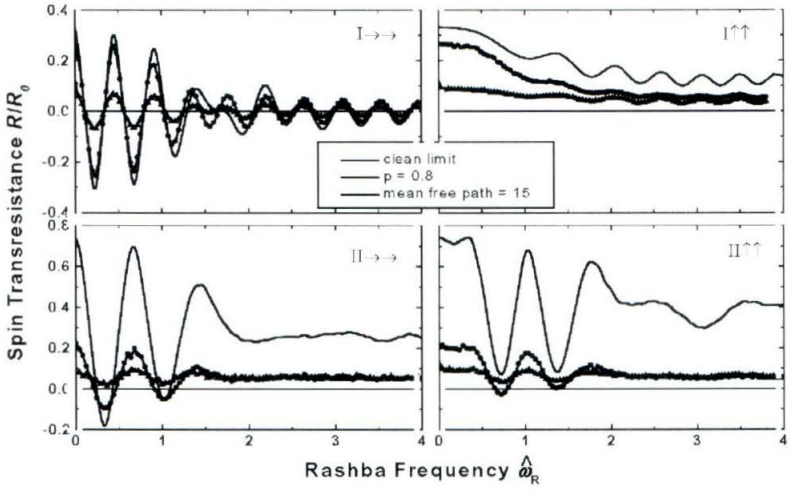

Fig. B.8 The influence of random scattering on spin transresistance as a function of the strength of the Rashba effect. Three scattering mechanisms are considered: junction scattering, impurity scattering, diffuse boundary scattering. The upper two panels are results from the four-probe model. The lower two panels are from eight-probe model.

B.5. Other Theoretical Treatments

Ballistic spin polarized transport in the presence of Rashba precession in semiconductor nanowires has also been recently addressed by Mireles *et al.* [231] and by Seba *et al.*[232]. The first authors include interfacial (Rashba) spin-orbit scattering, and extend the spin-independent Ando method [233] to generate a spin-dependent transfer matrix. By applying spin selective con-

tacts, an oscillatory conductance is calculated. The results they obtained are very similar in form to those generated previously by the simple approach described here, and displayed in Fig. B.4 and Fig. B.6.

The second recent approach to this problem, carried out by Seba *et al.* [232], treats a situation in which solely spin-orbit scattering is considered. A wave function similar to that originally employed by Elliott [234] is introduced to describe the spin flip process. They derive the rather surprising result that the spin-dependent transmission probabilities oscillate with increasing device length and may even reverse sign after traveling a certain distance through a region of disordered semiconductor containing a fixed concentration of scatterers.

In both of these recent theoretical models, the two-terminal conductance from a ferromagnetic source to a ferromagnetic drain is calculated. Their motivation is to interpret the recent experiment by Hu *et al.* [5]. We point out that hysteretic features in two-terminal resistance observed by Hu *et al.* are not a definitive demonstration of successful spin injection, since local Hall phenomena can not be precluded and a Hanle effect was not observed.

Appendix C. The QPC Spin Polarization Detector

C.1. Concept of a QPC detector

Quantum point contacts (QPC) or quantum dots (QD) can be employed to resolve the spin polarization attained after electric injection. In a QPC at zero magnetic field, conductance steps appear at quantized values proportional to $2g_0 = 2e^2/h$. (Fig. C.2a) It is well known that in a sufficiently large applied field, the quasi-1-D modes within the constriction become spin-split [225]. Hence, as the applied magnetic field is increased, the fundamental step height evolves to half its zero field value, $g_0 = e^2/h$ (Fig. C.2b). In effect, spin splitting induces a new set of plateaus that are not observed at zero field. The same phenomenon should be manifested when the spin bands become unequally populated within the constriction through *spin injection*.

Under the conditions of spin injection, one expects that the spin polarization of carriers within the 2DEG near the point of the injection will be spin-split. Thus there should exist a local nonequilibrium spin imbalance within the semiconductor electron gas, which we shall represent as $\Delta\mu = \mu_\uparrow - \mu_\downarrow$. If this spin polarized pool is used as the transport current within a QPC, the gate voltage dependence of the conductance will appear as

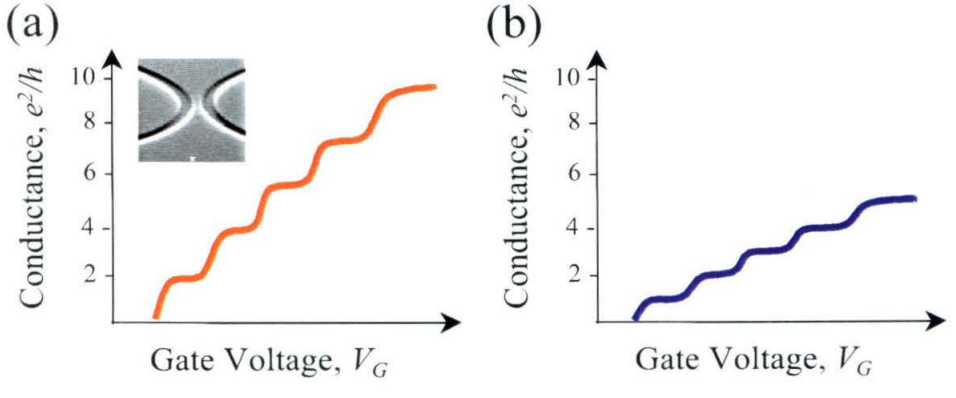

Fig. C.1. Conductance vs. gate voltage for a typical quantum point contact device.

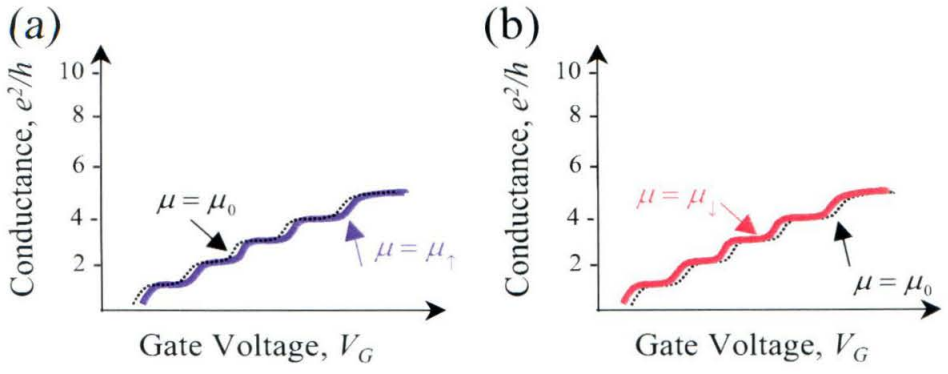

Fig. C.2. Conductance vs. gate voltage for spin-resolved quantum point contact device.

$$\sigma = \frac{1}{2}\left[\sigma\left(V_g + \Delta\mu/2e\right) + \sigma\left(V_g - \Delta\mu/2e\right)\right] \approx \sigma\left(V_g\right) + \frac{1}{2}\frac{\partial^2\sigma}{\partial V_g^{\,2}}\left(\frac{\Delta\mu}{2e}\right)^2. \tag{C.1}$$

Therefore, the perturbation to the conductance of the QPC is second order in the spin imbalance. In effect, compared to voltage positions of the plateaus expected in the equilibrium situation, the onset of the rising (to the quantum plateaus) is either accelerated or delayed for the spin-down and spin-up band, respectively, due to spin polarization. This shift is directly proportional to the spin splitting induced by injection.

C.2. Nonlinear a.c. Detection Scheme for Enhanced Sensitivity

The nonlinear dependence of the response of a QPC to spin injection offers a means of very sensitive detection. Schematic layout is shown in Fig. C.3. The QPC is formed by split gates at the center of the 2DEG channel, which are biased with respect to one end of the channel. The QPC is immersed in a spin polarized distribution of carriers, that have been spin injected from the single domain nanomagnets outward toward the Ohmic contact. Injector contacts formed by a variety of techniques, e.g., Ohmic, tunneling and Schottky, will be investigated.

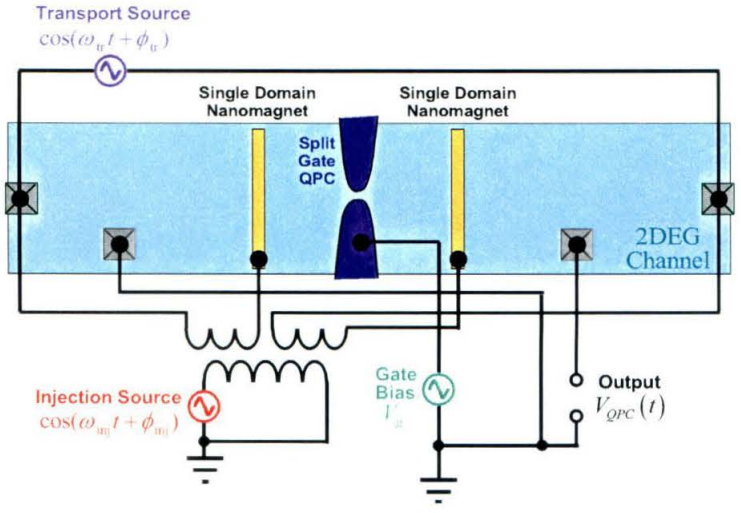

Fig. C.3. Schematic layout of the QPC spin polarization detector.

To achieve high sensitivity we proceed as follows: an a.c. injection current, applied at frequency ω_{inj} to spin polarize the channel, yields an electrochemical potential difference that will oscillate as

$$\Delta\mu(t) = \Delta\mu_0 \cos(\omega_{\text{inj}} t + \phi_{\text{inj}}) . \tag{C.2}$$

This current can be injected in a symmetric manner so that no net electrochemical potential difference appears between the (source and drain) contacts at either end of the QPC. If we then measure the QPC conductance using a separately modulated transport current, of the form

$$I(t) = I_0 \cos\left(\omega_{\text{tr}} t + \phi_{\text{tr}}\right), \tag{C.3}$$

the voltage drop from reservoir-to-reservoir (source to drain) along the QPC, $V_{QPC}(t)$, will then vary as

$$V_{QPC}(t) = I(t)\sigma_{QPC}^{-1} = I_0 \cos\left(\omega_{\text{tr}} t + \phi_{\text{tr}}\right)\left[\sigma(V_g)^{-1} - \frac{1}{8}\frac{\partial^2\sigma}{\partial V_g^{\,2}}\left(\frac{\Delta\mu_0}{e}\right)^2 \cos(\omega_{\text{inj}} t + \phi_{\text{inj}})^2\right]. \tag{C.4}$$

In Eq. 4.7 we have retained only second order terms in the small expansion parameter $\Delta\mu/(eV_g)$.

Expanding out the time-varying terms to determine the spectral response, we find three important harmonic components to the voltage waveform across the quantum point contact which we tabulate in Table C.1, where we have defined the following "resistances",

$$R(V_g) = \frac{1}{\sigma(V_g)}$$
$$R^{II}(V_g) = \frac{1}{16\sigma^2}\frac{\partial^2\sigma}{\partial V_g{}^2}\left(\frac{\Delta\mu_0}{e}\right)^2. \qquad \text{(C.5)}$$

These results show that by carefully nulling any voltage drop induced by the spin injection current (at its "carrier" frequency ω_{inj}), we can clearly select out the specific response from induced spin polarization by looking at the magnitude of either the $\omega_{tr} - 2\omega_{inj}$ or the $\omega_{tr} + 2\omega_{inj}$ terms. In fact, for small polarizations, with initial measurement of the (unpolarized)

Table C.1. Voltage waveform components across the QPC Spin Detector

Frequency	Phase	Magnitude
ω_{tr}	ϕ_{tr}	$I_0\left[R(V_g) + R^{II}(V_g)\right]$
$\omega_{tr} - 2\omega_{inj}$	$\phi_{tr} - 2\phi_{inj}$	$I_0 R^{II}(V_g)/2$
$\omega_{tr} + 2\omega_{inj}$	$\phi_{tr} + 2\phi_{inj}$	$I_0 R^{II}(V_g)/2$

$\sigma(V_g)$ and $\partial^2\sigma(V_g)/\partial V_g{}^2$ curves, it will be possible to directly extract the electrochemical potential difference in the vicinity of the QPC induced by spin injection.

The basic requirement in the above is that $V_{QPC} << k_B T/e$, and that $eV_{QPC} << \Delta\mu_0 << \varepsilon_F$. Another very important assumption is that the potential well of electron gas is rigid. In this case, application of V_g only shifts it upward or downward without changing its shape. This holds only locally for small changes about a fixed bias point, but should hold adequately to justify our present analysis.

If we vary the distance between the point contact and ferromagnets, we will expect the measured $\Delta\mu_0$ will decay exponentially with a characteristic length $\sqrt{D\tau_{sf}}$. This decay is schematically depicted in Fig. C.4.

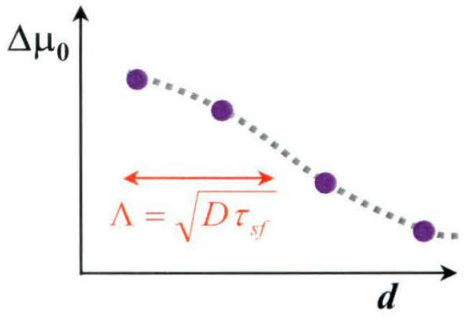

Fig. C.4. Schematic depiction of the spatial decay of the chemical potential difference arising from a spin injected current.

C.3. Estimate of Potential Sensitivity of the QPC Spin Polarization Detector

From (C.5), we find the ratio of the "resistances" is

$$\frac{R^{II}(V_g)}{R(V_g)} = \frac{1}{16\sigma}\frac{\partial^2\sigma}{\partial V_g^{\,2}}\left(\frac{\Delta\mu_0}{e}\right)^2 . \tag{C.6}$$

This ratio will allow us to determine the magnitude of the spin polarization signal compared to the (electrical) noise background, and thereby to place limits on the minimum detectable polarization via this technique.

To make progress, however, it is crucial to model the experimental smearing of the conductance steps since this will degrade the attainable resolution. If we assume that the broadening of the conductance steps originates solely from thermal smearing of the Fermi function, the conductance may be written as

$$\sigma = \frac{2e^2}{h}\sum_i \frac{1}{1+\exp\left[(E_i - E_F)/kT\right]} . \tag{C.7}$$

We note that, if desired, the broadening of the conductance curve due to elastic scattering can be empirically incorporated into this formula by take T as an effective scattering parameter, *i.e.*, T^*.

From this representation, it is not difficult to obtain the following relation

$$\frac{1}{\sigma}\frac{\partial^2\sigma}{\partial E_F{}^2} = \frac{1}{(kT)^2}\frac{\sum_i \frac{[\exp((E_i-E_F)/kT)-1]\exp((E_i-E_F)/kT)}{[1+\exp((E_i-E_F)/kT)]^3}}{\sum_i \frac{1}{1+\exp((E_i-E_F)/kT)}} \tag{C.8}$$

$$= \frac{1}{(kT)^2}\psi\left(\frac{E_i-E_F}{kT}\right).$$

This leads to the following ratio of magnitudes for the "resistances" defined in Eq. 4.8.

$$\frac{R^{II}(V_g)}{R(V_g)} = \frac{1}{16}\left(\frac{\Delta\mu_0}{kT}\right)^2\psi\left(\frac{E_i-E_F}{kT}\right). \tag{C.9}$$

We have already stated our assumption that $k_BT << \Delta\mu_0$. In Fig. C.5, this ratio Eq. (C.6) is depicted as function of subband spacing. Note that in a real device, the subband spacing is not identical to the change in V_g change but a small fraction (~0.1) of ΔV_g. Therefore, in real "device

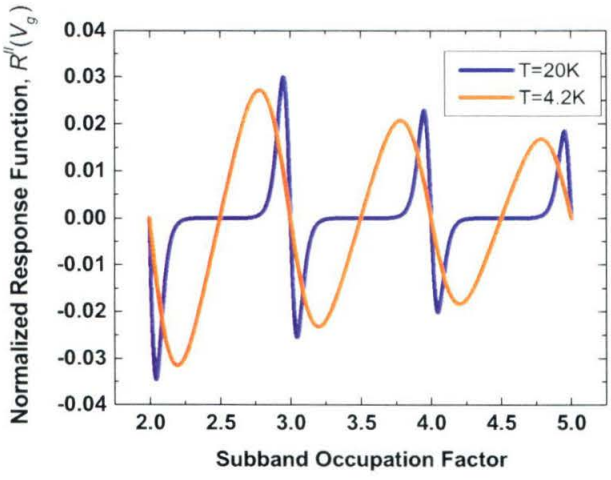

Fig. C.5. Normalized second derivative response function $(k_BT/e)^2\left[R^{II}(V_g)/R(V_g)\right]$ at two different effective electron temperatures 4.2 K and 20 K. Horizontal axis is represented in units of subband spacing.

units" the second derivative response may actually be scaled upward by a factor of order ~100.

To translate this to actual units, we assume that with state-of-the-art detection providing voltage sensitivity of order 0.1nV/√Hz, and transport currents of order 10 nA (which should obviate electron heating and its associated problems of undesired smearing, at least above roughly

~0.3K), a resistance noise floor of 10mΩ/√Hz is obtained. With 10s averaging times sensitivity of order a few mΩ should be possible. From Eq. 4.12 we arrive at the conclusion that

$$\Delta\mu_0 = k_B T \sqrt{16 \frac{\left[R^{II}(V_g)/R(V_g)\right]}{\left[\psi\left(E_i - E_F/k_B T\right)\right]}} \quad . \tag{C.10}$$

Hence, considering the results plotted in Fig. 4.8, and assuming we work below the second plateau ($R(V_g) \sim 8.6\,\mathrm{k\Omega}$, $R^{II}(V_g)\big|_{\min} / R(V_g) \sim 0.003/8600 = 3\times10^{-7}$) the minimum measurable chemical potential difference should be of order

$$\Delta\mu_0\big|_{\min} \sim k_B T \sqrt{16\,\frac{3\times10^{-7}}{3}} \sim 40\,\mathrm{neV} \text{ at } T=0.3\mathrm{K} \tag{C.11}$$

If the model of van Son *et al.* holds for our 2DEG systems, this would correspond to a minimum detectable polarization of order 0.01%. This high level of sensitivity will go a long way towards resolving outstanding issues regarding the efficiency of even the worst of current spin injection systems.

C.4. Initial QPC Spin Polarization Detection Devices

We have begun to investigate fabrication of various components of the QPC spin polarization detector schematically depicted in Fig. C.3. The first experimental issue is obtaining quantized conductance characteristics that are as sharp as possible. We have achieved remarkably good quantization with trench-etched devices even at T = 4.2K. As seen in the micrographs of Fig. C.6 and Fig. C.7, these are defined to have an adiabatic, gradually flared geometry to enhance the accuracy and robustness of the quantization. Although we have not yet tested these at temperatures below 1K, at liquid helium temperature they have provided the strongest quantized features that we have seen.

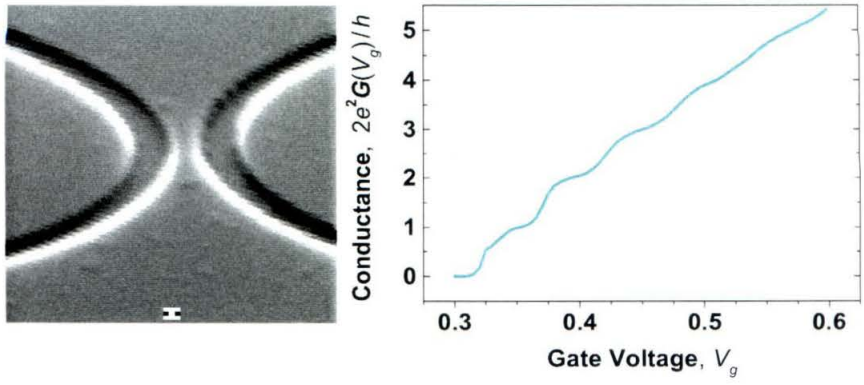

Fig. C.6. Experimental data from a trench isolated adiabatic point contact device at 4.2K.

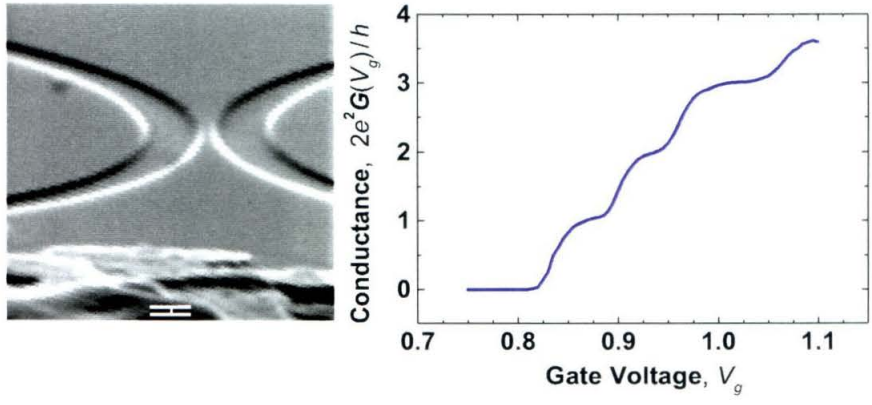

Fig. C.7. Experimental data from a second trench isolated adiabatic point contact device at 4.2K.

The fabrication of the in-plane self-gated QPC is great challenge. High mobility 2DEGs are usually very sensitive to defects induced in the fabrication process. Any dry etching process involved will be fatal in such a small structure, where the damage from side along can be as high as 100 nm deep. Though hard to control at submicron level, wet etching is the only existing technique that provides minimum perturbation to the electron gas. Before this work, there has been no recipe to achieve precise patterning of nanoscale devices in GaAs through a pure wet-etching process.

The quantum point contacts are fabricated from conventional high electron mobility transistor (HEMT) structures. The following layer sequence was grown by Molecular Beam Epitaxy (MBE): 1μm GaAs buffer, 20-40 nm $Ga_{0.7}Al_{0.3}As$ spacer, 20-40 nm $Ga_{0.7}Al_{0.3}As$ Si doped barrier layer, and a 5 nm GaAs cap layer. The 2DEG forms in the GaAs at the GaAs/GaAlAs interface. Three wafers with different spacer and barrier thickness are experimented, and correspondingly,

2DEG are buried at 45nm(GEN901), 65nm(GEN880), and 85nm(GEN901) below the surface of the heterostructure. At 4.2 K the carrier density is 1-3 × 10^{11} cm^{-2} and the mobility is 1.13 × 10^{6} cm^2/Vs, measured in the dark. GEN901 has very shallow 2DEG and allows a lower resistance for a Schottky type spin injection through the GaAlAs barriers.

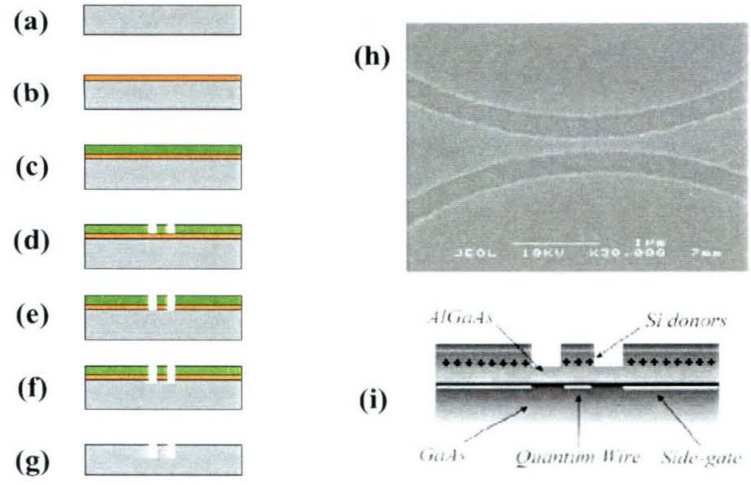

Fig. C.8. (a)-(g) Quantum point contact fabrication procedure: (a) Chip cleaning. (b) Very thin layer of photoresist is spun on the wafer. (c) PMMA coating. (d) Exposure and developing of PMMA. (e) Descum. (f) Citric acid etching. (g) Mask removal. (h) A top view of of semicircular shaped trenches in GaAs. (i) A side sketch of a shallow etched QPC with in-line gates.

In order to perform the shallow etch with well-controlled edges, we developed a special PMMA masked shallow wet-etching recipe to fabricate the in-plane gated QPC. The patterns are directly transferred from PMMA without any intermediate mask lift-off processes. This is a simple idea but not widely practiced mostly because PMMA does not stick very well to GaAs surface like photoresist.

The sample was processed with a 40 × 60 μm^2 mesa, etched 100nm, and AuGeNi ohmic contacts to the 2DEG were formed by conventional UV lithography and lift-off. In the process of wet etching, any kind of surface contamination will lead to preferential etching around the contaminations, evident from blurred edge profile and non-uniform etching on the sample. In addition, a clean surface is also required for a better adhesion to PMMA masking layer. An exhaustive cleaning procedure is performed before processing: The samples are first boiled in hot TCE, acetone, methanol respectively for 15 minutes; then the sample is dipped in 1IPA:4H_2O solution to remove metal particles trapped on the sample surface; after it is rinsed in DI water and

blow dried, the sample is transferred to an ozone dry stripper for 5 minutes to descum (vaporize) residual organic contamination on the chip surface, meanwhile forming a uniform oxide layer. This oxide layer is undesirable in that it causes initial delay in later wet-etch process and gives rise to uncontrolled etch rate. To remove this thin oxide layer, the sample is pre-etched in NH3:H_2O (1:10) solution for 10 seconds and dried in flowing N_2 gas. This also improves PMMA adhesion to the substrate. Within five minutes, the chip is baked to dehydrate or vapor primed in oven filled with N_2.

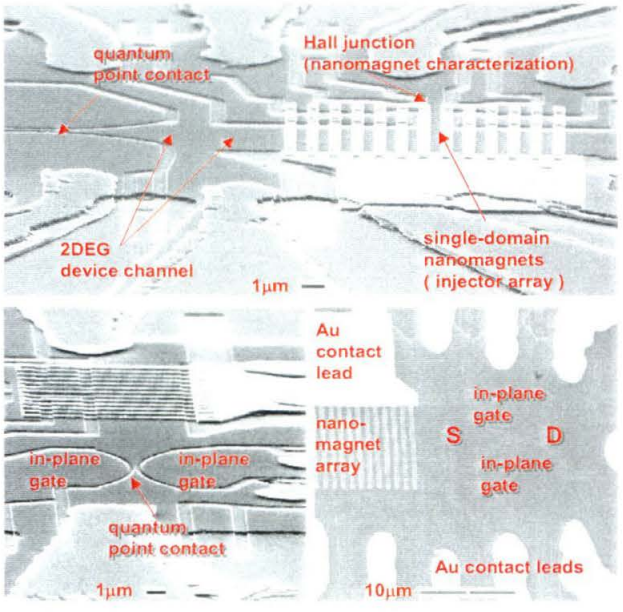

Fig. C.9. A complete QPC polarization detection device.

We use a very thin layer of photoresist as adhesion promotion layer for PMMA. Shipley photoresist 1813 is diluted until a very thin film (~20Å) can be obtained. After this very thin resist layer is spun and baked on the wafer, a 130nm thick PMMA layer is coated, and a normal treatment of PMMA is followed. PMMA is exposed and then developed to form a pattern consisting of two semicircular shaped trenches. The sample is then post baked for 3 minutes at 115°C, a temperature chosen to let PMMA just start to flow and seal the micro-poles formed during development, but without affecting the gap of the trenches. Afterward, the sample is ashed for 30s to remove residual photoresist at the bottom of the open trenches in PMMA. Transfer of the pattern into GaAs/GaAlAs heterostructure is performed by an etching solution of Citric acid: H_2O_2: H_2O solution (5:2:100 by volume, 120s). One drop of the solution is placed on the sample surface by means of a syringe. The surface tension will keep the drop remaining on sample

surface and the etching process is quenched by rinsing in deionized water. Simply dipping the sample into the etch solution destroys part of the resist layer and has very low yield. The overall fabrication process and a final device are illustrated in Fig. C.8.

In order to increase the total value of current that can be injected across the surface and to effectively dissipate heat generated by the sensing current, an array of identical magnets are employed in the first generation devices, in addition, an on-chip Hall cross on the their ends to

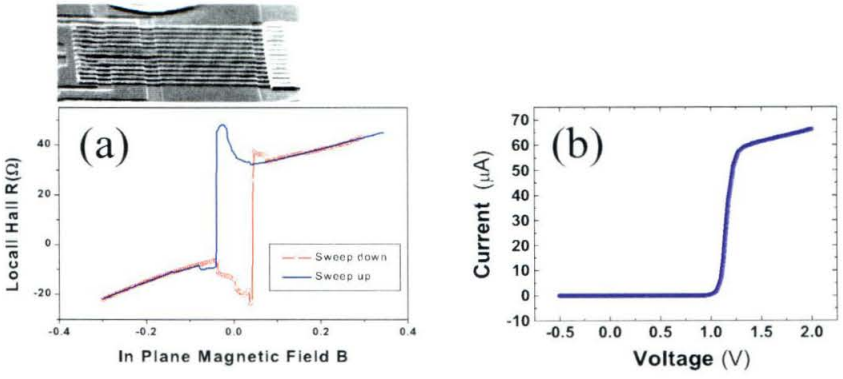

Fig. C.10. (a) Local Hall characterization of micro-magnet array. (b) I-V curve measured from the permalloy array/2DEG conctacts. In this device, the 2DEG is located about 85nm beneath the surface.

perform magnets characterization, as shown in Fig. C.9. By using the local Hall techniques, we found that the magnets switch coherently at well-defined in-plane magnetic field (Fig. C.10a). In Fig. C.10b, we display the I - V curve of the same magnet array. At a positive bias of 1.2V, we obtain a current density of 1.6×10^{6} A/m^2. The heterojunction used in this device has 2DEG layer buried 85nm below the heterostructure surface; injecting into shallower 2DEGs can significantly increase this injection current.

A complete prototype device displayed in Fig. C.9 will be tested shortly. Recently clear $0.5(2e^2/h)$ conductance steps have been observed[235] in a quantum point contact with a ferromagnetic Ni dot embedded at its center. Although how this Ni dot makes contact to 2DEG, and how it affects the electron gas are both unknown—this observation appears to confirm such an alternate scheme for detecting spin polarization.

Appendix D. Imaging Injected Nonequilibrium Spin Polarization by MRFM

Another potentially important form of detection maybe achievable through the emerging capabilities of magnetic resonance force microscopy (MRFM) [236-239]. The magnetic resonance force microscope is a novel scanned probe instrument that combines the three-dimensional capabilities of magnetic resonance imaging with the high sensitivity and resolution of atomic force microscopy. In the present context, it may allow non-destructive, scanned probe imaging of spin-polarized carriers within miniature spintronic devices.

When a spin-polarized current impinges on a paramagnetic acceptor it induces a difference in the chemical potentials at the interface for the up and down spin bands ($\mu_\uparrow$ and $\mu_\downarrow$, respectively, with $\Delta\mu = \mu_\uparrow - \mu_\downarrow$),

$$\Delta\mu = Pej\ell_{sf} / \sigma_F , \tag{D.1}$$

where P is the spin polarization of the injected current, e is the electron charge and σ_F is the electrical conductivity within the injector. If the acceptor's density of states at the Fermi energy ε_F is written as $N(\varepsilon_F)$, then the induced magnetization M within it can be written as

$$M = P\Delta\mu N(\varepsilon_F)\mu_B . \tag{D.2}$$

To provide an initial estimate of the spatial resolution we can attain, we consider injection from a semimagnetic MnZnSe Ohmic contact (injector) into an n+ GaAs epilayer. (Similar estimate could be made on the injection from ferromagnetic semiconductor GaMnAs Ohmic contact to p+GaAs.) We assume a carrier density of $n = 10^{17}$ cm^{-3}, a bulk GaAs mobility μ = 4×10^3 A/cm^2 (P = 0.5). Using these values we find $M \sim 2\times10^{18}$ $\mu_B$cm^{-3} = $2\times10^6\mu_B\mu$m^{-3} immediately adjacent to the injection interface. We expect that this spin polarization will decay with distance from the interface on a length scale of 100 μm [133], although that length was determined for hot, optically injected carriers.

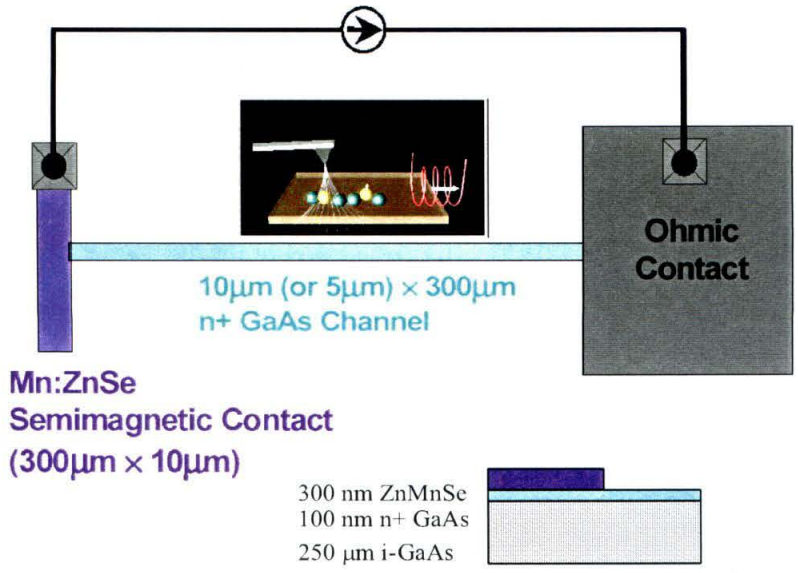

Fig. D.1. Geometry for imaging decay of injected spin polarization with distance from injection interface.

Given that the sensitivity of our present microscope is approximately 10^3 μ_B, this injected density will permit us resolve volumes with linear dimensions substantially smaller than 1 μm even on the tail of the spin accumulation curve far from injection interface. Recently, Martin [240] extended calculation to non-equilibrium spin current drift from ferromagnet into semiconductors and demonstrated significantly spin diffusion for a high non-equilibrium current density. Thurber *et al.* [241] accomplished the first spin polarization imaging by force-detected nuclear magnetic resonance. Instead of electron spin injection, they created and then observed nuclear spin polarization contrast in GaAs. Such nuclear spin contrast could be used indirectly to image electron spin polarization in GaAs-based spintronic devices.

Appendix E. Measurement Setup

Measurements in this thesis mostly are carried out in low temperature cryostats inserting into helium bath. If temperature variation is not desired, experiments were made at 4.2 K in a simple dipper that basically is a leak-tight brass can attached to a stainless steel tube. When temperature regulation is needed, a commercial He3 cryostat with a base temperature of about 300 mK is used.

Chips were mounted and bonded into a standard 28-pin chip carrier with wires running up the inside of the pumping line to connectors at the cryostat top. Heat sinking to the wires is provided at the coolest stage of the cryostat.

The measurement setups vary in each chapter of this thesis. But they base on an very simple electronics diagram shown in Figure E.1. In order to minimize noise from the line ground, separate ground is used for devices. The voltage output of a signal generator, usually at a frequency of 14 Hz (sometimes dc constant voltage), is fed into an opto-isolator, powered by a set of batteries and mounted in an electrically isolated panel. The voltage waveform at the output of the opto-isolator is reference to battery ground. This voltage is then applied across the series combination of a ballast resistor of 100 MΩ or 1 MΩ to provide a constant sensing ac or dc current.

The voltage signals generated in the standard four point measurement are in general sent to a differential preamplifier (EGG / Par / Stanford Research) with a gain of 10-10000 and then to a lock-in amplifier (or oscilloscope for dc measurement).

Magnetic field is supplied by feeding the current from magnetic power supply to a set of superconducting solenoids in the liquid helium bath. High field is achieved in a single 8 T superconducting solenoid in a separate dewar. In most measurements of the thesis, the magnetic fields are provided by a 3-axis superconducting magnet, consisting of one solenoid for the vertical and two split coils for the lateral in-plane fields. Each of these magnets could be operated alone to provide 1 T field, or could be operated together to generate a field up to 1 T in any direction.

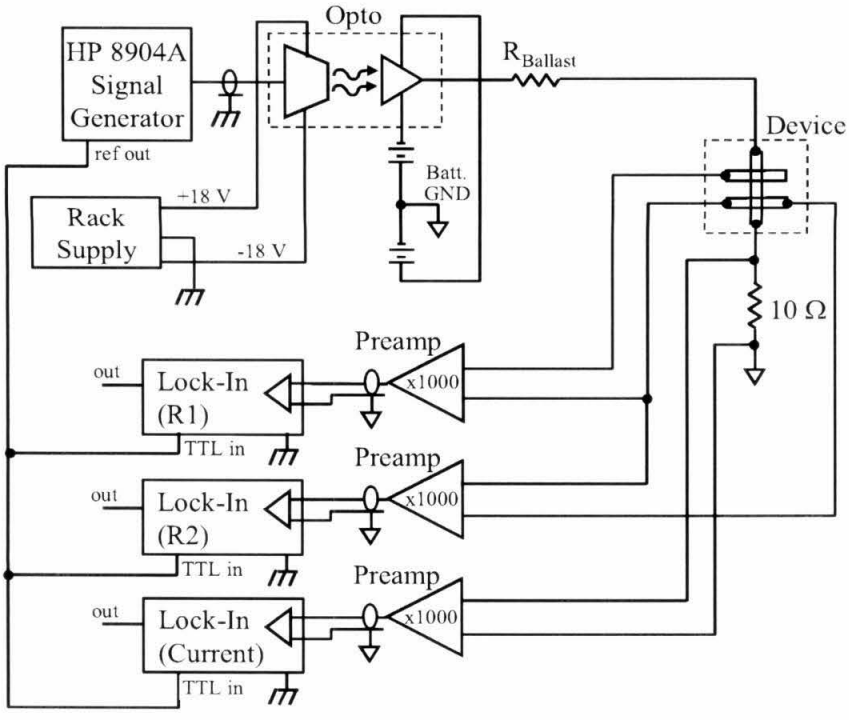

Fig. E.1. Schematic diagram of the experimental setup. All wires are coax and shielding is provided by the enclosure.

Reference

1. Parkin, S.S.P., IBM J. Res. Develop., 1998. 42: p. 3.
2. Moodera, J.S. and G. Mathon, J. Magn. Magn. Mater., 1999. 200: p. 248.
3. Datta, S. and B. Das, Appl. Phys. Lett., 1990. 56: p. 665.
4. Kikkawa, J.M. and D.D. Awschalom, Phys. Rev. Lett., 1998. 80: p. 4313.
5. Hu, C.M., et al., Phys. Rev. B, 2001. 63: p. 125333.
6. S.Gardelis, et al., Phys. Rev. B, 1999. 60: p. 7764.
7. Hammar, P.R., et al., Phys. Rev. Lett., 1999. 83: p. 203.
8. Monzon, F.G., D.S. Patterson, and M.L. Roukes, J. Magn. Magn. Mater., 1999. 198: p. 632.
9. Monzon, F.G. and M.L. Roukes, J. Magn. Magn. Mater, 1999. 195: p. 19.
10. Prins, M.W.J., et al., J. Phys. Cond. Matt., 1995. 7: p. 9447.
11. Filipe, A., et al., Phys. Rev. Lett., 1998. 80: p. 2425.
12. Schmidt, G., et al., Phys. Rev. B, 2000. 62: p. R4790.
13. Schmidt, G. and L.W. Molenkamp, Physica E, 2001. 10: p. 484.
14. Fiederling, R., et al., Nature, 1999. 402: p. 787.
15. Ohno, Y., et al., Nature, 1999. 402: p. 790.
16. Johnson, M. and R.H. Silsbee, Phys. Rev. Lett., 1985. 55: p. 1790.
17. Johnson, M., Science, 1993. 260: p. 320.
18. Jedema, F.J., A.T. Filip, and B.J.v. Wees, Nature, 2001. 410: p. 345.
19. Alvarado, S.F. and P. Renaud, Phys. Rev. Lett., 1992. 68: p. 1387.
20. Ferreira, R. and G. Bastard, Phys. Rev. B, 1991. 43: p. 9687.
21. Stoner, E.C. and E.P. Wohlfarth, Philos. Trans. R. Soc. London A, 1948. 240: p. 74.

22. Ohno, H., et al. in *Proceedings of the 23rd International Conference on the Physics of Semiconductors*. 1996. Berlin: World Scientific, Singapore.

23. When the field ramp range is large, coherent rotation of magnetization can be significant. We believe this explains the anomalous tails in M-H curves that are commonly observed in dilute magnetic semiconductors.

24. Fukumura, T., et al., Physica E, 2001. 10: p. 135.

25. Pan, J.P., *Galvanomagnetic and Thermomagnetic Effects in Metals*, in *Solid State Physics*, F. Seitz and D. Turnbull, Editors. 1957, New York Academic Press. p. 1-96.

26. Hong, K.M. and N. Giordano, Phys. Rev. B, 1995. 51: p. 9855.

27. Cowburn, R.P., et al., J. Appl. Phys., 1995. 78: p. 7210.

28. Hubert, A. and R. Schäfer, *Magnetic Domains*. 1998, Springer-Verlag: Berlin. p. 235.

29. Cowburn, R.P., S.J. Gray, and J.A.C. Bland, Phys. Rev. Lett., 1997. 79: p. 4018.

30. König, J., T. Jungwirth, and A.H. MacDonald, Phys. Rev. B, 2001. 64: p. 194423.

31. Abolfath, M., et al., Phys. Rev. B, 2001. 63: p. 054418.

32. Dietl, T., H. Ohno, and F. Matsukura, Phys. Rev. B, 2001. 63: p. 195205.

33. Dietl, T., et al., Science, 2000. 287: p. 1019.

34. Oiwa, A., et al., Phys. Stat. Sol., 1998. 205: p. 167.

35. Ono, T., et al., Science, 1999. 37: p. 468.

36. Wunderlich, J., et al., IEEE Trans. Magn., 2001. 37: p. 2104.

37. Yan, S.S., et al., J. Magn. Magn. Mater., 2000. 210: p. 309.

38. Ogrin, F.Y., S.L. Lee, and Y.F. Ogrin, J. Magn. Magn. Mater., 2000. 219: p. 331.

39. McGuire, T. and R.I. Potter, IEEE Trans. Magn., 1975. MAG-11: p. 1018.

40. Choe, S.B. and S.C. Shin, Phys. Rev. Lett., 2001. 86: p. 532.

41. Lemerle, S., et al., Phys. Rev. Lett., 1998. 80: p. 849.

42. Kooten, M.v., et al., J. Appl. Phys., 1994. 75: p. 5508.

43. Lyle, T.R. and J.M. Baldwin, Phil. Mag., 1906. 12: p. 434-68.

44. Weiss, P., J. Phys. Theor. Appl., 1907. 4E: p. 661-90.

45. Landau, L. and E. Lifshitz, Phys. Z. SowjUn., 1931(8): p. 153.

46. Sixtus, K.J. and L. Tonks, Phys. Rev., 1931. 37: p. 930.

47. Sixtus, K.J. and L. Tonks, Phys. Rev., 1932. 42: p. 419.

48. Shigeto, K., T. Shinjo, and T. Ono, Appl. Phys. Lett., 1999. 75: p. 2815.

49. Cullity, B.D., *Introduction to Mangetic Materials*. 1972, Addison-Wesley: Reading, MA.

50. Tsang, C.H., R.L. White, and R.M. White, J. Appl. Phys., 1978. 49: p. 60603.

51. Blatter, G., et al., Rev. Mod. Phys., 1994. 66: p. 1125.

52. Laurune, M., et al., J. Magn. Magn. Mater., 1989. 80: p. 211.

53. Cabrera, G.G. and L.M. Falicov, Phys. Status Solidi B, 1974. 61: p. 59.

54. Cabrera, G.G. and L.M. Falicov, Phys. Status Solidi, 1974. 62: p. 217.

55. Berger, L., J. Appl. Phys., 1978. 49: p. 2156.

56. Viret, M., et al., Phys. Rev. Lett., 2000. 85: p. 3962.

57. Ruediger, U., et al., Phys. Rev. Lett., 1998. 80: p. 3639.

58. Klein, L., et al., Phys. Rev. Lett., 2000. 84: p. 6090.

59. Danneau, R., et al., Phys. Rev. Lett, 2002. 88: p. 157201.

60. Ebels, U., et al., Phys. Rev. Lett., 2000. 84: p. 983.

61. Taniyama, T., et al., Phys. Rev. Lett., 1999. 82: p. 2780.

62. Xu, Y.B., et al., Phys. Rev. B, 2000. 61: p. R14901.

63. Levy, P.M. and S. Zhang, Phys. Rev. Lett., 1997. 78: p. 3773.

64. Gorkom, R.P.v., A. Brataas, and G.E.W. Bauer, Phys. Rev. Lett., 1999. 83: p. 4401.

65. Viret, M., et al., Phys. Rev. B, 1996. 53: p. 8464.

66. Vignale, G. and M.E. Flatté, Cond-mat/0202002, 2002.

67. Schwab, K., et al., Nature, 2000. 404: p. 974.

68. Tighe, T.S., J.M. Worlock, and M.L. Roukes, Appl. Phys. Lett., 1997. 70: p. 2687.

69. Beck, R.G., et al., Appl. Phys. Lett., 1996. 68: p. 3723.

70. Beck, R.G., et al., Appl. Phys. Lett., 1998. 73: p. 1149.

71. Chen, C.J., *Introduction to Scanning Tunneling Microscopy*. 1993, New York: Oxford University Press.

72. Cottam, R.I. and G.A. Sanders, in *Gallium Arsenide*, J.S. Blakemore, Editor. 1987, American Inistitute of Physics: New York.

73. Blakemore, J.S., *Gallium Arsenide*. 1987, New York: American Inistitute of Technology.

74. Adachi, S., J. Appl. Phys., 1985. 58: p. R1.

75. Fricke, K., J. Appl. Phys., 1991. 70: p. 914.

76. Fatti, N.D., et al., J. Chem. Phys., 1999. 110: p. 11484.

77. Kelly, M.J., J. Phys.: Solid State Phys., 1982. 15: p. L969.

78. Lee, K.L., et al., Electron. Lett., 1984. 20: p. 289.

79. Smith, C.G., H. Ahmed, and M.N. Wybourne.

80. Seyler, J. and M.N. Wybourne, Phys. Rev. Lett., 1992. 69: p. 1427.

81. Potts, A., et al., Semicond. Sci. Technol., 1992. 7: p. B231.

82. Fujisawa, T., et al., Science, 1998. 282: p. 932.

83. Thornton, T.J., et al., Phys. Rev. Lett., 1989. 63: p. 2128.

84. Houten, H.v., et al., Surf. Sci., 1988. 196: p. 144.

85. Pippard, A.B., *Magnetoresistance in Metals*. 1989, Cambridge: Cambridge University Press.

86. Akera, H. and T. Ando, Phys. Rev. B, 1991. 43(11676).

87. Roukes, M.L., et al., Phys. Rev. Lett., 1987. 59: p. 3011.

88. Chang, A.M., T.Y. Chang, and H.U. Baranger, Phys. Rev. Lett., 1989. 63: p. 996.

89. Beenakker, C.W.J. and H.v. Houten, Phys. Rev. Lett., 1989. 63: p. 1857.

90. Washburn, S. and R.A. Webb, Rep. Prog. Phys., 1992. 55: p. 1311.

91. Haucke, H., et al., Phys. Rev. B, 1990. 41: p. 12454.

92. Chang, A.M., et al., Superlatt. Microstruc., 1988. 4: p. 515.

93. Bird, J.P., et al., J. Phys.: Condens. Matter, 1990. 2: p. 7847.

94. Skocpol, W.J., et al., Phys. Rev. Lett., 1987. 58: p. 2347.

95. Beenakker, C.W.J. and H.v. Houten, eds. Solid State Physics, ed. H.E. Ehrenbach and D. Turnbull. 1991, CA: Academic: San Diego.

96. Beenakker, C.W.J. and H.v. Houten, Phys. Rev. B, 1988. 37: p. 6544.

97. Tilmans, H.A.C., M. Elwenspoek, and J.H.J. Fluitman, Sens. Actuators A, 1992. 30: p. 35.

98. Carr, D.W., et al., Appl. Phys. Lett., 1999. 75: p. 920.

99. Cleland, A.N. and M.L. Roukes, Appl. Phys. Lett., 1991. 75: p. 699.

100. Rugar, D. and P. Grutter, Phys. Rev. Lett., 1991. 67: p. 699.

101. Vries, D.K.d., P. Stelmaszyk, and A.D. Wieck, J. Appl. Phys., 1996. 79: p. 8087.

102. Tedrow, P.M. and R. Meservey, Phys. Rev. Lett., 1971. 26: p. 192.

103. Meservey, R., D. Paraskevopoulos, and P.M. Tedrow, Phys. Rev. Lett., 1976. 37: p. 858.

104. Tedrow, P.M., Physics Reports, 1994. 238: p. 173.

105. Stearns, M.B., J. Magn. Magn. Mater., 1977. 5: p. 167.

106. Sloncezwski, J.C., Phys. Rev. B, 1989. 39: p. 6995.

107. Zhang, S. and P.M. Levy, Phys. Rev. Lett., 1998. 81: p. 5660.

108. Maclaren, J.M., W.H. Butler, and X.-G. Zhang, J. Appl. Phys., 1998. 83: p. 6521.

109. Maclaren, J.M., et al., Phys. Rev. B, 1998. 59: p. 5470.

110. Tsymbal, E.Y. and D.G. Pettifor, J. Phys. Condens. Matter, 1997. 9: p. L411.

111. Tsymbal, E.Y. and D.G. Pettifor, Phys. Rev. B, 1998. 58: p. 432.

112. Julliere, M., Phys. Lett., 1975. 54A: p. 225.

113. Aronov, A.G., Pis'ma Zh. Eksp. Teor. Fiz., 1976. 24: p. 37.

114. Johnson, M. and R.H. Silsbee, Phys. Rev. B, 1988. 37: p. 5712.

115. Johnson, M. and R.H. Silsbee, Phys. Rev. B, 1988. 37: p. 5326.

116. Lubzens, D. and S. Schultz, Phys. Rev. Lett., 1976. 36: p. 1104.

117. Son, P.C.v., H.v. Kempen, and P. Wyder, Phys. Rev. Lett., 1987. 58: p. 2271.

118. Broad, W.J., in *New York Times*. 1993. p. p. C1.

119. Keller, J.J., in *The Wall Street Journal*. 1993. p. p. C21.

120. Johnson, M., Nanotechnology, 1996. 7: p. 390.

121. Prinz, G.A., Science, 1998. 282: p. 1660.

122. Zutic, I., J. Fabian, and S.D. Sarma, Phys. Rev. B, 2001. 64: p. 121201.

123. Zutic, I., J. Fabian, and S.D. Sarma, Appl. Phys. Lett., 2001. 79: p. 1558.

124. Flatte, M.E. and G. Vignale, Appl. Phys. Lett., 2001. 78: p. 1273.

125. Katine, J.A., et al., Phys. Rev. Lett., 2000. 84: p. 3149.

126. Kawakami, R.K., et al., Science, 2001. 294: p. 131.

127. Wees, B.J.v., et al., Phys. Rev. Lett., 1988. 60: p. 848.

128. Wharam, D.A., et al., J. Phys. C, 1988. 21: p. L209.

129. Yacoby, A., et al., Phys. Rev. Lett., 1996. 77: p. 4612.

130. Frank, S., et al., 33. Science, 1998. 280: p. 1744.

131. Kikkawa, J.M., et al., Science, 1997. 277: p. 1284.

132. Hagele, D., et al., Appl. Phys. Lett., 1998. 73: p. 1580.

133. Kikkawa, J.M. and D.D. Awschalom, Nature, 1999. 397: p. 139.

134. Potemski, M., et al., Solid State Commun., 1999. 110: p. 163.

135. Rashba, E.I., Fiz. Fiz. Tverd. Tela (Leningrad), 1960. 2: p. 1224.

136. Nitta, J., T. Akazaki, and H. Takayanagi, Phys. Rev. Lett., 1997. 78: p. 1335.

137. Hu, C.M., et al., Phys. Rev. B, 1999. 60: p. 7736.

138. Heida, J.P., et al., Phys. Rev. B, 1998. 57: p. 11911.

139. Papadakis, S.J., et al., Science, 1999. 283: p. 2056.

140. Rossler, U., Solid State Commun., 1984(49): p. 943.

141. Cardona, M., N.E. Christensen, and G. Fasol, Phys. Rev. B, 1988. 38: p. 1806.

142. Lommer, G., F. Malcher, and U. Rossler, Phys. Rev. Lett., 1988. 60: p. 728.

143. Mayer, H. and U. Rossler, Phys. Rev. B, 1991. 44: p. 9049.

144. For a review, s., in *Optical Orientation*, F. Maier and B. Zakharchenya, Editors. 1984, North-Holland: Amsterdam.

145. Riechert, H., H.J. Drouhin, and C. Hermann, Phys. Rev. B, 1988. 38: p. 4146.

146. Dresselhaus, P.D., et al., Phys. Rev. Let., 1992. 68: p. 106.

147. Jusserand, B., et al., Phys. Rev. Lett., 1992. 69: p. 848.

148. Luo, J., et al., Phys. Rev. B, 1988. 38: p. 10142.

149. Brosig, S., et al., Phys. Rev. B, 1999. 60: p. 13989.

150. Sasa, S., et al., Physica B, 1999. 272: p. 149.

151. Nitta, J., et al., Physica E, 1998. 2: p. 527.

152. Grundler, D., Phys. Rev. Lett, 2000. 84: p. 6074.

153. Matsuyama, T., et al., Phys. Rev. B, 2000. 61: p. 15588.

154. Stein, D., K.v. Klitzing, and G. Weimann, Phys. Rev. Lett., 1983 . 51: p. 130.

155. Lommer, G., F. Malcher, and U. Rossler, Phys. Rev. B, 1985. 32: p. 6965.

156. Ramvall, P., B. Kowalski, and P. Omling, Phys. Rev. B, 1997. 55: p. 7160.

157. Stormer, H.L., et al., Phys. Rev. Lett., 1983. 51: p. 126.

158. Eisensten, J.P., et al., Phys. Rev. Lett., 1984. 53: p. 2579.

159. Lu, J.P., et al., Phys. Rev. Lett., 1998. 81: p. 1282.

160. Das, B., et al., Phys. Rev. B, 1989. 39: p. 1411.

161. Yamada, S., et al., Physica E, 2000. 7: p. 992.

162. Engels, G., et al., Phys. Rev. B. 55: p. 1958.

163. Koester, S.J., et al., Phys. Rev. B, 1994. 50: p. 5710.

164. Chen, G.L., et al., Phys. Rev. B, 1993. 47: p. 4084.

165. Boggess, T.F., et al., Appl. Phys. Lett., 2000. 77: p. 1333.

166. D'yakanov, M.I. and V.I. Perel', Zh. Eskp. Teor. Fiz., 1971. 60: p. 1954.

167. Fert, A. and S.-F. Lee, Phys. Rev. B, 1996. 53: p. 6554.

168. Prins, M.W.J., R. Jansen, and H.v. Kempen, Phys. Rev. B, 1996. 53: p. 8105.

169. W.Y.Lee, et al., J. Appl. Phys., 1999. 85: p. 6682.

170. Filip, A.T., et al., Phys. Rev. B, 2000. 62: p. 9996.

171. Monzon, F.G., M. Johnson, and M.L. Roukes, Appl. Phys. Lett., 1997. 71: p. 3087.

172. Gijs, M.A.M. and G.E.W. Bauer, Advances in Physics, 1997. 46: p. 285.

173. Ansermet, J.-P., J. Phys. Condens. Matter, 1998. 10}: p. 6027.

174. Fert, A., I.A. Campbell, and J.d. Physique, Colloque C!, 1971. 32: p. C1-46.

175. Valet, T. and A. Fert, Phys. Rev. B, 1993. 48: p. 7099.

176. Johnson, M. and R.H. Silsbee, Phys. Rev. B, 1987. 35: p. 4959.

177. Dubois, S., et al., Phys. Rev. B, 1999. 60: p. 477-484.

178. Herschfield, S. and H.L. Zhao, Phys. Rev. B, 1997. 56: p. 3296.

179. Beuneu, F. and P. Monod, Physica B, 1977. 86-88: p. 265.

180. Brataas, A., Y.V. Nazarov, and G.E.W. Bauer, Phys. Rev. Lett., 2000. 84: p. 2481.

181. Rashba, E.I., Phys. Rev. B, 2000. 62: p. R16267.

182. See, e.g., and G.A. Prinz, Physics Today, 1995. 48: p. 58.

183. Nitta, J., Private Communication.

184. Jia, Y.Q., R.C. Shi, and S.Y. Chou, IEEE Trans. Magn., 1996. 32: p. 4707.

185. Alphenaar, B.W., K. Tsukagoshi, and M. Wagner, J. Appl. Phys., 2001. 89: p. 6863.

186. Awschalom, D.D. and J.M. Kikkawa, Physics Today, 1999. 52: p. 33.

187. Malajovich, I., et al., Phys. Rev. Lett., 2000. 84: p. 1015.

188. Malajovich, I., et al., Nature, 2001. 411: p. 770.

189. Kamper, K.P., et al., Phys. Rev. Lett., 1987. 59: p. 2788.

190. Groot, R.A.d., et al., Phys. Rev. Lett., 1983. 50: p. 2024.

191. Monzon, F.G., H.X. Tang, and M.L. Roukes, Phys. Rev. Lett., 2000. 84: p. 5022.

192. Wees, B.J.v., Phys. Rev. Lett., 2000. 84: p. 5023.

193. Hammar, P.R., et al., Phys. Rev. Lett., 2000. 84: p. 5024.

194. Johnson, M., Phys. Rev. B, 1998. 58: p. 9635.

195. Grundler, D., Phys. Rev. Lett., 2001. 86: p. 1058.

196. Hu, C.M. and T. Matsuyama, Phys. Rev. Lett., 2001. 87: p. 6803.

197. Silsbee, R.H., Phys. Rev. B, 2001. 63: p. 155303.

198. Molenkamp, L.W., G. Schmidt, and G.E.W. Bauer, Phys. Rev. B, 2001. 64: p. 121202.

199. Upadhyay, S.K., et al., Phys. Rev. Lett., 1998. 81: p. 3247.

200. Upadhyay, S.K., R.N.L. RN, and R.A. Buhrman, Appl. Phys. Lett., 1999. 74: p. 3881.

201. LaBella, V.P., et al., Science, 2001. 292: p. 1518.

202. Smith, D.L. and R.N. Silver, Phys. Rev. B, 2001. 64: p. 045323.

203. Heersche, H.B., et al., Phys. Rev. B, 2001. 64: p. 161307.

204. Prinz, G.A., G.T. Rado, and J.J. Krebs, J. Appl. Phys., 1982. 53: p. 2087.

205. Monchesky, T.L., et al., J. Appl. Phys., 2000. 87: p. 5167.

206. Krebs, J.J., B.T. Jonker, and G.A. Prinz, J. Appl. Phys., 1987. 61: p. 2596.

207. Daboo, C., et al., Phys. Rev. B, 1995. 51: p. 15964.

208. Filipe, A., A. Schuhl, and P. Galtier, Appl. Phys. Lett., 1997. 70: p. 129.

209. Bland, J.A.C., et al., J. Appl. Phys., 2001 . 89: p. 6740.

210. Chen, L.C., et al., J. Vac. Sci. Tech. B, 2000. 18: p. 2057.

211. Bensch, F., et al., J. Appl. Phys., 2001. 89: p. 7133.

212. Xu, Y.B., et al., Appl. Phys. Lett., 1998. 73: p. 399.

213. Xu, Y.B., et al., J. Appl. Phys., 1999. 85: p. 5369.

214. Lee, W.Y., et al., J. Appl. Phys., 2000. 87: p. 5926.

215. Kirczenow, G., Phys. Rev. B, 2001. 63: p. 054422.

216. Grundler, D., Phys. Rev. B, 2001. 63: p. R161307.

217. Smith, D.L., et al., Phys. Rev. B, 2000. 61: p. 13914.

218. Zhu, H.J., et al., Phys. Rev. Lett., 2001. 87: p. 016601.

219. Hanbicki, A.T., et al., Preprint: p. 2001.

220. Monsma, D., et al., Phys. Rev. Lett., 1995. 74: p. 5260.

221. Jansen, R., et al., J. Appl. Phys., 2001. 89: p. 7431.

222. Rippard, W.H. and R.A. Buhrmann, Phys. Rev. Lett., 2000. 84: p. 971.

223. Oestreich, M., et al., Appl. Phys. Lett., 1999. 74: p. 1251.

224. Jonker, B.T., et al., Phys. Rev. B, 2000. 62: p. 8180.

225. Beenakker, C.W.J. and H.v. Houten, in *Solid State Physics*. 1991, Academic Press. p. pp1-170.

226. Buttiker, M., Phys. Rev. Lett., 1986. 57: p. 1761.

227. Tang, H.X., et al., Phys. Rev. B, 2000. 61: p. 4437.

228. Beenakker, C.W.J. and H.v. Houten, Phys. Rev. Lett., 1989. 63: p. 1857.

229. Sharvin, Y.V., Zh. Eksp. Teor. Fiz., 1965. 48: p. 984.

230. Chambers, R.G., Proc. Phys. Soc., 877. London: p. 81.

231. Mireles, F. and G. Kirczenow, Phys. Rev. B, 2001. 64: p. 024426.

232. Seba, P., et al., Phys. Rev. Lett., 2001. 86: p. 1598.

233. Ando, T., Phys. Rev. B, 1991. 44: p. 8017.

234. Elliott, R.J., Phys. Rev., 1954. 96: p. 266.

235. Kikutani, T., N. Aoki, and S. Yamada, Phys. Rev. B, 2000. 61: p. 9956.

236. Sidles, J.A., Appl. Phys. Lett., 1991. 58: p. 2854.

237. Sidles, J.A., Phys. Rev. Lett., 1992. 68: p. 1124.

238. Rugar, D., C.S. Yannoni, and J.A. Sidles, Nature, 1992. 360: p. 563.

239. Hammel, P.C., et al., J. Low Temp. Phys., 1995. 101: p. 59.

240. Martin, I., cond-mat/0201481, 2002.

241. Thurber, K.R., et al., *cond-mat/0201216*. 2002.